NEUTRON SCATTERING FROM ^{28}Si AND ^{32}S: CROSS SECTIONS AND ANALYZING POWERS FROM 8 TO 40 MEV

by

Calvin R. Howell

Department of Physics
Duke University

Date: Feb 14, 1984

Approved:

Richard L Walter
Richard L. Walter, Supervisor

A dissertation submitted in partial fulfillment of the requirements for the degree of Doctor of Philosophy in the Department of Physics in the Graduate School of Duke University

1984

Abstract

NEUTRON SCATTERING FROM ^{28}Si AND ^{32}S:
CROSS SECTIONS AND ANALYZING POWERS FROM 8 TO 40 MEV

by

Calvin R. Howell

Department of Physics
Duke University

Date: Feb. 14, 1984

Approved:

Richard L Walter
Richard L. Walter, Supervisor

J R Tinsley

M.Y. Han

Henry R Weller

J K Bair

An abstract of a dissertation submitted in partial fulfillment of the requirements for the degree of Doctor of Philosophy in the Department of Physics in the Graduate School of Duke University

1984

ABSTRACT

NEUTRON SCATTERING FROM ^{28}Si AND ^{32}S:

CROSS SECTIONS AND ANALYZING POWERS FROM 8 TO 40 MEV

by

Calvin R. Howell

Analyzing powers $A_y(\theta)$ for neutron scattering to the ground and first excited states of natural silicon and sulfur from 20° to 155° c.m. have been measusred at incident neutron energies of 10, 14, and 17 MeV. To obtain these data, the 0° neutrons from the $^2H(\vec{d},\vec{n}_0)^3He$ polarization transfer reaction were scattered from cylindrical samples into two symmetrically positioned side detectors. Pulsing the polarized deuteron beam permitted the use of time-of-flight detection techniques. The corresponding differential cross sections $\sigma(\theta)$ at 8, 10, 12, 14, and 17 MeV were measured with the same detector system but using an unpolarized beam. Both $A_y(\theta)$ and $\sigma(\theta)$ data were corrected for flux attenuation, angular resolution, and multiple scattering. These data have been described with spherical optical models and with phenomenological coupled-channels calculations. To minimize the ambiguities in the optical-model parameters, $\sigma(\theta)$ data for incident neutron energies ranging from 10 to 40 MeV, which were previously reported, were included in this analysis. For both nuclei, a square-root energy dependence on the strength of the real potential was

necessary to describe the published neutron total cross sections at energies below 3.0 MeV.

In the CC calculations, ^{28}Si was modeled as a symmetric rotor with coupling between the 0^+, 2^+, and 4^+ states, and ^{32}S was modeled as a vibrator in which one-phonon and two-phonon states were mixed. Sensitivities of the data and of the calculations to the magnitude and sign of the quadrupole and hexadecapole deformation parameters, β_2 and β_4, were demonstrated for the case of ^{28}Si. Special emphasis was put on the determination of the spin-orbit potential parameters for each nucleus. The inelastic $A_y(\theta)$ data were used to determine the relative deformation of the spin-orbit potential to that of the central potential. In addition, these CC calculations were used to extract the Coulomb corrections to the real and absorptive parts of the optical model potentials for nucleon scattering from ^{28}Si and ^{32}S.

ACKNOWLEDGEMENTS

I would like to thank my advisor, Dr. R.L. Walter, for his supervision of this project and for his guidance in my education. His patience and sincere love for physics made working with him a pleasure. The time he invested and his insight were invaluable to the completion of this investigation.

The following people are recognized for their contributions in the acquisition of the cross section $\sigma(\theta)$ and analyzing power $A_y(\theta)$ data reported in this dissertation: R.S. Pedroni, G.M. Honoré, Dr. R.C. Byrd, Dr. P.P. Guss, H.G. Pfützner, Dr. C.E. Floyd, K. Murphy, and Dr. G. Tungate. Numerous discussions with Drs. P.P. Guss and R.C. Byrd about the finite geometry corrections applied to $A_y(\theta)$ and $\sigma(\theta)$ data near the minimum in $\sigma(\theta)$ provided essential information for correcting the present measurement of $A_y(\theta)$ near the first minimum in $\sigma(\theta)$ for neutron scattering from ^{28}Si at 14 MeV. Special appreciation is given to Dr. R.C. Byrd for unselfishly sharing his time and experience throughout the course of this project. The contributions of R.S. Pedroni in the normalization of the present cross section data are gratefully recognized. Special recognition is given to Drs. N.R. Roberson and C.R. Gould for their contributions to the development of the data acquisition and analysis system. Much thanks to Dr. T.B. Clegg for his supervision of the maintenance of the polarized ion source and for his efforts to improve the beam-pulsing system. I am indebted to Dr. S.A. Wender for his supervision in the development of the linear voltage ramp generator for the three-stage buncher system which was used to acquire the $A_y(\theta)$ data. During my collaboration with him I

acquired much useful experience in beam-pulsing techniques.

A special thanks is extended to the technical staff. A special appreciation goes to Mrs. Mike Bailey for drawing the illustrations in this dissertation. S.E. Edwards and P. Mulkey are acknowledged for maintaining the electronics and computer system. R.L. Rummel and P.E. Carter are recognized for their continual efforts in maintaining the accelerator. I am also grateful for the machine work of A.W. Lovette in building new apparatus and in repairing broken accelerator parts.

The numerous discussions with Dr. W.J. Thompson concerning the nuclear structure of the low-lying states in ^{28}Si and ^{32}S provided insight and helped establish the direction of this investigation. Drs. R.Y. Cusson and L.C. Biedenharn are recognized for their discussions concerning the compound nucleus (CN) calculations. The suggestions of Dr. P.A. Moldauer were helpful in adjusting the parameters in the level density formulas used in the CN calculations. Dr. C.R. Gould is gratefully recognized for obtaining the code HAUSSER*5 and installing it on the VAX to perform CN calculations.

I would like to thank Dr. R. DeVito for sharing his $\sigma(\theta)$ data for neutron scattering from silicon and sulfur at 30.3 and 40 MeV prior to it being published. Similarly, I am grateful of the $\sigma(\theta)$ data at 10 and 14.8 MeV that were given to us by Dr. G. Haouat. Dr. D.C. Larson is recognized for releasing his neutron total cross sections for silicon to us.

A deep gratitude goes to my parents and family for their continuous support, encouragement, and love during my entire education. I offer my thanks to my friends for their patience and kindness throughout this work.

This work was supported in part by the United States Department of Energy.

TABLE OF CONTENTS

LIST OF FIGURES

LIST OF TABLES

CHAPTER 1

INTRODUCTION

The nuclei in the 2s-1d shell, $16 < A \leq 40$, have received much theoretical and experimental consideration. This is especially true for the even-even T=0 nuclei of ^{28}Si and ^{32}S. These nuclei have intrigued both theorists and experimentalists because of the puzzling characteristics of their nuclear structure. One outstanding feature of these nuclei is the highly collective nature of their excited states. More practical attributes are that these nuclei are composed of enough nucleons for the statistical assumptions associated with many nuclear models to be valid and that the excited states are widely spaced. This wide separation between the energy levels make ^{28}Si and ^{32}S well suited for nucleon-scattering experiments. This feature is especially important in neutron-scattering experiments, since the energy resolution of the measuring aparatus is generally greater than 150 keV.

Contrary to the convenient features for obtaining data, the theoretical analysis of data for nucleon scattering from these nuclei has proven to be a difficult task. The difficulties lie in distinguishing the effects due to collective nuclear motion from those due to the formation of states of the one-particle/one-hole type (Glasgow 1971). Furthermore, there exists the possibility of an inverted coexistence of the ground-state rotational band and the first excited 0^+ state in these nuclei (Bar-Touv 1969).

Because of the large static quadrupole moments of ^{28}Si and ^{32}S, the

low-lying states are believed to be associated with collective excitations. The rotational character of the low-lying excited states in ^{28}Si has been well established (Mermaz 1969, Aleonard 1970, De Swiniarski 1973, and De Swiniarski 1976a). Measurements of the electromagnetic transition probability B(E2) for the $0^+ \rightarrow 2^+$ transition suggest that ^{28}Si has a large ground-state deformation. Within the scheme of the collective model of the nucleus, this implies that excitation of the 2^+ state sets the permanently deformed nucleus into rotation about some space-fixed axis. The energy level spectrum provides additional evidence of the rotational nature of ^{28}Si.

Prior to the work of Thompson and Eck (Thompson 1977), the sign of the quadrupole and hexadecapole deformation parameters, β_2 and β_4, in the optical-model potential (OMP) had been ambiguous. Since the shape of the nuclear potential is predominantly determined by the sign and magnitude of β_2, it was unclear whether ^{28}Si should be modeled as an oblate-shaped ($\beta_2 < 0$) or prolate-shaped ($\beta_2 > 0$) nucleus. Previous analyses have shown that the descriptions of elastic and inelastic scattering cross sections for neutron or proton scattering from ^{28}Si are nearly identical for both signs of β_2 (Böttcher 1983, Howell 1982a, De Swiniarski 1976a, and Obst 1973). However, it has been shown that the vector analyzing powers $A_y(\theta)$ for inelastically scattering polarized neutrons and protons from ^{28}Si are sensitive to the sign of β_2 (Böttcher 1983, Howell 1982a, and De Swiniarski 1976a). For neutron scattering at 10 and 14 MeV, the sensitivity was most pronounced at back angles in the $A_y(\theta)$ for scattering to the 2^+ state (Böttcher 1983 and Howell 1982a). The descriptions of these data preferred a negative β_2. On the other hand, the $A_y(\theta)$ of the

2^+ state for proton scattering at 30.3 MeV was fairly insensitive to the sign of β_2 (De Swiniarski 1976a); however, the fit to the $A_y(\theta)$ of the 4^+ state was appreciably better with a negative β_2.

Prior to the works of Howell *et al.* (Howell 1982a) and Böttcher *et al.* (Böttcher 1983), the spin-orbit part of the neutron-nucleus OMP for ^{28}Si had been taken from the analysis of proton-scattering data. The high quality of the $A_y(\theta)$ data for elastic scattering reported in the present dissertation permits the accurate determination of the spin-orbit parameters. Furthermore, the present $A_y(\theta)$ data for inelastic scattering is important for deducing the spin-orbit deformation.

Previous analyses of nucleon scattering from ^{32}S have concluded that data for elastic scattering and for inelastic scattering to the first 2^+ state can be described equally well with either a rotational or vibrational model (Obst 1973, De Swiniarski 1976a, Yamanouti 1977, Haouat 1982, and Tailor 1982). The large intrinsic quadrupole moment of ^{32}S (Lee 1972, Stelson 1965, and Häusser 1971) suggested that the nucleus was permanently deformed and therefore should be modeled as a rigid rotor. On the other hand, the energy level spacings, the results of lifetime studies (Garvey 1969, Ollerhead 1970, Garvey 1971, and Coetzee 1972), and the analyses of electromagnetic transition probabilities B(Eλ) (Häusser 1971, Ingebretsen 1971, Garvey 1971, and Coetzee 1972) were strongly indicative of the vibrational character of the collective states in ^{32}S. However, the splitting of the quadrupole triplet, 0_2^+, 2_2^+, 4^+, provided evidence that the collective excitations in ^{32}S deviate from the simple harmonic vibrational model. Furthermore, explanations of the non-zero B(E2) value for the $2_2^+ \rightarrow 0_1^+$ transition have required the mixing of the one-phonon 2_1^+

state with the two-phonon 2_2^+ state (Häusser 1971, Ingebretsen 1971, Garvey 1971, Coetzee 1972, and Olin 1974). In describing nucleon-scattering data, Lombard and Raynal (Lombard 1973) and Tailor (Tailor 1982) found that appreciably better fits could be obtained with an anharmonic vibrational model which incorporated the mixing of one-phonon and two-phonon states than could be achieved with a simple harmonic oscillator model.

For the present study, elastic and inelastic differential cross sections $\sigma(\theta)$ for neutron scattering to the ground and first excited states of ^{28}Si and ^{32}S were measured at incident neutron energies of 8, 10, 12, 14, and 17 MeV with the neutron time-of-flight (NTOF) facilities at the Triangle Universities Nuclear Laboratory (TUNL). The corresponding analyzing powers were measured at 10, 14, and 17 MeV using pulsed polarized deuterons, the $^2H(\vec{d},\vec{n}_0)^3He$ polarization transfer reaction, and the neutron time-of-flight system at TUNL. Both $\sigma(\theta)$ and $A_y(\theta)$ were measured with the same detector system; therefore, the capability of simultaneous measurements of both observables has been investigated (Howell 1983a). The $A_y(\theta)$ data accumulated for this project are the first reported neutron-polarization data for ^{28}Si and ^{32}S at energies above 8 MeV, with the exception of the $A_y(\theta)$ for ^{28}Si at 14 MeV reported by the Erlangen group (Böttcher 1983).

There are four primary objectives of this project. First, the systematic behavior of data for neutron scattering from ^{28}Si and ^{32}S will be studied. Second, the collective properties of the low-lying states in these nuclei will be investigated. Third, the present $A_y(\theta)$ data will be used to determine the spin-orbit part of the OMP for neutron scattering

from ^{28}Si and ^{32}S. And finally, the Coulomb-correction terms to the OMP for these T=0 self-conjugate nuclei will be deduced.

The systematic behavior of neutron scattering from ^{28}Si and ^{32}S will be studied with the aid of the spherical optical model (SOM). To minimize the ambiguities in the geometrical parameters and in the energy dependencies of the potential strengths, data from several references for incident neutron energies ranging from 10 to 40 MeV will be included in the analysis. The calculations with the SOM will serve as a guide for determining the consistency of the data from the various references, i.e., the smoothness of the variation of the data with energy and angle. The analysis of these data with the SOM will also provide a set of OM parameters that can be used in more involved calculations, such as, compound nucleus (CN) calculations, coupled-channels (CC) calculations, and distorted-wave Born-approximation (DWBA) calculations.

To investigate the collective features of the low-lying states in ^{28}Si and ^{32}S, the available data for neutron scattering from these nuclei will be descibed with CC calculations. The present analyses will be guided by the results of past analyses. The nucleus ^{28}Si will be modeled as a symmetric rotor with coupling between the 0^+ ground state and the 2^+ and 4^+ excited states. Calculations will be performed to test the sensitivity of the calculations and data to the sign of the quadrupole and hexadecapole deformation parameters. In addition, the inelastic $A_y(\theta)$ will be used to deduce the relative size of the deformation of the spin-orbit potential to that of the central potential. To be consistent with previous analyses (Lombard 1973 and Tailor 1982), ^{32}S will be modeled as a vibrator with admixing between the one-phonon and two-phonon states. The

calculated neutron total cross section σ_t for ^{32}S will be compared to the experimentally observed values to estimate the magnitude of the influences due to the formation of particle-hole states.

Prior to the work of Böttcher et al. (Böttcher 1983) at 14 MeV, the spin-orbit part of the OMP for neutron scattering from ^{28}Si had been taken from proton analyses. The present $A_y(\theta)$ data will permit the parameters of the spin-orbit potential for $^{28}Si+\vec{n}$ to be optimized at 10, 14, and 17 MeV. These optimum parameters will be used to compute an energy-averaged parameter set for the spin-orbit potential. In the case of ^{32}S, the present $A_y(\theta)$ data are the first reported polarization observables for neutron scattering from ^{32}S above 8 MeV. Similar to the analysis of the $^{28}Si+\vec{n}$ data, the elastic scattering data will be used to determine energy-averaged parameters for the spin-orbit potential and the $A_y(\theta)$ data for inelastic scattering will be used to determine the deformation of the spin-orbit potential.

There have been several attempts to extract the Coulomb correction to the real part of the OMP for nucleon scattering from ^{28}Si and ^{32}S (Rapaport 1982 and Tailor 1982). Rapaport analyzed nucleon-scattering data with a SOM and found that the magnitude of the correction for ^{28}Si was slightly lower than the standard value of $\Delta V_c = 0.4Z/A^{1/3}$ MeV (Perey 1963a) and significantly lower than the values he determined for ^{16}O, ^{32}S, and ^{40}Ca. Rapaport suggested that the discrepancy between the Coulomb corrections deduced for ^{28}Si and the other T=0 nuclei was due to the large nuclear deformation of ^{28}Si which distorted the parameters of his SOM. According to Rapaport, this discrepancy could be rectified by analyzing the data for nucleon scattering from ^{28}Si with CC calculations. Recently,

Tailor (Tailor 1982) attempted to extract the Coulomb corrections to the real and absorptive parts of the OMP for ^{28}Si and ^{32}S. He analyzed both proton and neutron scattering data with CC calculations. For both nuclei, he found the magnitude of the corrections to be smaller than their uncertainties. This was the case for both the real and absorptive potentials. Tailor concluded that more high-accuracy nucleon-scattering data, especially neutron-scattering data, was necessary to reduce the uncertainties in the extracted values. In addition to the above studies, Devito *et al.* (Devito 1983) used a SOM to deduce the Coulomb correction to the absorptive part of the OMP for ^{28}Si. In the present analysis, CC calculations will be used to describe the large neutron-data set that has been compiled. The available neutron data covers a broad enough energy range and is of high enough quality that it will be used to extract more precise values for the Coulomb corrections to the OMP for ^{28}Si and ^{32}S.

CHAPTER 2

EXPERIMENTAL DETAIL

2.1 Experimental Technique for Cross-Section Measurements

2.1.1 Introduction

Differential cross sections were measured using the time-of-flight (TOF) spectrometer shown in fig. 2.1. A pulsed beam of deuterons accelerated in the TUNL tandem Van de Graaff were incident on a deuterium filled gas cell. The nominal beam intensity was 2 μA and the full width at half maximum (fwhm) of each pulse of deuterons was about 2 ns. The neutrons emitted at 0° from the $^{2}H(d,n)^{3}He$ source reaction were scattered from the sample (silicon or sulfur) into two well-shielded side detectors respectively located nomimally at 4 m and 6 m from the sample. The anode signal from each detector started a time-to-amplitude converter (TAC) whose stop signal was derived from a capacitive pick-off for the deuteron beam pulses that was located immediately in front of the gas cell. Figure 2.2 illustrates TOF spectra obtained with the 6 m detector at incident neutron energies of 10 and 17 MeV. At all measured angles, the neutrons that elastically scattered from ^{28}Si were well resolved from those that scattered to the first excited state (Q = -1.78 MeV); this permitted the differential cross section $\sigma(\theta)$ for this 2^{+} state to be extracted also. The same condition was true for neutrons that were scattered from ^{32}S (Q = -2.23 MeV for scattering to the first excited state). The yields in the two side detectors were normalized to the incident neutron flux as

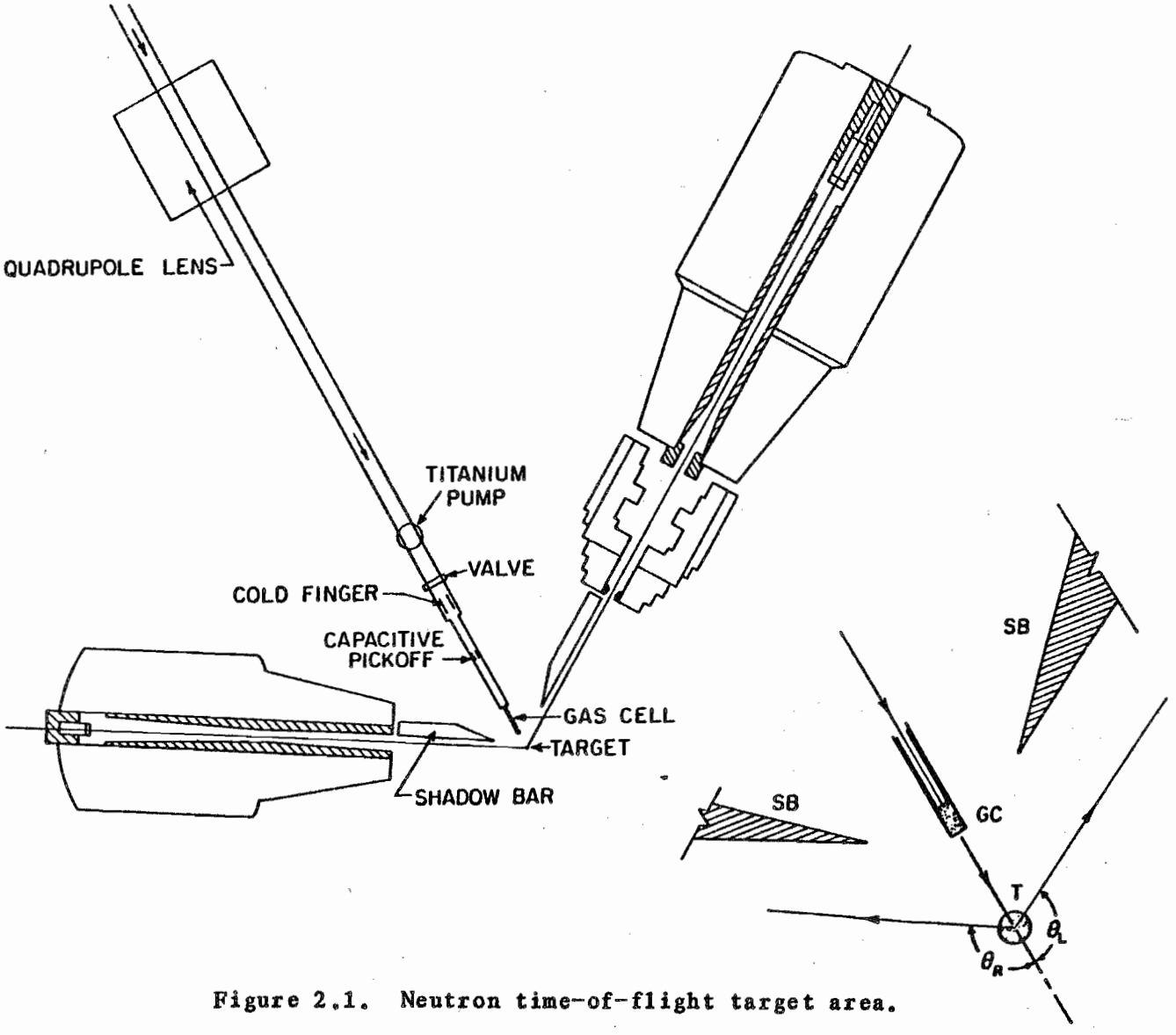

Figure 2.1. Neutron time-of-flight target area.

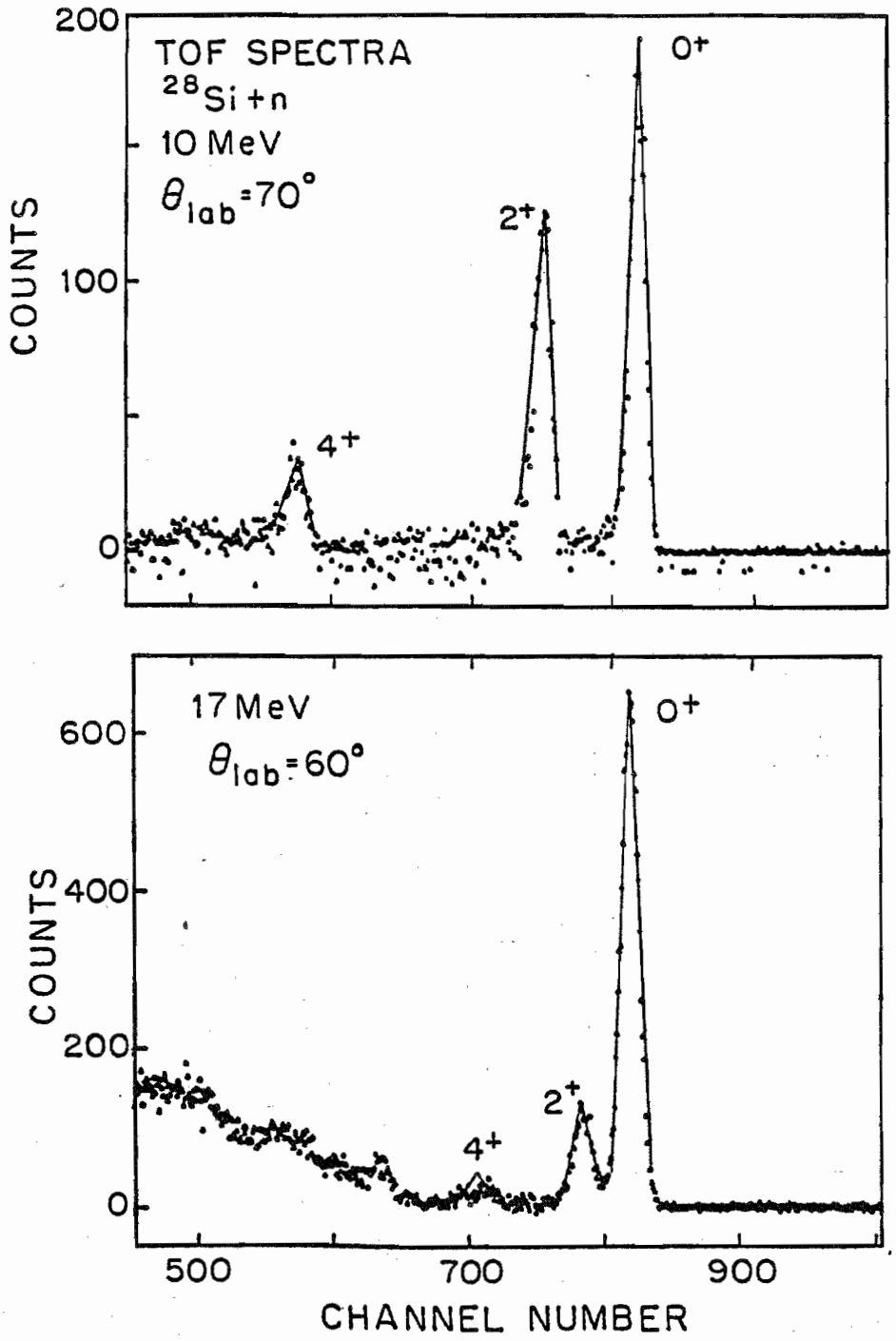

Figure 2.2. TOF spectrum of ^{28}Si + n at incident neutron energies of 10 and 17 MeV. These spectra were obtained with the 6 m detector positioned at $\theta = 70^{\circ}$ and $\theta = 60^{\circ}$, respectively. Both spectra were accumulated during $\sigma(\theta)$ measurements.

measured with a monitor detector. Absolute normalization was obtained by comparing the yields to that from $^{1}H(n,n)^{1}H$ scattering. The neutrons scattered from hydrogen were somewhat lower in energy than those scattered from the heavier nuclei ^{28}Si and ^{32}S, and therefore the relative efficiency of both side detectors had to be taken into account (El-Kadi 1981 and El-Kadi 1983).

2.1.2 Source Reaction

In order to perform neutron scattering experiments, a source of neutrons is necessary. The energy range of the FN tandem accelerator at TUNL will permit the use of several neutron source reactions. Figure 2.3 is a plot of cross sections at 0^{o} reaction angle versus neutron energy for the various mono-energetic neutron sources using hydrogen isotopes. The solid portions of the curves represent the energy regions obtainable using the tandem accelerator at TUNL (2 MeV $< E_{p} <$ 16 MeV). In the neutron energy range between 7 and 20 MeV, the cross section for the $^{2}H(d,n)^{3}He$ reaction is more than twice that of either T(p,n) or T(d,n). All experiments reported in this dissertation were conducted using the neutrons emerging at 0^{o} from the $^{2}H(d,n_{0})^{3}He$ neutron source reaction. The $^{2}H(d,n_{0})$ reaction was used because the neutron cross section is high at 0^{o}, the neutrons emitted at 0^{o} are the most energetic neutrons emanating from the reaction, and because both neutron energy and cross section decrease rapidly with increasing angle. These last two features are important for reducing backgrounds in the side detectors. In addition, the 3.3 MeV Q-value for the $^{3}He_{g.s.}$ reaction gives a 5 MeV separation from neutrons originating in deuteron breakup reactions in the deuterium gas or

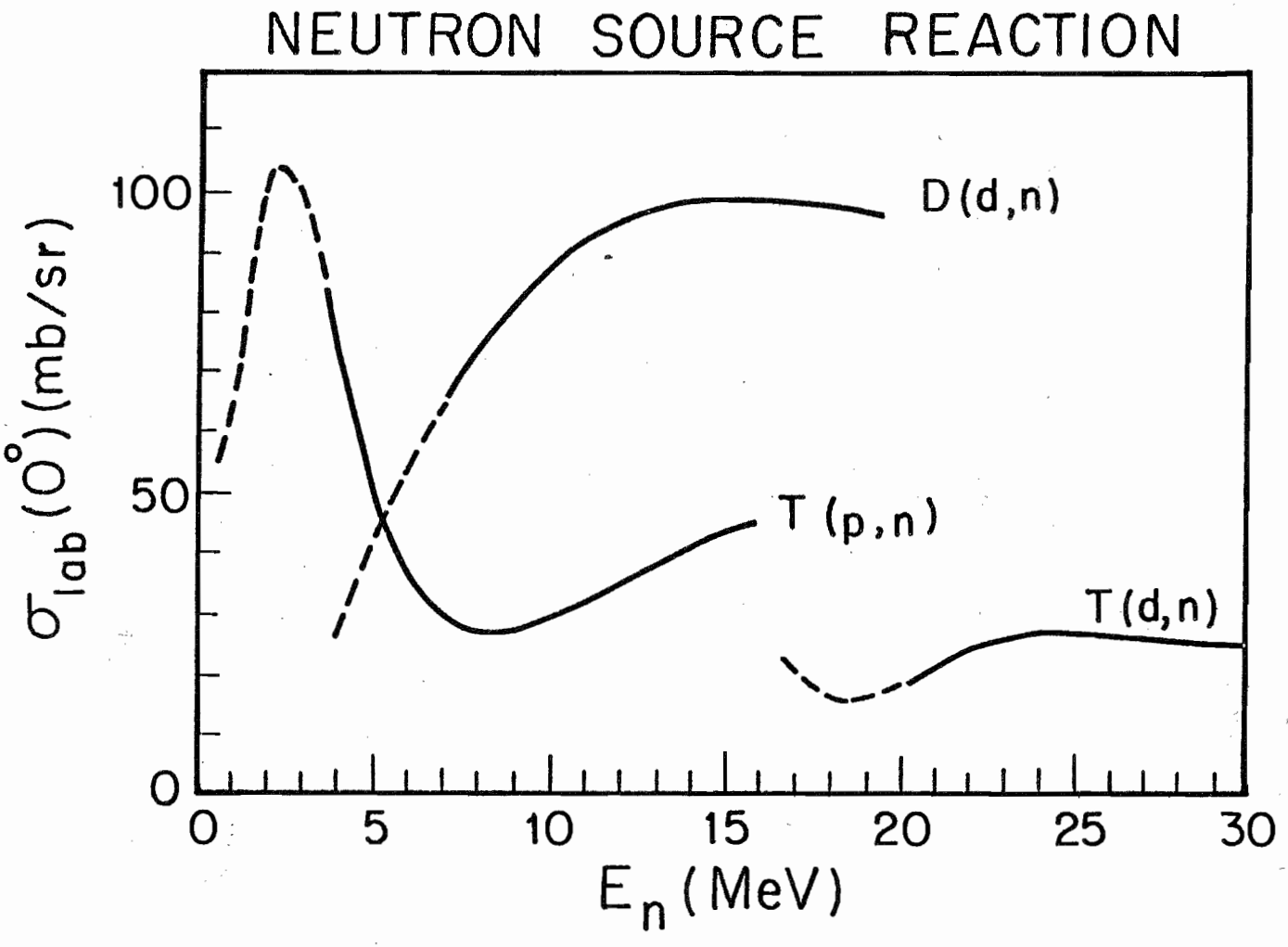

Figure 2.3. Cross sections at 0° for various neutron source reactions of hydrogen isotopes. The solid portions of the curves represent regions that are obtainable with the tandem accelerator at TUNL.

the tantalum beam stop. In conclusion, the $^{2}H(d,n_0)^{3}He$ reaction is an excellent source of mono-energetic neutrons to be used in experiments of elastic and inelastic scattering to close lying states at incident neutron energies below 20 MeV.

Because of the deuteron breakup (many-body reactions) which produces a continuum of neutron energies starting approximately 5 MeV below the main neutron group, the $^{2}H(d,n)$ reaction is not recommended when information about high lying states is desired. Since the binding energy of the deuteron is 2.2 MeV, it follows that the Q-values for the many-body reactions $^{2}H(d,np)^{2}H$ and $^{2}H(d,np)np$ are -2.2 MeV and -4.4 MeV, respectively. In both reactions the emitted neutrons have a continuum of energies starting at threshold, whereas the $^{2}H(d,n_0)^{3}He$ reaction produces a mono-energetic group of neutrons. As stated above, the Q-value of this reaction is 3.3 MeV. Thus, there is a 5.5 MeV separation between the mono-energetic neutron group produced by the $^{2}H(d,n)$ reaction and the continuum of neutrons produced by the deuteron breakup in the deuterium gas. At neutron energies above 17 MeV the $^{2}H(d,n)$ source reaction is strongly disfavored because the cross section of the continuum increases rapidly with energy, while the cross section of the mono-energetic neutron group decreases with energy. In this energy range the $^{3}H(d,n_0)^{4}He$ reaction with a Q = 17.6 MeV takes preference.

2.1.3 DENIS-II

The deuterons employed in the $^{2}H(d,n)$ reaction are produced by an ion source located on the low energy end of the tandem accelerator. A 50 keV deuteron beam is extracted from the duoplasmatron of a direct extraction

negative ion source. At present, there are two of these sources in operation at TUNL. The one used in these experiments produces a more intense beam and is the most recently constructed, and thus, it is referred to as DENIS-II. Although the energy spread of the deuteron beam produced by DENIS-II is larger than that of the beam produced by the other negative ion source, DENIS-II was used because it was designed to work in conjunction with the beam pulsing apparatus. Since the energy spread due to the ion source is usually negligible compared to other sources of energy spread in neutron scattering experiments, the quality of the DENIS-II beam is sufficient. Figure 2.4 is a schematic of DENIS-II. The source head and all associated power supplies are referenced to a negative 50 kV potential. The negative ion beam originates in the source head and is accelerated down to ground potential, thus producing an ion beam having an energy of 50 keV.

An arc is struck between the filament and anode electrode by boiling electrons off the filament and accelerating them toward the anode in a strong magnetic field. Deuterium gas is leaked into the region between the hot filament and the anode. The electrons spiral along the magnetic field lines and collide with deuterium atoms on their way to the anode. This produces an intense arc of D^+ and D^- ions. The very dense central core of the arc consists of D^+ ions, while the less dense halo around the core contains D^- ions. Most of the D^+ ions are accelerated back toward the filament, but some move toward the anode because of the potential gradients produced by space charge. Most of the ions in the D^- halo are accelerated toward the anode. Because the D^- ions are to be extracted, the opening in the anode is aligned slightly off center. The central core

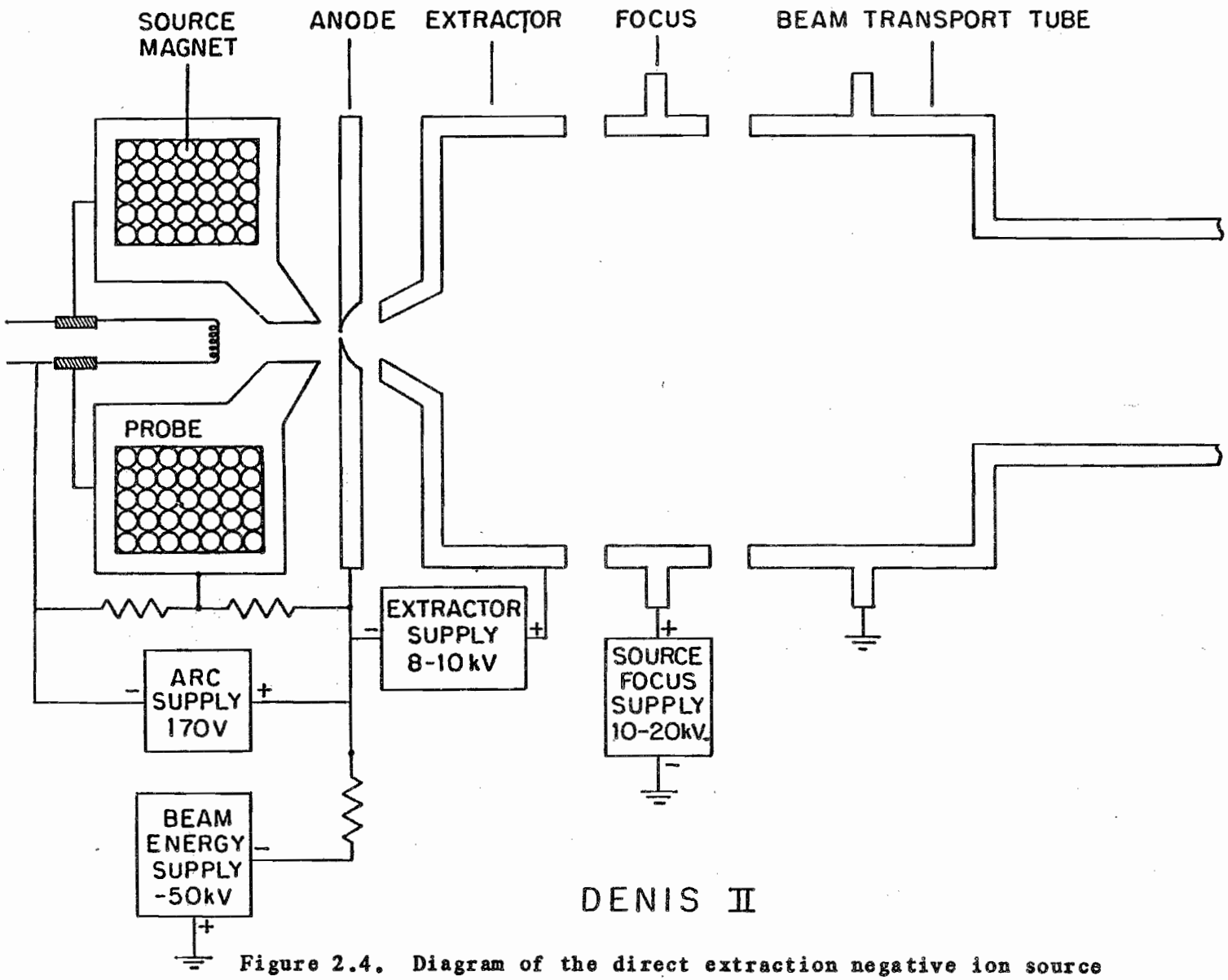

Figure 2.4. Diagram of the direct extraction negative ion source (DENIS-II) used in the $\sigma(\theta)$ experiments.

of positive beam and some of the electrons are stopped on the anode while the D^- ions collect at the opening, thus forming a high density plasma of D^- ions in this region. The D^- ions migrate through the opening due to the large concentration (pressure) gradient across the aperature. Once these ions have migrated into the region of the expansion cup of the anode, they are accelerated by the large electric field between the anode and the extractor electrode. Any other negative ions in the region between the anode and extractor electrodes will also be extracted. The extracted beams (D^-, e^-, O^-, etc.) are then focused by an electrostatic lens (labeled FOCUS in fig. 2.4) before being accelerated to the full 50 keV beam-transport energy. The D^- beam is selected by an analyzing magnet and bent onto the axis of the tandem accelerator. The optical elements on the low-energy end of the tandem are adjusted for optimal transmission through the accelerator.

2.1.4 Beam Pulsing

Both $\sigma(\theta)$ and analyzing powere $A_y(\theta)$ data were acquired with the neutron time-of-flight (TOF) facilities at TUNL. There are several advantages of using TOF techniques as opposed to analysis of proton recoil spectra as was used by Böttcher *et al.* (Böttcher 1983) in their measurement of the $A_y(\theta)$ for $^{28}Si + \vec{n}$. The advantages are:

1) a drastic increase in the efficiency of the detection system because a low pulse-height bias level can be employed;

2) the analysis of inelastically scattered neutrons is easier; neutron groups of different energies are separated in the TOF spectra by their flight times, whereas similar analysis using proton recoil spectra require complicated line shape fitting routines combined with some type of convolution program;

3) the determination of and corrections for backgrounds are easier.

The use of TOF techniques in neutron scattering experiments requires that the charged particles used in the neutron source reaction be pulsed. When using TOF techniques to measure the energies of detected neutrons, it is critical that the incident beam be compressed into narrow beam bursts that are sufficiently separated in time, so that the slowest neutrons in one burst may be detected before the arrival of the fastest neutrons of the subsequent bursts. The repetition rate of the beam bursts are generally less than 5 MHz for TOF experiments. At TUNL the repetition rate is 2 MHz (τ = 500 ns) for $\sigma(\theta)$ experiments and 4 MHz (τ = 250 ns) for $A_y(\theta)$ experiments.

Since many of the development contributions of the present author involved beam pulsing, a short review of beam pulsing and the bunching system at TUNL is given here. The simplest way to pulse a DC beam is to chop it into segments by subjecting it to a transverse electric field that varies periodically in time. A more elegant method is to compress the DC beam into sharp spikes by modulating the energy of the beam as a function time. The latter of the two techniques is known as "bunching" and the simpler method is referred to as "chopping". The combination of chopping and bunching is a very powerful method of pulsing charged-particle beams.

The function necessary to bunch the beam can be derived using elementary physics. Suppose a DC beam having an average energy E_0 is chopped into beam segments that are separated in time by an amount τ. Consider a beam segment in which the "head" (leading edge of the segment) arrives at the bunching plane at t=0 and the "tail" arrives at a later

time $t = \tau$. In order for the beam to be compressed into sharp bursts at the time focus (x_0, t_0), all deuterons leaving the bunching plane between the times t=0 and $t=\tau$ must arrive at position x_0 at time t_0. The time t_0 is the travel time needed for a deuteron leaving the bunching plane at t = 0 with energy E_0 to arrive at x_0. Recall from elementary physics,

$$E_0 = \frac{1}{2} m v_0^2$$

where,

$$v_0 = \frac{x_0}{t_0} \quad \text{for deuterons leaving at t=0.}$$

So, for a time focus at (x_0, t_0) the velocity required is

$$v(t) = \frac{x_0}{t_0 - t} \quad \text{for deuterons leaving at a later time t.}$$

Here, $0 \leq t \leq \tau$. Therefore, we have the requirement:

$$v(t) = \frac{v_0}{1 - \frac{t}{t_0}} .$$

This result agrees with intuition; the velocities of successive deuterons must be increased so that the tail of the beam segment will catch the head at the time focal point (x_0, t_0). Since the energy of each deuteron E is directly proportional to the square of its velocity,

$$E(t) = \frac{E_0}{(1 - \frac{t}{t_0})^2} .$$

A Taylor expansion of the quantity $\frac{1}{(1 - \frac{t}{t_0})^2}$ in the variable $\frac{t}{t_0}$ about $\frac{t}{t_0} = 0$, yields

$$\frac{1}{(1 - \frac{t}{t_0})^2} = 1 + 2\left[\frac{t}{t_0}\right] - 3\left[\frac{t}{t_0}\right]^2 + 4\left[\frac{t}{t_0}\right]^3 - 5\left[\frac{t}{t_0}\right]^4 + \cdots\cdots$$

and thus,

$$E(t) = E_0\left[1 + 2\left[\frac{t}{t_0}\right] - 3\left[\frac{t}{t_0}\right]^2 + 4\left[\frac{t}{t_0}\right]^3 - 5\left[\frac{t}{t_0}\right]^4 + \cdots\cdots\right] . \quad (2.1)$$

Since the period of bunching is usually much shorter than the transit time from the bunching plane to the target ($\tau << t_0$), it follows that $t << t_0$ must be true. For instance, the velocity of a 50 keV deuteron is 2.19×10^6 m/s, and the "effective distance" to target is approximately 3.0 m. Therefore,

$$t_0 = \frac{x_0}{v_0} = \frac{3.0 \text{ m}}{2.19 \times 10^6 \text{ m/s}} = 1.37 \times 10^{-6} \text{s} .$$

Using $\tau = 2.5 \times 10^{-7}$s, one gets that

$$\frac{t}{t_0} \leq \frac{\tau}{t_0} \text{ , which leads to}$$

$$\frac{t}{t_0} \leq 0.18.$$

This implies that to first order the energy of the deuterons must be modulated linearly in time. Accordingly,

$$E(t) \simeq E_0 + \left[\frac{2E_0}{t_0}\right]t \quad (2.2a)$$

with a resultant time-dependent energy increase given by

$$\delta E(t) \simeq \left[\frac{2E_0}{t_0}\right]t . \quad (2.2b)$$

Thus, the ideal waveform of the bunching voltage is a sawtooth. The

energy change in the beam induced by the buncher is given by eqn. (2.2b). Deuterons leaving the bunching plane at time τ will experience the maximum buncher voltage $(2\tau/t_0)V_0$, where V_0 is the accelerating voltage of the ion source. At TUNL, V_0 = 50 kV, τ = 250 ns, and t_0 = 1.4 μs. Therefore, the maximum buncher voltage required to compress the beam into pulses at the time focus (x_0,t_0) is V_{max} = 18 kV, and the energy spread introduced into the beam will be ΔE = 18 keV fwhm. Because it is extremely difficult to produce a 18 kV sawtooth voltage, the easier alternative of using the linear portion of a sine wave is exploited.

The buncher at TUNL is a cylindrical tube consisting of three electrically insulated sections, a long middle section with two short segments on either end. The end segments are grounded while the middle section is driven by a rf amplifier via a tuned circuit. Bunchers of this type are known as double gap bunchers, because the beam is bunched as it transverses each gap. The buncher is designed so the length of the middle section is equal to the distance traveled by the particles in one-half of an rf cycle. Therefore, the head of each beam segment is decelerated as it enters and exits the buncher tube. Similarly, the tails are accelerated as they enter and exit the buncher.

Figure 2.5 is a diagram of the buncher system at TUNL. The DC beam passes through two sets of deflection plates, first through a horizontal set and then through a vertical set. The voltage on the horizontal set of main-chopper plates is varied sinusoidally at a frequency of 2 MHz. Beam passing through these plates near the zero crossing of the sine wave receives little or no deflection. The remainer of the beam is swept onto a plate containing a circular aperture before the buncher tube. This

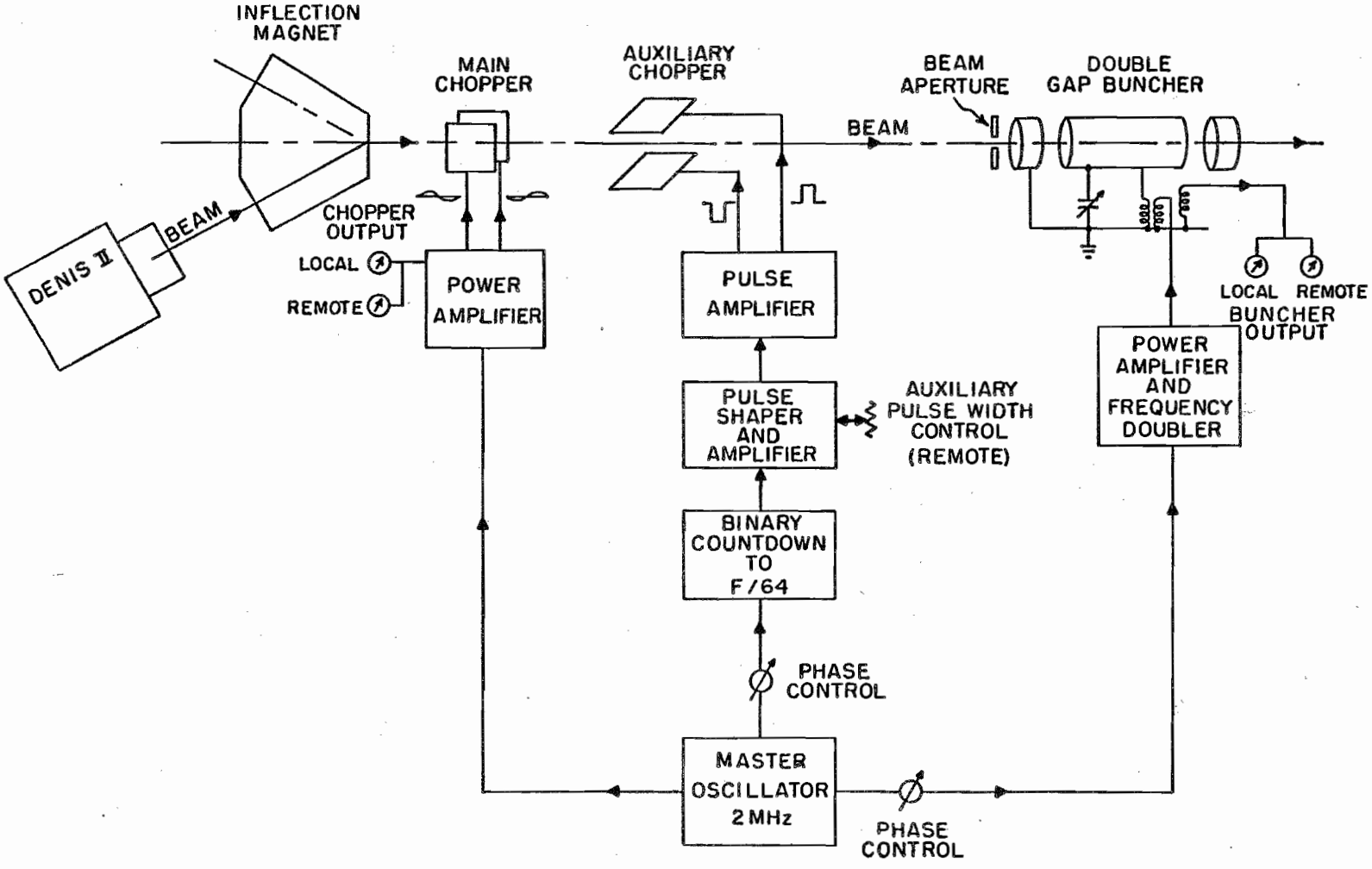

THE TUNL BUNCHER SYSTEM

Figure 2.5. Block diagram of the TUNL buncher system.

system effectively chops the DC beam into segments having a repetition rate of 4 MHz (4 million segments/sec). The vertical auxillary-chopper plates are driven with a square wave to deflect alternate beam segments that emerge from the sine wave chopper, thereby giving a pulse repetition rate of 2 MHz. One vertical plate is driven at +400 V, while the other at -400 V, thus producing a total deflection voltage of 800 V. The repetition rate of the square wave is actually variable from 2 MHz to 31 KHz, and the combination of the sine wave and square wave choppers allows the experimenter to vary both the repetition rate and the width of the beam segments. A double gap buncher is used to compress the beam segments from the chopper system into narrow beam pulses on target. The middle section of the buncher is driven with a 4 MHz sine wave. The length of the center section is L = 29 cm when pulsing 50 keV deuterons and 42 cm for pulsing the higher velocity 50 keV protons.

All components of the chopper and buncher system derive their trigger signals from a 2 MHz master oscillator. The DC beam emerging from DENIS-II is chopped into the phase acceptance of the double gap buncher. The phase acceptance (the linear portion of the sine wave) of the buncher is approximately 20% of the rf period (Wender 1980 and Wender 1981). The phase of the auxiliary chopper (square wave chopper) and the buncher are referenced to the main chopper (sine wave chopper). The phase and width of the auxiliary chopper are adjusted to sweep out alternate beam segments emerging from the main chopper. The buncher is phased in such a way that the head of each segment is deaccelerated and the tail is accelerated. The main chopper and buncher operate at fixed frequencies, 2 and 4 MHz, respectively. These frequencies are determined by the resonant frequency

of the tuned circuits used to drive them. The auxiliary chopper, on the other hand, is a square wave chopper and therefore its frequency and width are variable parameters. It is this feature that enables the experimenter to select the repetition rate of the beam pulses. The typical performance of this system is having beam bursts on target with a full width at half maximum (fwhm) of 2 ns. However, an optimal performance with a fwhm of 1.5 ns has been obtained.

2.1.5 Neutron TOF Spectrometer

Capacitive pick-off unit and associated electronics

Figure 2.6 is a diagram of the laboratory layout showing the path followed by the beam from the source to target. The pulsed beam is accelerated by the tandem, bent through 38^{o} by an analyzing magnet, passes through a capacitive pick-off unit and is incident on a deuterium filled gas cell. The capacitive pick-off unit is a cylindrical tube approximately 1.9 cm in diameter and 6.35 cm long. The length of the unit was optimized for 7 MeV deuterons, which produce 10 MeV neutrons via the $^{2}H(d,n)$ reaction. The length is chosen so that the entire beam burst is inside the tube before the leading edge starts to exit. The optimal length is $L = v_d \Delta t$, where v_d is the velocity of the deuteron beam and Δt is the full width at one-tenth height of the beam bursts. Figure 2.7 is a schematic of the beam pick-off unit and the associated electronics. As the positive beam pulse enters the pick-off unit it induces a negative charge on the tube by pulling electrons from ground through the preamp, thus producing a positive signal at the output of the preamps. As the beam exits the tube the current through the preamp is reversed and the

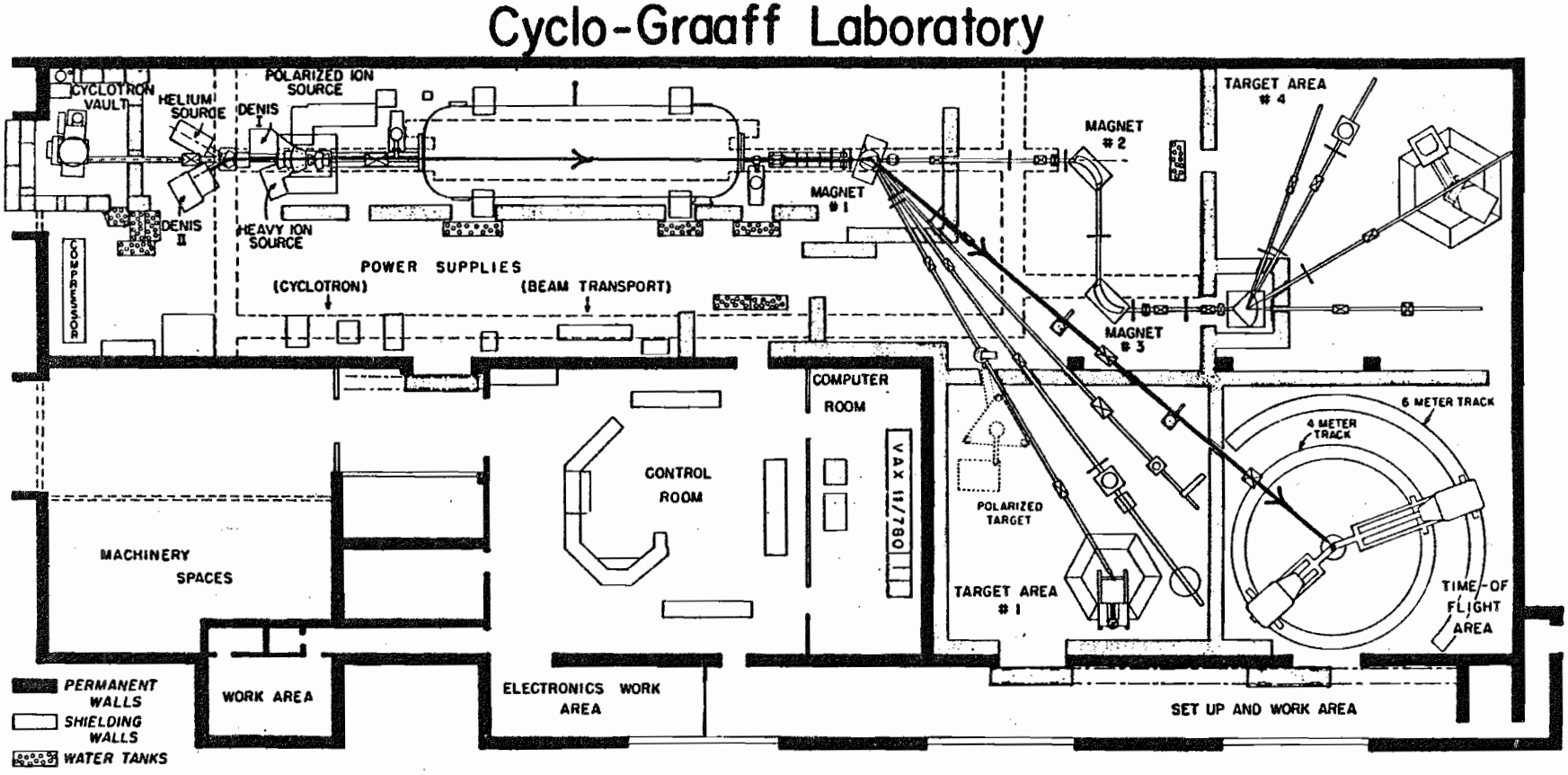

Figure 2.6. Floor plan of the Triangle Universities Nuclear Laboratory (TUNL). The bold line indicates the path of the beam in the $\sigma(\theta)$ experiments.

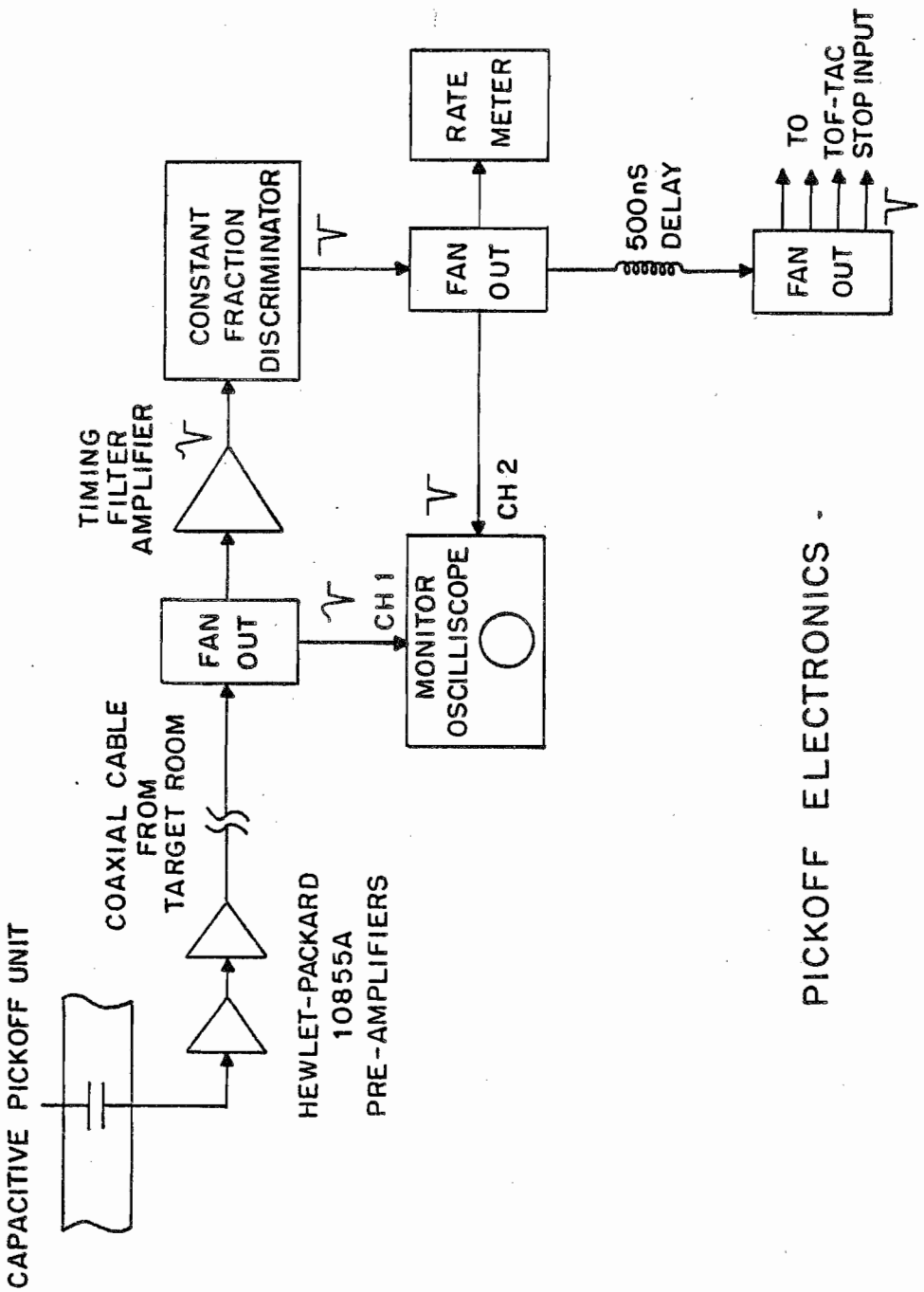

Figure 2.7. Block diagram of the beam pick-off electronics.

polarity of the output signal is reversed accordingly. Figure 2.8 illustrates the pick-off signal (output of two Hewlett-Packard (HP) preamps #10855A connected in series) observed on the oscilloscope shown in fig. 2.7. A profile of the particle beam corresponding to the pick-off signal is also shown in fig. 2.8. The amplitude of the pick-off signal is directly proportional to the beam intensity, and its sharpness is strongly correlated to the shape of the beam burst as it traverses the pick-off unit. The width at point A is a measure of the width of the beam burst and can be minimized by adjusting the bunching voltage and phase. The width at B is a measure of the tails on the beam bursts and can be minimized by adjusting the chopper parameters, phase and width of the auxiliary chopper, and the amplitude of the main chopper. The solid and dashed curves in fig. 2.8 illustrate two extreme modes of operating the buncher system; in one mode the peak is broad but symmetric, while in the other mode the peak is narrow but asymmetric with a large tail on the low-energy side of the beam burst. The optimal operating condition is a compromise between these two extreme modes.

The deuterium gas target

A deuterium gas target was used to produce the neutrons in all experiments. The gas was contained in a stainless steel cell with a thin metal foil on the beam entrance side. There were two different cells used in these experiments. Both cells were very similar: they were cylindrical tubes approximately 0.8 cm in diameter and about 3 cm long. The deuteron beam was stopped in a tantalum disc 0.051 cm thick which was held in place by a thin cylindrical tantalum sleeve. This sleeve also shielded the

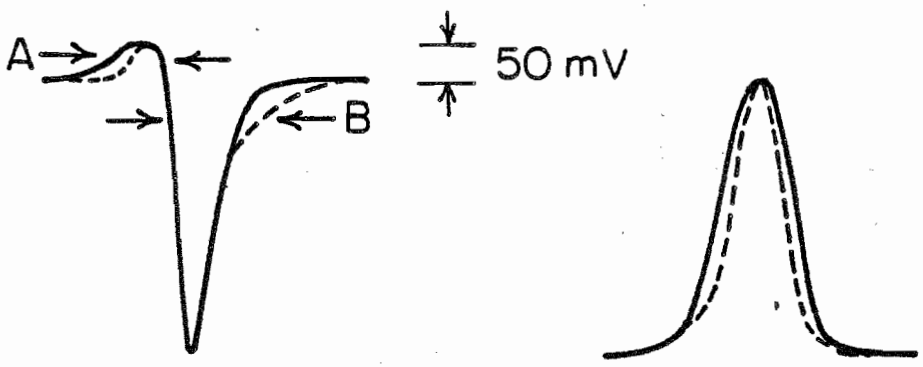

Figure 2.8. A typical pick-off signal and the corresponding deuteron beam profile. The solid and dashed curves represent two extreme shapes of pick-off signals along with the corresponding beam profile spectra.

stainless steel from the direct beam and ensured good charge collection. The gas cell was electrically isolated so that the amount of charge deposited in the cell could be monitored by beam current integration techniques. The charge deposited in the cell was discharged to ground through a beam current integrator (BCI), which outputs one digital pulse per fixed amount of charge. The number of pulses per unit charge could be adjusted by changing the integration scale on the BCI. The pulses from the BCI were counted by a scalar and stored in the computer.

The gas cell used in the acquisition of all data except the 17 MeV data and the measurement of the minimum of $\sigma(\theta)$ for ^{28}Si + n at 14 MeV has been described elsewhere (Beyerle 1981, Glendinning 1980, Guss 1982a). The absolute pressure of deuterium gas was 2 bar and the energy spread of the neutron beam emerging at 0^{o} ranged from 95 keV at E_n = 14 MeV to 190 keV at E_n = 8 MeV. A more recently designed gas cell was used to acquire the data that were excluded above. The main improvement in this cell over the older design is that the containment foil is held in place with glue instead of by compression, thereby permitting one to obtain higher gas pressures. This allowed the same gas cell to be used also in the $A_y(\theta)$ measurements where higher pressures are desirable. The deuterium gas pressure in the 17 MeV experiments for $\sigma(\theta)$ using this cell was about 8 bars. This corresponds to a neuteron energy spread of around 300 keV.

Samples and neutron detectors

Figure 2.1 is a floor plan of the target room. The neutrons emerging from the $^{2}H(d,n)$ reaction at 0^{o} were scattered off cylindrical samples. Table 2-1 contains the descriptions of the samples used in these

TABLE 2-1

DESCRIPTIONS OF THE SCATTERING SAMPLES

Target Sample	Isotopic Composition (% of Nuclei)			Mass (g)	Radius (cm)	Height (cm)
Silicon	^{28}Si	^{29}Si	^{30}Si	25.27	1.176	2.528
	92.55	4.55	2.90			
Sulfur	^{32}S	^{33}S	^{34}S	23.63	1.230	2.540
	95.28	0.74	3.98			
Polethylene*	^{1}H	^{12}C		3.410	0.715	2.314
	~66.6	~33.3				
Carbon	^{12}C	^{13}C		2.911	0.477	2.375
	99.0	1.0				

* Polyethylene and carbon used to normalize $\sigma(\theta)$ data.

experiments. The samples were suspended directly over the pivot point of the detectors by a thin (diameter = 0.8 mm) steel cable. As many as four samples could be mounted on the cable simultaneously. This enabled the experimenter to change samples without physically dismounting one sample and replacing it with another. Great care was taken to align the center of the sample with the beam axis, so that the neutron flux would illuminate the sample symmetrically about its center. The distance from the end of the gas cell to the center of the sample was 7.79 cm for the old cell and 9.21 cm for the new cell. The scattered neutrons were detected by two heavily shielded neutron detectors; one positioned on the left side of the beam axis (6 m detector) and the other on the right (4 m detector). These detectors were NE-218 liquid organic scintillators with very good pulse-shape-discrimination (PSD) characteristics. Both detectors were 5.08 cm thick. The diameter of the detector on the left was 12.7 cm, while the one on the right was 8.88 cm in diameter. The efficiencies of these detectors were reported by El-Kadi (El-Kadi 1981). Descriptions of the experimental configurations are presented in table 2-2. The distances from the center of the sample to the face of the detectors were 5.67 m for the left detector and 3.74 m for the right detector for the $\sigma(\Theta)$ measurements (Condition I in table 2-2).

Two small liquid scintillators were used to monitor the neutron flux from the source reaction. The flux monitor used for normalization was mounted in a fixture that hangs from the ceiling and was therefore referred to as the CEILING monitor. It viewed the source reaction at about 50° from the horizontal and was well collimated to reduce backgrounds. The flight path from the gas cell to this monitor was

TABLE 2-2

EXPERIMENTAL CONFIGURATIONS

Experimental Parameters	$\sigma(\theta)$ Experiments	$A_y(\theta)$ Experiments
GAS CELL		
Entrance foil[1]	0.00254 mm Molybdenum	0.00635 mm Havar
Entrance foil[2]	0.00635 mm Havar	0.00635 mm Havar
D^2 Gas Pressure[1]	2 bar	4 bar
D^2 Gas Pressure[2]	8 bar	8 bar
Gas Thickness[1]	0.978 mg/cm2	3.40 mg/cm2
Gas Thickness[2]	1.059 mg/cm2	4.13 mg/cm2
Center-of-Cell to [1]	9.25 cm	9.31 cm
Center-of-Sample Distance[2]	10.79 cm	10.79 cm
DETECTOR	CONDITION I	CONDITION II
Detector	(left,right)	(left,right)
Center-of-Sample to Detector face	(568,374) cm	(376,275) cm
Detector Thickness	(5.08,5.08) cm	(5.08,5.08) cm
Detector Radius	(6.35,4.44) cm	(6.35,4.44) cm

[1] Experimental configuration using the "old" gas cell. All data taken before March 1982 were acquired using these experimental parameters.

[2] Experimental configuration using the "new" gas cell. See table 4-1 for list of data acquired using this configuration.

approximately 1.8 m. Great care was taken in aiming this detector so that it was shielded from all neutrons that scattered from the sample. The other neutron flux monitor was mounted on a stand that was positioned at approximately 0^{o} and was located about 4.5 m from the scattering sample. This monitor was referred to as the ZERO DEGREE monitor. This scintillator detected the neutrons that were transmitted through the sample and therefore could not be easily used for normalization purposes. However, it was well suited for monitoring the beam pulsing because of its relatively long flight path, high count rates, and sufficiently low backgrounds. A more detailed description of the detectors is given in (Beyerle 1981, Guss 1982a).

Electronics

All processing of the signals from the four detectors was performed in the control room. The anode signal from each detector and the pick-off signal (output of the HP preamps) were piped into the control room through 50 Ω low loss cable. The electronics for each of the four detectors were identical. Figure 2.9 is a block diagram of the electronics for one. The incoming anode signal was fed into three modules; a pulse-shape discriminator, a constant-fraction discriminator (CFD), and a linear amplifier plus single-channel analyzer (SCA). Because the scintillators are sensitive to both neutrons and γ-rays, it was necessary to discriminate against the γ's to reduce backgrounds in the neutron TOF spectra and to simultaneously decrease the computer dead time (DT). Discriminating against low energy neutrons also reduced backgrounds in the TOF spectra and decreased computer DT.

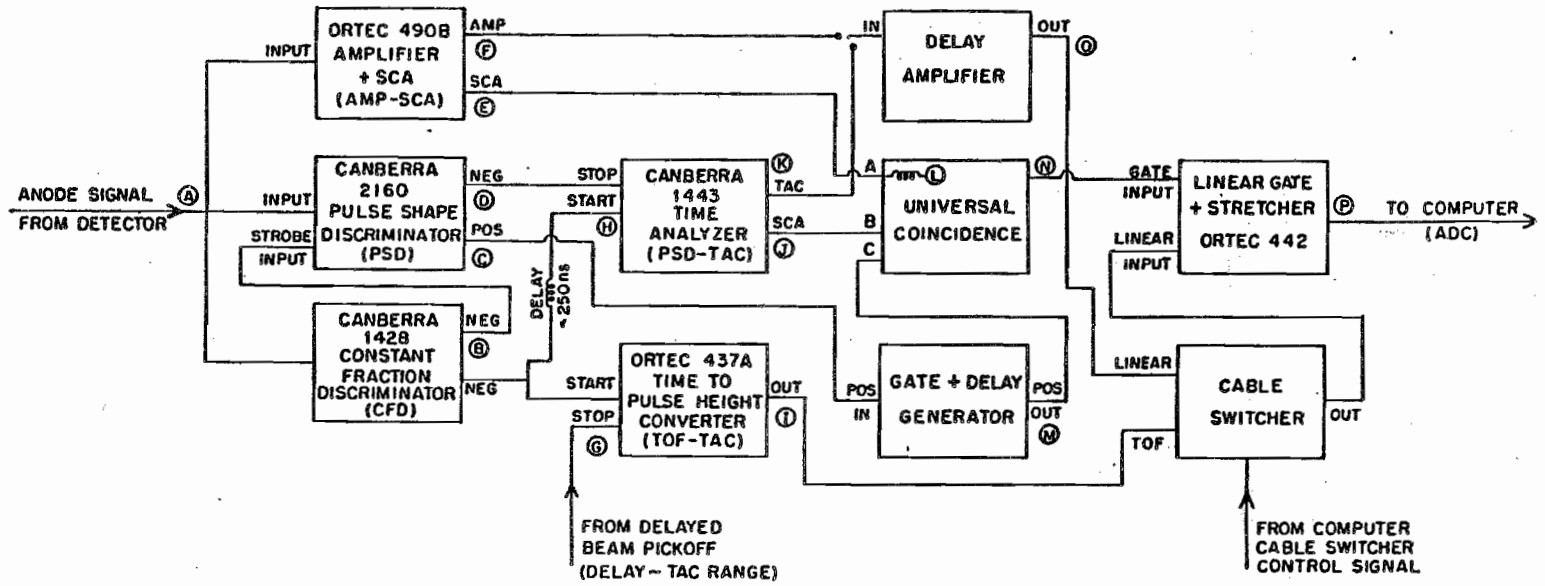

Figure 2.9. Block diagram of the electronics used in the $\sigma(\theta)$ and $A_y(\theta)$ experiments.

The n-γ discrinimation was done by using pulse-shape-discrimination (PSD) techniques. Because the γ-rays interact directly with the atomic electrons in the scintillator and the neutrons interact indirectly via n-p scattering, and since the decay response is different for low-ionizing particles (electrons) than for highly-ionizing particles (protons), the rise time of the anode signals produced by γ-ray interactions are shorter than those produced by neutron interactions. The pulse shape difference is illustrated in fig. 2.10(a). The PSD module outputs a logic pulse at a constant fraction of the "trailing" edge of the anode signal, thus outputing signals for neutrons and gammas at slightly different time intervals following the intial rise. The output of the CFD (see fig. 2.9) is used to start a time-to-amplitude converter (TAC) that is stopped by the output of the PSD module. The output voltage of the TAC is directly proportional to the time difference between the start and stop signals. Therefore, two groups of voltages are produced on the output of the TAC as shown in fig. 2.10(b). At the beginning of each experiment the PSD circuit is checked, and the discrimination level is set to the desired value. During the setup procedure the output of the PSD-TAC is digitized and sorted by the computer. A typical PSD spectrum is shown in fig. 2.10(c). The window on the SCA in the PSD-TAC is adjusted to give a logic pulse (gate) for all neutrons and for a minute fraction of the γ's. The thresholds for the $\sigma(\theta)$ and $A_y(\theta)$ experiments are indicated in fig. 2.10(c). The PSD gate is used in coincidence with the energy-bias requirement, descibed next.

All neutrons (i.e., recoil protons) having energies of less than 2 MeV were eliminated by means of pulse height discrimination. The anode

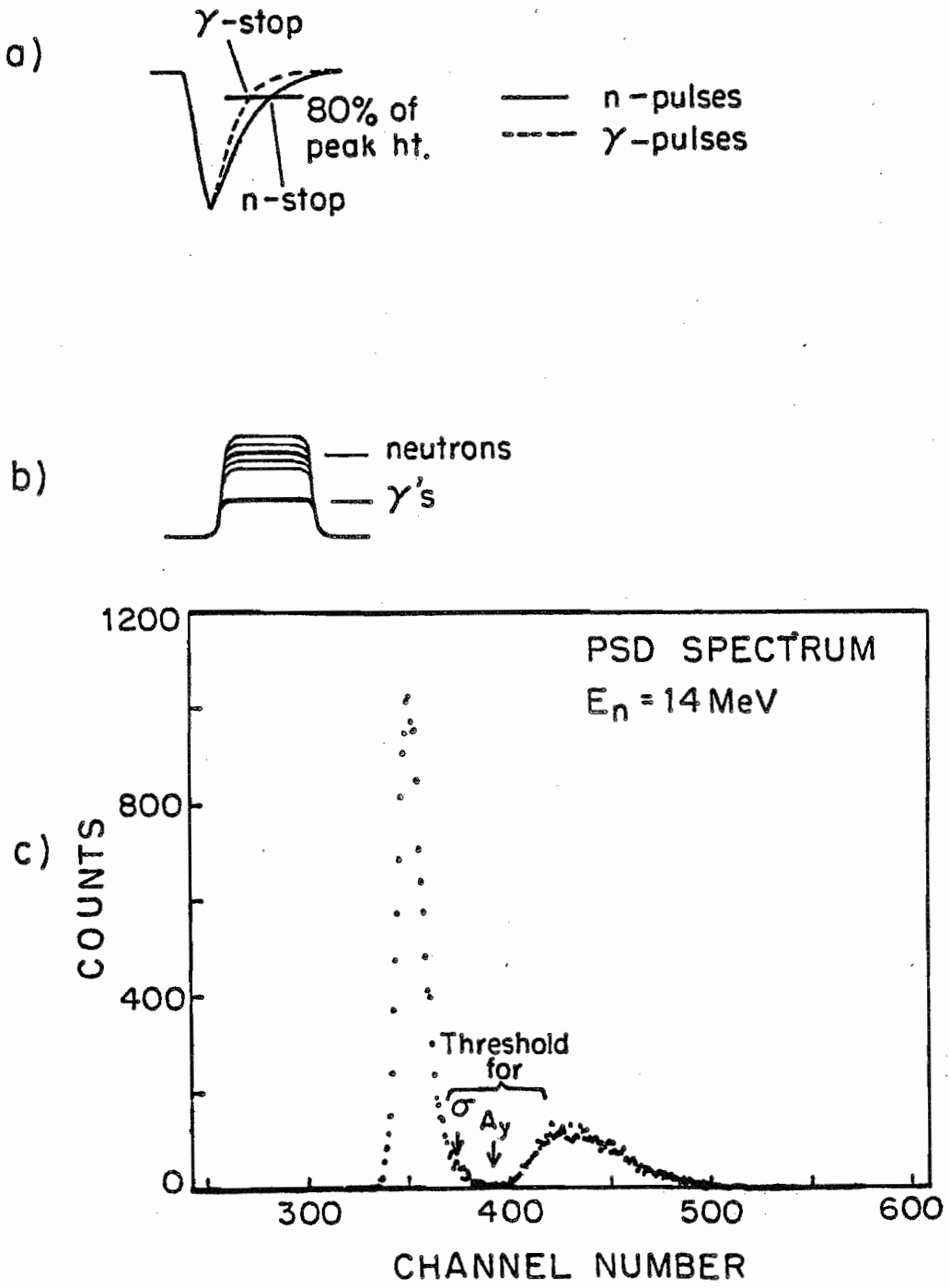

Figure 2.10. (a) Anode signals from the liquid scintillator.

(b) Output of the PSD-TAC

(c) A typical PSD spectrum indicating the threshold settings for the $\sigma(\theta)$ and $A_y(\theta)$ experiments.

signal was amplified and fed into a SCA. The lower level on the SCA was set on the recoil edge of ^{137}Cs which corresponds to proton recoil energies of about 2 MeV. A gate resulted for all voltages above this bias. This gate was used in coincidence with the PSD requirement.

The fast output of the CFD was used to start the TOF-TAC and the stop signal was derived from the pick-off signal. The output of the TAC was shaped by a linear gated stretcher that was gated by the dual coincidence requirements of PSD and low bias. The stretched TAC signals and gates were sent to the computer interface to be processed. The TAC signals were digitized by an analog-to-digital converter (ADC), and the gates were counted by a scaler. An event counter stored the number of events processed by the computer. The dead time correction (DTC) was computed as the ratio of the scaler to the number in the event counter. The DTC's were usually less than 1%.

2.2 Experimental Technique for Analyzing Power Measurements

2.2.1 Introduction

All analyzing power $A_y(\theta)$ experiments were conducted in the same target room as the $\sigma(\theta)$ experiments, using the same neutron TOF spectrometer. A DC beam of polarized deuterons produced by the TUNL Lamb-shift polarized ion source (PIS) was ramped, bunched, and chopped to create narrow beam pulses. Typical operating conditions were deuteron-beam intensities of 150 nA with 65% beam polarization on target. The neutrons emerging at 0^o from the $^2H(\vec{d},\vec{n})$ polarization transfer reaction were scattered from cylindrical samples and were detected by two heavily shielded neutron detectors; the same samples and detectors were used in the $\sigma(\theta)$ measurements. The $^2H(\vec{d},\vec{n})$ polarization transfer reaction was favored over other possible transfer reactions, because in addition to the features previously mentioned about the $^2H(d,n)$ reaction, it also has the advantage of a high polarization transfer (~ 90%), which is essentially constant in the energy range of these experiments (Lisowski 1975). The detectors were symmetrically positioned about the beam axis, and TOF spectra were accumulated for neutrons that scattered to the left and to the right for incident beams having neutron spin up, and successively, for incident beams having spin down. The acquisition of data in this manner was useful for reducing instrumental asymmetries.

2.2.2 Lamb-Shift Polarized Ion Source

The polarized beam of deuterons necessary for these experiments was produced by the TUNL Lamb-Shift polarized ion source (PIS). This source

has been described in much detail (Trainor 1973) and therefore will be described only briefly here. Figure 2.11 is a diagram of the PIS and the low-energy end of the tandem. The bold line with arrows indicate the path of the beam. The D^+ ions are produced in the duoplasmatron and are accelerated through the anode opening with an average energy of 1100 eV. They undergo charge exchange in the cesium canal and emerge as neutral atoms. This neutral beam then drifts through the spin filter, where the desired spin state is selected, and into the argon canal where it picks up another electron and emerges as a D^- ion beam. The D^- ions are accelerated through a potential difference of 50 kV. They are bent 90^o by an electrostatic mirror and pass through the spin precession solenoid. The direction of the B-field in this solenoid defines the axis of quantization. The ion beam is then bent another 90^o by a second electrostatic mirror onto the axis of the tandem accelerator.

2.2.3 High-Efficiency Buncher System

Because of the relatively low beam intensities produced by the PIS, one cannot afford to use standard chopping and bunching techniques to pulse the beam. Instead, the beam is prebunched into the phase acceptance of the double-drift buncher. The double-drift buncher is used instead of the single buncher because its efficiency (the percentage of DC beam that is compressed into the beam pulses) is nearly 65% as opposed to the 25% efficiency of a single buncher (Wender 1980 and Wender 1981). The double-drift buncher consists of two drift tubes separated by 55 cm as shown in fig. 2.12. The fundamental frequency of the first buncher is 4 MHz. The second buncher is driven at 8 MHz and with approximately half

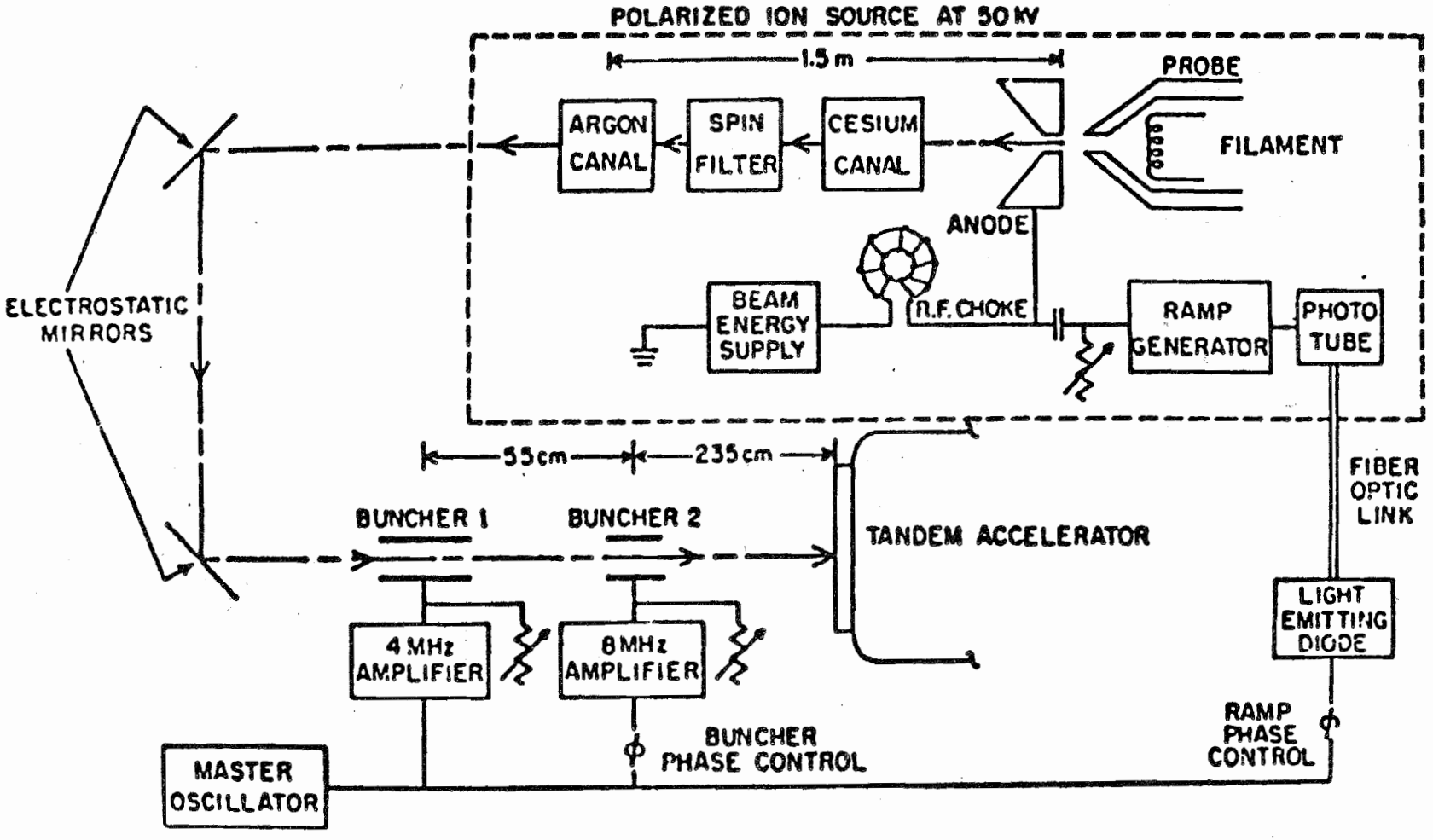

Figure 2.11. Top view of the TUNL Lamb-shift polarized ion source (PIS) and the double-drift buncher system. The bold line indicates the path traveled by the polarized beam.

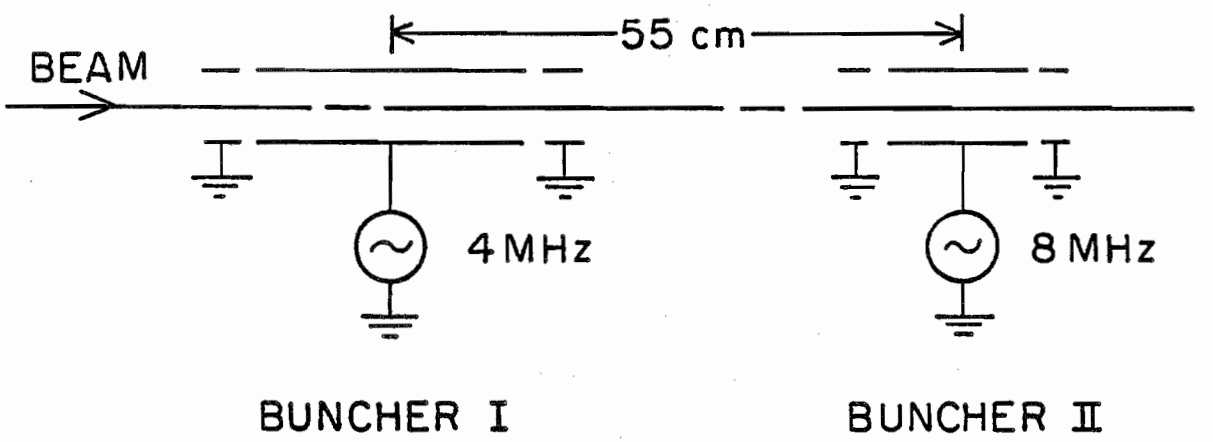

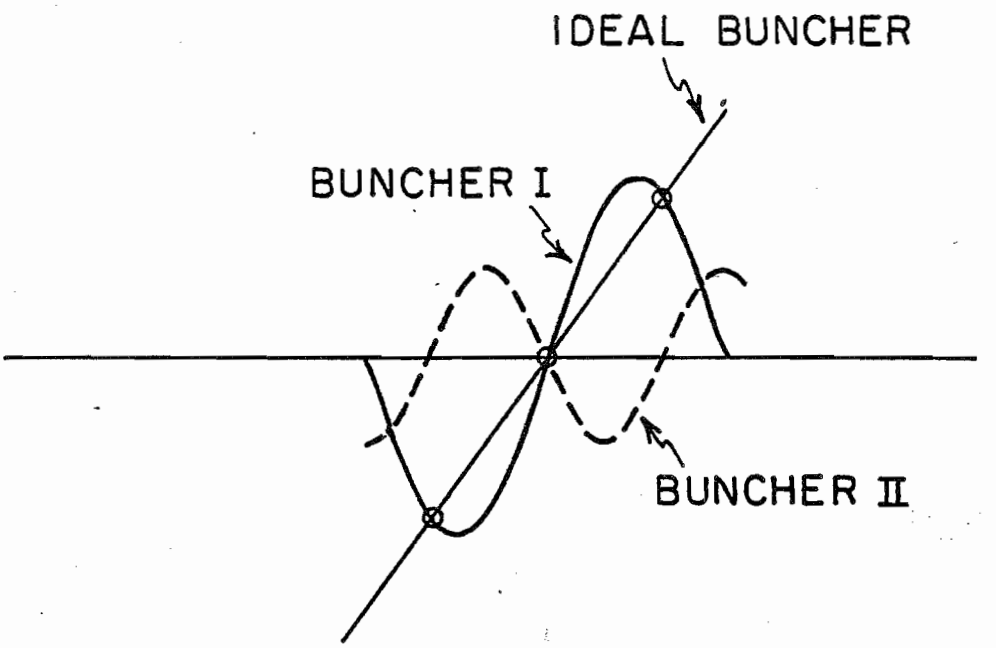

Figure 2.12. Side view of the double-drift buncher system. Top half shows the relative lengths and distance between buncher tubes. Bottom half shows the amplitude and phase relationships between the two buncher voltages and compares each to the (linear) voltage for an ideal buncher.

the amplitude of the first buncher. The first buncher "over-modulates" the energy of the beam, and the phase and amplitude of the second buncher is adjusted to correct for this over modulation so that the effective bunching voltage of the system is approximately linear (Milner 1979).

Because the double-drift buncher is only approximately 65% efficient (can compress only 140 ns of the DC beam into narrow pulses each 250 ns period), it is desirable to prebunch the beam into the phase acceptance of the buncher system (Wender 1980 and Wender 1981). This prebunching is done by the ramp generator, which modulates the energy of the particles leaving the duoplasmatron with a voltage that varies linearly in time. More details about the ramp generator and its performance are given in chapter 3. The amplitude of the ramping voltage is reasonably small, on the order of 70 V for deuterons at 4 MHz. It is possible to prebunch the beam with such a low ramping voltage because of the 1.5 m long path in which the deuterons drift as neutral beam at low energy. The combination of the ramp generator with the double-drift buncher compresses about 90% of the DC beam emerging from the PIS into beam bursts having a fwhm of 2 ns (Wender 1980, Wender 1981, and Howell 1982b). The remaining 10% of the beam, which would normally appear as background between the beam pulses, is swept away by a special sine wave chopper located at the low energy end of the tandem. This clean-up chopping assures good beam current integration, and improves the signal/noise ratio in the TOF spectra. This complete system has proven to be a very powerful technique for producing an intense beam of pulsed polarized deuterons. Normal operating conditions are deuteron beam intensities of 100 to 200 nA with 65% beam polarization.

Because the polarized beam was a factor of 10 lower in intensity than the unpolarized beams used in the $\sigma(\theta)$ measurements, if everything else was unchanged, the counting rates in the $A_y(\theta)$ experiments would be a factor of 10 lower than those in the corresponding $\sigma(\theta)$ experiments. To increase the counting rates in the $A_y(\theta)$ experiments, the gas pressure was increased by a factor of 3.3, and the flight paths of the detectors were decreased from 4 m and 6 m to 2.7 m and 3.7 m, respectively (see table 2-2). Increasing the gas pressure increased the energy spread of the neutrons from the source reaction, and thus the $A_y(\theta)$ measurements averaged over larger energy intervals. Decreasing the flight paths to the detectors degraded the resolution of the spectrometers, as can be seen by comparing the spectra in fig. 2.13, and thus could not be done for high incident neutron energies, i.e., above 14 MeV. For 17 MeV the $A_y(\theta)$ measurements were conducted at full flight paths. Spectra accumulated during $\sigma(\theta)$ and $A_y(\theta)$ experiments at 17 MeV are shown in fig. 2.14. To make comparisons easier, the horizontal scales in these figures were adjusted to give the same time calibration (time/channel) for the $^{28}Si + n$ and the $^{28}Si + \vec{n}$ spectra.

2.2.4 Simultaneous measurement of $A_y(\theta)$ and $\sigma(\theta)$

Because of the similarities between the $\sigma(\theta)$ and $A_y(\theta)$ experiments, the possibility of simultaneous measurements of both observables was investigated. The results of these tests have been reported in (Howell 1983a). Direct excerpts from this publication will be enclosed in quotes.

"Historically, many measurements of $\sigma(\theta)$ have been reported for the

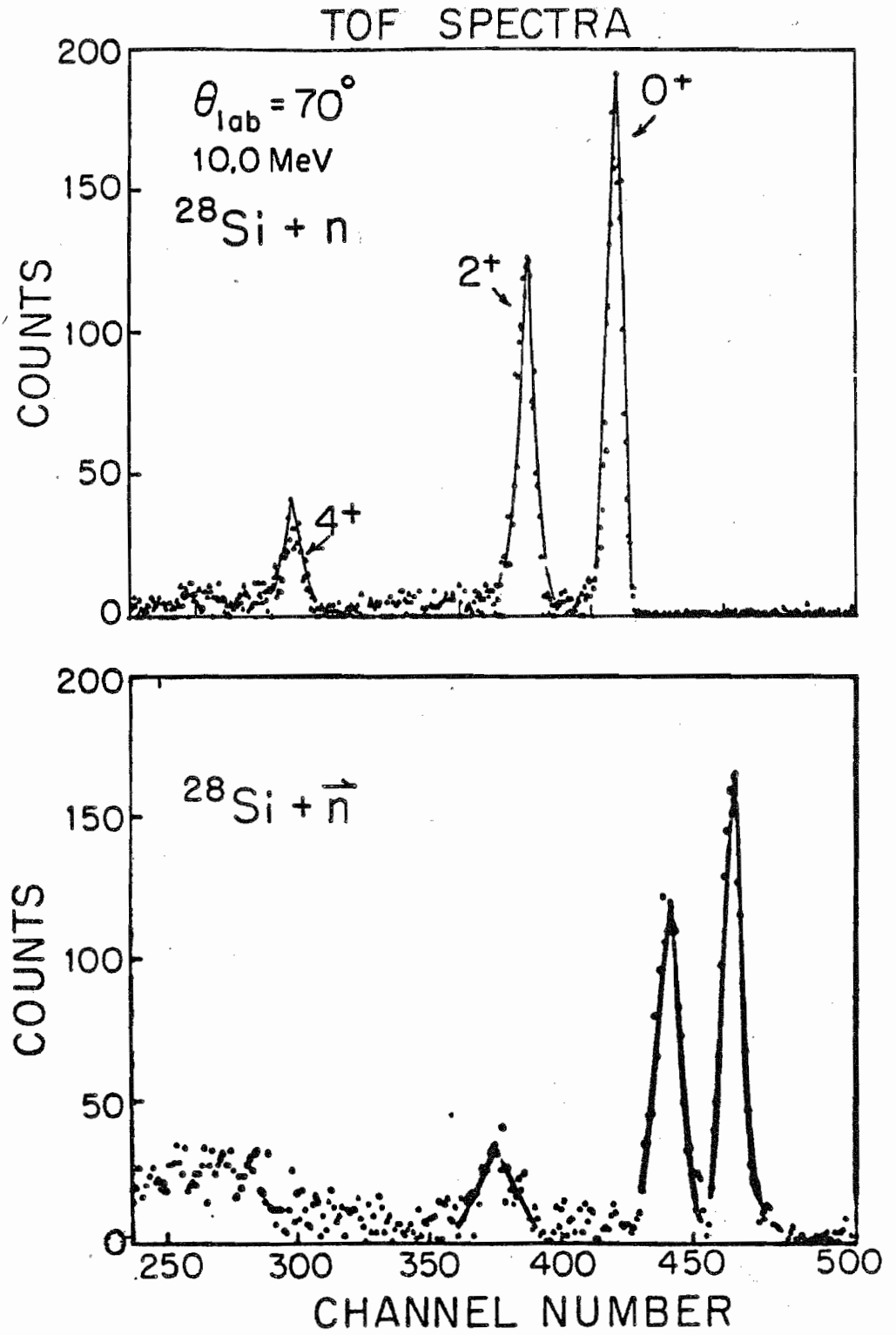

Figure 2.13. TOF spectra for $^{28}Si + n$ at $E_n = 10$ MeV.

Top half: Spectrum obtained in a $\sigma(\theta)$ measurement. Bottom half: Sum of the "spin-up" and "spin-down" spectra from the complementary $A_y(\theta)$ measurement.

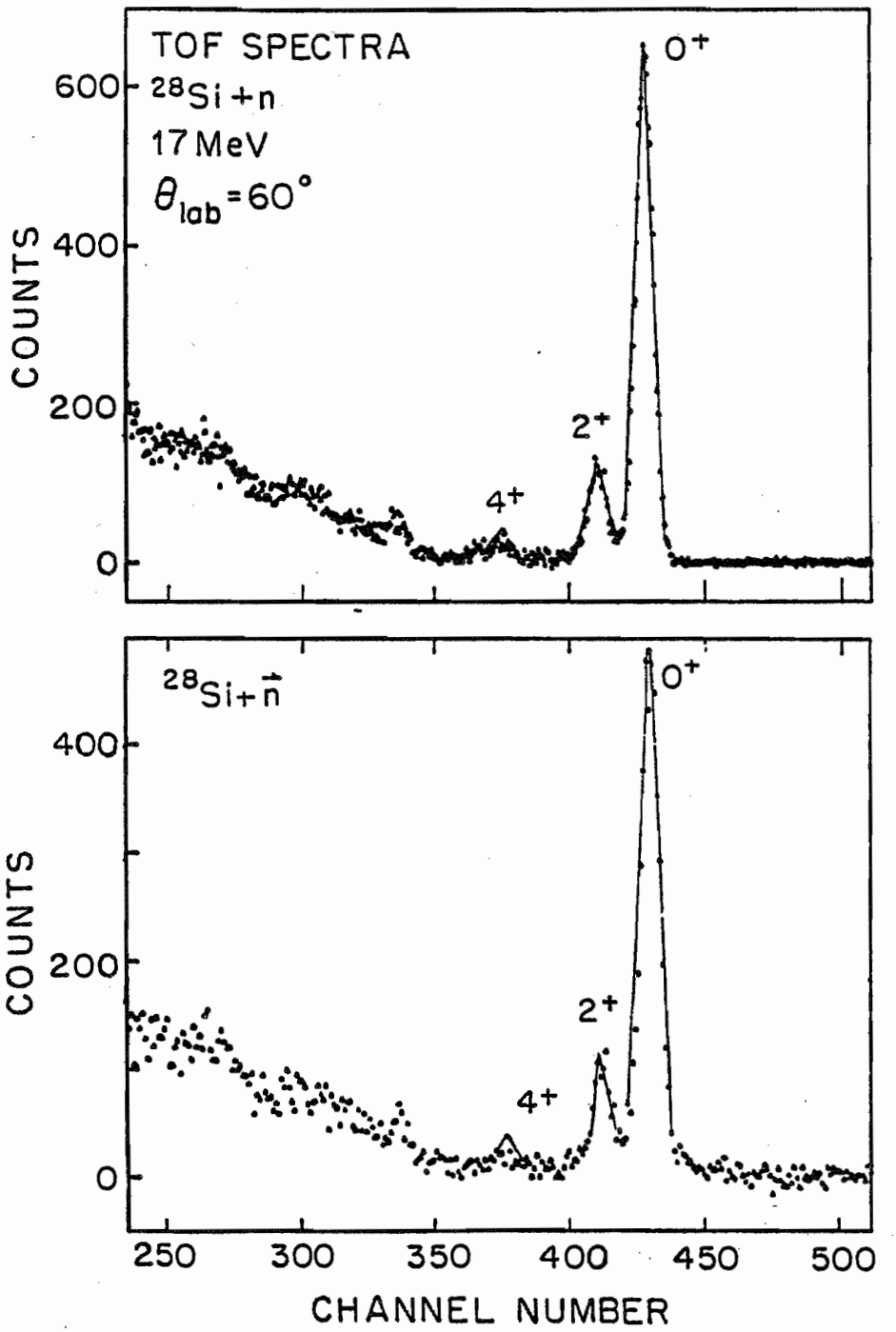

Figure 2.14. TOF spectra for ^{28}Si + n at E_n = 17 MeV.

Top half: Spectrum obtained in a $\sigma(\theta)$ measurement. Bottom half: Sum of the "spin-up" and "spin-down" spectra from the complementary $A_y(\theta)$ measurement.

neutron energy of 14 MeV and for energies below 8 MeV. The concentration of the effort at TUNL has been to fill the gap between 8 and 14 MeV in typical increments of 1 to 2 MeV. Measurements of $A_y(\theta)$ are very sparse for neutron energies energies above 4 MeV and the intent of the polarization program at TUNL has been to provide accurate and detailed information on $A_y(\theta)$ in the same energy region as our $\sigma(\theta)$ measurements. A group at Stuttgart has recently initiated a concerted effort to determine $A_y(\theta)$ at 8 MeV for many nuclei and their data is just beginning to appear in the literature (Bulski 1982). To our knowledge this group is the only one to ever report scattering measurements of the kind illustrated in the present paper where the neutron yields obtained for the $A_y(\theta)$ measurements are also used to provide accurate $\sigma(\theta)$ information. Attempts by K. Murphy (to be published) to obtain $\sigma(\theta)$ from data obtained for $A_y(\theta)$ determination for $(\vec{p},n)$ reactions are also underway at TUNL. "

In this test a relative cross section was extracted from the yields of an $A_y(\theta)$ and compared to the $\sigma(\theta)$ that was measured in a conventional neutron-scattering experiment with unpolarized beam. Only a relative cross section angular distribution could be determined from the yields in the $A_y(\theta)$ experiment, because initially we were only interested in a ratio of the spin-up and spin-down yields per BCI, N_u and N_d, an absolute normalization to $^1H(n,n)^1H$ scattering was not performed. The relative cross section was computed by averaging the spin-up and spin-down yields at each angle, $N_{av}(\theta) = \frac{1}{2}(N_u(\theta) + N_d(\theta))$.

"Figure 2.15 gives the comparison of the relative cross sections derived from the $A_y(\theta)$ data to the results of a conventional $\sigma_0(\theta)$ experiment performed with an unpolarized neutron beam. The triangles and

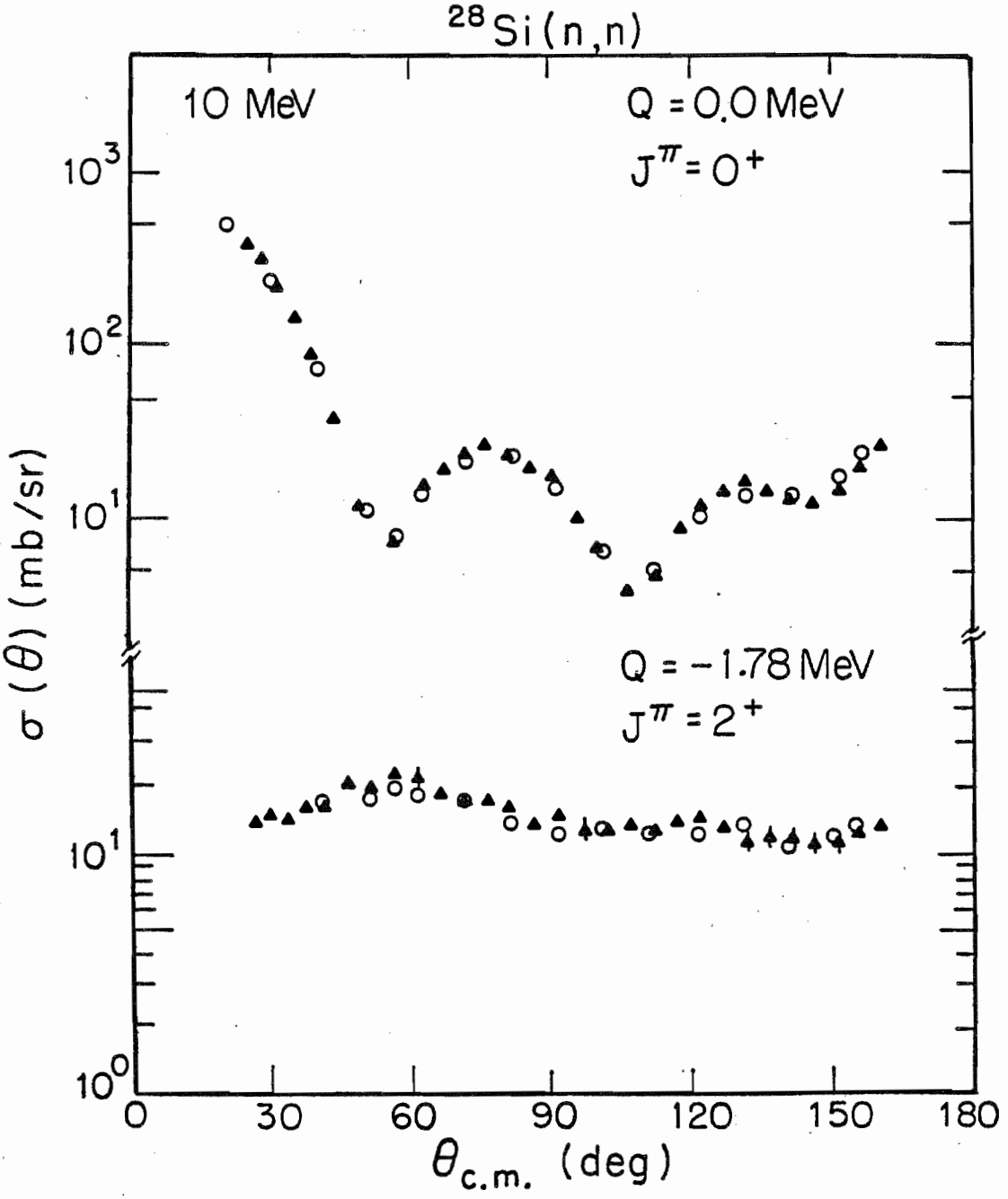

Figure 2.15. Cross sections for ^{28}Si(n,n_0) and ^{28}Si(n,n_1) derived from $\sigma(\theta)$ measurement (triangles) and $A_y(\theta)$ measurement (circles).

circles represent the $\sigma_0(\theta)$ and $N_{av}(\theta)$ data, respectively. For purposes of comparison, $N_{av}(\theta)$ was normalized to $\sigma_0(\theta)$ by comparing a region in the two angular distributions where the cross sections vary slowly with angle, $\theta = 60^o$ to $\theta = 90^o$. Both data sets have been corrected for multiple scattering, flux attenuation, and solid geometry. Because of the differences in the detector geometry and gas cell pressure used in the two experiments, these corrections were slightly different for the two data sets. The uncertainties in the data are typically less than $\pm 5\%$ over the entire angular distribution of both data sets. The agreement between the data sets is excellent, and this confirms our speculation that neutron-scattering experiments for measuring with polarized beams can provide accurate cross section data if the measurement is carefully controlled and if the relative detector efficiency as a function of neutron energy is known.

"The conclusion of the test reported here is that it is possible to perform accurate measurements of $\sigma(\theta)$ and $A_y(\theta)$ for neutron elastic and inelastic scattering if the experimental apparatus is properly designed. The present results for the sum $(\sigma_u + \sigma_d)$ had to be normalized using the σ_0 data. However, if it had been recognized during the measurement of $A_y(\theta)$ that the experiment was a possible test of an absolute $\sigma(\theta)$ measurement, then the proper normalization measurement to $^1H(n,n)^1H$ could have easily been conducted at that time; we have no doubt that the latter normalization measurement would have been as successful as in the conventional σ_0 experiment.

"Concerning the accuracy of the $\sigma(\theta)$ measurement with polarized beams, the limiting factor would not be the statistical uncertainties.

Typically, we determine $A_y(\theta)$ to about ± 0.03 with a neutron beam having $p_y=0.6$. In this case the yields in the detectors would lead to a determination of $\sigma(\theta)$ to better than $\pm 2\%$. For most $\sigma(\theta)$ needs, this statistical accuracy is sufficient.

"The future looks very promising for simultaneous $A_y(\theta)$ and $\sigma(\theta)$ measurements. As pointed out above, our $A_y(\theta)$ measurements are obtained with about 150 nA of pulsed deuteron beams compared to 1.5 μA for our σ_0 experiments. The measurements require 1/2 to 3 hours per angle. We note that the TUNL polarized ion source is about 10 years old and new commercial sources which deliver a factor of 10 more beam than our source at TUNL are now available. Therefore, we believe that $\sigma(\theta)$ measurements in the future can proceed with polarized neutron beams at a rate comparable to the present σ_0 measurements with unpolarized neutron beams. Furthermore, our system could be expanded to a larger array of neutron detectors so that several angles could be investigated simultaneously to save additional time. "

CHAPTER 3

LINEAR VOLTAGE RAMP GENARATOR FOR THE PIS

The $A_y(\theta)$ data reported in this dissertation were acquired using the three-stage buncher system described in chapter 2. The overall performance of the system is the product of the performance of each component. Until recently, the weakest link in this system was the linear voltage ramp (LVR) generator. Even though its performance as a prebuncher was adequate, its unreliability necessitated the development of an improved circuit. Spurious signals from the duoplasmatron of the PIS would frequently destroy the output stage of the LVR generator. Thus, the experiments were often interrupted to repair the damaged circuit. It was necessary to design, construct, and test a new LVR circuit which would have the following advantages over the previous generator: (1) simpler construction, (2) greater reliability, and (3) improved performance. Much of the text that follows was extracted directly from a publication by Howell and Wender (Howell 1982b). Direct excerpts from the manuscript will be enclosed in quotation marks.

"The schematic diagram for the LVR is shown in fig. 3.1. The trigger signal is obtained directly from the anode output of a photomultiplier tube. This signal is applied to the input of the LM306 discriminator. The discriminator output is inverted by the SN74S00N NAND gate, and is amplified and reinverted by the dual stage amplifier, Q1 and Q2. This signal is applied to the gate of the VN98AJ VMOS FET. The VN98AJ output is used to drive the high capacitance gate of the IRF332 high power HEX

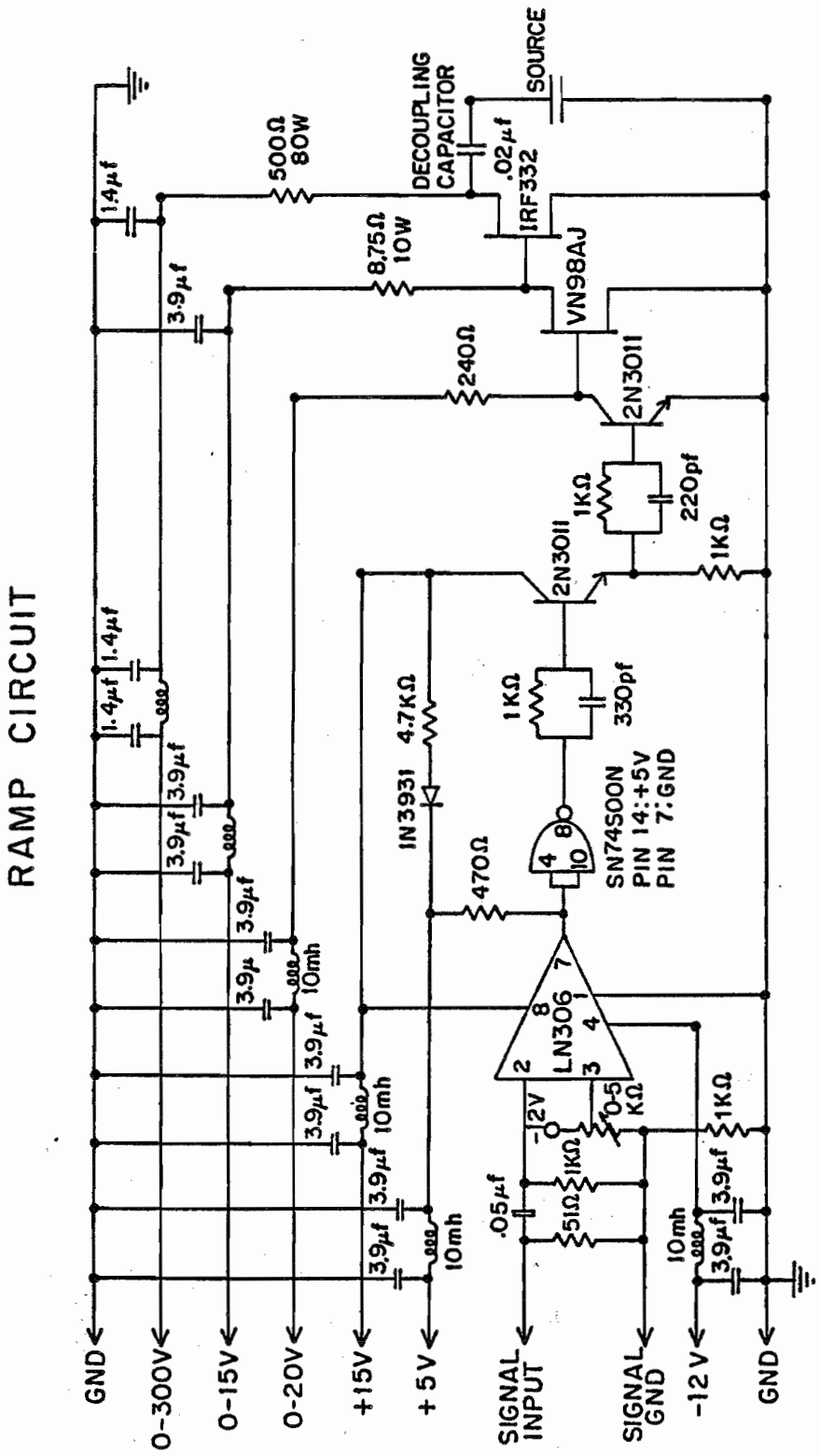

Figure 3.1. Schematic diagram of LVR generator built in 1981.

FET, which serves as the current switch to discharge the source capacitance to ground.

"Figure 3.2 shows the linearity and flyback time of a typical LVR waveform during operation of the source. It has a period of 250 ns, a peak-to-peak amplitude of 80 V, and a flyback time of slightly less than 40 ns. It is crucial to minimize the flyback since particles leaving the duoplasmatron during this time are lost as white background.

"Since the ions emerging from the source are not monoenergetic, a perfect time focus is not possible. If we assume a Gaussian distribution of energies with standard deviation σ (full width at half maximum (fwhm) of Γ), then the intensity as a function of position x and time t for an ion of mass m which leaves the duoplasmatron during the time τ is proportional to the following integral:

$$I(x,t) \propto \int_0^{\tau} \frac{mx}{(t-t')^3} \times \exp-\left[\left[\frac{m}{2}\left(\frac{x}{t-t'}\right)^2 - \frac{m}{2}\left(\frac{x}{t_0-t'}\right)^2\right]^2/2\sigma^2\right]dt' \qquad (3.1)$$

where t_0 is the transit time to the target for particles having energy E_0, the mean energy of the gaussian distribution. Using this expression it is possible to predict the shape of the beam pulse at a target position."

To measure the performance of the LVR, the bunching system was operated using the LVR alone. Figure 3.3 shows the electronics used to test the performance of the LVR generator. "The beam was accelerated to 6.0 MeV and elastically scattered from a silver foil into a charged particle detector. Pulses from the detector were used to start a time-to-amplitude converter (TAC), and stop pulses were obtained from the

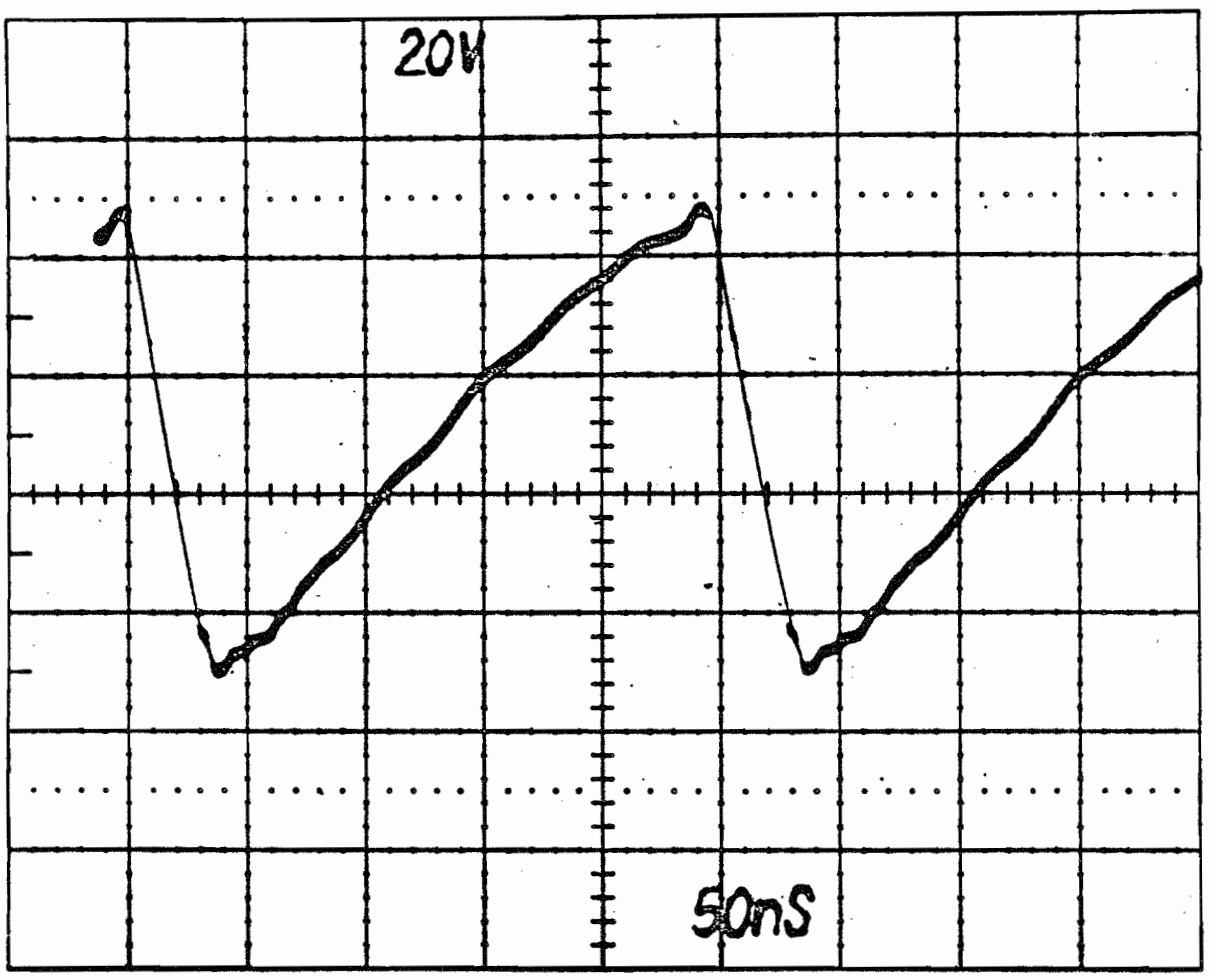

Figure 3.2. Photograph of the waveform of the LVR when connected to the anode of the duoplasmatron with the ion source in operation. The maximum voltage in 80 V, the period is 250 ns and the discharge time is approximately 40 ns.

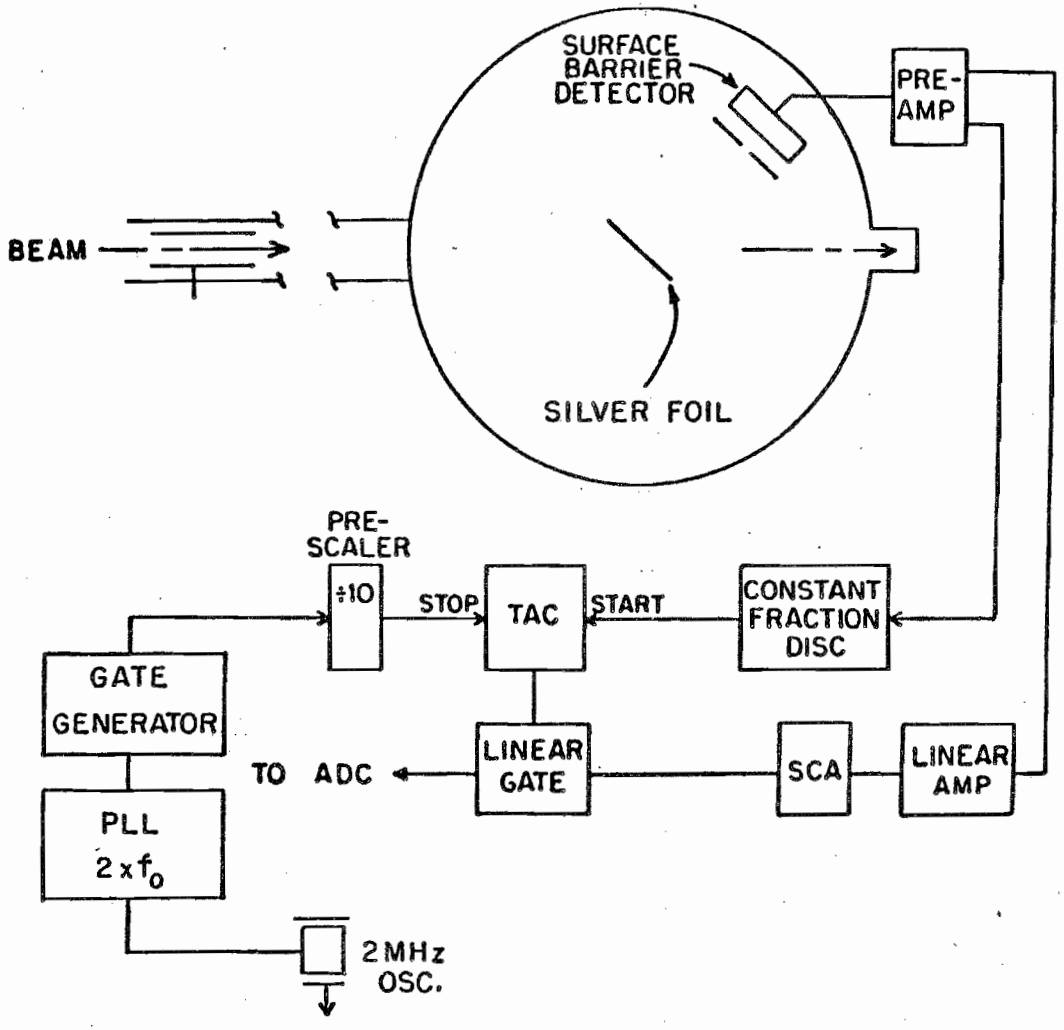

Figure 3.3. Diagram of experimental arrangement and electronics used in testing the performance of the LVR generator.

oscillator. Some typical time spectra of pulsed deuterons at 4 Mhz with maximum ramp voltages of 20 V, 80 V, and 130 V are shown in fig. 3.4. The solid line in each case is a prediction using the integral in eqn. (3.1). At a ramp voltage of 20 V (fig. 3.4a), the beam has a fwhm of 186 ns, and the corresponding plot of position verses time shows the time focus occurring after the target. At 80 V (fig. 3.4b) the beam is compressed to 65 ns with the time focus occurring at the target. The non-zero width is a result of the energy spread of the source. Increasing the ramp voltage to 130 V will move the time focus ahead of the target as shown in fig. 3.4c."

"Beam profile spectra were taken for several ramp voltages for deuterons and protons at 4 MHz and 2 MHz. The results of these measurements are plotted in fig. 3.5. The solid line in each case is a fit to the data, which were produced by varying x_0, the effective drift length, and σ in eqn. (3.1). The difficulty in fitting protons at 2 MHz for ramp voltages over 90 V is presumably due to the relatively large energy spread given the beam, and the problem of transporting such a beam through the optics of the source.

"Because the minimum width of the beam bursts produced by the LVR depends on the energy spread of the source, it is possible to infer an upper limit on the energy spread of the source. An upper limit of Γ' = 20 eV was found for deuterons and Γ' = 12 eV for protons. The difference in energy spread for these two ions is believed to be due to differences in their mobility and their resulting space charge densities in the region between the probe and anode electrodes in the duoplasmatron (Lejeune 1974).

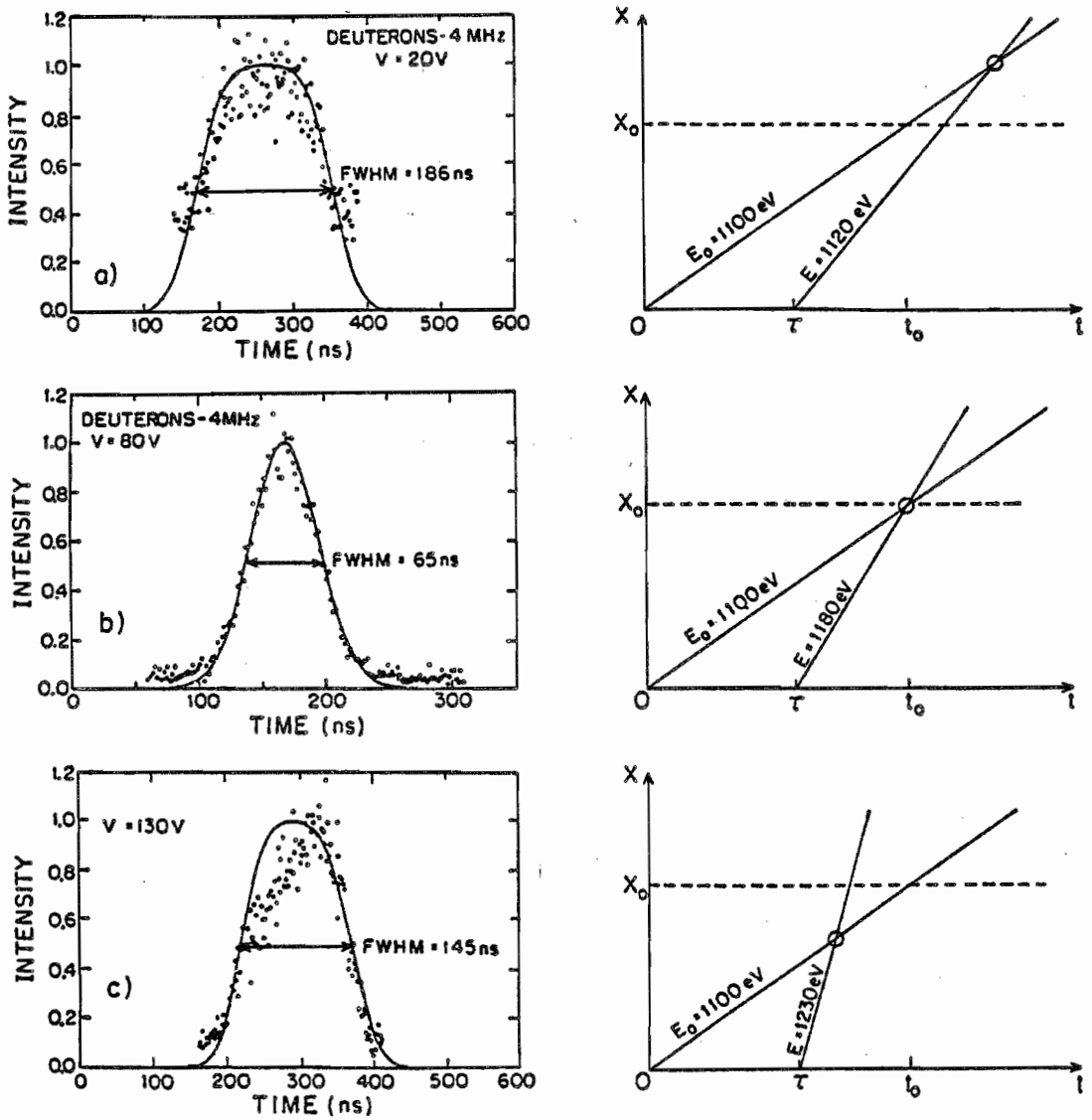

Figure 3.4. Typical time spectra for 6.0 MeV deuterons elastically scattered from a silver foil for LVR voltages of 20 V, 80 V and 130 V. On the right are position versus time plots showing the position of the time focus for each of these voltages. The solid curves are the predictions of eqn. (3.1).

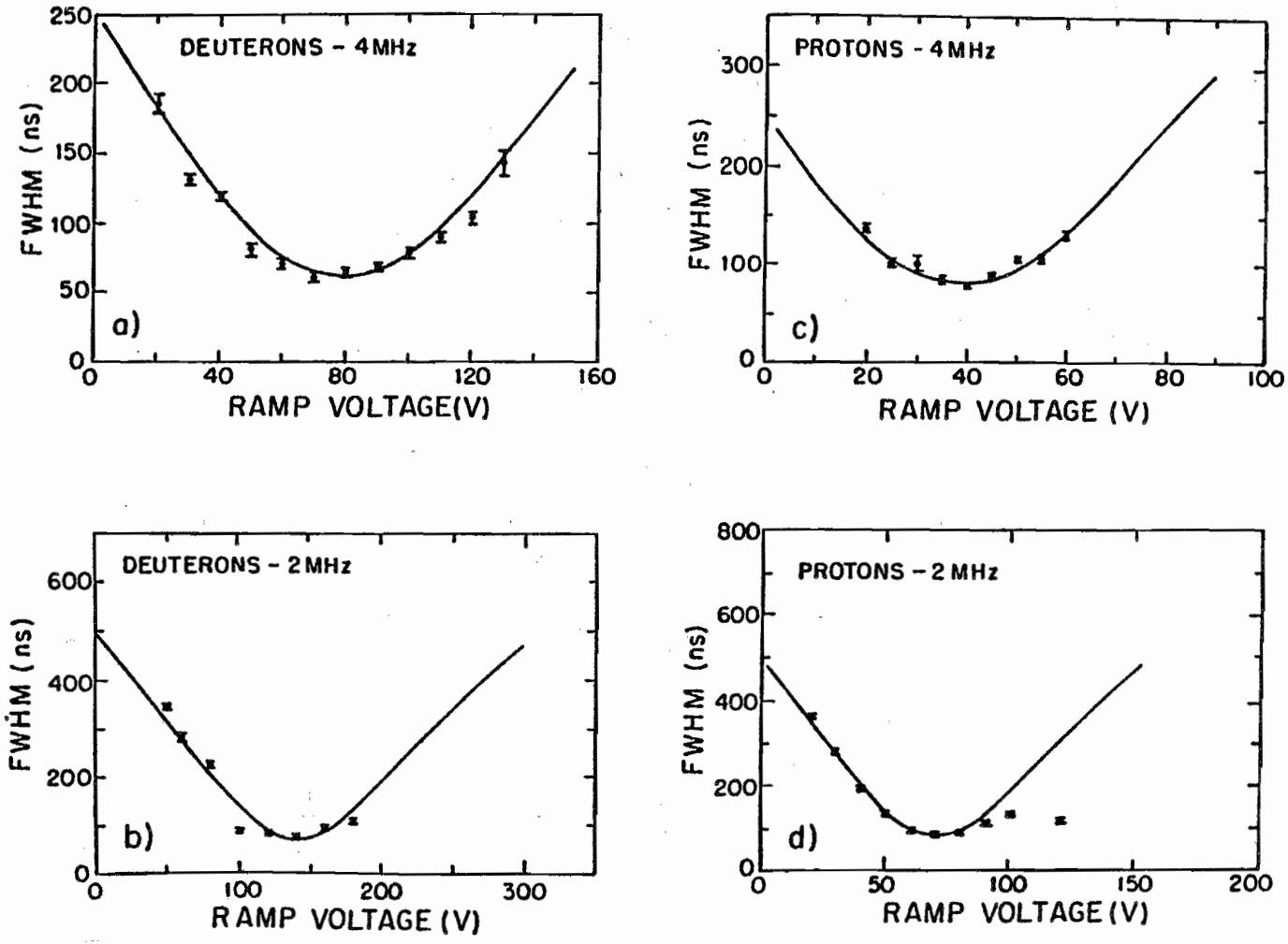

Figure 3.5. Plots of the fwhm of the beam as a function of maximum LVR voltages for (a) deuterons at 4 MHz, (b) deuterons at 2 MHz, (c) protons at 4 MHz, and (d) protons at 2 MHz. The lines are predictions of eqn. (3.1).

"A summary of the LVR performance is given in table 3-1. The efficiency is defined as the ratio of the number of counts in 140 ns, which is the approximate time acceptance of the double drift buncher, to the number of counts in one period. Thus, by prebunching the beam with the LVR before injection into the double drift buncher, we can produce beam pulses that contain 90% of the beam with a fwhm of 2 ns and a 1000:1 peak-to-background ratio."

Since the completion of the above project, the author has been involved in the development of a high-powered LVR generator to pulse ion beams into the phase acceptance of the cyclotron at TUNL. The circuit developed for this task is capable of producing peak-to-peak voltages of 600 V with rise times of less than 40 ns. More details about the design and construction of this high-power, high-speed switching circuit and the pulsing system for the cyclotron injector are given in the TUNL annual reports (Howell 1982c and Howell 1983b).

The experience gained from the cyclotron-injector project then led to the design and construction of an even more improved low-voltage LVR generator for the PIS. Figure 3.6 is a schematic diagram of the most recent LVR generator for the PIS. (This circuit was designed by the author and fabricated by Jeffrey Whisnant, a physics student at the University of North Carolina at Chapel Hill. The construction and testing of the LVR circuit was a major portion of Whisnant's senior project.) The major improvements in this circuit over the generator discussed above are: (1) it has fewer adjustable parameters and therefore is easier for users to operate, and (2) its flyback time is typically 30 to 40 ns instead of the 40 to 50 ns obtained with the other generator.

TABLE 3-1

SUMMARY OF RESULTS

	Deuterons		Protons	
Observables	4 MHz	2 MHz	4 MHz	2 MHz
Γ(eV)*	20	20	12	12
Voltage	70	140	40	70
fwhm(ns)	61	76	78	85
Efficiency(%)	89	95	85	94

* These values are estimates of the upper limits on the energy spread of the source (see text for details).

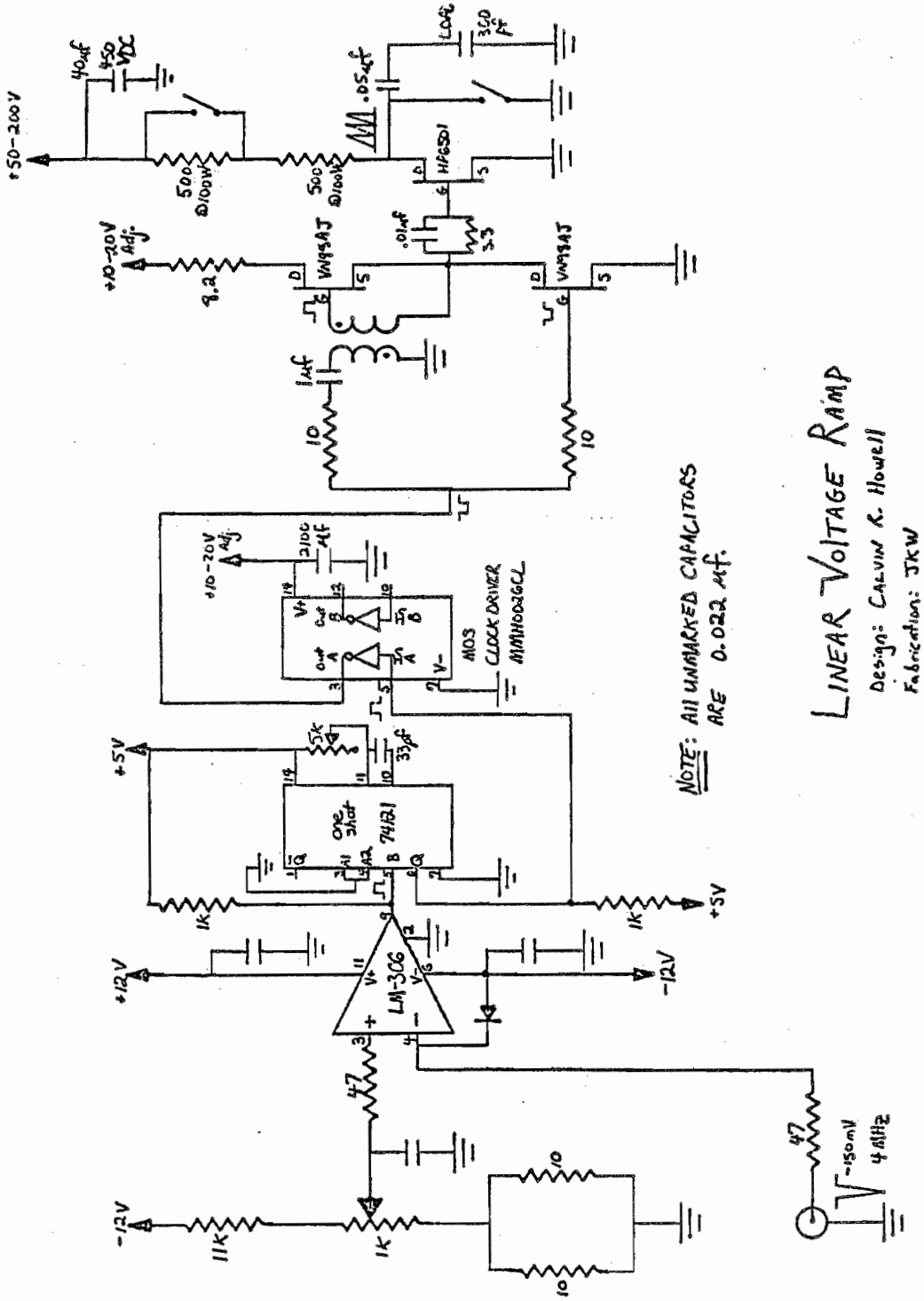

Figure 3.6. Schematic diagram of most recent LVR generator (built in 1983).

CHAPTER 4

DATA ACQUISITION

4.1 Introduction

Table 4-1 provides a summary of the $\sigma(\theta)$ and $A_y(\theta)$ data acquired for this dissertation. These data were accumulated over a period of $2\frac{1}{2}$ years and represent about 500 hours of actual accelerator time. The differential elastic and inelastic scattering cross sections of silicon and sulfur were measured at incident neutron energies of 8, 10, 12, 14 and 17 MeV. The analyzing powers of these nuclei were measured at incident neutron energies of 10, 14, and 17 MeV. All data were acquired using the tandem accelerator and neutron TOF facilities at TUNL (described in chapter 2). The angular range for each distribution was from 20° to around 160° (c.m.). The average statistical uncertainty in the $\sigma(\theta)$ data was about 2% for the elastic distributions and around 6% for the inelastic data. For the $A_y(\theta)$ measurements, the average statistical uncertainities were 4% for the elastically scattered neutrons and nearly 7% for the inelastic group.

These data were acquired with two computer systems. Data taken before August 1981 were obtained using a DDP-224 computer. This computer and the corresponding data acquisition system have been described in (Hogue 1977, Beyerle 1981, Guss 1982a). All other data were acquired with the recently installed VAX-11/780 computer system. The data acquisition system for the VAX is CAMAC based and is controlled by a microprogrammed

TABLE 4-1

SUMMARY OF DATA

Nucleus	State J^{π}	Q-Value (MeV)	$\sigma(\theta)$ Energies (MeV)	$A_y(\theta)$ Energies (MeV)
^{28}Si	0^+	0.00	8,10,12,14,17*	10,14,17*
	2^+	-1.78	8,10,12,14,17*	10,14,17*
	0^+	0.00	14**	14**
^{32}S	0^+	0.00	8,10,12,14,17*	10,10*,14,17*
	2^+	-2.23	8,10,12,14,17*	10,10*,14,17*

* Denotes data taken since March 1982. These data were acquired using the "new" gas cell. The physical dimensions of the experimental arrangements are listed in table 2-2.

** These measurements were part of a series of experiments to accurately determine $A_y(\theta)$ near the first minimum in $\sigma(\theta)$ at 14 MeV (see chapter 6 for details).

branch driver MBD-11. An overview of the present data acquisition system at TUNL is presented in (Gould 1981, Roberson 1981, King 1981). Event sorting is performed with the event analysis language EVAL. For a detailed description of EVAL see (Gould 1981, Holzweig 1981).

The codes NTOF and PTOF are the data acquisition packages for the $\sigma(\theta)$ and $A_y(\theta)$ measurements, respectively. They are modular structured systems based on XSYS commands. The core of these packages is the use of subprocesses to sort data, read scalers, control data acquisition with a monitor (or scaler) preset, and to display scalers along with other information on the scaler display screen. There is a sorting subprocess for each independent detector. The association between hardware and software is made in the DAP files. These files relate the ADC, the MBD channel, and the EVAL program to each other.

The detected neutron events are converted into electrical pulses by the photomultipler tube. These pulses are processed by fast electronics, digitized by ADC's and sorted into spectra by the computer. An event occurs in the detector, the detector outputs a pulse that is used to start a TAC which is stopped by a beam pick-off signal. The output of the TAC is fed into a linear gate stretcher which is gated by two coincidence requirements, high bias and PSD. If the coincidence requirements are met (a valid neutron event), then the output is passed to the VAX, and the corresponding channel in the TOF spectrum is incremented. The listing of the EVAL program used to sort the 4 m detector events in the $\sigma(\theta)$ measurements follows:

```
C       TOF4.EVL - SORTING ALGORITHM FOR 4M DETECTOR
C                  IN CROSS-SECTION EXPERIMENT.
C
C
C
C  DEFINE SPECTRA
C
     SPEC FIN  1
     SPEC FOUT 2
     VARIABLE ISTATUS 1
C
C  SET EVENT SIZE
C
     DATA EVSIZE=1
C
C  DEFINE DATA EVENTS
C
     FORMAT TAC4 1 10 1
C
C  INCREMENT SPECTRUM
C
     GET A TAC4
C
     IF ISTATUS EQ 1
          TINC A FIN
     ELSE
          TINC A FOUT
     ENDIF
     END
```

The sorting algorithms used in the $A_y(\theta)$ experiments are slightly more complicated because the data must be sorted according to the spin direction of the incident projectile. Because the counting rates are much lower and because there are twice as many spectra in the $A_y(\theta)$ measurements as in the $\sigma(\theta)$ experiments, the length of the TOF spectra are reduced from 1024 channels to 512 channels.

4.2 Acquisition of Cross-Section Data

4.2.1 Procedure

At each angle in the $\sigma(\theta)$ measurements, TOF spectra were accumulated for neutrons scattering from silicon and sulfur. The target sample was suspended over the pivot point of the detectors with its center positioned on the beam axis directly behind the gas cell. This arrangement will be denoted as the SAMPLE IN situation. After sufficient statistics were accumulated for SAMPLE IN, the sample was replaced with a bare thin steel wire, and SAMPLE OUT spectra were collected. After a suitable measuring interval the second sample was inserted. Because the SAMPLE OUT spectra determined the sample-uncorrelated backgrounds, the same OUT spectra were used for both samples whenever possible. All other backgrounds as discussed in (Guss 1982a) were minimized by careful selection of experimental conditions.

After both IN and OUT spectra were accumulated, difference (DIFF) spectra were generated as follows:

$$\text{DIFF} = \text{IN} - \text{OUT}\left[\frac{\text{DIFF}}{\text{MONI}}\right] .$$

Here MONI and MONO are the sum of counts in the peak of the CEILING monitor spectra for SAMPLE IN and SAMPLE OUT, respectively. The yields per monitor were generated by summing the peaks of interest in the 4 m and 6 m difference spectra and dividing by MONI:

$$\text{YIELD} = \frac{\text{DIFF}}{\text{MONI}} .$$

The yields were plotted as a function of angle in order to monitor the systematics of the data during the acquisition. Data points that were inconsistent with the distribution (points that were apparently too high or too low) were remeasured.

Most of the angular distributions were acquired in 5° steps, depending on the systematics of the data. Occasionally, $\sigma(\theta)$ measurements were repeated to check for systematic electronic drifts. The angular position of the detectors was known to within 0.1° relative to an optical axis corresponding to a scattering angle of 0°. Angles forward of the first minimum in the differential cross section were taken with both side detectors symmetrically positioned about the beam axis; and since the efficiency of each detector, including the solid angle subtended between the sample and the detector, was very well known, the comparison of the elastic yields measured in the two detectors provided a very sensitive measure of the difference in scattering angle between the two detectors. The sensitivity of this difference measurement was enhanced at forward angles by the steep slope in $\sigma(\theta)$; an angle shift of 0.5° sometimes resulted in yields that differed by as much as 30% between the two detectors. If the 4 m yeilds were consistently higher than those in the 6 m detector, then it was concluded that the 4 m detector was at smaller scattering angles than the 6 m detector. This difference in scattering angle was attributed to an error in determining the axis between the effective center of the deuteron beam in the gas cell and the center of the scatterer, i.e., the neutron beam axis. Typically, the angle difference between the two detectors was less than 1°, which means the beam was $1/2^{\circ}$ from the optically aligned 0° axis. An error of $1/2^{\circ}$

corresponds to a situation where the beam was 0.75 mm off to one side in the gas cell. (This was determined by realizing that the critical distance is the cell-to-scatterer separation for calculating $\Delta\theta = s/R$.) This conclusion was checked by performing two-detector measurements at back angles where the slope of $\sigma(\theta)$ was opposite to that at forward angles. At these angles the 4 m yields were expected to be less than those of the 6 m detector. The magnitude of the angle difference was determined by shifting the 6 m data in alignment with the 4 m points so that all data points fell on a smooth curve, and then assigning 1/2 of the shift to each detector.

At the beginning, midpoint, and end of each angular distribution, the yield/monitor for neutron scattering from hydrogen was measured for normalization purposes. These three measurements of n-p scattering also provided a check for systematic drifts. Neutrons scattered from a polyethylene (poly) sample were stored in the IN spectra, and neutrons scattered from a carbon sample were stored in the OUT spectra. The hydrogen yields were computed from the difference spectra. Fig. 4.1 shows typical IN, OUT, and DIFF spectra used to extract the hydrogen yields. The spectra in fig. 4.1 were collected using the 6 m detector positioned at $\theta_p = 32^o$ with an incident neutron energy of 10 MeV. The peaks in channels 825 and 600 correspond respectively to elastic scattering from ^{12}C and inelastically scattering to the first excited state of ^{12}C at 4.43 MeV. The peak in channel 725 corresponds to scattering from hydrogen. The optimum sizes of the poly and carbon samples for each incident neutron energy were determined using the Monte Carlo code EFFIGY. A compromise between count rates and multiple-scattering effects

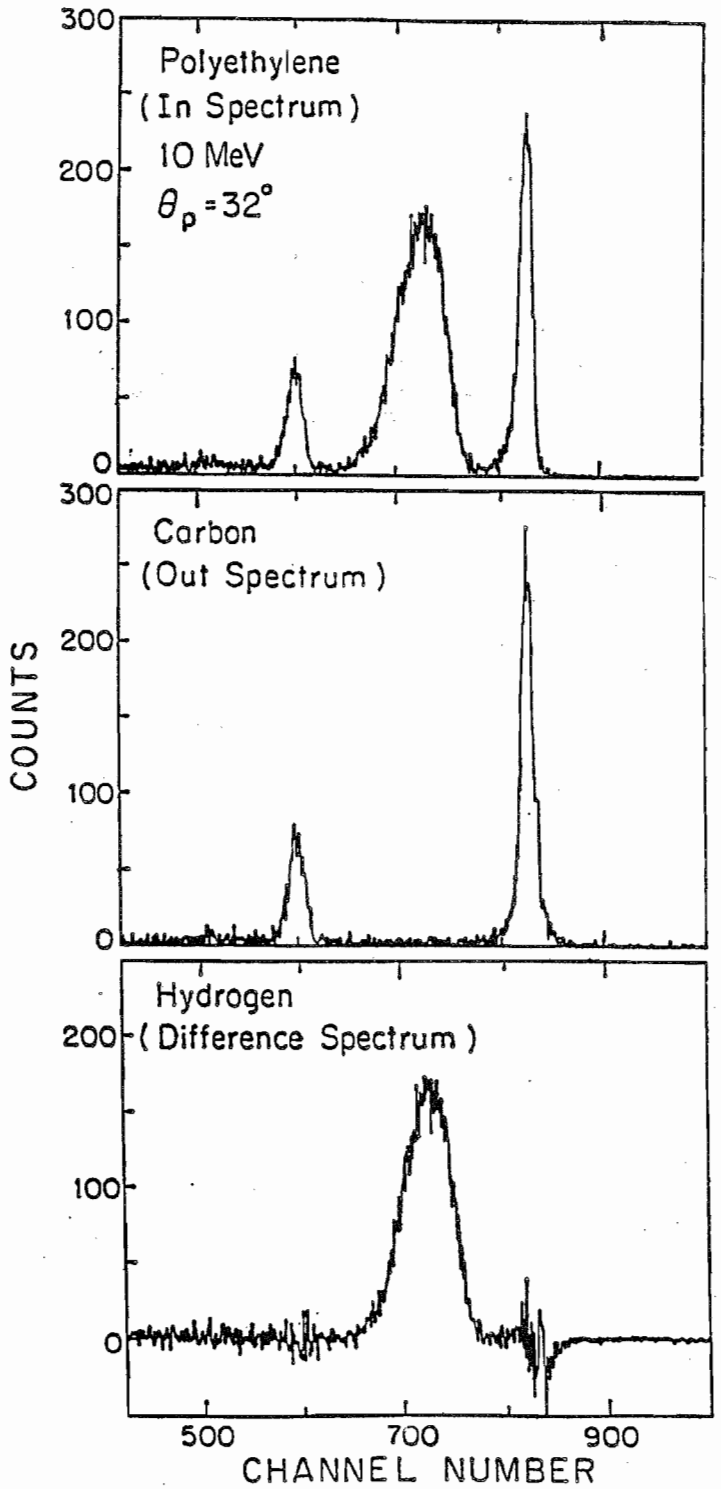

Figure 4.1. Polyethylene, carbon, and DIFFERENCE spectra at $\theta_p = 32°$ with an incident neutron energy of 10 MeV. Spectra were collected with the 6 M detector. The time of flight increases with decreasing channel number.

was made. The physical dimensions of the poly and carbon samples used in these measurements are given in table 2-1. The optimum scattering angles to resolve the n-p peak from the carbon peaks were also determined using the code EFFIGY.

4.2.2 Monitor Spectra

In order to properly interpret the spectra produced by the scattered neutrons, it is necessary to understand the source spectrum. The neutron flux is monitored by the ZERO DEGREE and CEILING monitors. The ZERO DEGREE monitor is mounted on a floor stand and views the 0^{o} neutron flux transmitted through the scatterer. This monitor is not suited for normalization because the detected neutron flux is dependent upon whether the sample or the bare wire is in place. However, it is a very good detector for monitoring the time characteristics of beam pulses and contaminants in the source reaction.

Because inelastic yields were extracted, it was important to know the source of all neutrons in the source spectrum. Tests were conducted at neutron energies of 14 and 17 MeV to determine the cause of the background neutrons in the source spectrum. Figure 4.2 illustrates TOF spectra that were accumulated with the ZERO DEGREE monitor for the cases of gas in and gas out. In the gas-in case the cell was pressurized to 2 bars. Both spectra were accumulated for equal amounts of BCI. Such spectra as these were instrumental in determining the cause of backgrounds in the source spectrum. The results of the tests indicated that there were three contributions to the backgrounds, the first two of which were expected: (1) deuteron breakup in gas and on beam stop, (2) $^{2}H(d,n)$ from "drive-in"

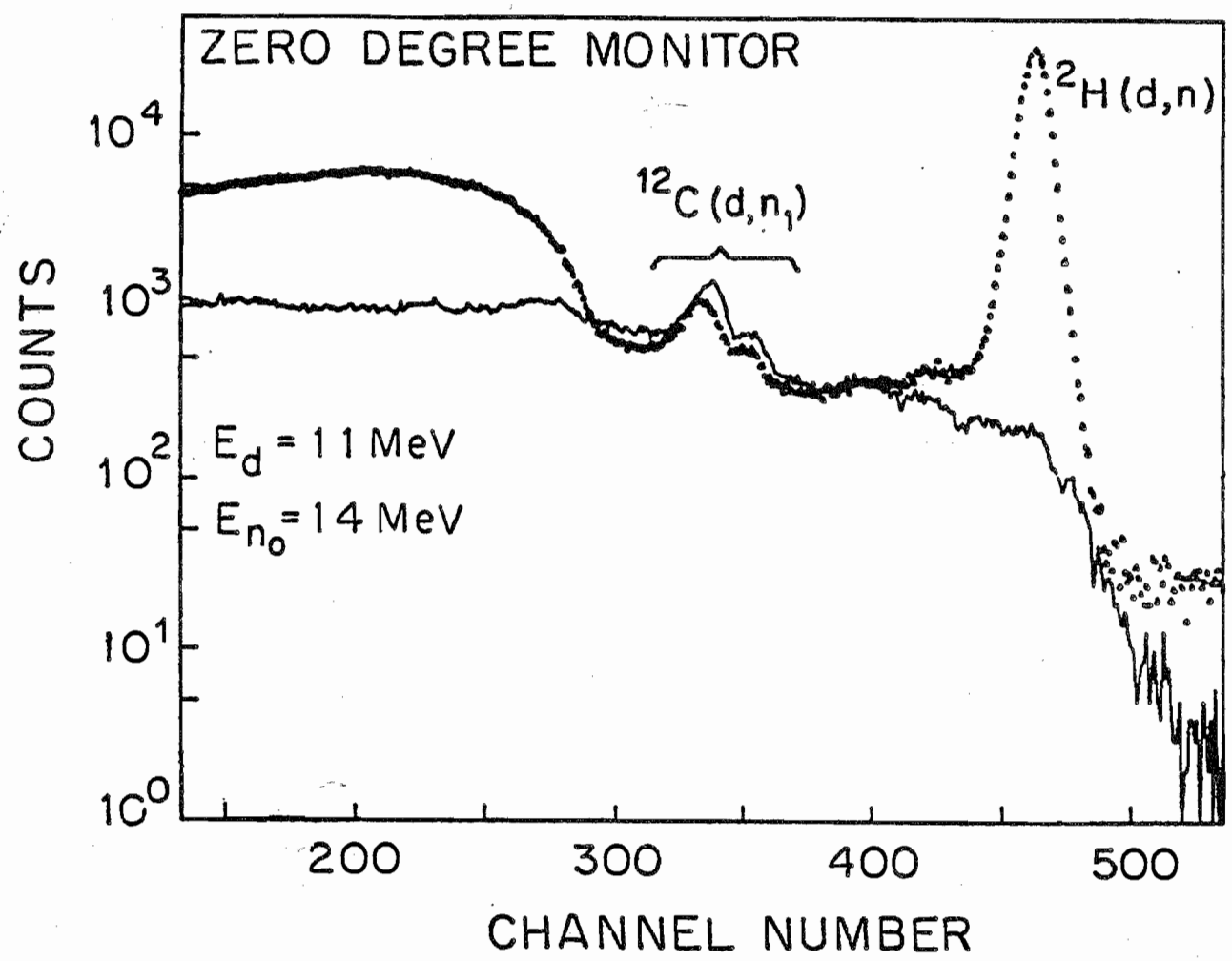

Figure 4.2. ZERO DEGREE monitor spectra at E_n = 14 MeV. The points and solid line represent the deuterium gas-in and gas-out cases, respectively. For the gas-in spectrum the cell was pressurized to 2 bar.

deuterons in the beam stop, and (3) peaks from the $^{12}C(d,n_1)$ reaction (and to a much smaller extent $^{12}C(d,n_0)$ due to carbon build-up on the collimator immediately in front of the gas cell, the exterior surface of the foil, and on the beam stop. The neutrons produced by deuteron breakup are much lower in energy than the mono-energetic group and therfore are far away from the neutrons of interest in the 4 m and 6 m spectra. The neutrons produced by the "drive-in" deuterons in the tantalum beam stop also scatter from the sample and appear in the 4 m and 6 m spectra as a flat background that starts at the "foot" of the elastic peak and extends down to zero energy. The neutrons produced by the $^{12}C(d,n_1)$ reaction scatter from the sample and appear in the 4 m and 6 m spectra as peaks about 5 MeV down from the $^{2}H(d,n_0)^{3}He$ neutrons. The "contaminant" peaks are flagged in figures 4.2 and 4.4.

The tests at 17 MeV revealed that all backgrounds grow with increasing incident deuteron energy. The deuterium gas pressure was increased from 2 bar to about 8 bar to compensate for these effects, thus improving the signal-to-noise ratio in monitor and side detector spectra. For our purposes we defined the signal-to-noise ratio to be the ratio of counts in the centroid of the peak to the level about five peak widths away from the centroid. A good signal-to-noise ratio for our system operating at 2 ns pulse width is around 100:1 in the ZERO DEGREE spectra.

The CEILING monitor hangs from the ceiling and views the gas cell at an angle of about 50^{o} with the horizontal. The flux detected by this monitor was used to normalize the yields of the scattered neutrons. For this reason it was important to understand the CEILING monitor spectra. The neutrons emerging at 50^{o} from the $^{2}H(d,n_0)^{3}He$ reaction are less

energetic than those that emerge at 0^{o} and therefore are closer to the continuum of neutrons caused by the deuteron breakup. The ratio of mono-energetic neutrons to continuum neutrons is low because the cross section of the continuum neutrons is essentially isotropic, whereas the $^{2}H(d,n_{0})^{3}He$ cross section drops by about an order of magnitude at 50^{o}. Comparison of spectra that were accumulated with and without gas in the cell provided information about the background underneath the main neutron peak. Figure 4.3 shows the spectra that were accumulated with the cell pressurized to 2 bar and with the cell evacuated for a neutron beam energy of 14 MeV.

4.2.3 TOF Spectra of ^{28}Si and ^{32}S

Figures 4.4 and 4.5 are TOF spectra of neutron scattering from silicon and sulfur, respectively. These spectra were accumulated with the 6 m detector and an incident neutron energy of 10 MeV. The overall time resolution of the spectrometer was approximately 2 ns. This was sufficient to resolve many of the excited states in both nuclei. The peak due to the carbon contaminant was identified by comparing silicon and sulfur spectra at several angles to the source spectrum as detected by the ZERO DEGREE monitor. The peak due to the carbon contaminant was consistently about 5 MeV down from the ground state neutrons. Although some information about the cross sections for the higher excited states might be learned from the spectra obtained in this work, the present study deals only with TUNL data for the ground state (0_{1}^{+}) near channel number 800 and the first excited state (2^{+}) to the left of the 0_{1}^{+} state.

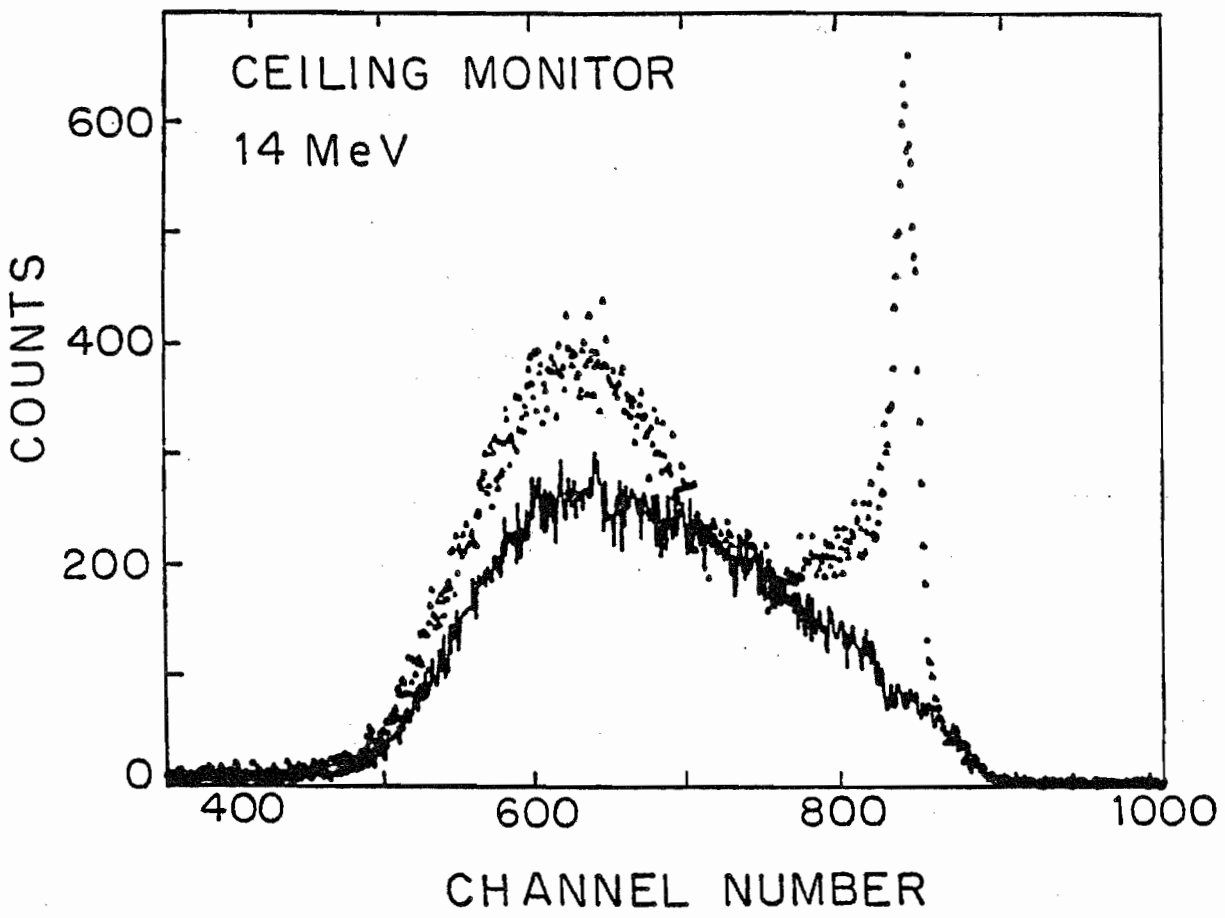

Figure 4.3. CEILING monitor spectra at E_n = 14 MeV. The points and solid line represent the deuterium gas-in and gas-out cases, respectively. For the gas-in spectrum the cell was pressurized to 2 bar.

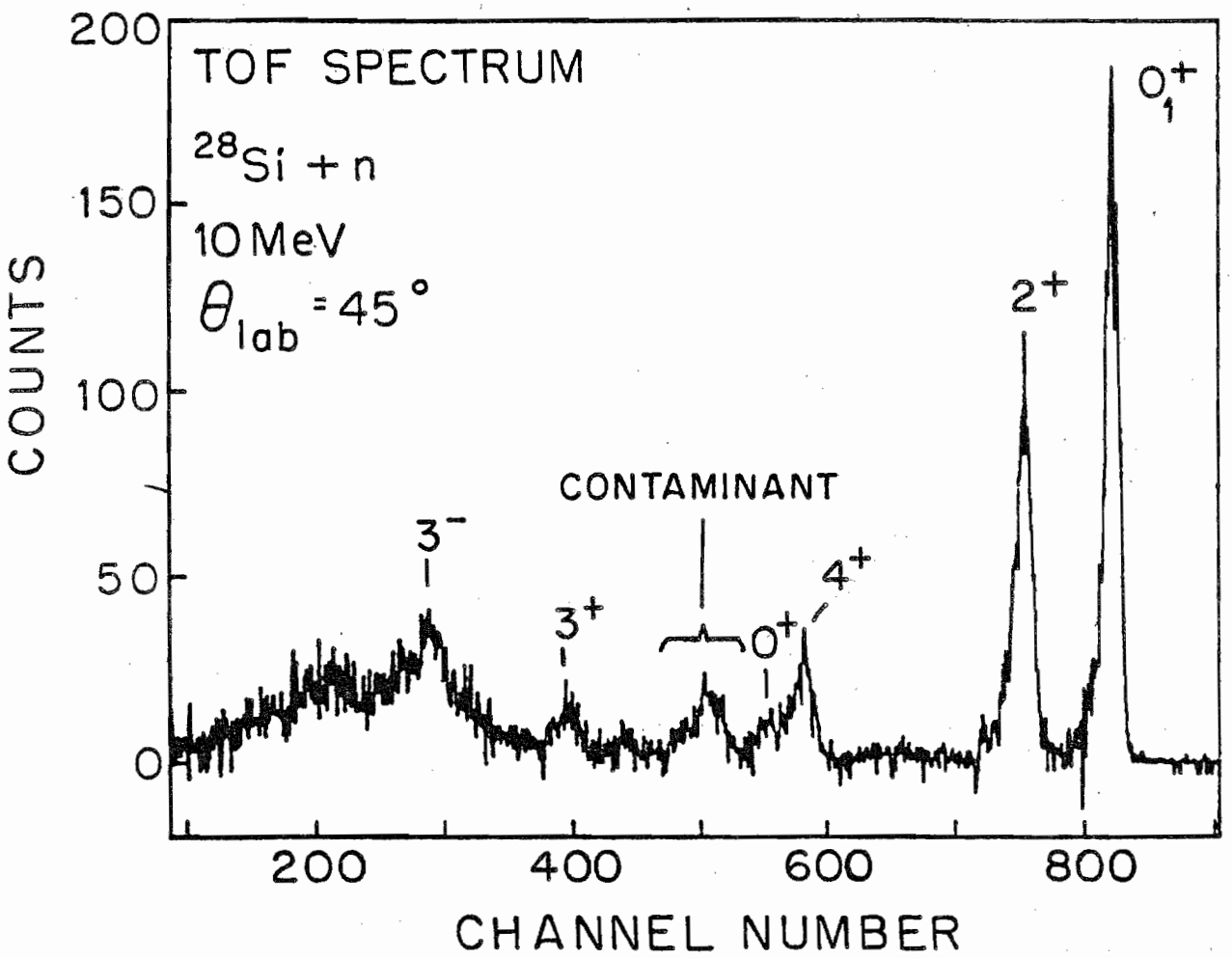

Figure 4.4. TOF spectrum of ^{28}Si + n accumulated with the 6 M detector positioned at $\theta_{lab} = 45^{\circ}$ and with E_n = 10 MeV. The time of flight increases with decreasing channel number.

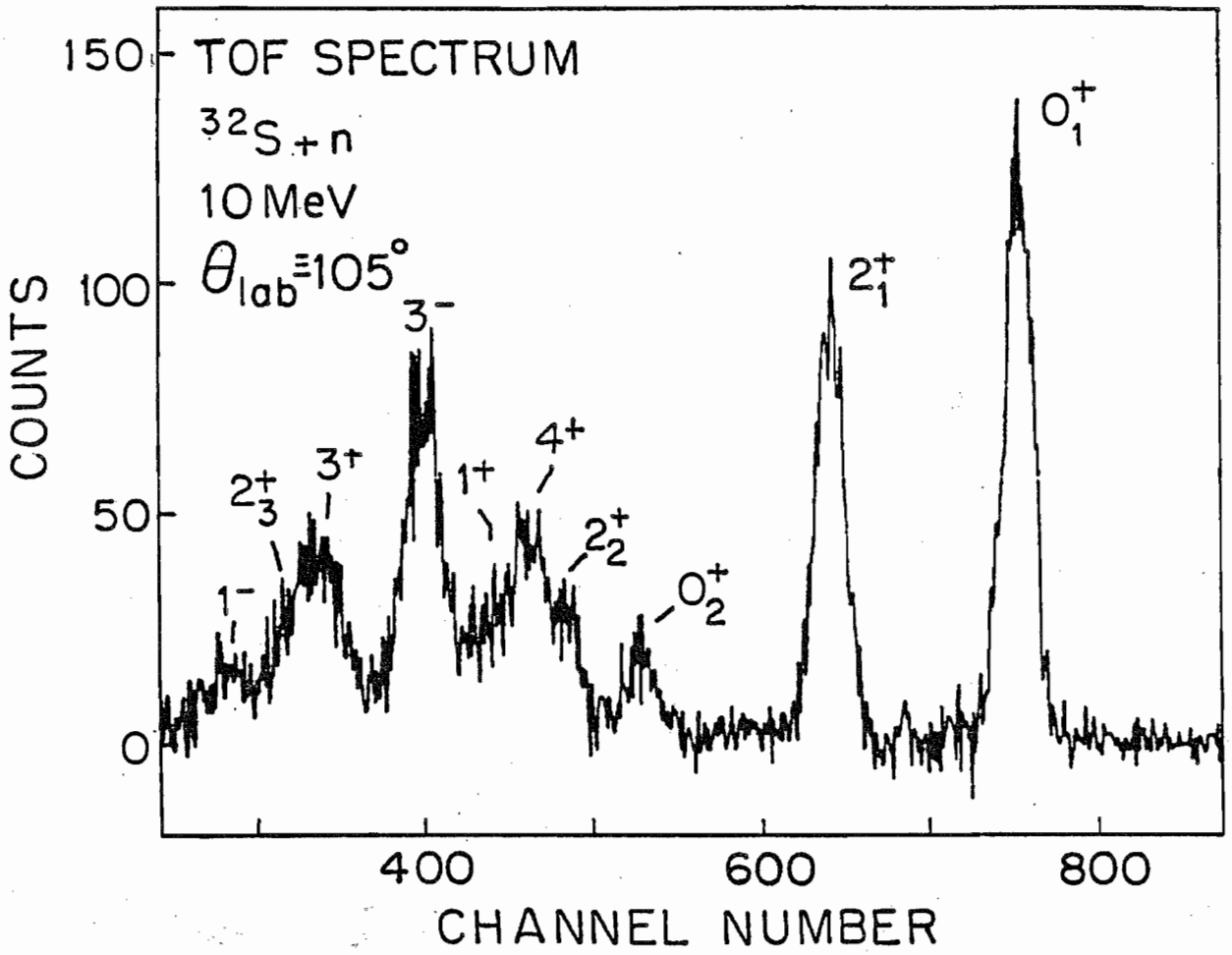

Figure 4.5. TOF spectrum of ^{32}S + n accumulated with 6 M detector positioned at $\theta_{lab} = 105^{\circ}$ and with E_n = 10 MeV. The time of flight increases with decreasing channel number.

4.3 Acquisition of Analyzing Power Data

The analyzing power $A_y(\theta)$ measurements were conducted in the same target room as the $\sigma(\theta)$ experiments, using the same samples and detectors. TOF spectra were accumulated for neutrons scattered to the left (6 m detector) and to the right (4 m detector) for incident neutron beams having the polarization vector oriented spin up and successively for incident beams oriented spin down. In these experiments both detectors were always positioned at equal angles on opposite sides of the beam axis, and the ratio of their yields were combined to eliminate instrumental asymmetries in the determination of $A_y(\theta)$. With this method the error in the beam axis alignment cancels to first order, and the angle uncertainty reduces to the $\pm 0.2^{\circ}$ for the optical alignment of each detector. Four TOF spectra were accumulated in each detector: both spin up and spin down for both SAMPLE IN and SAMPLE OUT. The $A_y(\theta)$ was computed from the yields that were extracted from the peaks in the difference spectra.

The deuteron beam polarization p_d was measured by using the quench-ratio method as described in (Ohlsen 1973, Trainor 1973, and Guss 1982a). The quench ratio Q is the ratio of the unquenched beam intensity to the quenched beam intensity:

$$Q = \frac{I_u}{I_Q}$$

and

$$p_d = 1 - \frac{1}{Q} .$$

The quench ratio was measured about every 10 minutes so that small drifts

in the beam polarization could be properly averaged into the $A_y(\theta)$ measurements, and drastic changes in p_d would be quickly noticed. The spin direction of the incident beam was flipped roughly every 20 minutes, half as often as p_d was measured. The data were acquired in UP-DOWN and DOWN-UP pairs so that spin-up and spin-down data would average equally over drifts in the system. After each pair, the yields and analyzing powers were generated. Calculating the yields and analyzing powers in these short time intervals provided a constant monitor of the system's stability. At least two pairs of data were obtained for each $A_y(\theta)$ measurement and typically four pairs were used.

The neutron flux was monitored with BCI instead of with a neutron detector as in the $\sigma(\theta)$ measurements. Monitoring the incident neutron flux with the BCI is simpler because it avoids the complicated electronics and computer software associated with neutron detectors. In addition, a flux monitor positioned at any angle will measure the analyzing power of the transfer reaction, and therefore its yields must be adjusted accordingly before being used for normalization. Although a detector at 0^o is insensitive to this effect, the yields from a monitor located at 0^o must be corrected for flux attenuation in the sample. The BCI monitor proved to be a useful flux monitor when the deuterium gas pressure was stable. In this case it is possible to obtain relative $\sigma(\theta)$ data from the yields obtained in the $A_y(\theta)$ measurements, provided the detector biases are carefully set as in the $\sigma(\theta)$ experiments. This method for simultaneously obtaining $\sigma(\theta)$ and $A_y(\theta)$ data for neutrons was verified in the present work and is described in section 2.2.4.

CHAPTER 5

DATA REDUCTION

5.1 Cross-Section Data

5.1.1 Peak Stripping and Yields

Time-of-flight (TOF) spectra for SAMPLE IN and SAMPLE OUT were accumulated at each detector angle. These spectra were 1024 channels long and were collected on a 200 ns TAC range. The time calibration for each spectum was approximately 0.18 ns per channel. Difference spectra were generated for the 4 m and 6 m detectors by normalizing the incident neutron flux in the OUT count to that of the IN count and calculating:

$$DIFF = IN - OUT\left[\frac{MONI}{MONO}\right]$$

IN => SAMPLE IN spectrum corrected for computer plus ADC DT;

OUT => SAMPLE OUT spectrum corrected DT;

MONI => Sum of counts in the peak of the SAMPLE IN spectrum accumulated with the CEILING monitor, corrected for DT;

MONO => Sum of counts in the peak of the SAMPLE OUT spectrum accumulated with the CEILING monitor, corrected for DT.

Figure 5.1 shows an IN, a normalized OUT, and a DIFF spectrum for $^{28}Si + n$ at $\theta = 60^{o}$ for an incident neutron energy of 14 MeV. Notice that the background in the region of interest in the difference spectrum in non-zero. This occurs because the sample-correlated backgrounds are not measured in the OUT count. The residual background in each DIFF spectrum

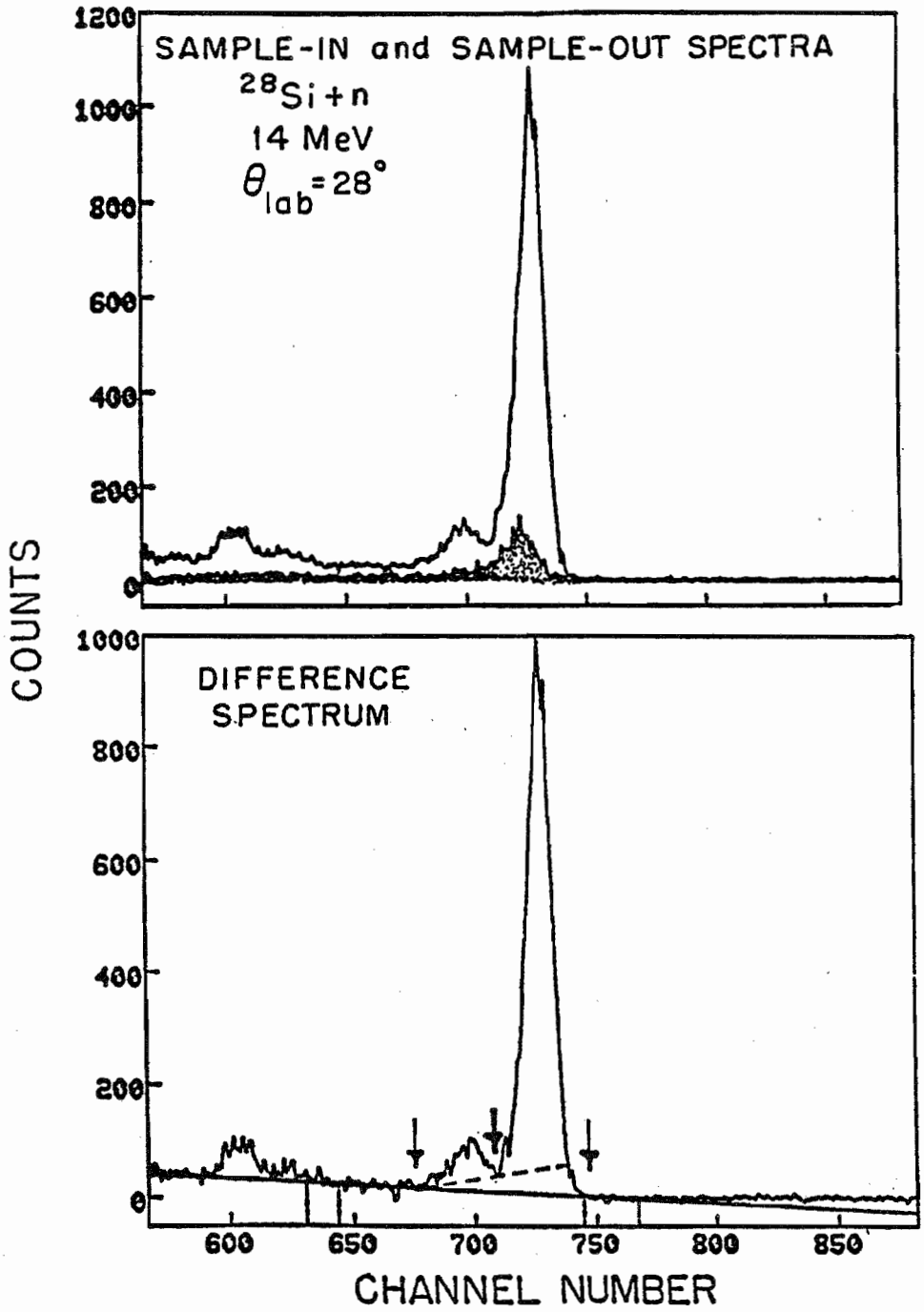

Figure 5.1. TOF spectra for ^{28}Si + n at 14 MeV with the 4 M detector positioned at the forward angle of 28°. Top: SAMPLE IN and SAMPLE OUT spectra. Bottom: DIFF spectrum. The solid and dashed curves represent the backgrounds drawn to extract elastic and inelastic yields, respectively. The arrows indicate the windows for summing the peaks.

was described with a polynomial function. In most cases, a first order polynomial, a straight line, adequately described the residual background.

The choice of the polynomial function to describe the background in the region of the inelastic peak played an extremely important part in the extraction of inelastic yields. Two choices of background were drawn in spectra where the elastic peak was very large relative to the peak for inelastic scattering to the 2^+ state. A low and a high background was selected to extract elastic and inelastic yields, respectively. The high background was necessary because the "tail" of the elastic peak (which contained valid elastic counts) extended under the inelastic group and therefore had to be subtracted from the inelastic yields as a sample-correlated background. When this was not done, the shape of the $\sigma(\theta)$ for inelastic scattering followed the forward peaking trend of the $\sigma(\theta)$ for the elastic data at forward angles. The two background choices are illustrated in the bottom of fig. 5.1. The solid and dashed curves represent the backgrounds drawn under the elastic and inelastic peaks, respectively. These curves also specify upper and lower limits on the background underneath the inelastic peak. In cases where the background choice under the inelastic peak was uncertain, the average of the upper and lower limits were taken and the uncertainty in the yield was increased to reflect both extremes.

The yield per monitor for each peak in the DIFF spectrum was calculated by summing the counts in the peak, subtracting the area under the background curve, and dividing by the monitor yield:

$$Y_s(\theta_L) = \frac{\text{DIFF-BACK(DIFF)}}{\text{MONI-BACK(MONI)}}$$

where,

BACK(DIFF) => Area under background curve in DIFF spectrum,

BACK(MONI) => area under background curve in SAMPLE IN spectrum of CEILING monitor.

The arrows in fig. 5.1 indicate the channels summed in calculating the yields.

Figure 5.2 is a typical CEILING monitor spectrum at E_n = 14 MeV. This spectrum was accumulated simultaneously with the spectrum shown in fig. 5.1. A linear background was drawn to account for the background underneath the mono-energetic neutron group. The choice of this particular background was a result of tests that were conducted to determine the causes of the backgrounds in the source spectra. These tests have been discussed in section 4.2.2. To assure that the neutron flux was consistently monitored during the entire experiment, the background choice and window for computing yields in the monitor spectra were kept constant.

The backgrounds in the CEILING monitor spectra were drawn by fitting regions on either side of the peak with a least-square fitting routine. The regions were chosen large enough so that statistical flucuations would not change the background appreciably. The background curve shown in fig. 5.2 was produced by fitting the regions indicated by the dashed-vertical lines. The window for summing the peak was chosen wide enough to avoid the steep slopes on the peak so that small timing shifts would not noticeably affect the monitor yields.

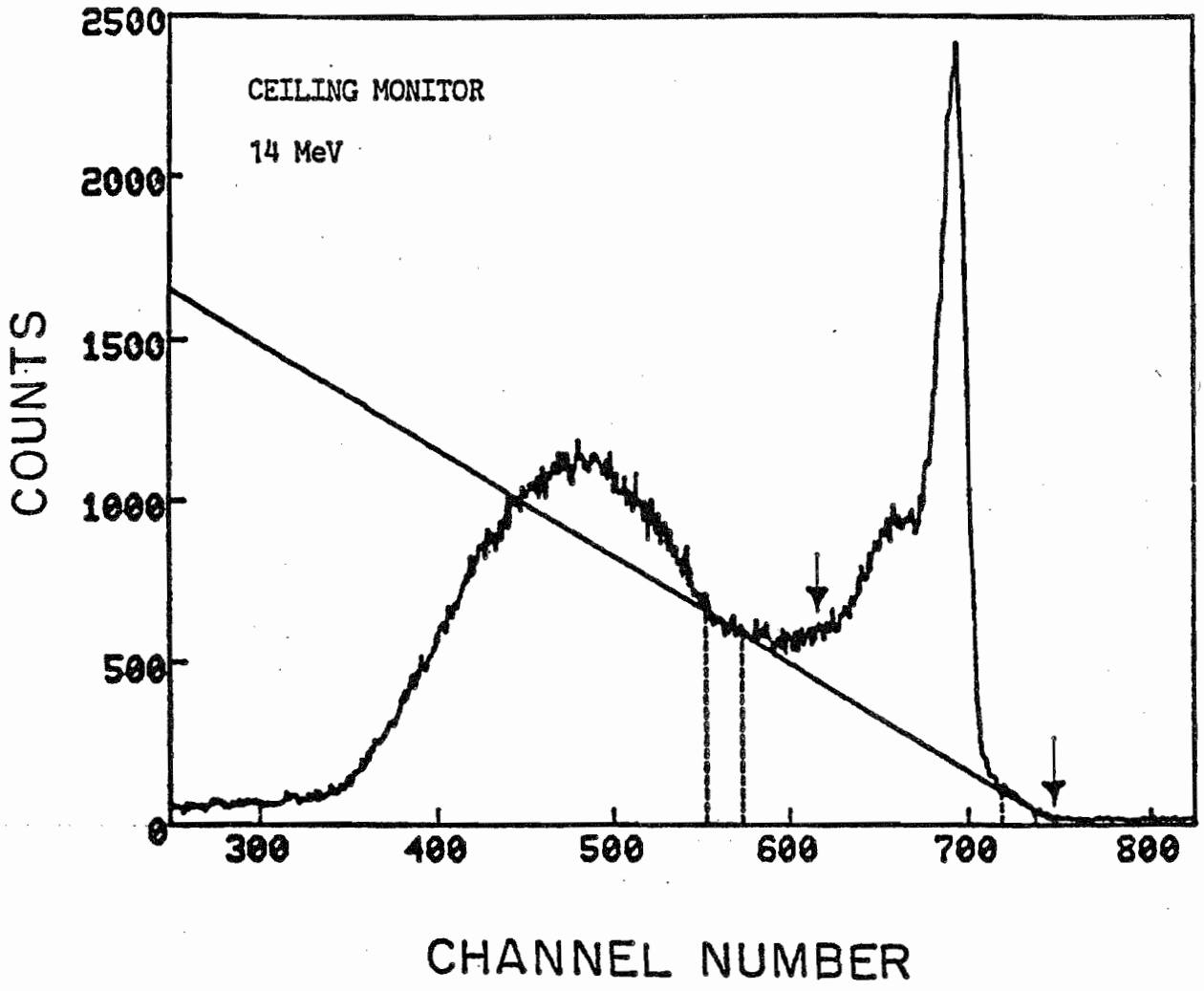

Figure 5.2. TOF spectrum accumulated with CEILING monitor at E_n = 14 MeV. The curve underneath the monoenergetic-neutron peak represents the background drawn to extract the monitor yields. The dashed vertical lines denote the regions used to draw the background curve. The arrows indicate the window used to sum the peak.

5.1.2 Data Normalization

Absolute normalization was obtained by comparing the yields for neutron scattering from the samples to the yields for scattering from hydrogen. The observed cross section at each scattering angle θ_L was calculated as

$$\sigma(\theta_L, E_n) = \frac{Y_s(\theta_L)}{Y_p(\theta_p)} \cdot \frac{1}{C_p(\theta_p)} \cdot \frac{n_H}{n_s} \cdot \frac{\varepsilon(E_p)}{\varepsilon(E_s)} \cdot \sigma_{np}(\theta_p, E_n) \qquad (5.1)$$

$Y_s(\theta_L)$, $Y_p(\theta_p)$ => Yields for neutron scattering from sample and from hydrogen, respectively;

$C_p(\theta_p)$ => Poly correction factor; this number includes all finite geometry corrections except angle corrections;

n_s, n_H => The number of nuclei in sample and in hydrogen scatterer, respectively;

$\varepsilon(E_s)$, $\varepsilon(E_p)$ => The detector efficiencies at the energies of the neutrons that were scattered from the sample and from hydrogen, respectively;

$\sigma_{np}(\theta_p, E_n)$ => Neutron cross section for scattering from hydrogen at energy E_n and angle θ_p.

Because the detector efficiency enters as a ratio of efficiencies in the above expression for $\sigma(\theta_L, E_n)$, it was only necessary to know the shape of the detector efficiency calibration curve, i.e., the relative efficiency curve.

5.1.3 Finite Geometry Corrections to Data

The count rates are lower in neutron-scattering measurements than in the corresponding charged-particle experiments. This is because neutron-scattering experiments, as in the present case, involve double-reaction

processes, and therefore the count rates depend on the product of two nuclear cross sections. In addition, the detection of neutrons is dependent upon nuclear cross sections, whereas charged particles interact directly with the atomic electrons in the detector, yielding 100% detection efficiency. The general trend in neutron-scattering experiments is to use large-volume detectors and large scattering samples to increase the counting rates. In addition, the counting rates can be enhanced by placing the samples close to the neutron-production target. For this reason, the observed cross sections have to be corrected for finite geometry effects, multiple scattering, and flux attenuation in the samples.

For the present $\sigma(\theta)$ experiments, the corrections were applied to the data with the code EFFIGY, which used Monte Carlo techniques to simulate the experimental results. The procedure used to correct these data is described in (Guss 1982a), and the specifics of the experimental arrangement have been presented in chapter 2. The finite geometry corrections to these data were generally small. The angle shifts due to averaging over the angular resolution of the sample and the detectors were usually less than 1°, although they were as high as 2.5° on the steep slopes of the elastic cross section. The flux attenuation in the samples over the energies of these experiments were less than 18% for silicon and below 16% for sulfur. The multiple-scattering corrections were less than 7% at most angles but were as high as 20% in the forward angle minima of $\sigma(\theta)$.

The code EFFIGY simulates the experimental data. In order to achieve this task, the code must keep track of all the orders of scattering within

the sample: single, double, and triple scattering. One important requirement in the simulations is that sufficient neutron histories are run so that the uncertainties in the correction factors computed from the simulated yields are substantially less than the experimental uncertainties. For the corrections to the present data, the uncertainties in the correction factors were reduced to less than one-tenth of the experimental uncertainties. Figure 5.3 is a plot of the relative yields for each order of scattering from the ground state of ^{28}Si. To check the statistical stability of the algorithms used to simulate the experiments, plots of several quantities, for which the analytic behaviors are well known, are examined for deviations from their accepted behaviors. Such checks include plots of the relative yields as shown in fig. 5.3, the multiple/total ratios, and the angle shifts.

5.1.4 Legendre Polynomial Description of Cross Section Data

After the data were corrected for finite geometry effects, they were described with Legendre polynomials. The same method of fitting the data with Legendre polynomials outlined in (Guss 1982a) was employed here. Figures 5.4 through 5.7 are plots of the $\sigma(\theta)$ data with the corresponding polynomial fits. Tabulations of the data and the coefficients used to generate these curves are given in Appendix I.

5.1.5 Uncertainties in Data

There are two types of uncertainties associated with the $\sigma(\theta)$ data: relative uncertainties and normalization uncertainties. The relative errors represent uncertainties in the shapes of the distributions, whereas

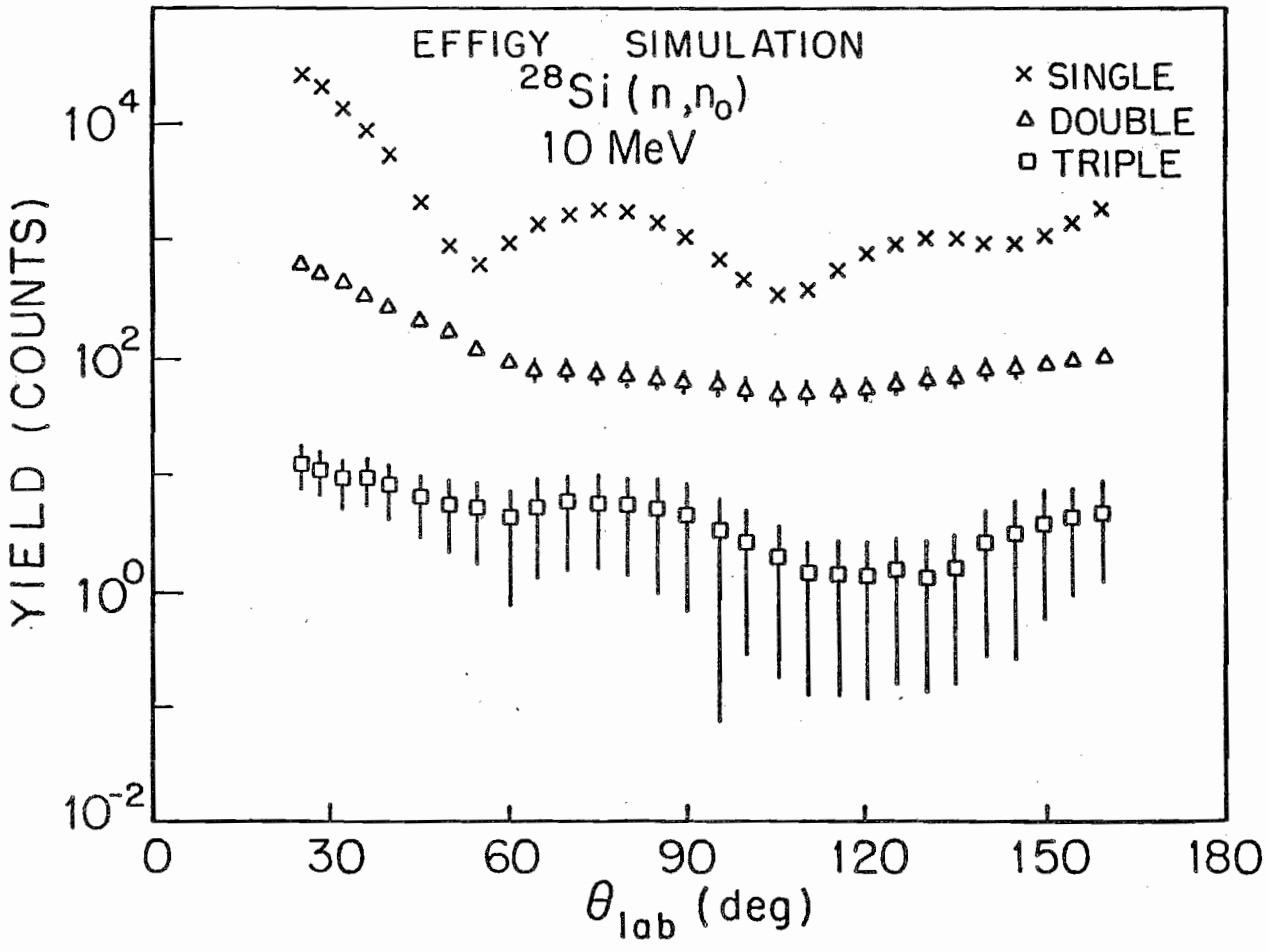

Figure 5.3. Plot of relative yields for different orders of scattering in the silicon sample at E_n = 10 MeV. These yields were computed with the code EFFIGY.

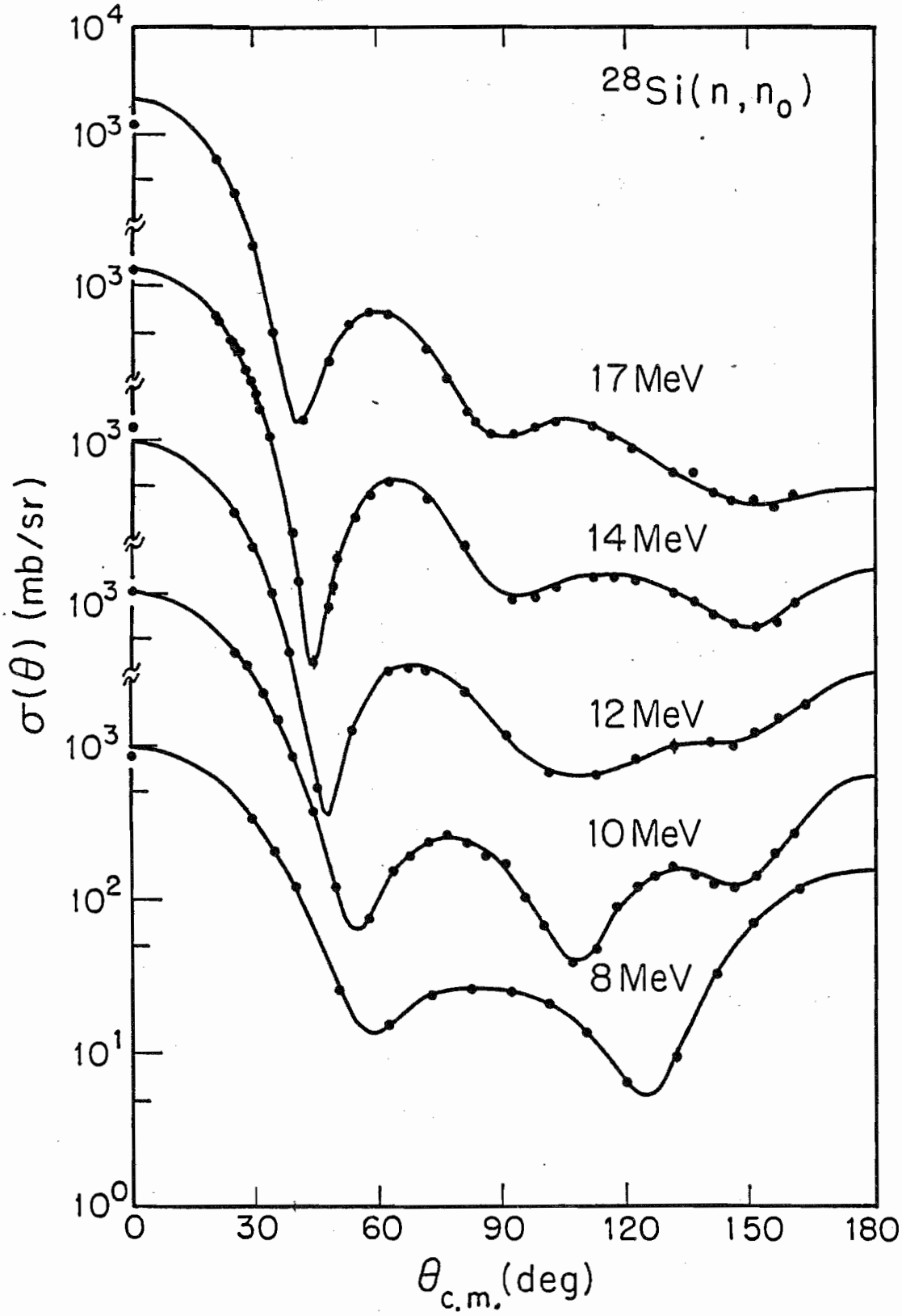

Figure 5.4. The $\sigma(\theta)$ for elastic neutron scattering from ^{28}Si. Curves are Legendre polynomials fits.

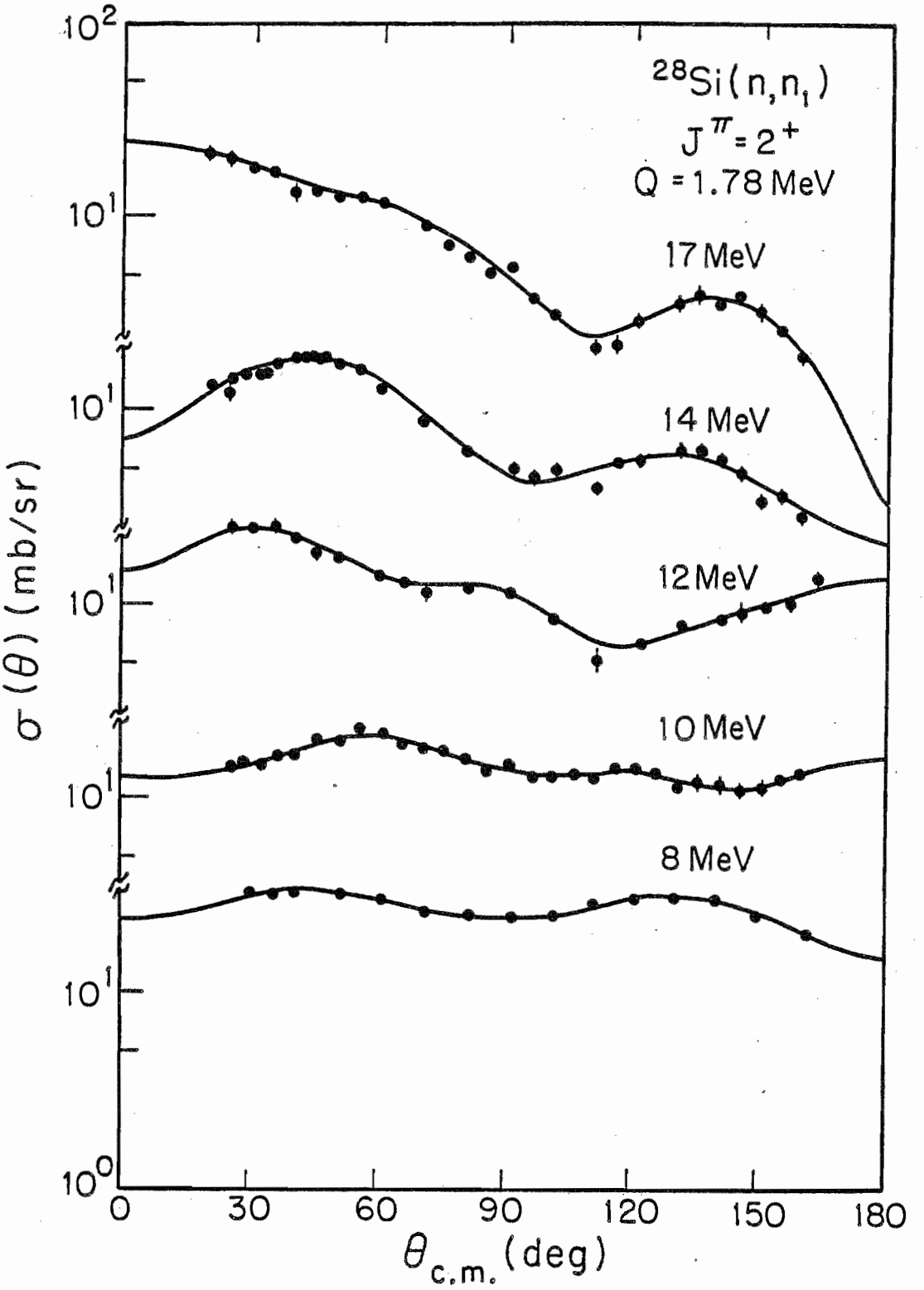

Figure 5.5. The $\sigma(\theta)$ for neutron inelastic scattering to the 2^+ state in ^{28}Si. Curves are Legendre polynomials fits.

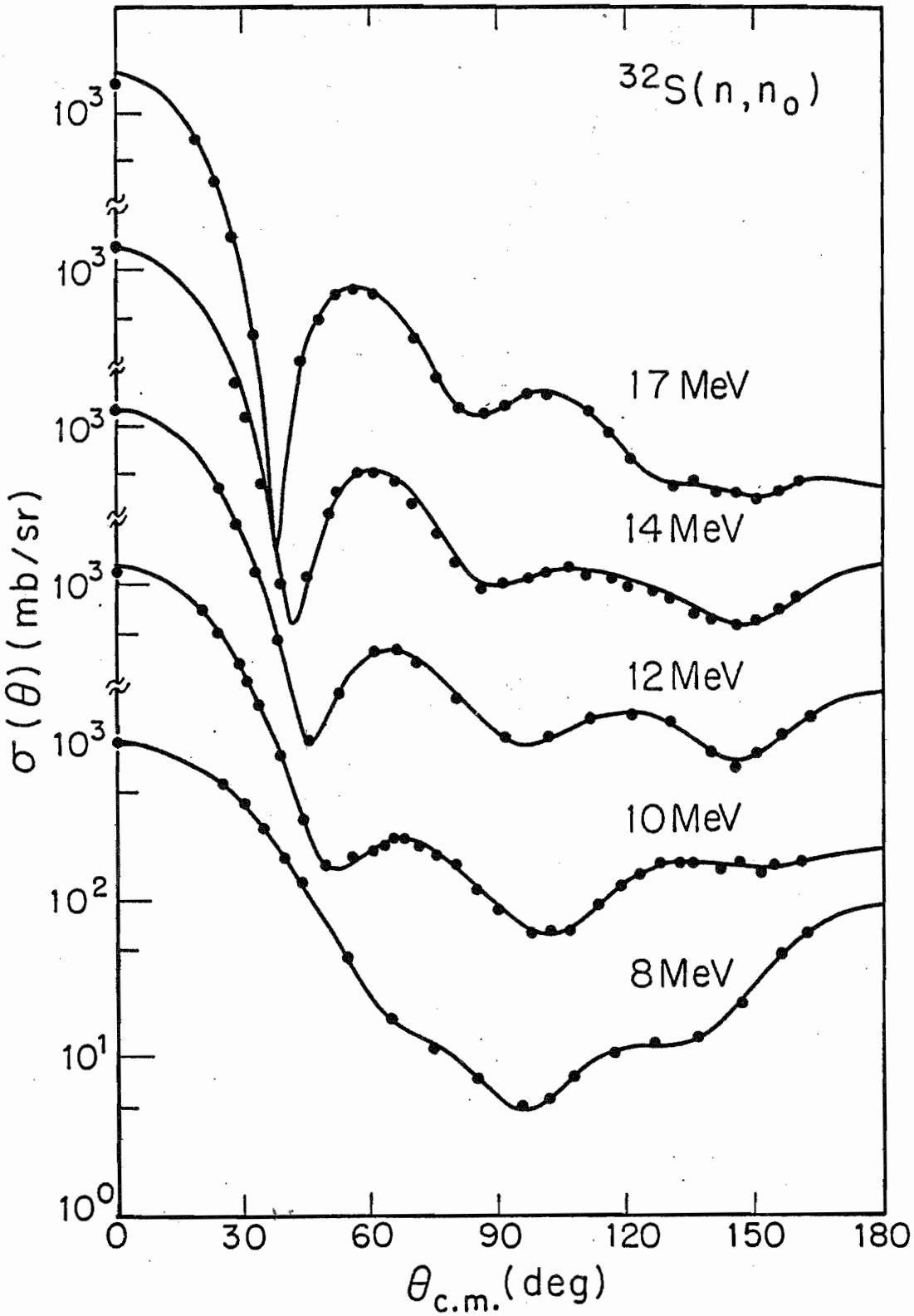

Figure 5.6. The $\sigma(\theta)$ for elastic neutron scattering from ^{32}S. Curves are Legendre polynomials fits.

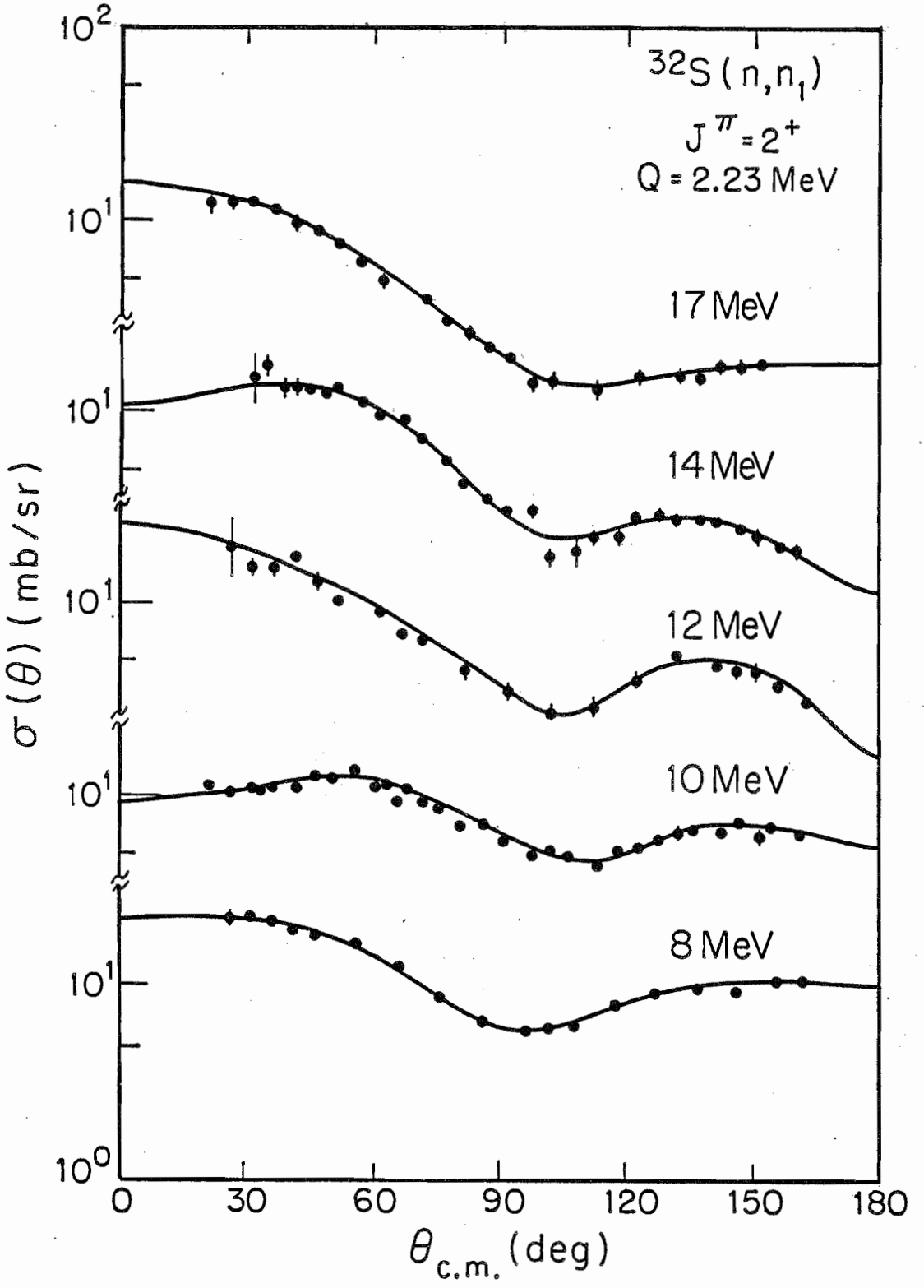

Figure 5.7. The $\sigma(\theta)$ for neutron inelastic scattering to the 2^+ state in ^{32}S. Curves are Legendre polynomials fits.

the normalization errors encompass the scale uncertainties in the data. Each term in the expression for the differential cross section (eqn. 5.1) has an uncertainty associated with it and therefore contributes to the uncertainty in $\sigma(\theta)$. Because of the large abundance of the T=0 isotopes of ^{28}Si and ^{32}S in the natural silicon and sulfur samples, no uncertainties were included for the T≠0 impurities.

The relative uncertainties in the present data varied from 3% to 10% for the elastic scattering cross sections and from 3% to 20% for the inelastic scattering cross sections. These uncertainties included the uncertainties in the yields for neutron scattering from the sample $Y_s(\theta_L)$, the relative detector efficiency, and the multiple-scattering corrections. The uncertainty in $Y_s(\theta_L)$ was due to counting statistics and to the uncertainty in the background underneath the peaks of interest. These uncertainties ranged from 1% to 5% for the elastic scattering yields and from 2% to 15% for the inelastic scattering yields. Because the present cross sections were measured relative to n-p scattering, the detector efficiency entered into the expression for $\sigma(\theta)$ as a ratio (see eqn. 5.1), and consequently, the uncertainty in the absolute detector efficiency canceled. However, the uncertainty in the shape of the efficiency curve increased the relative errors in the data due to the energy span covered on the efficiency curve by the neutrons that scattered from the ^{28}Si and ^{32}S samples. The errors due to the uncertainties in the detector efficiency were about 2.5% for the elastic scattering cross sections and ranged from 0% to 2.5% for the inelastic distributions.

The combined uncertainties in the calculation of the flux attenuation, the multiple-scattering correction factors, and the angle

corrections were less than 1%. However, when the results of the multiple-scattering calculations were applied to the data, the errors in the data were significantly enhanced, particularly in the minimum of $\sigma(\theta)$. The error enhancement was caused by the subtraction of multiple-scattered neutrons from the observed yields. This subtraction effectively reduced the valid number of neutrons in the peaks of interest and consequently increased the percent error. Thus, we found that the uncertainties due to the multiple-scattering corrections depended on both the precision of the simulations and on the magnitude of the effects. For instance, the errors were enhanced by as much as 30% in the minima of the elastic scattering cross sections.

The overall normalization uncertainty assigned to each angular distribution was 5%. This normalization uncertainty included the uncertainties in the n-p cross section, the hydrogen yields, the analytic corrections applied to the hydrogen yields to deduce $\sigma_p(\theta_p)$, the ratio of the number of hydrogen nuclei to the number of nuclei in the sample n_H/n_s, and the electronic dead time. The uncertainty in the n-p cross section ranged from 0.7% to 1.3%. These values were calculated by combining the 0.5% to 1.0% uncertainties reported by Hopkins and Breit (Hopkins 1971) with an additional uncertainty due to an angle uncertainty of $\pm$ 0.25°. The hydrogen yields were measured to an accuracy of 1% to 2%. There was a 2% to 3% uncertainty in the polyethylene-correction factor $C_p(\theta_p)$. The uncertainty in the ratio of n_H/n_s was about 1%. Because the counting rates in these experiments were usually much slower than the speed of the electronics, the dead time due to signal processing was negligible. The above uncertainties were combined as uncorrelated errors as prescribed in

(Bevington 1969). The error bars assigned to the present $\sigma(\theta)$ data do not reflect the above 5% normalization uncertainty.

5.2 Analyzing Power Data

5.2.1 Peak Stripping and Calculation of Analyzing Powers

At each detector angle, time-of-flight spectra were accumulated for the incident beam having its polarization vector oriented up and then for the incident beam having its polarizatio vector down. The sample uncorrected backgrounds were determined by repeating the above pair of measurements with the sample removed. However, to minimize the amount of time spent measuring the background, the OUT counts were taken with an unpolarized incident beam at angles where the backgrounds near the peaks of interest had no apparent structure. Each difference spectrum was generated by scaling the SAMPLE OUT spectrum to the incident neutron flux of the corresponding IN count and subtracting it from the SAMPLE IN spectrum. Although all the sources of the residual background after the subtraction are not understood, some of it was due to neutrons that scattered first from the sample and then from various objects in the target room, such as the collimators or shadow bars, before reaching the detector. Based on experience, a linear function was chosen in each difference spectrum to describe the residual background. Great care was taken in drawing the background curve so as to avoid introducing a falsely polarized background. The yield for each peak was generated by summing the counts within a window set around the peak and subtracting the portion of the area under the background curve that lies within the window. The sides of the windows were chosen about 20% up the peak to minimize the effects of backgrounds without significantly reducing the counting statistics.

In order to accurately extract analyzing powers from the yields, it was necessary to know the magnitude of the residual background and its asymmetry for spin-up to spin -down beams. To deduce information about the asymmetry of the background underneath the peaks, the spin-up and spin-down spectra were superimposed and the background levels in the region of interest were compared. This comparison was an extremely useful aid in chosing the background curves. The magnitude of the asymmetry of the background was usually statistically consistent with zero. Fortunately, the magnitude of the background was usually small compared to the area under the elastic peak.

The level of the background under the inelastic peak was also relatively small except at angles where the "tail" on the elastic peak extended underneath the inelastic group. At these angles, analyzing powers were computed for several window settings on the inelastic peak. The lower side of each window was set about 20% up the peak, and the upper side was initially set about 10% above the background and then was progressively walked up the peak until the computed analyzing powers did not change more than the uncertainty in the data. Again, fortunately the $A_y(\theta)$ for the elastic scattering was usually small at the most forward angles where the "tail" problem was most severe.

The yields that were extracted from the peaks in the difference spectra were combined to eliminate instrumental asymmetries in the determination of $A_y(\theta)$, using the relations:

$$\alpha = \left[\frac{L_\uparrow R_\downarrow}{L_\downarrow R_\uparrow}\right]^{\frac{1}{2}}$$

and

$$A_y = \frac{1}{p_n}\left[\frac{\alpha-1}{\alpha+1}\right],$$

where p_n is the neutron beam polarization, and $L_\uparrow$, $L_\downarrow$, $R_\uparrow$, and $R_\downarrow$ are the detected yields for spin-up and spin-down in left and right detectors, respectively. Since α is a product of ratios, instrumental asymmetries such as BCI and detector efficiencies cancel to first order (Ohlsen 1973, Byrd 1983).

The neutron beam polarization p_n was calculated from the incident deuteron beam polarization p_z using the polarization transfer function reported by Ohlsen and Keaton (Ohlsen 1973):

$$p_n(0^\circ,E_d) = \frac{\frac{3}{2}K_y^y(0^\circ,E_d)\cdot p_z}{1-\frac{1}{4}A_{zz}(0^\circ,E_d)\cdot p_{zz}},$$

where the values of $K_y^y(0^\circ,E_d)$ and $A_{zz}(0^\circ,E_d)$ were taken from (Lisowski 1975). For our source operating in "state 1", $p_z = p_{zz} \sim 0.65$.

5.2.2 Finite Geometry Corrections to Data

As with the cross section data, the analyzing power data must also be corrected for finite geometry effects such as multiple scattering, flux attenuation, and angle averaging effects. The observed analyzing power is a weighted average of the analyzing powers of the neutrons that scatter only once in the sample with those that scatter multiple times. The observed analyzing power can therefore be written as

$$A_y^{EXP} = P^S A_y^S + P^M A_y^M \qquad (5.2)$$

where,

A_y^{EXP}, A_y^S, A_y^M => Experimentally observed A_y, A_y of single-scattered neutrons, and A_y of multiple-scattered neutrons, respectively;

P^S => Probability of a neutron single scattering from the sample;

P^M => Probability of a neutron scattering multiple times in the sample.

The code JANE by Woye and Tornow (Woye 1980) was used to calculate P^S, P^M, and A_y^M and to solve for the analyzing power of the singly scattered neutrons. The code also uses Monte Carlo techniques to simulate the experiment. The trajectory of a neutron from the gas cell through the sample and into the detector is referred to as a neutron history. The philosophy of the code is very similar to that of EFFIGY. In addition to following the history of each neutron, JANE must also keep track of the analyzing powers of the scattered neutrons. This complicates the algorithm and increases the amount of computer time by more than a factor of two. Because the code keeps track of the analyzing powers of the scattered neutrons, it is necessary to construct a library of both $\sigma(\theta)$'s and $A_y(\theta)$'s.

In these simulations scatterings to the ground state and to the first excited state were considered. Three orders of scattering were simulated: single, double, and triple. Nine scattering processes were included in the simulations. Table 5-1 shows the scattering processes that effected the measured analyzing powers of the neutrons that elastically and inelastically scattered from the samples. For each neutron history a site of production was picked in the gas cell, scattering sites were selected in the sample, and a point of interaction

TABLE 5-1

MULTIPLE-SCATTERING PROCESSES INCLUDED IN JANE CALCULATIONS

Scattering Order	Elastic Peak	Inelastic Peak
Single	0^+	2^+
Double	$0^+ \rightarrow 0^+$	$0^+ \rightarrow 2^+$
		$2^+ \rightarrow 0^+$
Triple	$0^+ \rightarrow 0^+ \rightarrow 0^+$	$0^+ \rightarrow 0^+ \rightarrow 2^+$
		$0^+ \rightarrow 2^+ \rightarrow 0^+$
		$2^+ \rightarrow 0^+ \rightarrow 0^+$

in the detector was chosen. To ensure statistical stability in the calculations many neutron histories were run. For these simulations 20 groups consisting of 1000 multiple-scattering processes and 50 single-scattering processes were performed for each neutron spin direction.

The corrections to the data are made in an iterative fashion as explained in (Guss 1982a). For each iteration the code performs a fixed number of single and multiple scattering processes. The probability for each process is computed based on the differential cross sections. These probabilities are used to generate spectra from which the yields are extracted. Spectra are simulated for incident neutrons with spin up and for incident neutrons with spin down. Figure 5.8 is a comparison of a simulated spectrum to the corresponding experimentally measured spectrum. The yields from the simulated spectra are used to calculate A_y^S, A_y^M, P^S, and P^M. The analyzing power of the single-scattered and double-scattered neutrons are calculated as follows:

$$A_y^S = \frac{S_\uparrow - S_\downarrow}{S}$$

and likewise,

$$A_y^M = \frac{M_\uparrow - M_\downarrow}{M}$$

where,

$$T_\uparrow = S_\uparrow + M_\uparrow$$

$$T_\downarrow = S_\downarrow + M_\downarrow$$

$$S = S_\uparrow + S_\downarrow$$

and

$$M = M_\uparrow + M_\downarrow .$$

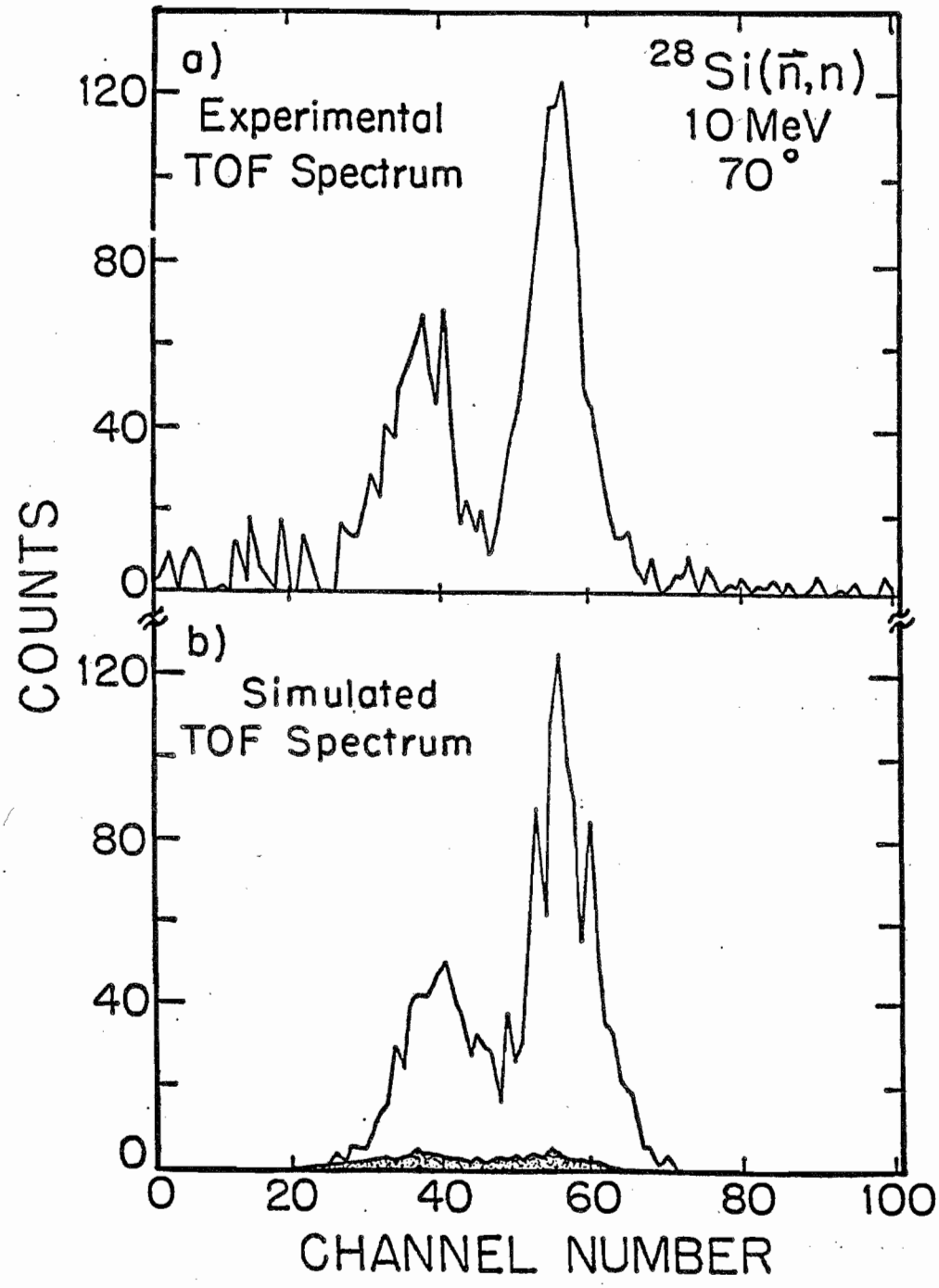

Figure 5.8. Experimental TOF spectrum and simulated (JANE) TOF spectrum from $A_y(\theta)$ measurements. The shaded region in the simulated spectrum represents the contributions from the multiple scattered neutrons.

The analyzing power of all the neutrons that scattered from the sample is

$$A_y^T = \frac{T_\uparrow - T_\downarrow}{T}$$

$$A_y^T = \frac{S}{T} A_y^S + \frac{M}{T} A_y^M$$

which can be written as,

$$A_y^T = P^S A_y^S + P^M A_y^M \qquad (5.3)$$

where

$S_\uparrow$, $S_\downarrow$ => Yields extracted from simulated spectra for singly scattered neutrons with incident neutron spin up and with incident neutron spin down, respectively;

$M_\uparrow$, $M_\downarrow$ => Yields extracted from simulated spectra for multiply scattered neutrons with incident neutron spin up and with incident neutron spin down, respectively.

The final simulated analyzing power A_y^T is the analyzing power of all neutrons scattered from the sample in the simulation. This quantity is to be compared to the experimentally measured analyzing power. With each iteration one obtains a better estimate of A_y^S and the finite geometry correction F due to angle averaging.

The corrections to the data were small. The corrections to the elastic data were usually less than 5%, however in the minima of the cross sections they were as high as 15%. The corrections to the inelastic data were normally around 2%. These corrections include: corrections for multiple-scattering and flux attenuation in the sample, corrections to the scattering angle due to the finite resolution of the spectrometer, and finite geometry correction F. The multiple-scattering and flux attenuation corrections were normally smaller than 5% for the elastics and less than 2% for the inelastics. The angle corrections were less than 1^o, except on the steep slope in $\sigma(\theta)$, where they were around 2%. And the

finite geometry corrections due to angle averaging were normally less than 2%, except in the angular regions where A_y was changing rapidly and therefore were as high as 12%. Some situations with large corrections to the $A_y(\theta)$ data are considered later in the special measurements discussed in chapter 6.

5.2.3 Uncertainties in the Data

The relative uncertainties in the $A_y(\theta)$ angular distributions for elastic scattering are about 4%, except in the minima of $\sigma(\theta)$ where they are as high as 8%. The average uncertainties in the inelastic data are about 7% for silicon and around 12% for sulfur. These uncertainties include statistical uncertainties, uncertainties in the magnitude and analyzing powers of the backgrounds, uncertainty in the beam polarization, and the precision of the finite geometry corrections that were applied to the data. In addition to the relative errors, there is a 3% overall normalization uncertainty in the data due to the uncertainty in the value of $K_y^y(0^o,E_d)$. The error bars on these data do not reflect this latter uncertainty, since it enters as a scale factor across the entire angular distribution.

5.2.4 Legendre Polynomial Description of the Analyzing Power Data

The present data were described with curves that were derived from fitting an associated Legendre polynomial expansion to the product of $A_y(\theta)\cdot\sigma(\theta)$. This product was fit instead of $A_y(\theta)$ because it is a simpler function and therefore is easier to describe with associated Legendre polynomials. Figures 5.9 and 5.10 are plots of the product of $A_y(\theta)$ data

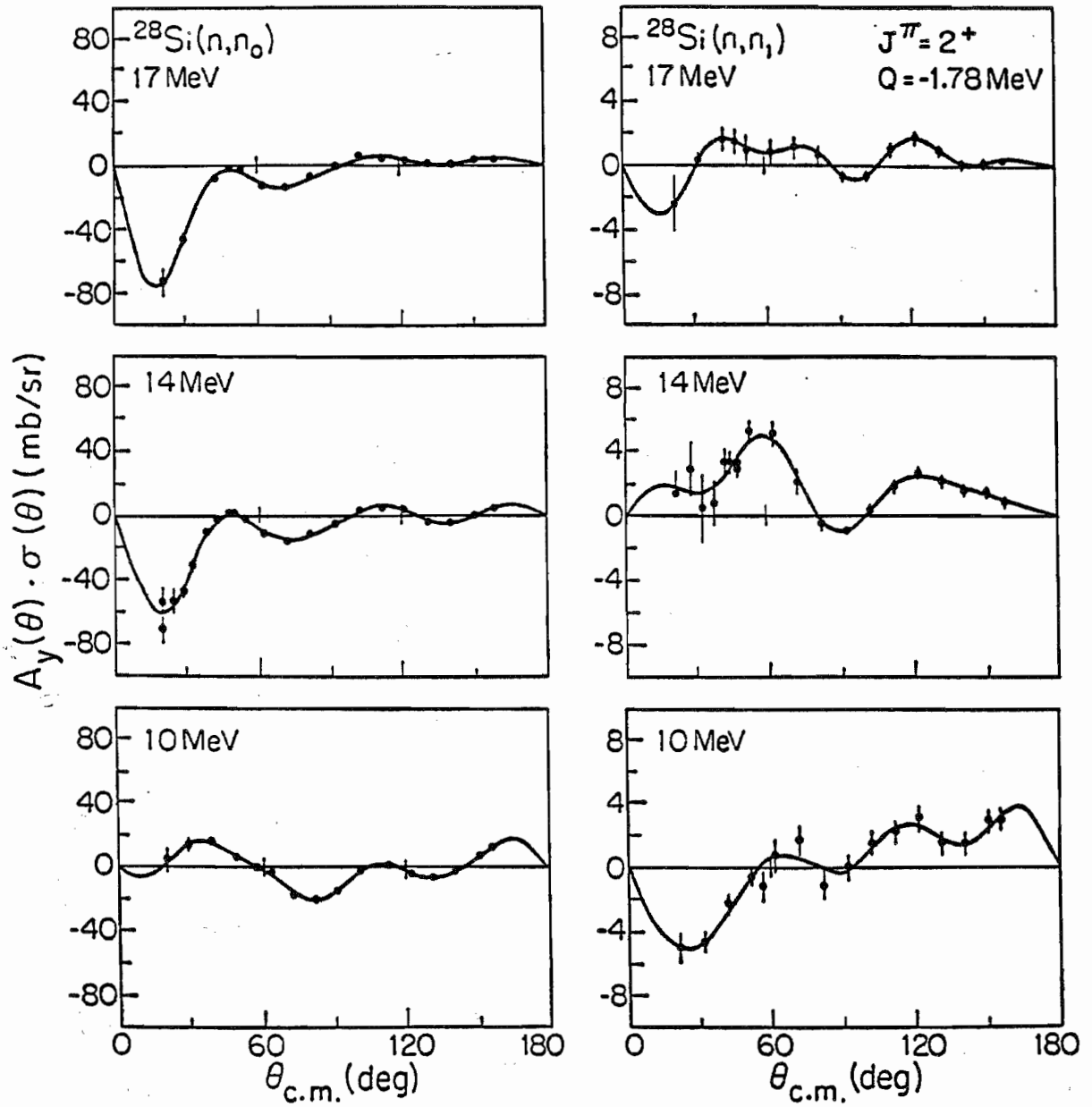

Figure 5.9. Data for the product $\sigma(\theta,E)\cdot A_y(\theta,E)$ for ^{28}Si. Curves are associated Legendre polynomials fits.

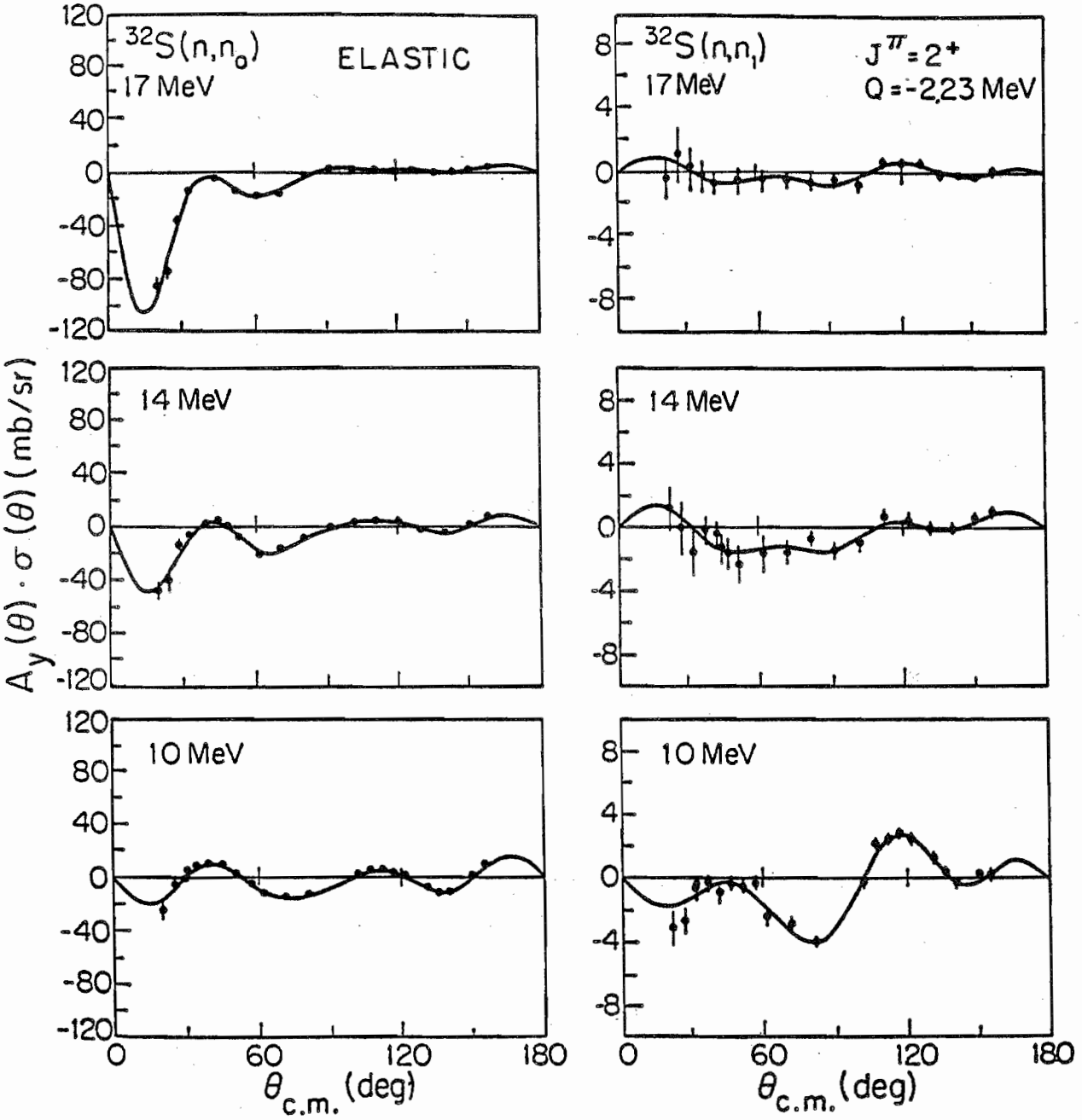

Figure 5.10. Data for the product $\sigma(\theta,E)\cdot A_y(\theta,E)$ for ^{32}S. Curves are associated Legendre polynomials fits.

and $\sigma(\theta)$ data along with the corresponding fits. Figures 5.11 and 5.12 are plots of the analyzing power data with the corresponding fits. These fits were obtained by dividing the curves for $A_y(\theta)\cdot\sigma(\theta)$ by the fits to the $\sigma(\theta)$ data. All data were described with the least number of ℓ values possible. Tabulations of the $A_y(\theta)$ data and the coefficients used to generate the fits to $A_y(\theta)\cdot\sigma(\theta)$ are presented in Appendix II.

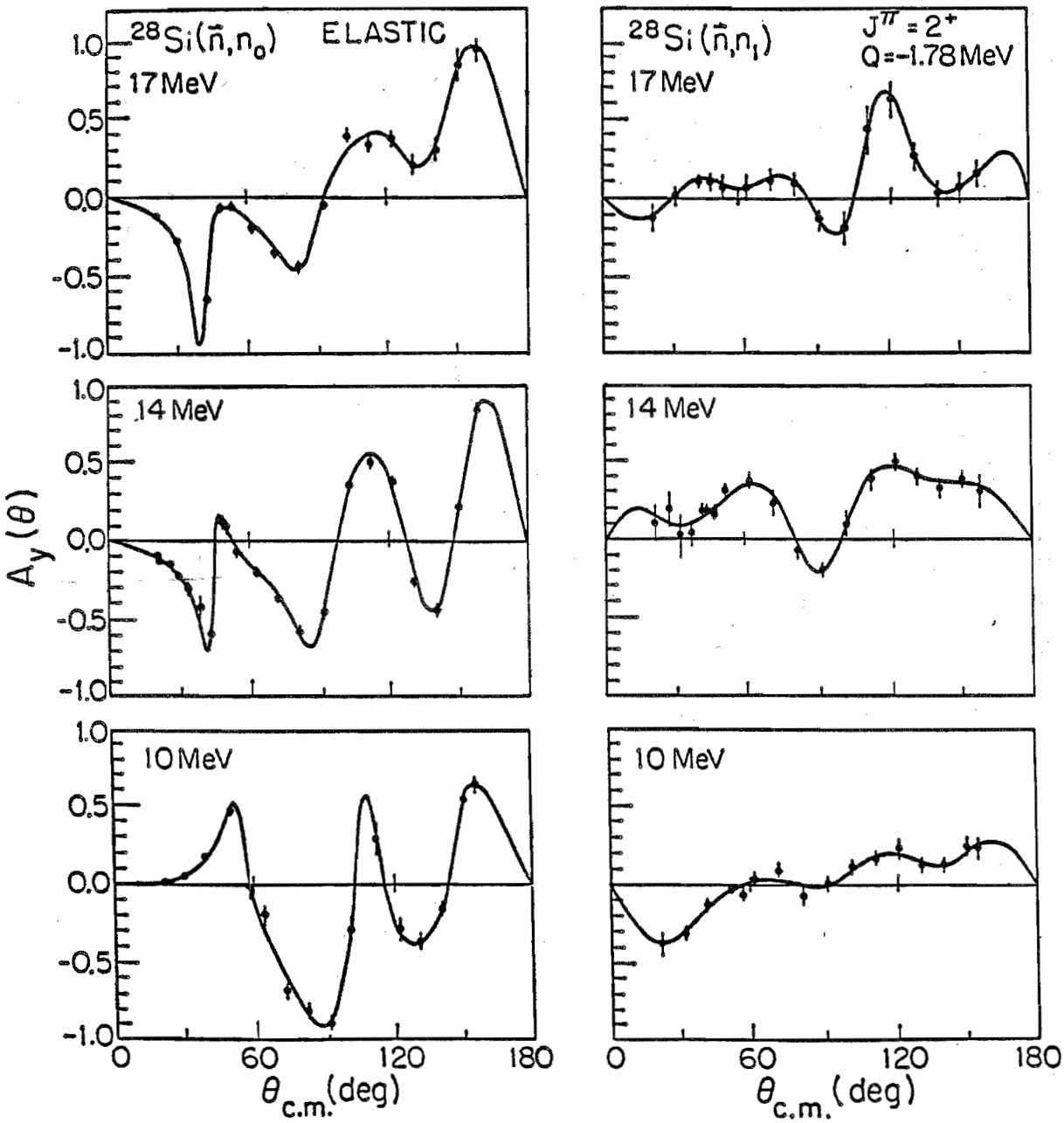

Figure 5.11. Measured values of $A_y(\theta,E)$ for $^{28}Si(\vec{n},n)$. Curves are derived from associated Legendre polynomials fits to $\sigma(\theta,E)\cdot A_y(\theta,E)$.

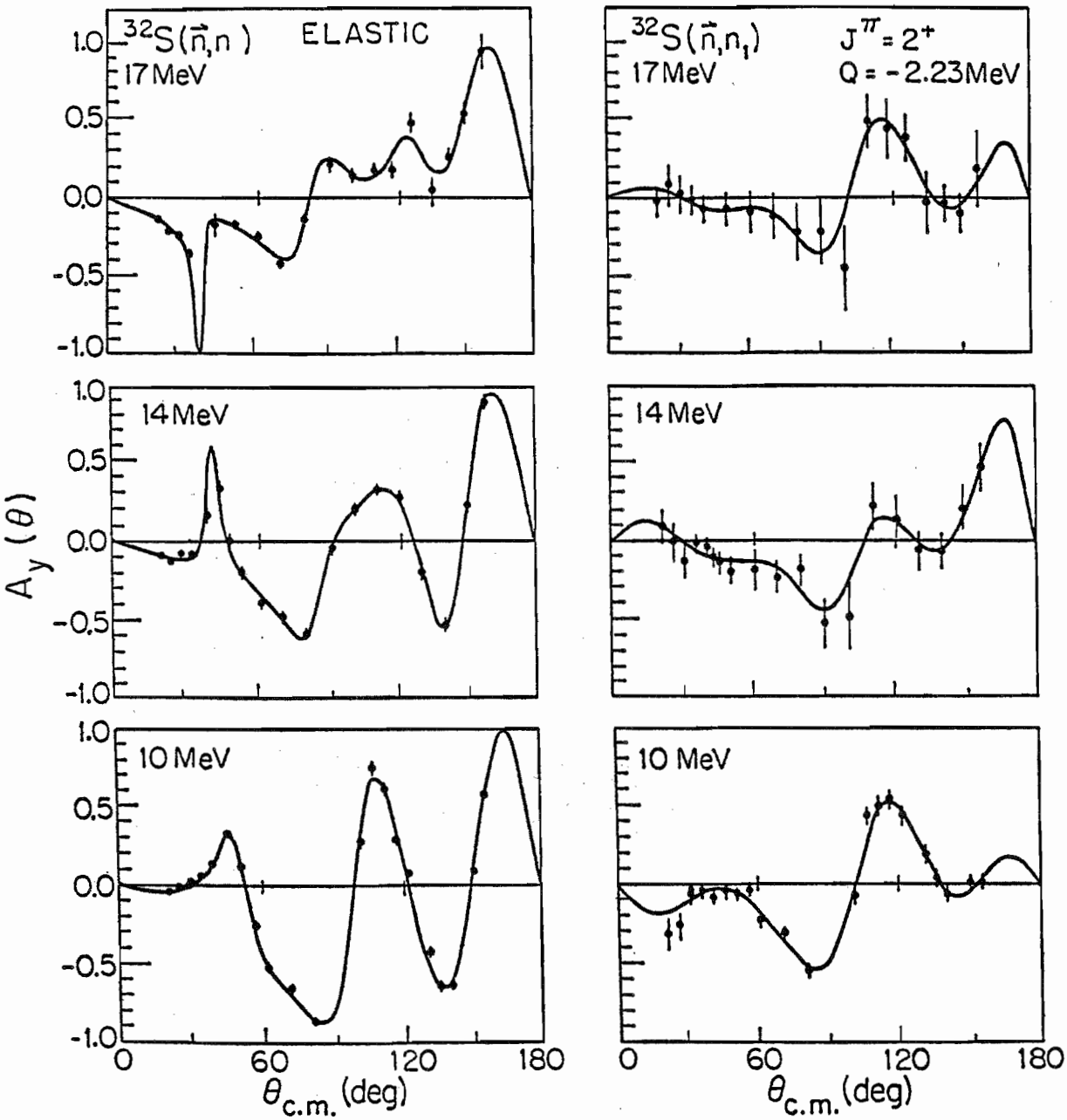

Figure 5.12. Measured values of $A_y(\theta,E)$ for $^{32}S(\vec{n},n)$. Curves are derived from associated Legendre polynomials fits to $\sigma(\theta,E)\cdot A_y(\theta,E)$.

CHAPTER 6

$A_y(\theta)$ MEASUREMENTS IN THE MINIMUM OF $\sigma(\theta)$

6.1 Introduction

A series of analyzing power $A_y(\theta)$ measurements for polarized neutron scattering from ^{28}Si near the first minimum of the differential cross section were performed at TUNL. These measurements were performed to resolve the apparent discrepancy at 14 MeV between the present $A_y(\theta)$ data and the data very recently reported by Böttcher *et al.* (Böttcher 1983) and to verify the validity of the correction factor generated using the code JANE. The data reported by Böttcher *et al.* will be referred to as the Erlangen data. Figure 6.1 is a comparison of the two data sets for elastic and inelastic scattering. The error bars indicate the uncertainties assigned by the two groups. Both data sets are of high quality for neutron analyzing power measurements, and both sets appear to have few fluctuations that would fall outside statistics. With the exceptions of the data around 40° and 110° c.m., the elastic analyzing powers measured at TUNL are in good agreement with the Erlangen data. The large positive A_y around 40° c.m. reported by Erlangen seems to be inconsistent with the TUNL data and caused us much concern. However, it will be shown that these data indeed are consistent, provided the appropriate uncertainities are assigned to the data. The A_y values of the Erlangen data around 110° c.m. are consistently lower than the corresponding values measured at TUNL. These latter differences are

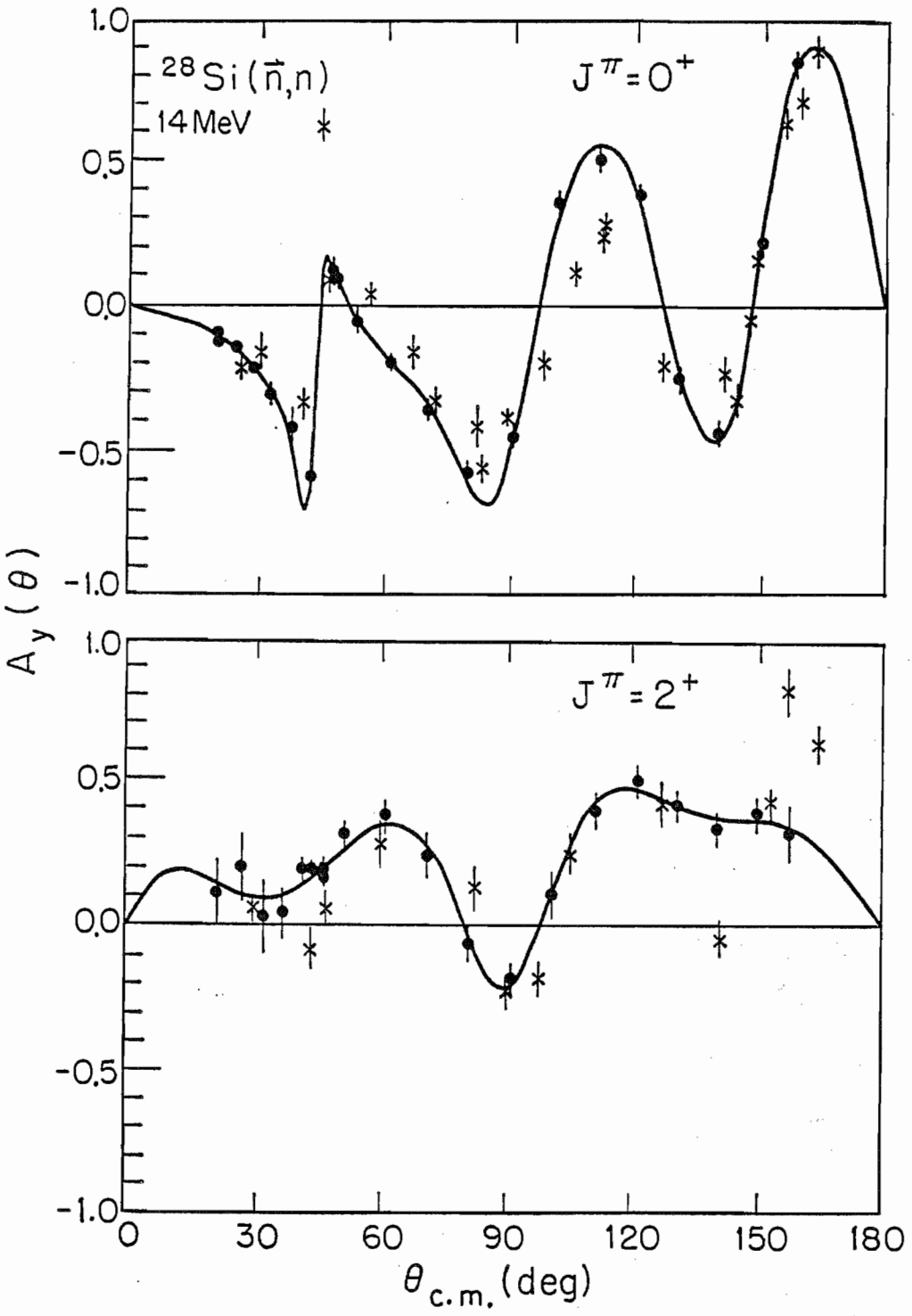

Figure 6.1. The $A_y(\theta)$ data for elastic and inelastic neutron scattering from ^{28}Si at 14 MeV. The circles are the present data and the crosses represent the data reported by Böttcher et al. (Böttcher 1983). The curves are fits derived from Legendre polynomial fits to $A_y(\theta)\cdot\sigma(\theta)$ of the present TUNL data.

believed to be due to Erlangen's inability to completely resolve the elastically scattered neutrons from those that scattered inelastically to the first excited state; this problem would systematically reduce the magnitude of their measured A_y values. It is very difficult using their experimental techniques, i.e., analysis of proton recoil spectra, to completely filter the inelastically scattered neutrons from those that elastically scattered without sacrificing the statistical accuracy. For inelastic scattering, the data are in good agreement forward of 140° c.m. as shown in the bottom of fig. 6.1. We now believe the shape of the inelastic scattering analyzing powers of the Erlangen data at back angles is influenced by the A_y of the elastically scattered neutrons.

There were primarily two reasons why it was important to resolve the apparent discrepancy around 40° c.m. First, according to the results of the coupled-channels analysis reported in (Böttcher 1983), the prediction of a narrow positive spike in $A_y(\theta)$, as exemplified by the Erlangen data, was very sensitive to the spin-orbit potential parameters, especially to the diffuseness a_{so}. They also stated that this finding was true only if the parameters of the imaginary well have been accurately determined by fitting data for inelastic scattering and the total cross section. The results of preliminary coupled-channels calculations performed at TUNL confirmed Erlangen's findings and additionally suggested that the prediction of the positive spike was strongly dependent upon the central well parameters, both real and imaginary. Because the calculations showed this strong sensitivity to the shape of $A_y(\theta)$ in the angular region around 40° c.m., it was felt that it was necessary to measure or at least verify the presence of the large positive spike before a complete optical model

analysis could be conducted. Second, measurements in the vicinity of such sharp structure with the neutron spectrometer at TUNL would be a test of the angular resolution capabilities of the system and furthermore would test the computer codes that are used to correct the observed asymmetries for finite geometry effects, such as multiple scattering, flux attenuation, and angle averaging. Because multiple scattering and angle averaging tend to smooth out any structure in $A_y(\theta)$, corrections for these effects will enhance the structure in the experimentally observed angular distributions.

A series of measurements were designed to search for the spike and to test the ability of our multiple-scattering codes to produce consistent results for different experimental configurations and to predict sharp structure that has been grossly smeared due to finite geometry effects. Once again, the code JANE was used to correct the observed $A_y(\theta)$ for the above effects. The code attempts to reproduce the experimental results using Monte Carlo simulations that are based on the cross section and analyzing power libraries and and the physical dimensions of the scattering geometry. The corrections to the experimentally observed analyzing powers are applied in an iterative fashion as described in (Guss 1982a). The initial $A_y(\theta)$ library is usually a fit to the experimentally observed data, and with each iteration, the $A_y(\theta)$ library is updated to reflect the most recent corrections to the data. After convergence, the final values obtained for the corrected data should represent the physical values of $A_y(\theta)$ and therefore should be independent of the geometry of the experimental set-up.

6.2 Experimental Considerations

6.2.1 Introduction

The design of our experiment to measure the apparent positive spike in the analyzing power of ^{28}Si as reported by Böttcher *et al.* required a detailed understanding of finite geometry effects in scattering experiments. One notices from the geometries listed in table 6-1 that the TUNL data for these tests were measured using three different experimental configurations. The most important difference between the arrangements was the distances from the gas cell to the sample. The initial angular distribution was measured with the geometry in Set-1 of table 6-1. Each observed data point in this distribution represented an average over a $\pm$ 8° angular spread. This experiment was conducted prior to the report by Böttcher *et al.*, and therefore was not designed to measure the sharp structure in $A_y(\theta)$ around 40° c.m. The major concern in this measurement was to maximize the counting rate in the side detectors without grossly enhancing the size of the finite geometry effects. Typically, the size of the corrections to the data due to finite geometry effects were less than 10%, except in the minimum of $\sigma(\theta)$ where they were as high as 40%.

The experiments using geometries listed in Set-2 and Set-3 of table 6-1 were specifically designed to locate and measure the sharp structure in $A_y(\theta)$ around 40° c.m. In these geometries the gas cell was shorter and was located farther from the sample than in the initial setup. The optimum angle for observing the positive spike was predetermined by performing Monte Carlo simulations of the experiment using the code JANE.

TABLE 6-1

EXPERIMENTAL CONFIGURATIONS USED TO MEASURE $A_y(\theta)$ IN MINIMUM OF $\sigma(\theta)$

Experiment	Source Length (cm)	D^2 Press. (bar)	D^* (cm)	Sample Radius (cm)	Sample Height (cm)	Flight Path (cm)	Detector Radius (cm)	$\Delta E_n{}^*$ (keV)	$\Delta\theta^*$ (degree)	Number of Angles
TUNL Set-1	5.08	4.0	9.3	1.27	2.53	275	4.44	325	7.84	18
TUNL Set-2	3.16	8.0	10.8	1.27	2.53	374	4.44	350	6.74	2
TUNL Set-3	3.16	8.0	15.3	1.27	2.53	374	4.44	325	4.79	1
Böttcher et al.	5.00	5.0	150.0	2.00	8.00	45	2.54	310	4.19	24

D = center-to-center distance from gas cell to sample

ΔE_n = energy spread at fwhm

$\Delta\theta$ = angular spread at fwhm

The $A_y(\theta)$ library used in these simulations was a fit to the TUNL data with the inclusion of the large positive A_y around 40° c.m. that was reported by Böttcher *et al.*. The predicted optimum angle was a strong function of the position and magnitude of the positive spike in $A_y(\theta)$ coupled with the location and depth of the minimum in $\sigma(\theta)$. As a first attempt to verify the presence of the positive spike, measurements were made using the geometry of Set-2 with the neutron detectors symmetrically positioned at 42° with respect to the beam axis. Although the incident neutron flux on the sample was only lowered by approximately 30% from the flux of the initial setup, the angular spread in the measurements was reduced to $\pm 6.7^\circ$ from $\pm 8^\circ$. Therefore, this configuraton was well suited for preliminary tests in the planning of experiments that would be more sensitive to the sharp structure in $A_y(\theta)$.

6.2.2 Angular Resolution

In order to directly observe the narrow structure in $A_y(\theta)$, the angular resolution of the detection system must be less than the angular range of the structure. The angular resolution (denoted as $\Delta\theta$ and for our purposes defined as half of the full angular spead) of the neutron time-of-flight (NTOF) spectrometer at TUNL is a combination of the angular spread between the gas cell and the sample $\Delta\theta_{samp}$ and the angular spread between the sample and the detector $\Delta\theta_{det}$:

$$\Delta\theta = \left[(\Delta\theta_{samp})^2 + (\Delta\theta_{det})^2\right]^{1/2} .$$

Therefore, a detector positioned at an angle θ_0 in the lab will detect neutrons that are scattered to angles between $\theta_0-\Delta\theta$ and $\theta_0+\Delta\theta$. The mean

scattering angle is computed as

$$\theta_{mean} = \frac{\int_{\theta_0-\Delta\theta}^{\theta_0+\Delta\theta} Y(\theta)\ \theta\ d\theta}{\int_{\theta_0-\Delta\theta}^{\theta_0+\Delta\theta} Y(\theta)\ d\theta}\ .$$

The quantity $Y(\theta)$ is the detected yields at angle θ. The extreme angles in the above average receive less weight because the scattering samples are cylindrical, and therefore the number of nuclei intersected by the incident neutron flux is less at the edge of the samples. Thus, $\Delta\theta$ is not quite as large as one would calculate by simply computing $\tan(\theta_{samp})$ as the ratio of the sample radius to D, the distance from the center of the gas cell to the center of the sample. If θ_0 is in an angular region where $\sigma(\theta)$ is increasing with angle, then the mean scattering angle is larger than θ_0, and vice versa. In regions where $\sigma(\theta)$ is flat, θ_{mean} is approximately equal to θ_0. Knowledge of how to compute θ_{mean} is essential in determining where to position the side detectors in the proposed experiment.

The observed analyzing power at each angle is a weighted average of all the analyzing powers over the angular resolution of the spectrometer. That is,

$$A_y(\theta_0) = \frac{\int_{\theta_0-\Delta\theta}^{\theta_0+\Delta\theta} Y(\theta)\ A_y(\theta)\ d\theta}{\int_{\theta_0-\Delta\theta}^{\theta_0+\Delta\theta} Y(\theta)\ d\theta}\ .$$

Because of this averaging, any sharp structure in $A_y(\theta)$ will be smoothed. The magnitude of the smearing effect can be decreased by reducing the angular spread $\Delta\theta$. This is especially important when measuring $A_y(\theta)$ near the minimum of $\sigma(\theta)$, because most of the detected neutrons are scattered from neighboring angles. Therefore, information about $A_y(\theta)$ in the minimum of $\sigma(\theta)$ is washed out by the angular average.

According to the Erlangen data and calculations, the positive spike in $A_y(\theta)$ spans an angular region of about $\pm 5^\circ$. In order to observe the spike directly, the angular resolution of the NTOF spectrometer at TUNL was reduced to less than 5° using the geometry of Set-3. The predominant source of angular spread in the spectrometer was the angle subtended between the gas cell and the sample. Therefore, the most obvious means of reducing the angular resolution of the spectrometer were to increase the distance from the gas cell to the sample D and/or to decrease the diameter of the sample. The more efficient method of increasing D was chosen in order to improve the angular resolution with minimal loss of counting rates. Increasing D from 10.8 cm to the maximum distance of 15.3 cm reduced the angular spread from $\Delta\theta = \pm 6.7^\circ$ to $\Delta\theta = \pm 4.8^\circ$, which was only slightly less than 5°. The maximum distance for D was limited by the SLANG structural supports for the vacuum cold trap located immediately behind the gas cell. The location of these supports placed rigid constraints on the minimum angular resolution obtainable without major design changes.

6.2.3 Sources of Energy Spread

Another characteristic of the measuring apparatus that can mask the presence of sharp structure in either $\sigma(\theta)$ or $A_y(\theta)$ is its energy resolution. The major source of energy spread in the measurements using the NTOF spectrometer at TUNL is the energy spread in the neutron beam incident on the sample. The primary causes of the energy spread in the incident neutron beam are the energy spread of the deutron beam in the gas and the kinematics of the $^2H(d,n_0)^3He$ reaction over the angle subtended by the sample at the gas cell.

The predominant sources of energy spread in the deuteron beam are straggling through the entrance foil to the gas cell and energy loss in the deuterium gas due to ionization. The distribution of the energy straggling of the deuterons through the foil is assumed to be gaussian with a width that is to first order energy independent (Klein 1982). The full width at half maximum (fwhm) is calculated using the code STRAGL which was developed at Los Alamos. Because the code can only calculate straggling through monoisotopic foils, the fwhm of the beam in the 0.25 mil havar foil is computed by mocking it as a cobalt foil of the same thickness. The fwhm is essentially constant from 5 to 15 MeV incident deuteron energy with the value ΔE_{str} = 45 keV. The energy distribution of the deuterons in the gas is rectangular with a width equal to the energy loss in the gas.

According to Klein *et al.* (Klein 1982), the superposition of the gaussian distribution due to straggling in the foil with the rectangular distribution in the gas obeys a cubic law:

$$\Delta E_d = \left[(\Delta E_{str})^3 + (\Delta E_{gas})^3 \right]^{1/3} .$$

In addition to the above relationship, Klein et al. also derived an expression for computing the energy spread of the neutrons incident on the sample:

$$\Delta E_n = \left[\left(\frac{\partial E_n}{\partial E_d} \Delta E_d\right)^\alpha + \left(\frac{\partial E_n}{\partial \theta_n} \Delta\theta_n\right)^\alpha \right]^{1/\alpha} \qquad (6.1)$$

where

ΔE_d = energy loss in gas (keV);

$\Delta\theta_n$ = full angular spread in degrees from gas cell to sample.

Since the rectangular distribution of the energy loss in the gas dominates in the energy region of our experiments, $\alpha = 3$ was used in the above expression. The values for ΔE_d and $\Delta\theta_n$ are listed in table 6-1. The angular spread given in the table must be doubled before being used in eqn. (6.1) because $\Delta\theta_n$ is the full angular spread. The partial derivative $\partial E_n/\partial\theta_n$ was derived by comparing the kinematics of the ^{2}H(d,n) reaction from 0° to 10° lab at various neutron energies. The relationship

$$\frac{\partial E_n}{\partial \theta_n} \simeq 1.6 E_n \text{ (keV/deg·MeV)} - 6 \text{ (keV/deg)}$$

resulted from the comparisons. The value for $\partial E_n/\partial E_d$ was determined by substituting the energy spreads that were computed from the distributions shown in fig. 6.2 into eqn. (6.1) and solving for $\partial E_n/\partial E_d$. The distributions shown in fig. 6.2 are the results of Monte Carlo simulations using the code JANE. A mean value of $\partial E_n/\partial E_d = 0.90$ was obtained using the four cases illustrated in fig. 6.2.

The energy distribution of the neutrons incident on the sample is a

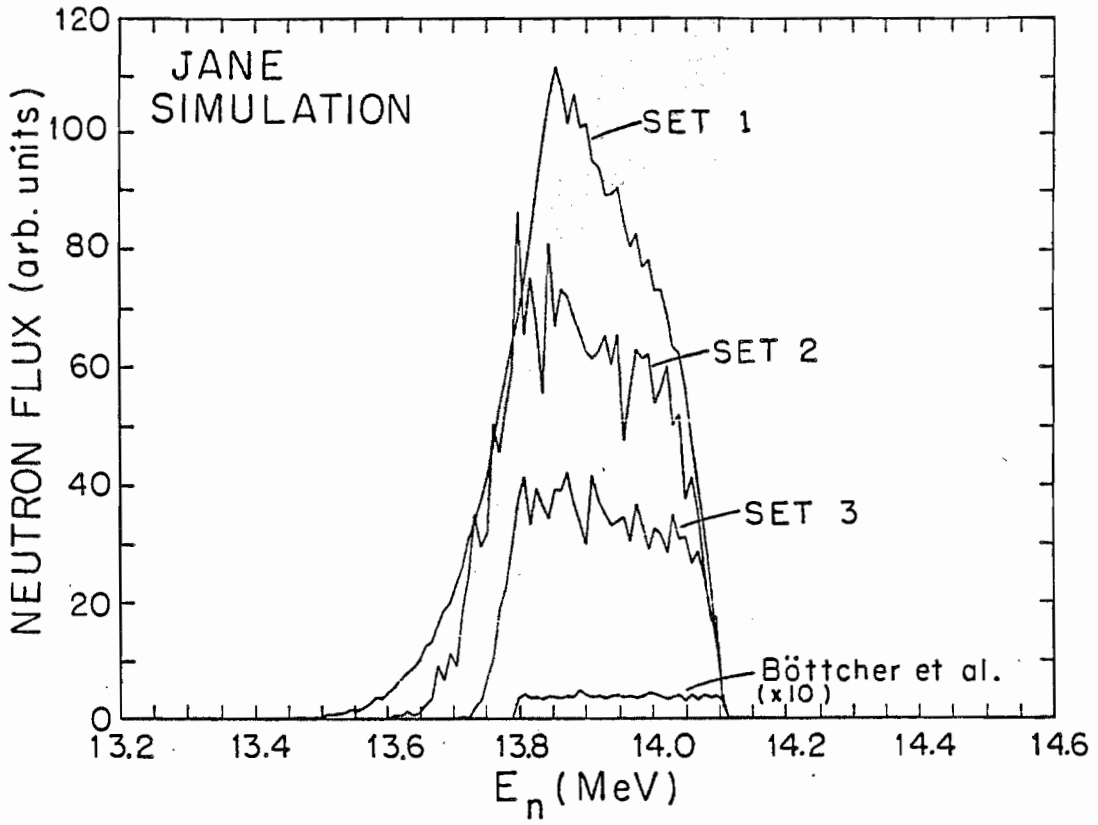

Figure 6.2. Neutron energy distributions intercepted by the scattering sample for geometries listed in table 6-1. All distributions were computed using the Monte Carlo code JANE.

superposition of three distributions: (1) the dominant rectangular distribution due to the deuteron energy loss in the gas, (2) the gaussian distribution due to straggling in the foil, and (3) the gaussian distribution due to the kinematics of the $^{2}H(d,n)$ reaction over the angle subtended by the sample. According to Klein et al., these distributions can be combined using a cubic law and the fwhm of the resultant distribution may be computed using eqn. 6.1. The effect of the gaussian distributions is to round the edges of the rectangle. The distribution simulated using the geometry of the Erlangen experiment (Böttcher 1983) is rectangular with rounded edges due to straggling in the foil. Comparison of the energy distributions in fig. 6.2 suggest that the gaussian distribution due to averaging over the angle subtended by the sample causes tails on the low energy side and slants the top of the rectangular distribution.

6.2.4 Backgrounds

If the experimenter is not careful, then the signal-to-noise in the TOF spectra of measurements near the minimum of $\sigma(\theta)$ can be significantly depreciated. As the minimum in $\sigma(\theta)$ is approached, the number of neutrons that are scattered from the sample decreases, while the number of neutrons that randomly scatter into the detectors remains constant. The signal-to-noise can be greatly improved by measuring the sample-uncorrected backgrounds, measured with SAMPLE-OUT spectra, and subtracting them from the SAMPLE-IN spectra.

The observed analyzing power A_y^{obs} is a weighted average of the analyzing power of neutrons that scatter from the sample A_y^{samp}, and the

analyzing power of the background that appears under the peaks of interest in the TOF spectra. The two most obvious contributors to the background are (1) an unpolarized component due to neutrons that bounce around the target room before finally reaching the detector, and (2) a polarized component due to neutrons that scatter from air. The background component due to random scattering is usually negligible, and thus the observed analyzing power may be written as

$$A_y^{obs} = \left[\frac{Y_{samp}}{Y}\right] A_y^{samp} + \left[\frac{Y_{air}}{Y}\right] A_y^{air}$$

where

$$Y = Y_{samp} + Y_{air} .$$

For elastic scattering, usually $Y_{samp} \gg Y_{air}$, and therefore A_y^{obs} is not significantly effected by air scattering. However, this is not the case for inelastic scattering and elastic scattering near the minimum of the differential cross section. Therefore, A_y^{air} and Y_{air} must be measured accurately in order to reduce the statistical uncertainty in A_y^{obs}. In many cases, especially for inelastic scattering, this requires counting for equal lengths of time for SAMPLE IN and SAMPLE OUT. The reduction of the amount of air scattering can decrease the time spent on the SAMPLE OUT by as much as a factor of 2 and simultaneously improve the signal-to-noise in the TOF spectra, thereby producing cleaner spectra for analysis.

The amount of air scattering was significantly reduced in the present measurements by the addition of a second shadow bar to each detector shielding. This second shadow bar, comprised of 10 to 20 cm of copper,

shielded the detector from the forward angled cone of neutrons that scatter from air in the vicinity of the sample. With this arrangement, the SAMPLE OUT spectra near the minimum of $\sigma(\theta)$ could be accumulated in approximately one-half the amount of time needed to accumulate the SAMPLE IN spectra.

6.3 Measurement of the Minimum in the Differential Cross Section

Because the analyzing power $A_y(\theta)$ and the differential cross section $\sigma(\theta)$ are intimately related, a detailed understanding of the simpler function $\sigma(\theta)$ is necessary to appreciate fine details in the more complicated function $A_y(\theta)$. The design of an experiment to observe the narrow structure in $A_y(\theta)$ around 40° c.m., as reported by Böttcher *et al.*, has necessitated the acquisition of high quality $\sigma(\theta)$ data in the same angular region. As an aid in planning the $A_y(\theta)$ experiment, Monte Carlo simulations were performed to predict the experimentally observed data for different scattering geometries. These simulations were useful in optimizing the geometry of the experimental setup. The goal was to minimize the distortions due to finite geometry effects, while simultaneously maintaining reasonable counting rates in the side detectors. The predictions of $A_y(\theta)$ based on these simulations depended heavily on the shape of $\sigma(\theta)$ in the angular region around the minimum. The location of the minimum in $\sigma(\theta)$ was used to determine the angle to position the detectors in order to observe the largest positive A_y value. The magnitude of $\sigma(\theta)$ around the minimum scaled the size of the predicted A_y.

It is impossible to directly observe the narrow structure in $A_y(\theta)$

because of the smearing effects due to multiple scattering in the sample and due to averaging over the angular spread of the spectrometer. Therefore, a high level of confidence must be placed on the methods applied to correct the data for these effects. The size and uncertainities in the finite geometry corrections are strongly dependent on $\sigma(\theta)$. This is especially true near the minimum of $\sigma(\theta)$, where the corrections are generally the largest. Therefore, an accurate determination of $\sigma(\theta)$ near the minimum is necessary to make reliable corrections to the $A_y(\theta)$ data.

Because both the planning of the experiment to measure $A_y(\theta)$ near the minimum of $\sigma(\theta)$ and the corrections to the measured data require accurate $\sigma(\theta)$ knowledge, an experiment was conducted to accurately determine the minimum of $\sigma(\theta)$. These measurements were conducted with the same NTOF spectrometer used in the $A_y(\theta)$ experiments and in the previous $\sigma(\theta)$ measurements. The center-to-center distance from the gas cell to the sample D was increased to the maximum allowable length in order to minimize the angular spread of the spectrometer $\Delta\theta$, and thus permit a more direct measure of the minimum in $\sigma(\theta)$. Figure 6.3 is a plot of the (multiple scattering)/(total scattering) ratios for both geometries. The circles represent the ratios with the close geometry, D = 9.25 cm, and the squares represent the ratios with the wide geometry, D = 15.33 cm. This figure indicates that the (multiple scattering)/(total scattering) ratio increases as the measurement approaches the minimum of $\sigma(\theta)$. Obviously, this is because the number of multiple-scattered neutrons leaving the sample is roughly a constant in angle, while the number of single-scattered neutrons vary as $\sigma(\theta)$. Notice that the previous $\sigma(\theta)$

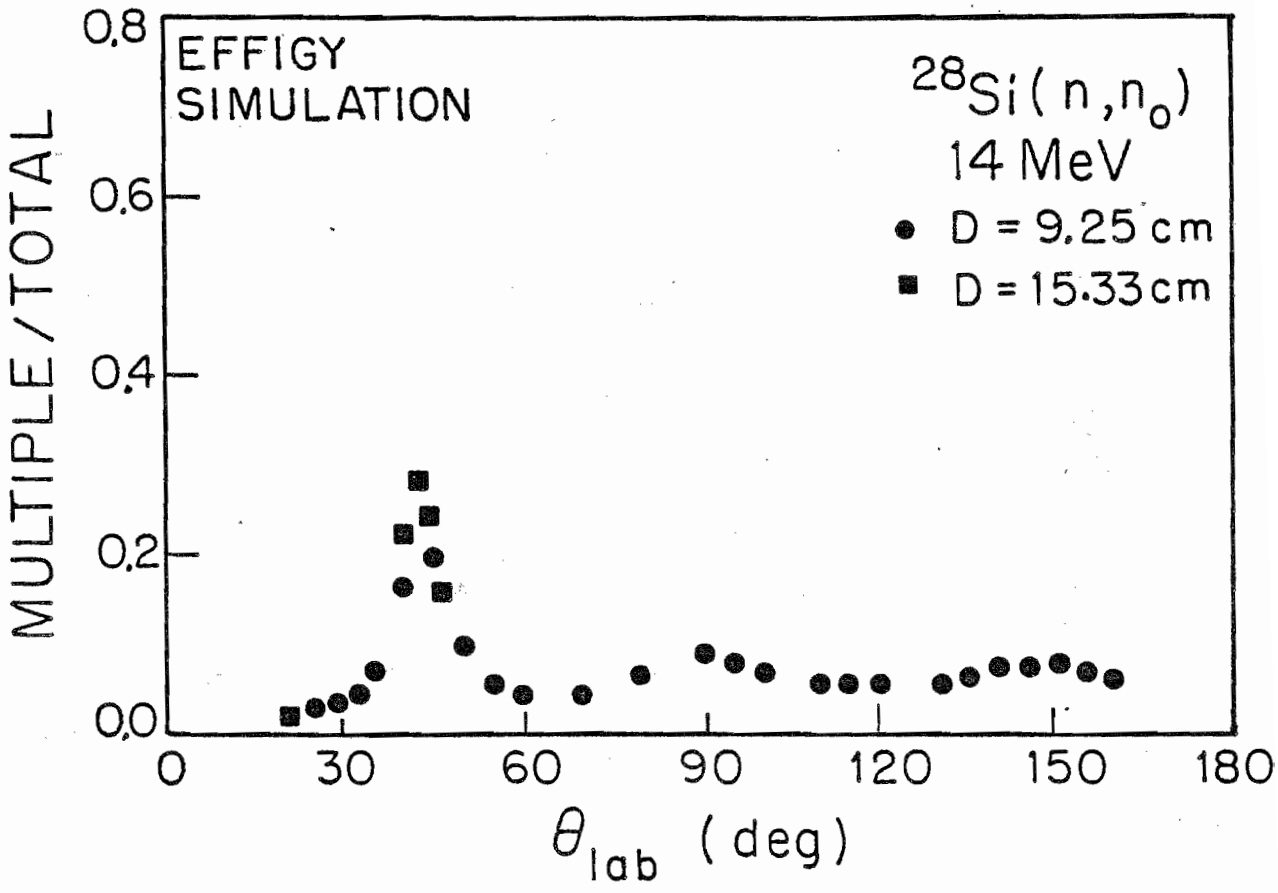

Figure 6.3. Plot of the ratios for multiple scattered events/total scattered events for the close geometry (D = 9.25 cm) and for the wide geometry (D = 15.33 cm). The circles and squares represent the close and wide geometries, respectively.

experiment, i.e., the measurement using the close geometry, was conducted on sides of the minimum, and furthermore, the "mean" scattering angles in this region were spread apart, thus creating a gap around the minimum. In the wide geometry experiment this gap was filled by reducing $\Delta\theta$ and measuring in small angular increments. The measurements were made in 2^{o} steps across the 40^{o} to 46^{o} lab angular region. In addition, a couple of measurements at forward angles and one at 60^{o} were conducted to help compare these data to the previously measured cross sections. As usual, the absolute normalization was obtained from n-p scattering.

In addition to providing accurate $\sigma(\theta)$ data in the minimum, these data were also useful in testing the methods employed to correct the measured $\sigma(\theta)$ data for finite geometry effects and for absolute data normalization. The yields extracted from the peaks in the TOF spectra were converted to cross sections by eqn. (5.1). This expression does not overtly depend on the scattering geometry. However, the geometry of the experimental arrangement subtly enters the expression in the polyethylene correction factor $C_{p}(\theta_{p})$. Because the data near the minimum were measured with a wider geometry than the remainder of the distribution, $C_{p}(\theta_{p})$ was smaller.

Figure 6.4 is a plot of the elastic $\sigma(\theta)$ taken with both geometries. Both data sets have been corrected for finite geometry effects and properly normalized. The curve through the data is a Legendre polynomial fit. The points measured on the steep slope of $\sigma(\theta)$ at forward angles provided an extremely sensitive test of the finite geometry corrections applied to the data. The code EFFIGY was used to correct the $\sigma(\theta)$ data for multiple scattering, flux attenuation, and angle averaging effects.

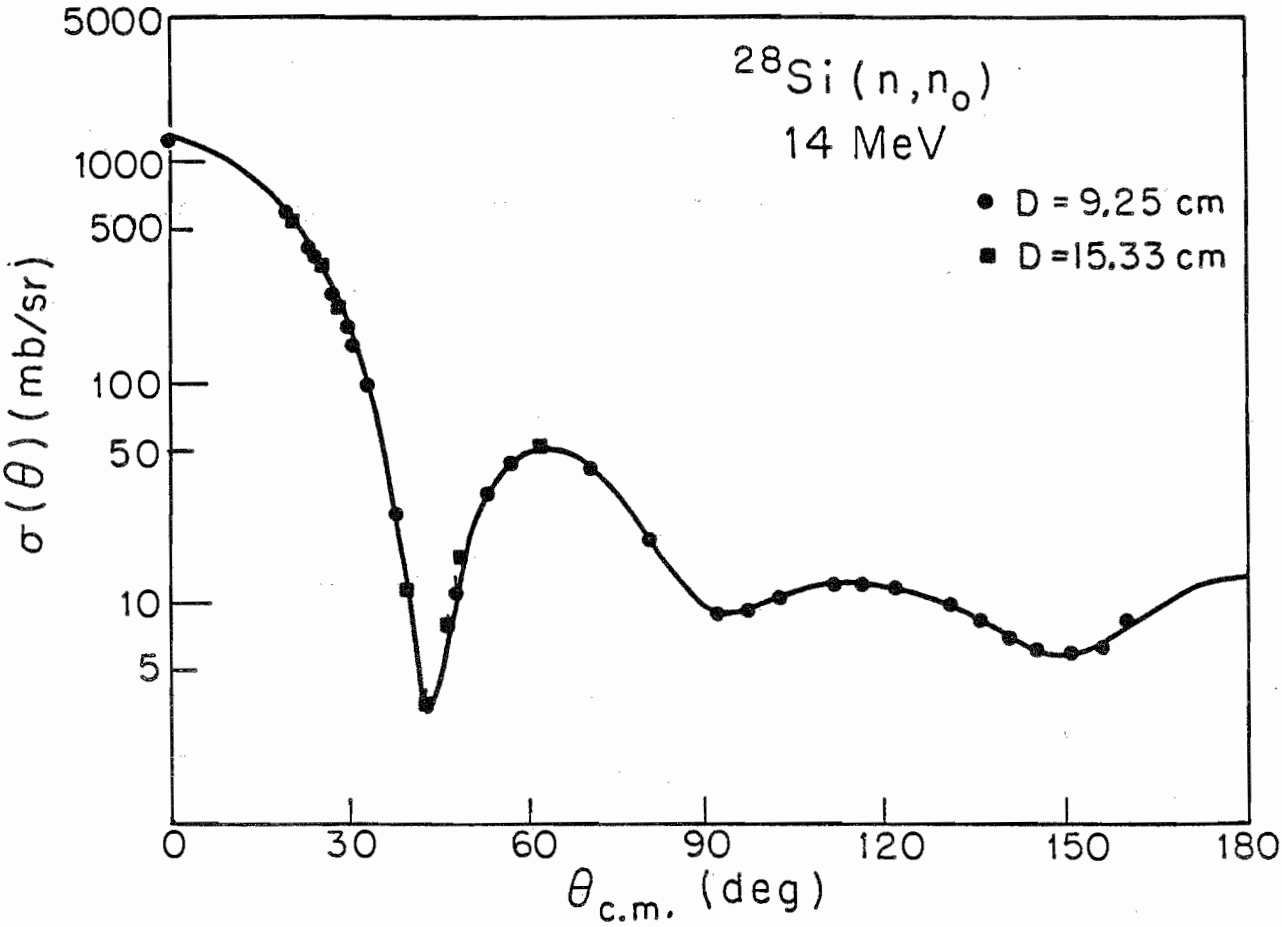

Figure 6.4. Plots of the $\sigma(\theta)$ for neutron elastic scattering from ^{28}Si at 14 MeV. The circles represent the close geometry (D = 9.25 cm) and the squares represent the wide geometry, (D = 15.33 cm). The curve through the data is a Legendre polynomial fit.

The data point measured at 60^{o} lab where $\sigma(\theta)$ was flat and the finite geometry corrections were small provided a test of the data normalization method. After the appropriate corrections and normalizations were applied, the data measured with the wide geometry were in excellent agreement with the earlier measurements, as can be seen in fig. 6.4.

Based on the above results, it was concluded that our method of absolute normalization and correction of the data for finite geometry effects provide a unique solution within the accuracy of the data. In addition, the magnitude and location of the cross section minimum were accurately determined. These data provided vital information for planning the experiment to measure the apparent narrow positive spike in $A_y(\theta)$. The accuracy of these data were also sufficient to reduce the uncertainities in the finite geometry corrections to the $A_y(\theta)$ data near the minimum of $\sigma(\theta)$.

6.4 Deduction of $A_y(\theta)$ near the Minimum of $\sigma(\theta)$

A direct measure of $A_y(\theta)$ can not be performed using the present sample and spectrometer at TUNL because of the influences of multiple scattering in the sample and averaging over the angular spread of the system. The observed analyzing power at the detector angle θ_0 is a weighted average of all single- and multiple-scattered neutrons in the $\theta \pm \Delta\theta$ angular range. The analyzing power for all detected neutrons may be written as,

$$a_y^t = p^s a_y^s + p^m a_y^m \qquad (6.2)$$

and

$$t = s + m$$

where

p^s, $p^m = \frac{s}{t}, \frac{m}{t}$ => probabilities of single and multiple scattering in the sample, respectively;

a_y^s, a_y^m => analyzing powers of single- and multiple-scattered neutrons, respectively;

a_y^t => analyzing power of all detected neutrons.

In the present measurements, the code JANE was used to deduce $A_y^p(\theta)$ the analyzing power of neutrons that scattered from a single nucleus into a point detector located at angle θ. All quantities in eqn. 6.2 were computed using Monte Carlo simulations. The simulations were based on $\sigma(\theta)$ and $A_y(\theta)$ libraries which were derived from fits to the point scattering data.

The $A_y(\theta)$ data were corrected for multiple scattering and other finite geometry effects in an iterative fashion. During this discussion there will be an interchange of lower and upper case letters to distinguish between analyzing powers that were derived solely from the simulations, and those that were admixtures of experimentally observed data and simulations. The p^s and p^m were consequences of the $\sigma(\theta)$ library and therefore did not change with each iteration. The a_y^m changed only slightly between iterations since it represented an average over the entire angular distribution. The quantities that were changing most rapidly between iterations were a_y^s and the finite geometry correction due to angle averaging F. The quantity F was computed as

$$F = A_y^p - a_y^s \quad . \tag{6.3}$$

The value of A_y^p was taken directly from the $A_y(\theta)$ library. The initial $A_y(\theta)$ library was a fit to the experimentally observed analyzing power A_y^{exp}. A better estimate of A_y^s and F were obtained with each iteration by comparing a_y^t to A_y^{exp}. The iterative procedure is listed below.

1. Perform simulation using fit to A_y^{exp} data as initial $A_y(\theta)$ library.

2. Substitute A_y^{exp} for a_y^t in eqn. (6.2) and solve for A_y^s, a guess at the analyzing power of the single-scattered neutrons.

3. Compute F using eqn. (6.3).

4. Compute the most recent guess at the final corrected data:

   $A_y^c = A_y^s + F$.

5. Update the $A_y(\theta)$ library with fit to A_y^c.

6. Run JANE again to make new estimates of a_y^s, a_y^m and F.

7. Test for convergence in two steps:

   a) substitute A_y^s of previous iteration into eqn. (6.2) and compare A_y^t to A_y^{exp}; if the agreement is consistently less than one-quarter of the experimental uncertainties, then go to step b), otherwise go back to step 2 and try again;

   b) a more rigorous test of the $A_y(\theta)$ library is to compare a_y^t to A_y^{exp}; if these quantities agree within the uncertainties of the data, then the process has converged, otherwise go back to step 2.

8. The final corrected data are the A_y^c values that were used to create the $A_y(\theta)$ library used in the simulation that passed the convergence test.

6.5 The $A_y(\theta)$ Measurement near the Minimum of $\sigma(\theta)$

The analyzing powers were measured using the three experimental geometries listed in table 6-1. Notice that only three angles were measured with the wide geometries: 20° and 42° with Set-2 and 45° with Set-3. The 20° point was taken to tie the measurements made with Set-2 to the initial measurements, which were made with Set-1. The choices of 42° and 45° were based on the results of Monte Carlo simulations. These angles were predicted to exhibit the most obvious indication of the presence of the narrow positive spike. The analyzing power library used in these predictions was a spline fit to the 14 MeV point-scattering data of TUNL plus the large positive point at 44° c.m. reported by Böttcher et al.. In order to reproduce the sharp structure around 40° c.m., the data was described with a spline fit instead of with Legendre polynomials. The solid curve in fig. 6.5 represents the $A_y(\theta)$ library used in these simulations. The corresponding $\sigma(\theta)$ library is shown in fig. 6.4. At both angles 42° and 45° lab, the predicted A_y values were two error bars more positive than the experimentally observed data.

Because of the discrepancy between the measured analyzing powers and the predictions, a series of calculations were performed using the code JANE to deduce the true shape of $A_y(\theta)$ in the angular region between 40° and 45° c.m. The shape of the $A_y(\theta)$ library around 45° c.m. was varied systematically to test the sensitivity of the predicted analyzing powers to the shape of the library. The initial $A_y(\theta)$ library included the positive spike reported by Böttcher et al. In each subsequent calculation the magnitude of the spike was reduced until finally it was completely

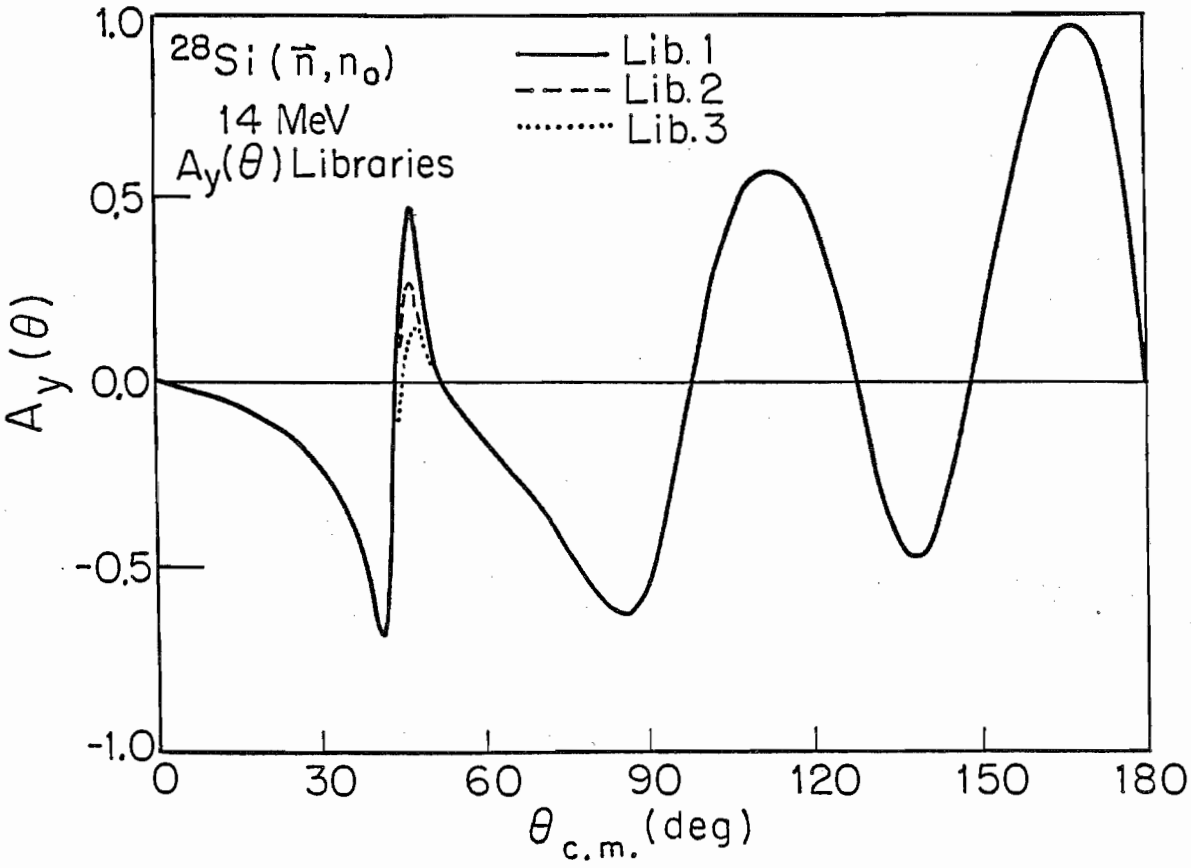

Figure 6.5. Various $A_y(\theta)$ libraries used to deduce $A_y(\theta)$ in the minimum of $\sigma(\theta)$.

removed. Figure 6.5 is a plot of three of the libraries used in these tests. A summary of the results is presented in table 6-2.

6.6 Conclusions

Based on changes in the quantity χ, as defined and listed in table 6-2, the data that showed the most sensitivity to the differences in the three $A_y(\theta)$ libraries, shown in fig. 6.5, were between 40° and 45° lab. The prediction of A_y at 42° lab constrained the upper limit of the spike, and the A_y at 45° lab defined the lower limit. Since the predicted $A_y(\theta)$ based on library 1 over estimated the observed A_y values both at 42° and 45° lab by nearly two error bars, it was concluded that the value of the spike in this library was too high. The predictions using libraries 2 and 3 were within one error bar of the observed A_y values at the above two angles, however, slightly between agreement was obtained with library 3. Combining the results of the above evaluation with the very accurate $\sigma(\theta)$ data, the location of the positive spike was determined to be at $\theta_{c.m.} = 44 \pm 0.5^\circ$ and its magnitude was deduced to be $A_y = +0.20 \pm 0.10$.

These results are inconsistent with the A_y and uncertainty reported by Böttcher *et al*. We presently believe that the disagreement is due partially to the data reduction methods applied in their spectrum anlaysis and in part to their method of applying finite geometry corrections and determining the associated increase in the statistical uncertainty. Their measured values for the elastic scattering analyzing powers between 40° and 45° c.m. are probably significantly influenced by the unresolved contaminant of neutrons that inelastically scatter to the first excited state. Since in this angular region the cross section for scattering to

TABLE 6-2

SUMMARY OF JANE SIMULATIONS

θ_{lab} (degree)	A_y^{exp}	ΔA_y^{exp}	χ			F		
			Lib-1	Lib-2	Lib-3	Lib-1	Lib-2	Lib-3
45[a]	-0.2255	0.0135	+1.26	+1.21	+1.20	0.003	0.004	0.004
35[a]	-0.3020	0.0335	+0.58	+0.49	+0.47	0.009	0.012	0.013
40[a]	-0.2400	0.0600	-0.85	-1.12	-1.24	-0.146	-0.147	-0.141
45[a]	-0.0349	0.0317	+0.54	-0.09	-0.48	0.107	0.127	0.138
50[a]	-0.0547	0.0354	+0.60	+0.48	+0.40	-0.011	-0.007	-0.004
42[b]	-0.2846	0.0439	+1.91	+1.22	+0.83	-0.261	-0.230	-0.209
45[c]	0.0139	0.0440	+1.83	+0.86	+0.19	0.087	0.089	0.083

[a,b,c] These data were taken using the geometries in Set-1, Set-2, and Set-3 of table 6-1, respectively.

The F is the finite geometry correction due to angle averaging.

$$\chi = \frac{a_y^t - A_y^{exp}}{\Delta A_y^{exp}}$$

the 2^+ state is more than twice that for elastic scattering, the inability to completely resolve or account for the neutrons that inelastically scatter will tend to pull the observed A_y values for elastic scattering in the direction of the A_y for scattering to the 2^+ state. Once the elastic scattering analyzing powers in this narrow angular region have been distorted as described above, the finite geometry corrections will enhance the distortion.

Various sensitivity tests using the code JANE suggest that the size and uncertainty in the finite geometry corrections are strongly correlated to the magnitude and location of the cross-section minimum. Böttcher et al. used the $\sigma(\theta)$ data reported by Kliczewski and Lewandowski (Kliczewski 1978) in their analysis. Because Kliczewski and Lewandowski reported only a few data points around the minimum of $\sigma(\theta)$, it is difficult to believe that Böttcher et al. could have located the minimum to an accuracy of better than $\pm 1^{\circ}$, or could have determined the magnitude of $\sigma(\theta)$ in the minimum to within a factor of two. These uncertainties in $\sigma(\theta)$ propagate as large uncertainties in the finite geometry corrections. Furthermore, a reduced $\sigma(\theta)$ will magnify the statistical uncertainty of the singly scattered neutrons. With these concerns in mind, for our purposes the uncertainty in the large positive A_y reported by Böttcher et al. was increased to be consistent with our findings. This adjustment amounted to increasing their uncertainty by a factor of five. Their data point with theisenlarged error was inserted into the TUNL $A_y(\theta)$ data set for our theoretical analyses in chapters 8 and 9.

CHAPTER 7

COMPOUND NUCLEUS CORRECTIONS

7.1 Introduction

In order to be able to describe nuclear scattering cross sections with a conventional optical model, the cross sections must vary both smoothly with energy for a single nucleus and smoothly at a single energy as a function of atomic mass A. If data does not show the above systematic trend with energy, then there is little hope in describing it with even a specialized optical model, and some other approach must be devised to explain the behavior of the data. In many cases, irregularities in scattering cross sections are due to the formation of a compound nucleus. A compound nucleus is formed when the target nucleus absorbs the incident particle and forms a compound system in an excited state. The compound nucleus decays from its excited state to the ground state by emitting particles through energetically permissible channels. Because the life time of the compound nucleus (CN) is extremely short ($\sim 10^{-25}$ s), the particles that are emitted from the decay of the compound system are experimentally indistinguishable from those that result from direct-reaction processes involving the incident projectile and the target nucleus. Sometimes the compound nucleus will re-emit the incident particle; in this case the process is called compound elastic scattering or compound inelastic scattering, depending on whether the residual nucleus is left in an excited state. The probability of the compound

nucleus decaying through the entrance channel is largest when few other reaction channels are open. This typically occurs at low bombaring energies, e.g., for neutrons below 10 MeV.

Most experimentally observed scattering data can be considered as being composed of the contributions due to the direct interaction of the incident projectile with the target nucleus (shape scattering) and the contributions due to the formation and decay of a compound nucleus. Because the above contributions are experimentally inseparable, computational methods have been developed to calculate the CN contributions. However, such CN calculations are extremely tedious and usually very time consuming. Therefore, it is convenient to devise a scheme for estimating the magnitude of the CN contributions in order to deside the necessity for performing the rigorous CN calculations. Such a scheme will be outlined below.

Because the CN cross sections have large flucuations due to the nuclear structure of the compound system, irregularities in observed scattering cross sections usually suggest the presence of CN reactions. This is particularly true in light nuclei ($A \leq 40$) where the energy levels are usually spaced far apart. However, smooth structure in the experimentally observed cross sections does not necessarily imply the absence of CN contributions. For instance, in heavy nuclei ($A > 50$), the nucleons have more degrees of freedom causing the energy levels to be closely spaced; consequently, the CN cross sections are averaged over several resonances and therefore show smooth behavior as a function of incident projectile energy. In addition, the resonance structure exhibited in light nuclei averaged over the energy spread ΔE of an

experiment can result in smooth behavior of the observed scattering cross sections at energies where the CN cross sections are significant compared to the shape scattering cross sections. Therefore, it is important to know the nuclear structure of the nuclei being studied and to have a detailed understanding of the energy spread of the experimental apparatus. The proper combination of the above two pieces of information should enable the experimenter to determine the significance of the CN contributions to the observed scattering cross sections.

The above scheme was applied to the present cases of neutron scattering from ^{28}Si and ^{32}S. For each case, the resonance structure in the neutron total cross section around and below 10 MeV suggested that the CN contributions were sizeable at 10 MeV and below. Another indication that the CN contributions were substantial below 10 MeV was the rapid change in the shapes of the elastic scattering angular distributions between 8 and 10 MeV. In addition, in going from 8 to 10 MeV, the large drops in the integrated cross sections for inelastic scattering to the 2^+ state in both nuclei were strongly indicative of the relatively large CN cross sections. To present an example of the types of irregularities that are suggestive of sizable CN contributions, a table of the integrated cross sections for neutron scattering to the 2^+ in ^{28}Si and ^{32}S has been listed below.

E_n (MeV)	$^{28}Si(n,n_1)$ σ(mb)	$^{32}S(n,n_1)$ σ(mb)
8	346	139
10	191	97
12	152	86
14	104	74
17	94	52

For both nuclei, the change in the cross section between 8 and 10 MeV was almost a factor of four larger than the change between any other two adjacent energies. Because of the irregularities displayed in the neutron total cross sections, in the shape of the elastic scattering angular distributions between 8 and 10 MeV, and in the magnitude of the inelastic scattering cross sections, we concluded that it was necessary to account for the CN contributions to the present data.

Once it has been determined that an observed cross section has significant contributions due to the formation of a compound nucleus, it becomes important to calculate the relative amounts of direct-interaction (DI) and compound nucleus cross sections. Because the compound nucleus has many possible exit channels, it would be extremely tedious and also impractical to attempt to calculate the cross section for each exit channel individually. Instead, the problem is handled through a statistical model.

The scattering cross section for an entrance channel α and exit channel β can be written in terms of the unitary collision matrix elements

(Marmier 1971).

$$\sigma_{\alpha\beta} = \frac{\lambda^2}{4\pi} | \delta_{\alpha\beta} - U_{\alpha\beta} |^2 \ . \qquad (7.1)$$

Here the notation of (Marmier 1971) is used. Because of the presence of sharp resonances, $U_{\alpha\beta}(E)$ fluctuates rapidly with energy. Therefore, it is convenient to separate the matrix elements into two parts; an average part $\bar{U}_{\alpha\beta}$ which is constant over a given energy interval and a fluctuating part $\tilde{U}_{\alpha\beta}$ which varies appreciably with energy and averages to zero over a large interval. Therefore, $U_{\alpha\beta}(E)$ may be written as,

$$U_{\alpha\beta} = \bar{U}_{\alpha\beta} + \tilde{U}_{\alpha\beta} \qquad (7.2)$$

with

$$\bar{U}_{\alpha\beta} = \langle U_{\alpha\beta} \rangle = \text{constant}$$

and

$$\tilde{U}_{\alpha\beta} \neq \text{constant but } \langle U_{\alpha\beta} \rangle \equiv 0 \ .$$

The physical interpretation of eqn. (7.2) associates $\bar{U}_{\alpha\beta}$ to the contribution due to direct interaction (DI) and $\tilde{U}_{\alpha\beta}$ to the compound nucleus (CN) contribution. Substitution of eqn. (7.2) into eqn. (7.1) and averaging over a sufficiently large energy interval gives

$$\langle \sigma_{\alpha\beta} \rangle = \frac{\lambda_\alpha^2}{4\pi} | \delta_{\alpha\beta} - \bar{U}_{\alpha\beta} |^2 + \frac{\lambda_\alpha^2}{4\pi} \langle | \tilde{U}_{\alpha\beta} |^2 \rangle \qquad (7.3)$$

$$\simeq \sigma_{\alpha\beta}^{(DI)} + \sigma_{\alpha\beta}^{(CN)}$$

The DI cross section can be calculated using the optical model and the CN is estimated using Hauser-Feshbach theory plus other statistical models.

7.2 A Review of the Hauser-Feshbach Theory of Nuclear Reactions

The assumptions of the Hauser-Feshbach (HF) theory are

1) Flux is conserved; this condition simply requires the collision matrix U to be unitary.

2) The decay of the CN is independent of its mode of formation; this eliminates interference terms in the expressions for the various cross sections. Because this assumption is not completely accurate, the computed cross sections must be multipled by a correction factor to account for interference between states in the compound system.

3) Time-reversal invariance holds.

The expression for the CN cross section in eqn. (7.3) can be rewritten as

$$\sigma_{\alpha\beta}^{CN} = \frac{\lambda_\alpha^2}{4\pi} \langle | \tilde{U}_{\alpha\beta} |^2 \rangle = \sigma_\alpha^{CN} P_\beta \qquad (7.4)$$

where,

σ_α^{CN} = cross section for formation of CN in state α

P_β = probability of CN decaying through channel β .

Since flux is conserved, the probability of formation must equal the sum of the decay probabilities for each exit channel:

$$\sigma_{\alpha}^{CN} = \sum_{\beta} \sigma_{\alpha\beta}^{CN} = \frac{\lambda_{\alpha}^2}{4\pi} \sum_{\beta} \langle |\tilde{U}_{\alpha\beta}|^2 \rangle .$$

By applying the unitary conditions and the condition that $\langle \tilde{U}_{\alpha\beta} \rangle = 0$ when averaged over a sufficient energy range, one finds that

$$\sigma_{\alpha}^{CN} = \frac{\lambda_{\alpha}^2}{4\pi}(1 - \sum_{\beta} |\bar{U}_{\alpha\beta}|^2) . \qquad (7.5)$$

And hence, the cross section for CN formation has been expressed in terms of the DI matrix elements $\bar{U}_{\alpha\beta}$. This implies that σ_{α}^{CN} can be computed using matrix elements that are derived from the optical model. With this in mind, we rewrite eqn. (7.4) in terms of "transmission coefficients"

$$T_{\alpha} \equiv 1 - \sum_{\beta} |\bar{U}_{\alpha\beta}|^2 .$$

Thus,

$$\sigma_{\alpha}^{CN} = \frac{\lambda_{\alpha}^2}{4\pi} T_{\alpha}$$

and eqn. (7.4) can be written as

$$\sigma_{\alpha\beta}^{CN} = \frac{\lambda_{\alpha}^2}{4\pi} T_{\alpha} P_{\beta} . \qquad (7.6)$$

Since the total probability of decay of the CN must be unity, P_{β} can be expressed as a ratio of transmission coefficients

$$P_{\beta} = \frac{T_{\beta}}{\sum_{\gamma} T_{\gamma}}$$

where

$$\sum_{\beta} P_{\beta} = 1 .$$

Substituting this into eqn. (7.6) gives

$$\sigma_{\alpha\beta}^{CN} = \frac{\lambda_\alpha^2}{4\pi} \frac{T_\alpha T_\beta}{\sum_\gamma T_\gamma} . \qquad (7.7)$$

Thus far, the subscripts α, β, and γ have represented the entire quantum description of the incident and exit channels. Rewriting eqn. (7.7) with the appropriate subscripts give

$$\sigma_{\alpha\beta}^{CN} = \frac{\lambda_\alpha^2}{4\pi} \sum_{J j_\alpha \ell_\alpha} \left[\frac{2J+1}{(2I_0+1)(2s_\alpha+1)} \right] \frac{T_{\ell_\alpha j_\alpha}(E_\alpha)\, T_{\ell_\beta j_\beta}(E_\beta)}{\sum_{\ell_\gamma j_\gamma E_\gamma} T_{\ell_\gamma j_\gamma}(E_\gamma)} \qquad (7.8)$$

where

J = spin of CN;

I_0 = spin of target nucleus;

s_α, s_β = spin of incident and exiting particle, respectively;

ℓ_α, ℓ_β = orbital angular momentum of incident and exiting particle, respectively.

If the spin-orbit interaction is neglected, then the transmission coefficients become independent of the spin orientation of the incident and exiting particles. This is because the spin dependence is averaged over all possible j values

$$T_\ell(E) = \sum_{j=\ell-s}^{\ell+s} \frac{2j+1}{(2\ell+1)(2s+1)} T_{\ell j}(E) .$$

Elimination of the spin orientation dependence drastically simplifies eqn. (7.8) to

$$\sigma_{\alpha\beta}^{CN} = \frac{\lambda_\alpha^2}{4\pi} \sum_{\ell_\alpha} (2\ell_\alpha+1) \frac{T_{\ell_\alpha}(E_\alpha) T_{\ell_\beta}(E_\beta)}{\sum_{\ell_\gamma E_\gamma} T_{\ell_\gamma}(E_\gamma)} . \tag{7.9}$$

The derivation of the expression for the differential cross section $\sigma(\theta)$ is very lengthy and therefore will not be performed here. One can refer to (Hodgson 1971) for the derivation of $\sigma(\theta)$:

$$\sigma_{\alpha\beta}(\theta) = \frac{\lambda_\alpha^2}{4\pi} \sum_{J^\pi j_\alpha \ell_\alpha j_\beta \ell_\beta} \frac{2\ell_\alpha+1}{(2I_0+1)(2s_\alpha+1)} \cdot A_J(j_\alpha\ell_\alpha, j_\beta\ell_\beta;\theta) \frac{T^{J^\pi}_{\ell_\alpha j_\alpha} T^{J^\pi}_{\ell_\beta j_\beta}}{\sum_{\ell_\alpha j_\alpha} T^{J^\pi}_{\ell_\alpha j_\alpha}} . \tag{7.10}$$

where the angular information is in the function

$$A_J(j_\alpha\ell_\alpha, j_\beta\ell_\beta;\theta) = \frac{(2\ell_\beta+1)(2J+1)^2}{4\pi} \times \left| \sum_L C^{L\ell_\alpha\ell_\alpha}_{000} C^{L\ell_\beta\ell_\beta}_{000} W(JJ\ell_\alpha\ell_\alpha;Lj_\alpha) \cdot W(JJ\ell_\beta\ell_\beta;Lj_\beta) P_L(\cos(\theta)) \right| .$$

Here L is an even integer with the range given by $0 \leq L \leq \min(2\ell_\alpha, 2\ell_\beta, 2J)$. Since L is even, the angular distributions for the CN cross sections are symmetrical about 90°. The C and W coefficients are the Clebsch Gordon and Racah coefficients, respectively.

7.3 Level Densities

In order to evaluate $\sigma_{\alpha\beta}$, it is sufficient to know only the initial and final spins of the interaction along with the transmission coefficients. The transmission coefficients for the incident channel may be obtained from an optical model calculation for elastic scattering from the target nucleus, and those for the exit channels may be obtained from optical model calculations of elastic scattering of the outgoing particle from the various residual nuclei. However, at high bombarding energies, hundreds of exit channels become available. Because the spin and parity of all the exit channels is not known in most cases, it is impossible to evaluate the sum over the $T_{\ell}^{J^{\pi}}$'s. Even if the spins and parities of all the exit channels were well defined, it would be impractical to sum over each channel separately. It is more efficient to sum over the first few discrete states in each residual nucleus and then use level densities and average $T_{\ell}^{J^{\pi}}$'s for the remainder of the outgoing states:

$$\sum T^{J^{\pi}}_{\ell_a j_a} = \sum_{\ell_a j_a}{}' T^{J^{\pi}}_{\ell_a j_a} + \int_{E_1}^{E_2} T^{J^{\pi}}(E)\ \rho^{J^{\pi}}(E)\ dE\ . \qquad (7.11)$$

The primed summation Σ' indicates that the sum is over only the first few discrete levels in each residual nucleus and $\rho^{J^{\pi}}(E)$ is the density of levels of spin and parity J^{π} in the residual nuclei. As the energy of the incident particle is increased, the second term in the above summation begins to dominate and an accurate description of the level density becomes important.

There are two forms of the level density formula. The constant

temperature formula is used at low excitation energies, i.e., below 10 MeV. It is a straight line on a log plot and is written as

$$\rho(E) = \frac{e^{(E-E_0)/T}}{T} . \qquad (7.12)$$

The slope of the line is 1/T, where T is the nuclear temperature. The intercept is $-(E_0/T + \ln T)$. The Fermi gas formula is used at high excitation energies:

$$\rho(E) = \frac{e^{2[a(E-\Delta)]^{1/2}}}{12(2)^{1/2}\,\sigma\,a^{1/4}\,(E-\Delta)^{5/4}} \qquad (7.13)$$

with

σ = spin cut-off parameter;

a = same as in the Bethe formula (Gilbert and Cameron 1965);

Δ = pairing energy in Fermi gas distribution;

E = excitation energy;

E_0 = pairing energy in the constant temperature formula.

The spin and parity are included by a multiplicative factor

$$\rho^{J^{\pi}}(E) = \frac{\rho(E)(2J+1)}{2\sigma^2}\, e^{-(J+1/2)^2/2\sigma^2} . \qquad (7.14)$$

All level density parameters for the CN cross section calculations for ^{28}Si+n and ^{32}S+n were taken from (Gilbert 1965). Table 7-1 is a listing of the level density parameters used in these calculations. Because the predicted CN cross section for any particular outgoing channel is directly dependent upon the total number of open channels, it is

TABLE 7-1

LEVEL DENSITY PARAMETERS USED IN CN CALCULATIONS

Nucleus	Δ (MeV)	a $(MeV)^{-1}$	σ	E_x (MeV)	E_0 (MeV)	T (MeV)
^{28}Si	3.89	3.05	2.0	12.9	3.20	2.09
^{28}Al	0.00	3.45	2.2	9.6	-0.70	1.50
^{27}Al	1.80	3.45	2.0	9.6	-0.35	2.08
^{25}Mg	2.46	3.85	2.15	12.4	-1.00	2.12
^{29}Si	2.09	3.57	2.1	8.1	0.75	1.91
^{32}S	3.29	3.39	2.0	10.0	1.75	2.05
^{32}P	0.00	3.45	2.2	6.0	-1.75	1.96
^{31}P	1.67	3.87	2.0	7.5	0.40	1.78
^{29}Si	2.09	3.57	2.1	8.1	0.75	1.91
^{33}S	1.62	4.36	2.2	8.0	0.00	1.68

essential that all possible exit channels are properly included in the calculations. Therefore, it is critical that the level density formula accurately describes the level spacings in the outgoing channels. If $\rho(E)$ is too small, then the CN cross sections will be overestimated for all exit channels, and conversely, if $\rho(E)$ is too large, then the CN cross sections will be underestimated. Figure 7.1 shows plots of the number of resonances versus excitation energy for the four predominant particle exit channels in the ^{28}Si+n compound nucleus. The stair steps represent the number of observed levels (Browne 1978) and the lines are plots of the number of states using the constant temperature formula:

$$N(E^*) = e^{(E^*-E_0)/T} \qquad (7.14)$$

where E^* represnets the excitation energy of the residual nucleus. The arrows indicate the excitation energies at which the sums over discete states in eqn. (7.11) were terminated and the integrals using $\rho(E)$ were evaluated.

For the compound systems of ^{28}Si + n and ^{32}S + n, the level density parameters obtained from (Gilbert 1965) consistently underestimated the number of nuclear states in all particle exit channels, as shown in fig. 7.1 for the case of ^{28}Si + n. Therefore, the sum in eqn. (7.11) was extended to high enough energies to ensure that all open channels were properly counted; for the case of ^{28}Si + n, the sums were extended up to the energies indicated by the arrows in fig. 7.1.

In cases where reliable level density parameters are not available, they can be determined using the procedure outlined by Gilbert and Cameron

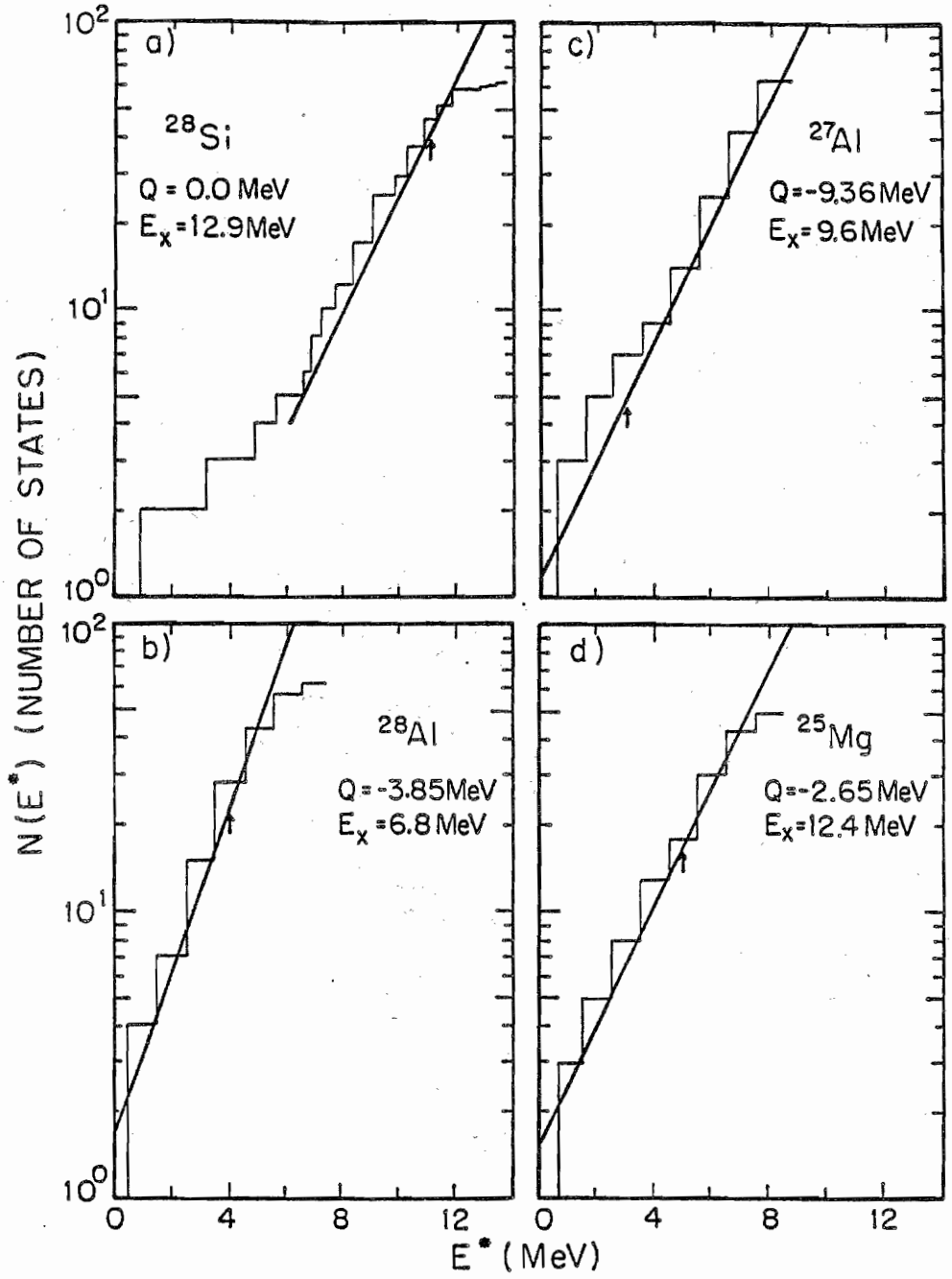

Figure 7.1. Plots of N(E*) versus E^* for the residual nuclei in the ^{28}Si+n compound system. The lines through the stair steps were computed using the constant temperature formula $\rho(E)$.

(Gilbert 1965). A summary of the procedure is presented below.

1) Let $\rho_1(E,E_0,T)$ represent the level density at low excitation energies. This is the constant temperature formula expressed in eqn. (7.12). And let the Fermi gas density formula $\rho_2(E,a,\Delta,\sigma)$ in eqn. (7.13) describe the upper levels.

2) Determine E_0 and T in ρ_1 by comparing eqn. (7.13) to the number of observed levels at low excitation energies. On a log plot, $N(E^*)$ is a line with slope 1/T and intercept $-E_0/T$. Staircase plots as in fig. 7.1 are very useful in determining these parameters. Using such plots, one only needs to draw a line through the steps (coming as close as possible to the center of each step) and compute the slope and intercept of the resultant line. A more elegant method is to use a least square fitting routine. Although a fitting routine is more exact, it is usually not necessary.

3) Determine a, Δ, and σ in the Fermi gas formula. The pairing energy Δ can be found in (Gilbert 1965). This parameter is included to account for even-odd and shell effects. The a parameter is determined by comparing $\rho_2(E=B_n)$ to $1/D_{obs}$, where D_{obs} is the average observed level spacing and B_n is the neutron binding energy. The relation is:

$$\rho_2(E=B_n) = \frac{1}{D_{obs}} .$$

Lastly, the spin cut-off parameter σ is related to the parameter a by

$$\sigma^2 = 0.0888[a(E-\Delta)]^{1/2} A^{2/3}$$

4) The final and most tedious step is to connect ρ_1 to ρ_2. The conditions are that the level densities and their first derivatives must be continuous (meaning that the functions must connect smoothly). That is,

$$\rho_1(E_x) = \rho_2(E_x)$$

and

$$\frac{d}{dE}[\ln\rho_1(E_x)] = \frac{d}{dE}[\ln\rho_2(E_x)] .$$

The densities are connected by making small changes in E_0, T and a,

and therefore slightly compromising the conditions that were previously fulfilled in steps 2 and 3.

7.4 Transmission Coefficients

The particle transmission coefficients were obtained from an optical model analysis of elastic scattering from each residual nucleus. The optical potential included an imaginary well to account for all nonelastic interactions. The Schroedinger equation was solved with the complex potential (V+iW) to obtain the phase shift between incoming and outgoing waves. The T_ℓ's were calculated from the phase shifts according to

$$T_\ell = 1 - |e^{2i(\xi_\ell + i\eta_\ell)}|^2 .$$

The T_ℓ's computed using a spherical optical potential will over estimate the CN contributions when the cross section for inelastic scattering is large. In the case of neutron scattering from ^{28}Si, the 2^+ and 4^+ states are strongly excited. Analysis of the elastic scattering data with a spherical optical model (SOM) will account for the large inelastic cross sections by increasing the absorptive well W. This effect consequently increases the size of the T_ℓ's and thereby overestimates the CN cross sections. In these situations, the T_ℓ's should be computed using coupled-channels (CC) formalism so that the large inelastic cross sections are overtly accounted for through coupling. Plots of the T_ℓ's used in the ^{28}Si+n CN calculation are shown in fig. 7.2. Only the first three even L-values are plotted since they dominate the sum in the calculation of $\sigma^{CN}_{\alpha\beta}(\theta)$. The T_ℓ's for the neutron channel were calculated with the CC code

ECIS79 by Raynal (Raynal 1979). All other T_ℓ's were calculated with the code HAUSER*5 (Mann 1979), which used a SOM without spin-orbit interaction.

7.5 Width Fluctuation Corrections

Thus far it has been assumed that there are no correlations between the initial and final states of the compound nucleus system. This assumption is not completely true, and the effects of the correlations between the formation and decay of the CN can be accounted for with a multiplicative factor. The expressions for $\sigma_{\alpha\beta}$ should be multiplied by a width fluctuation factor $W_{\alpha\beta}$. Thus, all CN cross sections become

$$\sigma_{\alpha\beta} \rightarrow \sigma_{\alpha\beta} W_{\alpha\beta}$$

where

$$W_{\alpha\beta} \sim 1 + 2\delta_{\alpha\beta}/\gamma_\beta \ .$$

The number of degrees of freedom γ_β varies from 1 to 2 (Gruppelaar 1976). So the effect of $W_{\alpha\beta}$ is to enhance the elastic CN cross section and to leave the reaction channels essentially unchanged.

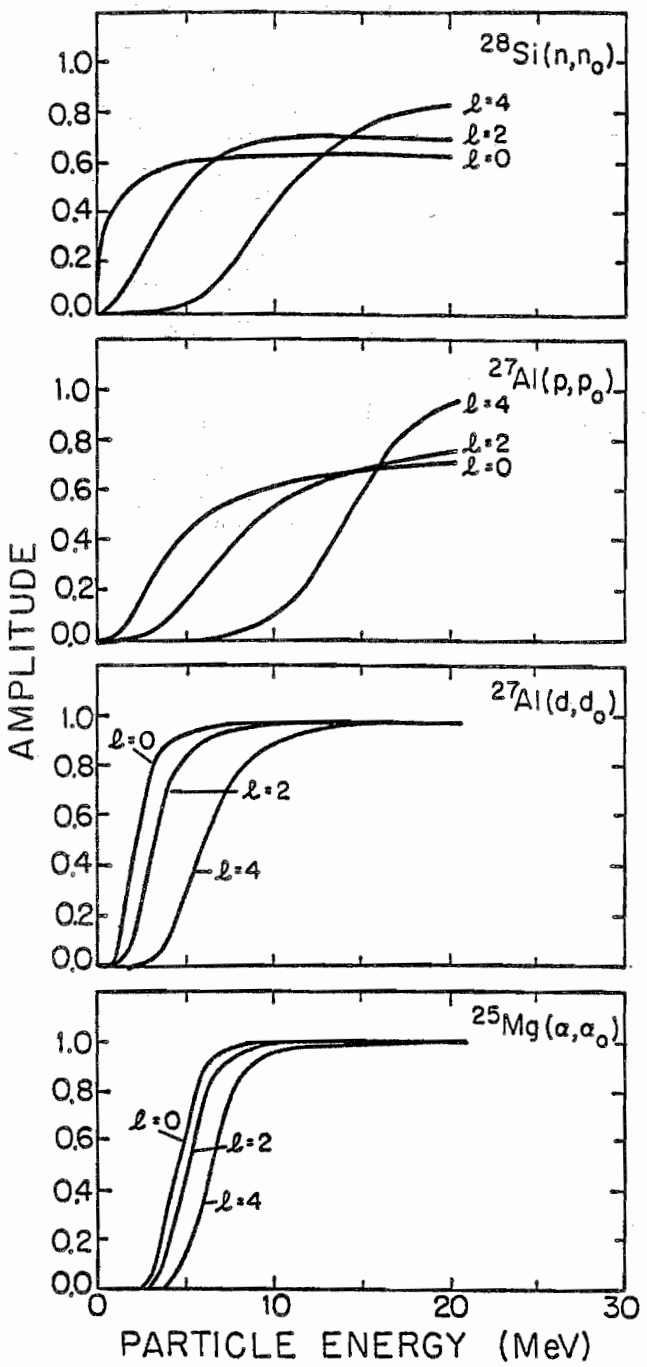

Figure 7.2. Particle transmission coefficients T_ℓ's for predominant particle exit channels in $^{28}Si+n$ compound system.

7.6 CN Calculations for $^{28}Si+n$ and $^{32}S+n$

All CN calculations were performed with the computer code HAUSER*5. The code was developed by the Nuclear Analysis group at the Hanford Engineering Development Laboratory (HEDL) (Mann 1979). It had the capability of predicting total nuclear cross sections for bombarding energies up to 60 MeV. The code was based on three models of nuclear reactions; the statistical model (Hauser-Feshbach), the pre-equilibrium model, and the statistical model for direct reactions.

The present calculations included four particle channels plus the γ-ray channel. The decay schemes were as follows:

Reaction	Q(MeV)
$^{28}Si + n \rightarrow {}^{29}Si \rightarrow {}^{28}Si + n$	0.00
$\rightarrow {}^{28}Al + p$	-3.85
$\rightarrow {}^{27}Al + d$	-9.36
$\rightarrow {}^{25}Mg + \alpha$	-2.65
$\rightarrow {}^{29}Si + \gamma$	8.48

and similarly,

$^{32}S + n \rightarrow {}^{33}S \rightarrow {}^{32}S + n$	0.00
$\rightarrow {}^{32}P + p$	-1.04

$\rightarrow {}^{31}P + d$ -6.64

$\rightarrow {}^{29}Si + \alpha$ 1.53

$\rightarrow {}^{33}S + \gamma$ 8.07

Although the γ-ray cross sections were negligible, they were included for completeness. Two-particle exit channels such as (n,2n), (n,pn) and (n,αn) were neglected because of their large negative Q-values and low cross sections at incident energies below 15 MeV, where the CN contributions are most significant in the elastic and low lying excited states.

The particle T_ℓ's were calculated using the optical model parameters that resulted from the analyses of elastic scattering data. The optical model parameters used in these calculations for the various exit channels are listed in table 7-2. Plots of the T_ℓ's are shown in fig. 7.2. The T_ℓ's for the neutron channel in ^{28}Si were computed with the coupled-channels code ECIS79 to explicitly account for the large inelastic cross sections through coupling. The SOM was adequate for computing the T_ℓ's in the ^{32}S+n calculation.

The predicted total reaction cross sections for ^{28}Si+n and ^{32}S+n are in good agreement with the experimental results. Figure 7.3 is a plot of the $^{28}Si(n,p)$ and $^{28}Si(n,\alpha)$ cross sections for the sum of the ground state and lower three excited states in ^{28}Al and ^{25}Mg. The curves through the data are our predictions using the code HAUSER*5. The (n,α) predictions are consistently lower than the measured cross sections between 7 and 10 MeV, while the (n,p) cross sections are in good agreement with the

TABLE 7-2

OPTICAL-MODEL PARAMETERS USED IN CN CALCULATIONS

Reaction	V_{OR} (MeV)	r_R (fm)	a_R (fm)	α_R	W_{os} (MeV)	W_v (MeV)	r_I (fm)	a_I (fm)	α_s	α_v	V_{so} (MeV)	r_{so} (fm)	a_{so} (fm)	Reference
$^{28}Si(n,n_0)$	53.9	1.17	0.62	-0.28	3.93	0.00	1.28	0.58	0.10	0.00	5.70	1.01	0.50	[1]
$^{27}Al(p,p_0)$	55.9	1.25	0.65	-0.55	1.38	3.00	1.25	0.47	0.21	0.00	7.50	1.25	0.65	Perey 1963a
$^{27}Al(d,d_0)$	89.7	1.15	0.81	-0.22	14.40	0.00	1.34	0.68	0.00	0.00				Perey 1963b
$^{24}Mg(\alpha,\alpha_0)$	100.0	1.47	0.58	0.00	0.00	27.60	1.60	0.47	0.00	0.00				Duhm 1968
$^{32}S(n,n_0)$	53.5	1.18	0.70	-0.27	9.73	0.00	1.26	0.53	-0.10	0.00	6.31	1.01	0.50	[2]
$^{32}P(p,p_0)$	56.9	1.25	0.65	-0.55	4.38	0.00	1.25	0.47	0.21	0.00	7.50	1.25	0.65	Perey 1963a
$^{31}P(d,d_0)$	44.6	1.15	0.87	-0.51	22.70	0.00	1.37	0.70	0.00					Perey 1963b
$^{29}Si(\alpha,\alpha_0)$	100.0	1.47	0.58	0.00	0.00	27.60	1.60	0.47	0.00	0.00				Duhm 1968

[1] These parameters were taken from preliminary CC calculations; $\beta_2 = -0.36$ and $\beta_4 = 0.20$ with $\delta_{so} = 1.4\delta_c$.

[2] These parameters were taken from preliminary SOM calculations.

Potentials

$V_R = V_{OR} + \alpha_R E$

$W_s = W_{os} + \alpha_s E$

$W_v = W_{ov} + \alpha_v E$

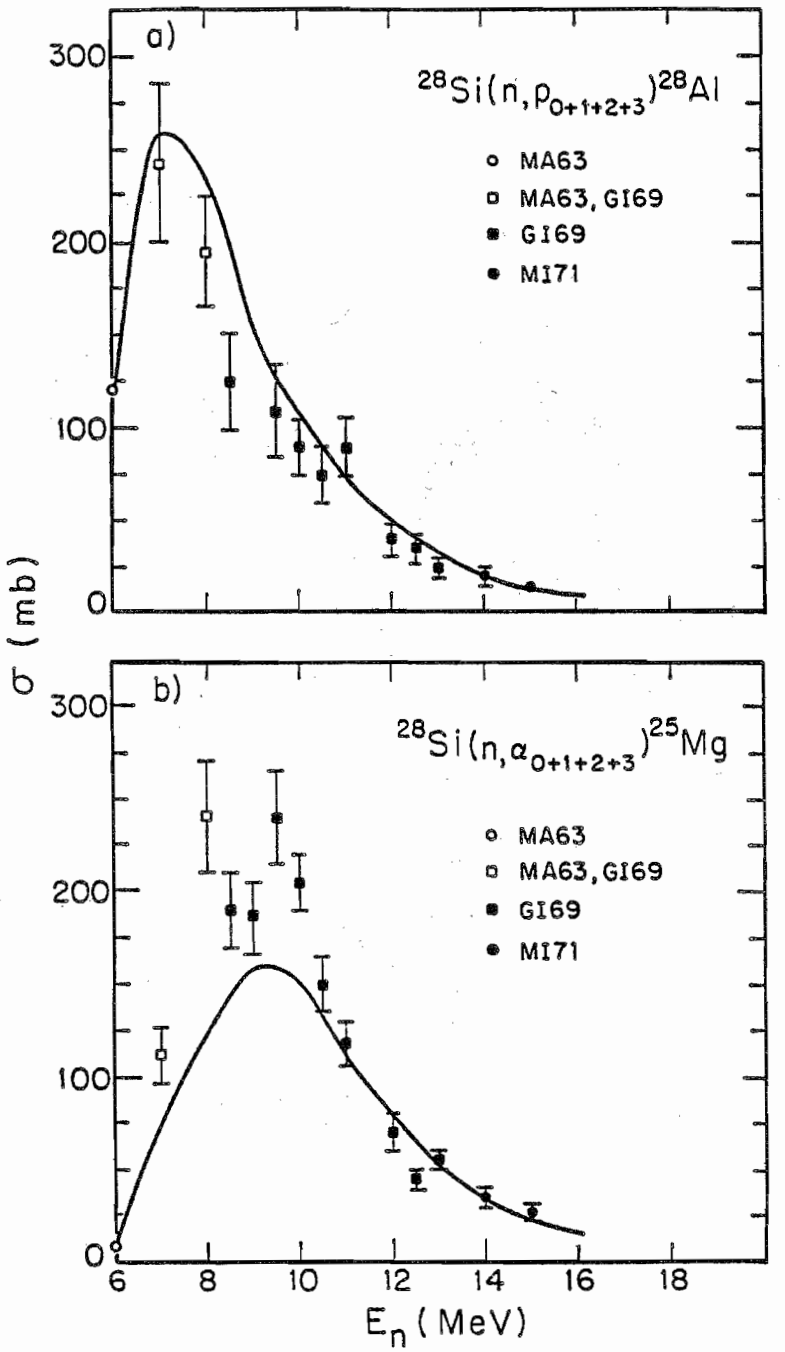

Figure 7.3. Plots of the $^{28}Si(n,p)$ and $^{28}Si(n,\alpha)$ cross sections. The curves through the data are predictions based on the present CN calculations.

experimentally observed values. In order to compensate for this discrepancy and simultaneously conserve flux, cross section was taken from the neutron channels and put into the α-particle channels. Data for the (n,d) reaction are not shown because of its small effect on the CN calculations. A transfer of flux from one channel to another was not necessary in the ^{32}S+n calculations.

7.7 Corrections to Optical Model Calculations for CN

Because the CN cross sections were computed external to our SOM and CC codes, the data sets had to be adjusted for CN effects before being fitted. After the OM parameters had been adjusted for optimum descriptions of the data, the experimentally observed data were plotted along with the sum of the DI calculations and the CN cross sections. The theoretical values for the observed differential cross sections were assumed to be the incoherent sum of the DI and CN cross sections,

$$\sigma^{obs}(\theta) = \sigma^{DI}(\theta) + \sigma^{CN}(\theta) \ .$$

Since the compound nucleus forgets the spin orientation of the incident particle, $A_y^{CN} \equiv 0$. Thus, the theoretical values for the observed analyzing powers were computed as

$$A_y^{obs}(\theta) = \left[1 - \frac{\sigma^{CN}(\theta)}{\sigma^{obs}(\theta)}\right] A_y(\theta)^{DI}.$$

The CN cross sections for the ground state and first excited states of silicon and sulfur were large at 8 MeV and decreased rapidly with energy.

At 14 MeV the size of the CN corrections for the ground states and 2^+ states in ^{28}Si and ^{32}S were smaller than the uncertainty in our CN calculations. For this reason, the corrections were not applied to these states for incident neutron energies above 14 MeV. However, since it is sometimes easier to excite high spin states by the formation of a compound nucleus, it was necessary to account for the CN cross sections for scattering to the high spin states at incident energies up to 17 MeV. Figures 7.4 and 7.5 illustrate the relative amounts of CN cross section at E_n = 10 and 15 MeV for neutron scattering to the 0^+, 2^+, and 4^+ states in ^{28}Si. Notice at 15 MeV that the CN contributions to the 0^+ and 2^+ states were very small, while the contribution to the 4^+ state was still significant in comparison to the DI cross section. Figure 7.6 illustrates the CN contributions to the ^{32}S + n scattering cross sections at 10 MeV. As in the case of ^{28}Si, the inelastic scattering cross sections for ^{32}S at 10 MeV were dominated by CN contributions; the CN cross sections decreased rapidly with increasing incident neutron energy and were negligible above 17 MeV.

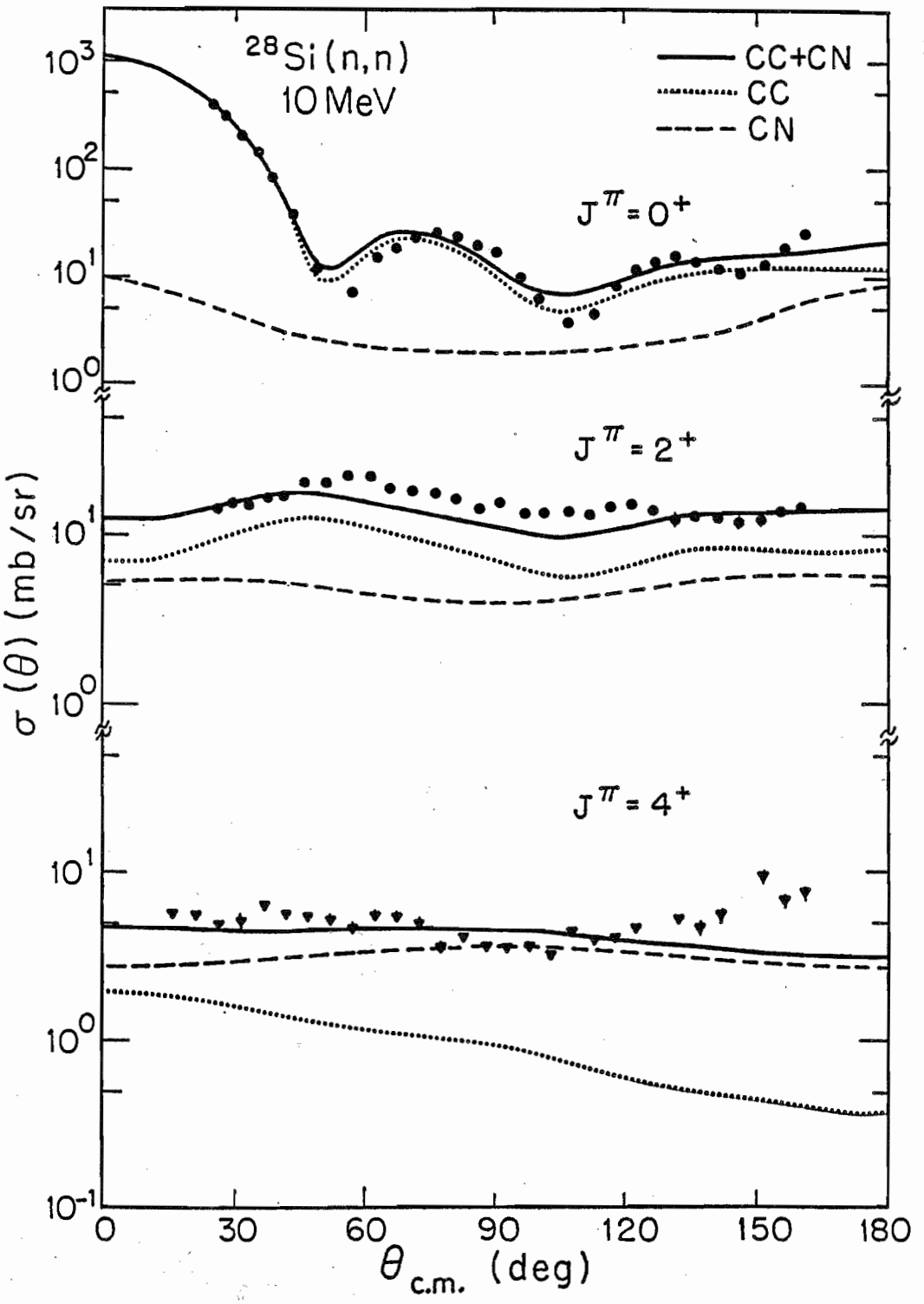

Figure 7.4. Plots of $\sigma(\theta)$ at 10 MeV for elastic and inelastic scattering of neutrons from ^{28}Si. The dotted curves through the data are CC calculations (DI) from chapter 9, the dashed curves represent the CN contributions, and the solid curves are the sum of the CC calculations and CN contributions.

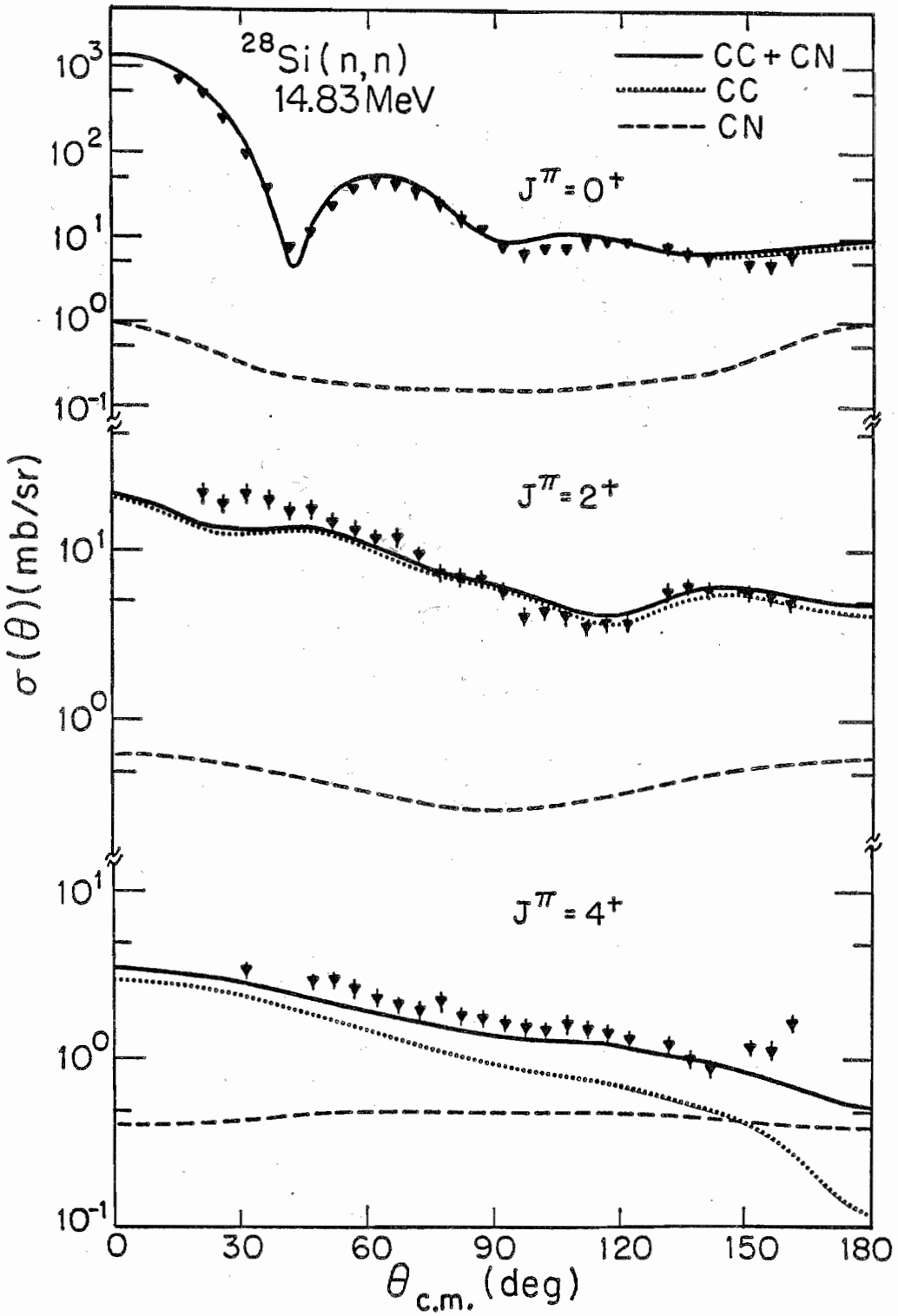

Figure 7.5. Plots of σ(θ) at 14.8 MeV for elastic and inelastic scattering of neutrons from ^{28}Si. The dotted curves through the data are CC calculations (DI) from chapter 9, the dashed curves represent the CN contributions, and the solid curves are the sum of the CC calculations and CN contributions.

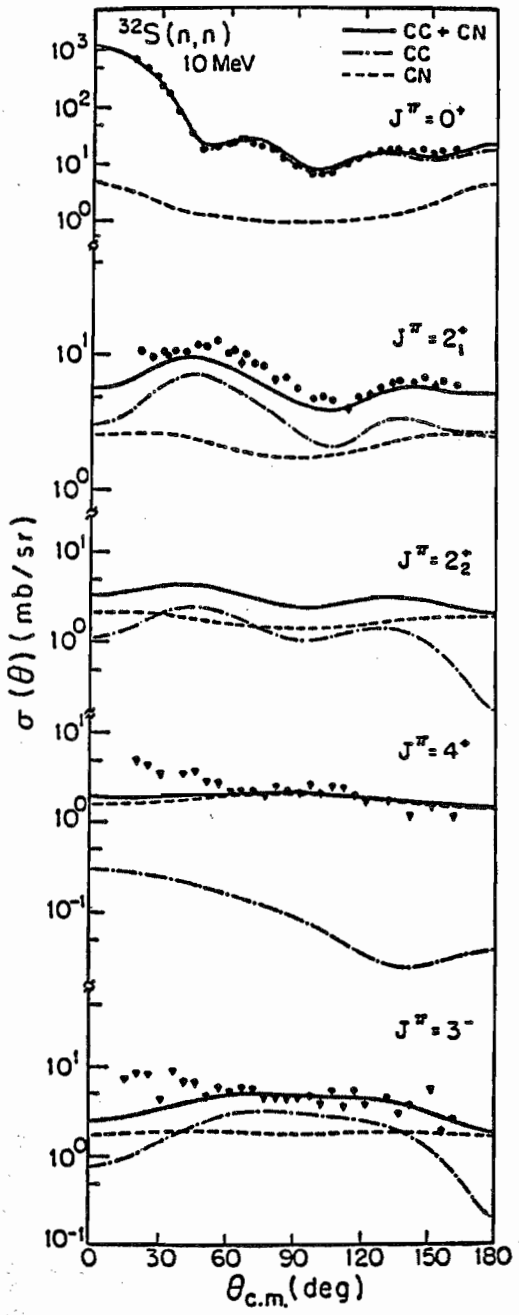

Figure 7.6. Plots of $\sigma(\theta)$ at 10 MeV for elastic and inelastic scattering of neutrons from ^{32}S. The dot-dashed curves through the data are CC calculations (DI) from chapter 9, the dashed curves represent the CN contributions, and the solid curves are the sum of the CC calculations and CN contributions.

CHAPTER 8

SPHERICAL OPTICAL MODEL

8.1 Introduction

The spherical optical model (SOM) has proven to be an extremely useful device for the systematic study of elastic neutron scattering data. Both cross section and polarization observables for elastic neutron scattering from a wide range of nuclei can be accurately described with this model. The model works best for medium and heavy nuclei ($A > 40$) and especially well on nuclei with closed neutron and/or proton shells. It can be used to describe elastic scattering data at a single incident energy over a wide range of atomic masses to deduce mass dependent features of the scattering observables. It can also be used to determine energy dependent properties of scattering observables by describing data for scattering from a single nucleus over a large energy range. The combination of describing neutron scattering data from a number of nuclei over a broad energy range paints an intriguing picture of the behavior of neutron-nucleus scattering. An analysis of this type is referred to as a global SOM. Comparisons of global optical model (OM) predictions to experimental data are useful in determining nuclei and energies that deviate from the trend of the OM. The influences of resonances and shell effects become apparent in such comparisons. The SOM can also be used to generate initial OM parameters to be employed in more complex calculations such as DWBA, coupled-channels (CC) calculations, and

compound nucleus (CN) calculations. Because of the SOM's simplicity and ability to accurately predict scattering observables in regions where data are not available or readily accessible, it has become an extremely useful tool in nuclear applications and in the planning of neutron scattering experiments. Of a more fundamental nature, the parameters and form factors of the SOM provide a common ground for theoretical comparison of the nucleon-nucleus interaction.

There are three primary objectives of the present SOM analysis. First, it is to form a basis for determining the feasibility of describing the available data for neutron scattering from silicon and sulfur with phenomenological CC calculations using an optical model potential (OMP). Because CC calculations are usually very tedious and time consuming, it is important that the data sets included in such an analysis are accurate and consistent with each other. The computer time required for a thorough CC analysis can sometimes be doubled by the inclusion of "bad" data, data that is experimentally incorrect and/or data that does not follow the trend of the OM due to resonance structure, shell effects, or non-direct processes such as CN formation. Furthermore, the inclusion of bad data can distort the resultant parameters, and therefore lead to erroneous conclusions. The second objective of the SOM analysis is to provide OM parameters that can be used in the initial CN calculations and as the starting parameters in the CC calculations. The third objective is to provide a consistent set of OM parameters that can be used in systematic studies which compare OM parameters for a wide range of nuclei.

The SOM is an ideal tool for evaluating data sets that are to be used in CC analyses. It is a single channel calculation, and therefore it

requires little computer time per computation. By describing the data with a SOM which has constant geometry parameters over the entire energy range of the available data and which incorporates smooth energy dependences, bad data becomes apparent. This method of identifying bad data is simply a restatement of the requirement that the data must vary smoothly with energy in order to be described with an OM. The above condition is especially important for neutron scattering data because of the known difficulties associated with the absolute normalization and the corrections applied to account for finite geometry effects.

To reduce the ambiguities in the OM parameters, the analysis was extended over a wide energy range by including data from several references. High quality neutron scattering data from recent publications (published after 1978) were collected and collated to form complete data sets for the present analyses. These data sets are the most complete collections of differential cross sections and analyzing powers for neutron scattering from ^{28}Si and ^{32}S in existence. Each data set spans an energy range from 8 to 40 MeV and consists of 22 cross section angular distributions and 6 analyzing power angular distributions. Differential cross sections $\sigma(\theta)$ at incident neutron energies of 8, 10, 12, 14, and 17 MeV were measured at TUNL and have been described in chapter 5. Cross sections at 9.8 and 14.8 MeV were obtained from (BLC 1982). The data at 11, 20, and 26 MeV were measured at Ohio University and were reported in (Tailor 1982). Differential cross sections for elastic scattering at 30 and 40 MeV were obtained from (Devito 1983). All analyzing power $A_y(\theta)$ data were measured at TUNL and have been described in chapter 5. Total cross sections were taken from ENDF/B-5 for neutron energies below 20 MeV

and from (Larson 1980) for the higher energies.

Although both nuclei are known to have large deformations from a spherical shape, the success of describing these data with a SOM was very good. As will be shown below, these data were described at incident neutron energies ranging from 8 to 40 MeV with constant geometries and linear energy dependencies on the well depths. The inclusion of the $A_y(\theta)$ data in these analyses made it possible to determine the spin-orbit parameterizations for both nuclei. A complex optical potential with Wood-Saxon form factors was used. The imaginary part of the potential consisted of both surface and volume absorption terms. The potential was defined as the sum of the following parts:

REAL

$$U(r,r_R,a_R) = -V_R f(r,r_R,a_R)$$

IMAGINARY

$$W(r,r_I,a_I) = -W_v f(r,r_I,a_I) - 4a_I W_D \frac{d}{dr} f(r,r_I,a_I)$$

SPIN-ORBIT INTERACTION

$$V_{so}(r,r_{so},a_{so}) = \vec{\sigma}\cdot\vec{l}\left[\frac{\hbar}{2m_\pi c}\right]^2 \frac{V_{so}}{r}\frac{d}{dr} f(r,r_{so},a_{so}) \ .$$

In these expressions, the function $f(r,r_0,a_0)$ is the usual Wood-Saxon form factor

$$f(r,r_0,a_0) = \left[1 + e^{(r-r_0A^{1/3})/a_0}\right]^{-1} \ .$$

Because only neutron scattering data were considered, no Coulomb potential was necessary. The expression for V_{so} represents the conventional Thomas form of the spin-orbit interaction. After some tests were made, it was concluded that the description of the $A_y(\theta)$ data did not require the inclusion of an imaginary spin-orbit term. A modified version of the SOM code GENOA which included a correction term for the Mott-Schwinger interaction (Floyd 1982) was used to solve the Schroedinger equation for the above optical potential.

This analysis provided OM parameters that were used in the initial CN calculations (the final CN calculations were made with the OM parameters of preliminary CC calculations) and as the starting parameters in the present CC calculations. In addition, the SOM was used to determine the energy dependencies of the volume absorption strength W_v and of the imaginary spin-orbit strength W_{so} prior to the CC calculations. It was found for both silicon and sulfur that the data could be described equally well with or without the inclusion of an imaginary spin-orbit term. Many calculations were necessary to determine the behavior of W_v and W_{so}. If the CC code had been used to determine the characteristics of these parameters, then it would have taken approximately ten times more computer time to reach very similar conclusions.

8.2 Best Fits

The SOM calculations were performed with the code GENOA which has the capability to search on several parameters simultaneously. At each energy, the code varied specified parameters to minimize the quantity

$$\frac{\chi^2}{N} = \frac{1}{N_s}\sum_{i=1}^{N_s}\left[\frac{\sigma^{th}(\theta_i) - \sigma^{exp}(\theta_i)}{\Delta\sigma^{exp}(\theta_i)}\right]^2 + \frac{1}{N_p}\sum_{i=1}^{N_p}\left[\frac{A_y^{th}(\theta_i) - A_y^{exp}(\theta_i)}{\Delta A_y^{exp}(\theta_i)}\right]^2$$

where N_s and N_p are the number of cross section and analyzing power points, respectively. The above expression is referred to as the chi-square-per-point of the fits and represents a direct comparison of the theoretical calculations to the experimentally observed data.

All parameters were varied to obtain "best" fits at each energy. The starting parameters were those of Böttcher *et al.* (Böttcher 1983) for silicon and those of Rapaport *et al.* (Rapaport 1977) for sulfur. In order to define the spin-orbit parameters early in the analysis, the energies at which both cross section and analyzing power data were available were considered first. The "mean" spin-orbit parameters were computed by averaging the parameters that resulted from fitting the data at 10, 14, and 17 MeV. The parameters resulting from fitting the 14 MeV data were given the most weight in this average.

The best fits were acquired in an iterative fashion. First, the potential well strengths were searched upon to minimize chi square. In these searches, the W_v was set to zero at incident energies below 20 MeV, and the W_{so} was set to zero at all energies. At energies where no $A_y(\theta)$ data were available, the mean spin-orbit parameters were used. Second,

the geometrical parameters were searched upon. Third, both potential strengths and geometrical parameters were searched upon simultaneously. In all searches the notorious $V_R r_R$, $W_v r_I$, and $W_D a_I$ ambiguities were avoided. The rigid constraints that $r_I \geq r_R > r_{so}$ and $a_R \geq a_I > a_{so}$ imposed by Van Oers et al. (Van Oers 1974) were also implemented in this analysis. In addition, all radius and diffuseness parameters were required to be greater than 1.0 fm and 0.5 fm, respectively. These last requirements were implemented because the $A_y(\theta)$ data consistently favored $r_{so} < 1.0$ fm and $a_{so} < 0.5$ fm. The resultant parameters for the best fits are listed as set-A in tables 8-1 and 8-2. The corresponding fits are represented by the dashed curves in figures 8.1 through 8.4. Compound nucleus contributions were added to both $\sigma(\theta)$ and $A_y(\theta)$ calculations for energies below 14 MeV.

8.3 Fits with Constant Geometry

In the next step of the analysis, all geometrical parameters of the central well were fixed to the average of the values resulting from the best fits at energies above 10 MeV. The spin-orbit parameters were taken as the average of the best-fit parameters, with the least weight given to the 10 MeV data. Then, at each energy, the fits were optimized by searching on V_R and W_D. Because of the ambiguities between W_D and W_v, W_v was eventually fixed to the value taken from the line shown in figures 8.5 or 8.6; these lines were determined from prior searches on V_R, W_D, and W_v at energies above 17 MeV.

The parameters resulting from the searches on V_R and W_D are listed as set-B in tables 8-1 and 8-2, and the corresponding fits are shown as the

TABLE 8-1

SPHERICAL-OPTICAL-MODEL PARAMETERS FOR ^{28}Si+n

	E_n (MeV)	V_R [a] (MeV)	r_R (fm)	a_R (fm)	W_D [a] (MeV)	W_V (MeV)	r_I (fm)	a_I (fm)	V_{so} [d] (MeV)	J_V/A (MeV·fm^3)	J_W/A (MeV·fm^3)	χ^2/N_σ	χ^2/N_A
Set-A	8.0	52.5 ± 0.7	1.13	0.759	6.8 ± 1.1	0.0 [b]	1.13	0.56	6.60 [b]	470 ± 7	87 ± 14	24.0	
	10.0	53.6 ± 0.5	1.16	0.699	9.4 ± 0.5	0.0 [b]	1.16	0.56	7.02	486 ± 5	127 ± 7	10.2	25.8
	11.0	50.4 ± 0.5	1.18	0.739	10.6 ± 0.5	0.0 [b]	1.18	0.54	6.60 [b]	492 ± 5	141 ± 7	8.7	
	12.0	50.9 ± 0.7	1.16	0.666	8.4 ± 0.3	0.0 [b]	1.29	0.56	6.60 [b]	450 ± 6	139 ± 5	19.5	
	14.0	49.3 ± 0.5	1.15	0.659	7.2 ± 0.1	0.0 [b]	1.32	0.58	5.85	425 ± 4	129 ± 2	8.2	9.8
	14.8	48.3 ± 1.0	1.15	0.625	7.6 ± 0.3	0.0 [b]	1.32	0.58	6.60 [b]	405 ± 6	136 ± 5	2.7	
	17.0	48.6 ± 0.5	1.16	0.670	7.0 ± 0.1	0.0 [b]	1.31	0.57	4.99	431 ± 4	121 ± 2	21.7	12.2
	20.0	46.6 ± 0.8	1.18	0.600	6.4 ± 0.2	1.0 [b]	1.30	0.57	6.60 [b]	406 ± 7	121 ± 5	3.2	
	26.0	45.3 ± 0.5	1.16	0.664	6.8 ± 0.2	1.9 [b]	1.31	0.58	6.60 [b]	400 ± 4	141 ± 5	2.1	
	30.3	44.5 ± 1.0	1.17	0.631	6.2 ± 0.4	2.6 [b]	1.31	0.58	6.60 [b]	391 ± 9	138 ± 10	8.3	
	40.0	41.9 ± 0.7	1.16	0.694	4.8 ± 0.2	4.0 [b]	1.30	0.58	6.60 [b]	379 ± 6	128 ± 6	4.4	

TABLE 8-1 Continued

	E_n (MeV)	V_R[a] (MeV)	r_R (fm)	a_R (fm)	W_D[a] (MeV)	W_v (MeV)	r_I (fm)	a_I (fm)	V_{so}[d] (MeV)	J_v/A (MeV·fm^3)	J_w/A (MeV·fm^3)	χ^2/N_σ	χ^2/N_A
Set-B	8.0	51.5 ± 0.7	1.16[b]	0.689[b]	7.5 ± 1.2	0.0[b]	1.31[b]	0.574[b]	6.60[b]	464 ± 7	129 ± 21	46.3	
	10.0	51.0 ± 0.5	1.16[b]	0.689[b]	7.6 ± 0.4	0.0[b]	1.31[b]	0.574[b]	6.60[b]	459 ± 5	132 ± 7	45.0	23.3
	11.0	50.5 ± 0.5	1.16[b]	0.689[b]	7.7 ± 0.4	0.0[b]	1.31[b]	0.574[b]	6.60[b]	455 ± 5	134 ± 7	61.1	
	12.0	50.5 ± 0.7	1.16[b]	0.689[b]	7.8 ± 0.3	0.0[b]	1.31[b]	0.574[b]	6.60[b]	455 ± 6	136 ± 5	27.3	
	14.0	49.2 ± 0.5	1.16[b]	0.689[b]	7.6 ± 0.1	0.1[c]	1.31[b]	0.574[b]	6.60[b]	442 ± 4	133 ± 2	9.2	11.4
	14.8	49.5 ± 0.1	1.16[b]	0.689[b]	7.6 ± 0.3	0.3[c]	1.31[b]	0.574[b]	6.60[b]	446 ± 9	133 ± 5	3.0	
	17.0	49.0 ± 0.5	1.16[b]	0.689[b]	7.0 ± 0.1	0.6[c]	1.31[b]	0.574[b]	6.60[b]	441 ± 4	128 ± 2	37.7	11.3
	20.0	47.8 ± 0.9	1.16[b]	0.689[b]	7.0 ± 0.3	1.0[c]	1.31[b]	0.574[b]	6.60[b]	431 ± 8	133 ± 5	4.6	
	26.0	45.5 ± 0.5	1.16[b]	0.589[b]	6.4 ± 0.2	1.9[c]	1.31[b]	0.574[b]	6.60[b]	410 ± 4	133 ± 4	4.5	
	30.3	44.5 ± 1.0	1.16[b]	0.589[b]	6.0 ± 0.4	2.6[c]	1.31[b]	0.574[b]	6.60[b]	401 ± 9	133 ± 9	10.7	
	40.0	41.5 ± 0.7	1.16[b]	0.589[b]	5.0 ± 0.2	4.0[c]	1.31[b]	0.574[b]	6.60[b]	374 ± 6	132 ± 6	6.7	

a) The uncertainties in the potential-strength parameters were computed by searching on the strengths with the geometrical parameters fixed to the values listd in the above table.

b) These parameters were held constant in search.

c) In set-B, the values of W_v were taken from the line $W_v = -2.0 + 0.15E_n$ for $E_n > 13.3$ MeV.

d) The values of r_{so} and a_{so} were fixed to 1.01 fm and 0.50 fm, respectively (see text for details).

TABLE 8-2

SPHERICAL-OPTICAL-MODEL PARAMETERS FOR $^{32}S+n$

	E_n (MeV)	V_R [a] (MeV)	r_R (fm)	a_R (fm)	W_D [a] (MeV)	W_v (MeV)	r_I (fm)	a_I (fm)	V_{so} [d] (MeV)	J_v/A (MeV·fm^3)	J_w/A (MeV·fm^3)	χ^2/N_σ	χ^2/N_A
Set-A	8.0	54.6 ± 0.8	1.154	0.695	8.0 ± 1.3	0.00 [b]	1.20	0.516	6.31 [b]	476 ± 7	100 ± 16	21.9	
	10.0	50.7 ± 0.5	1.174	0.762	9.7 ± 0.5	0.00 [b]	1.30	0.513	6.16	485 ± 5	139 ± 8	10.0	17.0
	11.0	50.5 ± 0.5	1.180	0.702	9.4 ± 0.5	0.00 [b]	1.32	0.520	6.31 [b]	468 ± 5	141 ± 7	2.0	
	12.0	50.5 ± 0.7	1.180	0.729	9.1 ± 0.1	0.00 [b]	1.26	0.520	6.31 [b]	477 ± 7	125 ± 5	6.2	
	14.0	49.4 ± 0.5	1.180	0.659	8.4 ± 0.2	0.00 [b]	1.29	0.520	6.02	443 ± 4	121 ± 2	5.3	9.4
	14.8	49.8 ± 1.0	1.184	0.710	9.6 ± 0.4	0.00 [b]	1.26	0.525	6.31 [b]	468 ± 9	134 ± 5	2.4	
	17.0	47.3 ± 0.5	1.186	0.714	7.9 ± 0.1	0.00 [b]	1.30	0.527	4.72	448 ± 5	118 ± 2	4.9	5.8
	20.0	48.3 ± 0.9	1.186	0.730	9.4 ± 0.4	0.75 [b]	1.19	0.527	6.31 [b]	463 ± 8	125 ± 5	1.3	
	26.0	46.0 ± 0.5	1.186	0.681	7.5 ± 0.3	2.00 [b]	1.24	0.527	6.31 [b]	425 ± 4	120 ± 4	3.4	
	30.3	44.9 ± 1.0	1.186	0.740	7.3 ± 0.5	2.20 [b]	1.27	0.527	6.31 [b]	433 ± 10	126 ± 9	16.7	
	40.0	42.8 ± 0.7	1.186	0.686	6.2 ± 0.3	3.80 [b]	1.27	0.527	6.31 [b]	397 ± 7	126 ± 6	4.2	

TABLE 8-2 Continued

	E_n (MeV)	V_R[a] (MeV)	r_R (fm)	a_R (fm)	W_D[a] (MeV)	W_v (MeV)	r_I (fm)	a_I (fm)	V_{so}[d] (MeV)	J_v/A (MeV·fm^3)	J_w/A (MeV·fm^3)	χ^2/N_σ	χ^2/N_A
Set-B	8.0	52.3 ± 0.7	1.184[b]	0.703[b]	8.1 ± 1.3	0.00[b]	1.26[b]	0.525[b]	6.31[b]	489 ± 7	113 ± 18	35.3	
	10.0	50.7 ± 0.5	1.184[b]	0.703[b]	8.3 ± 0.5	0.00[b]	1.26[b]	0.525[b]	6.31[b]	474 ± 5	116 ± 6	19.7	25.5
	11.0	51.1 ± 0.5	1.184[b]	0.703[b]	8.4 ± 0.4	0.00[b]	1.26[b]	0.525[b]	6.31[b]	477 ± 5	117 ± 6	17.6	
	12.0	50.1 ± 0.7	1.184[b]	0.703[b]	8.5 ± 0.3	0.00[b]	1.26[b]	0.525[b]	6.31[b]	468 ± 7	118 ± 4	9.6	
	14.0	49.5 ± 0.5	1.184[b]	0.703[b]	8.5 ± 0.2	0.25[c]	1.26[b]	0.525[b]	6.31[b]	463 ± 5	120 ± 2	5.2	11.1
	14.8	49.0 ± 1.0	1.184[b]	0.703[b]	8.3 ± 0.3	0.40[c]	1.26[b]	0.525[b]	6.31[b]	458 ± 9	119 ± 5	1.8	
	17.0	48.8 ± 0.5	1.184[b]	0.703[b]	8.1 ± 0.2	0.75[c]	1.26[b]	0.525[b]	6.31[b]	456 ± 5	120 ± 2	12.2	5.8
	20.0	47.6 ± 0.9	1.184[b]	0.703[b]	7.8 ± 0.3	1.25[c]	1.26[b]	0.525[b]	6.31[b]	445 ± 8	121 ± 5	1.5	
	26.0	46.2 ± 0.5	1.184[b]	0.703[b]	7.3 ± 0.2	2.25[c]	1.26[b]	0.525[b]	6.31[b]	432 ± 4	124 ± 4	3.5	
	30.3	44.7 ± 1.0	1.184[b]	0.703[b]	6.8 ± 0.5	3.00[c]	1.26[b]	0.525[b]	6.31[b]	418 ± 9	124 ± 9	20.1	
	40.0	43.0 ± 0.7	1.184[b]	0.703[b]	6.0 ± 0.3	4.60[c]	1.26[b]	0.525[b]	6.31[b]	402 ± 7	128 ± 6	4.3	

a) The uncertainties in the potential-strength parameters were computed by searching on the strengths with the geometrical parameters fixed to the values listd in the above table.

b) These parameters were held constant in search.

c) In set-B, the values of W_v were taken from the line $W_v = -2.09 + 0.17E_n$ for $E_n > 12.5$ MeV.

d) The values of r_{so} and a_{so} were fixed to 1.01 fm and 0.50 fm, respectively (see text for details).

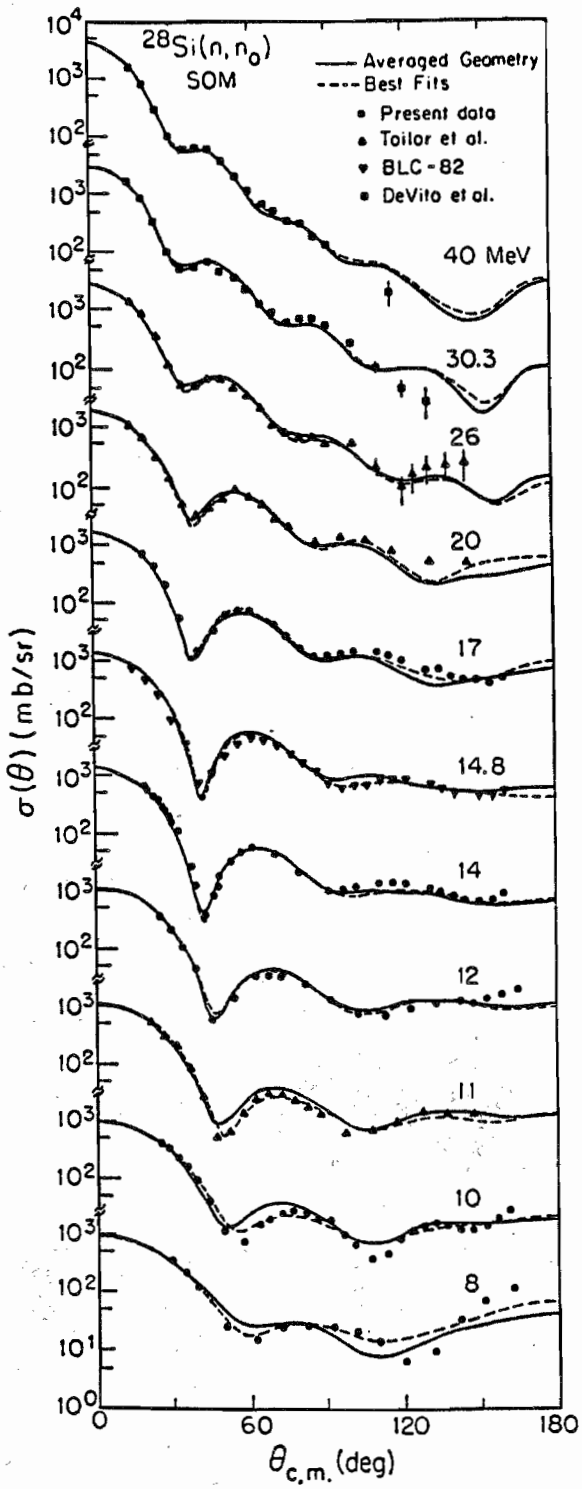

Figure 8.1. SOM calculations compared to $\sigma(\theta)$ data for ^{28}Si+n. The solid curves represent the fits with constant geometry, and the dashed curves are the "best" fits. All curves include the calculated contribution for CN elastic scattering.

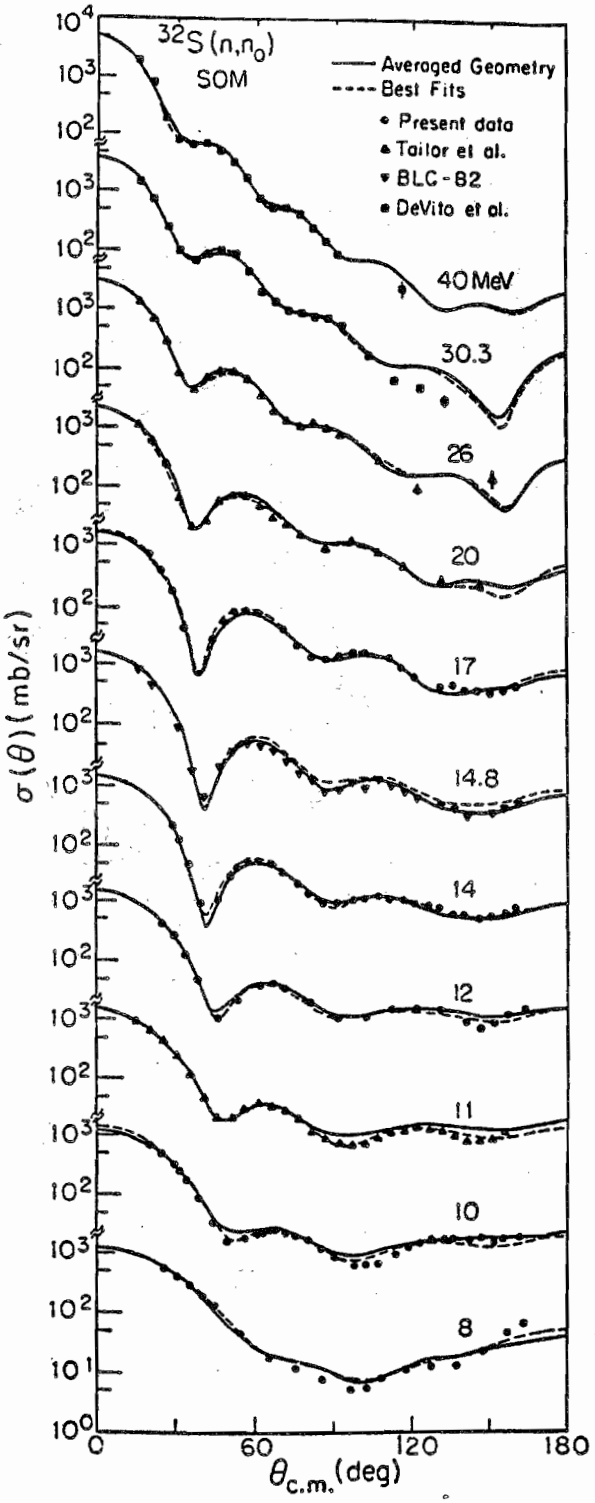

Figure 8.2. SOM calculations compared to $\sigma(\theta)$ data for $^{32}S+n$. The solid curves represent the fits with constant geometry, and the dashed curves are the "best" fits. All curves include the calculated contribution for CN elastic scattering.

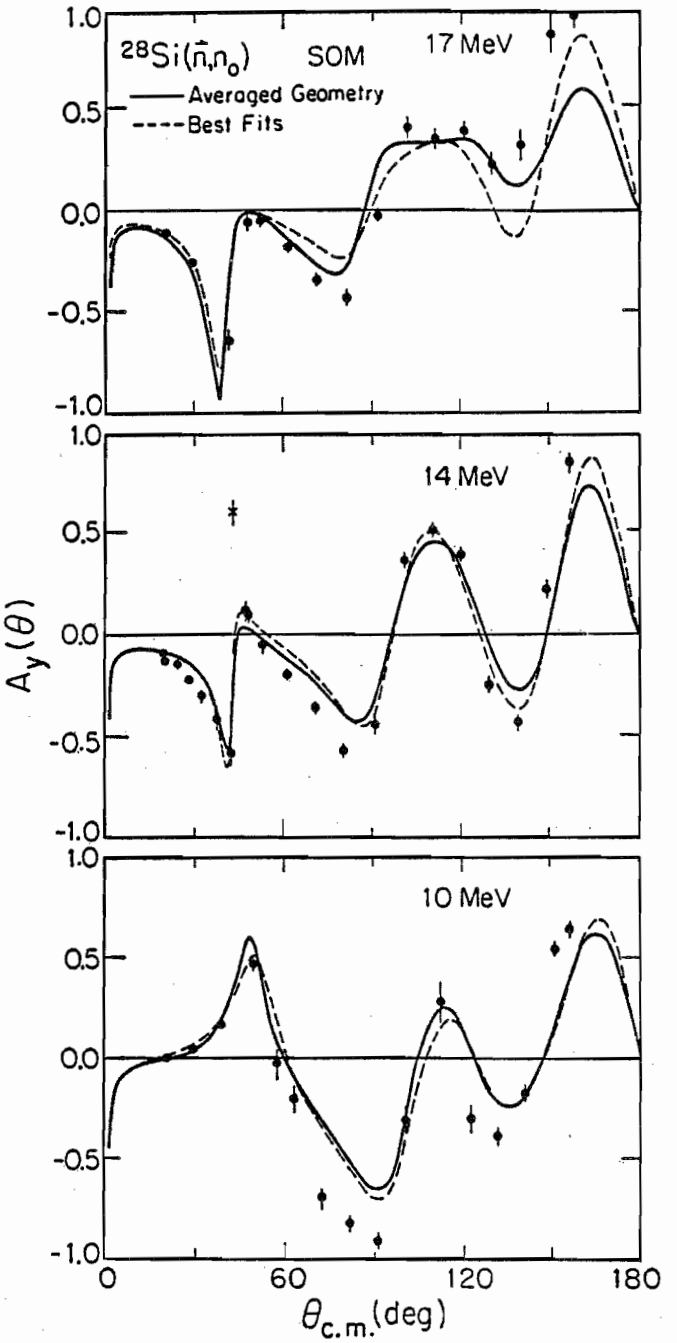

Figure 8.3. SOM calculations compared to $A_y(\theta)$ data for $^{28}Si+\vec{n}$. The solid curves represent the fits with constant geometry, and the dashed curves are the "best" fits. All curves include the calculated contribution (with $A_y^{CN} \equiv 0$) for CN elastic scattering.

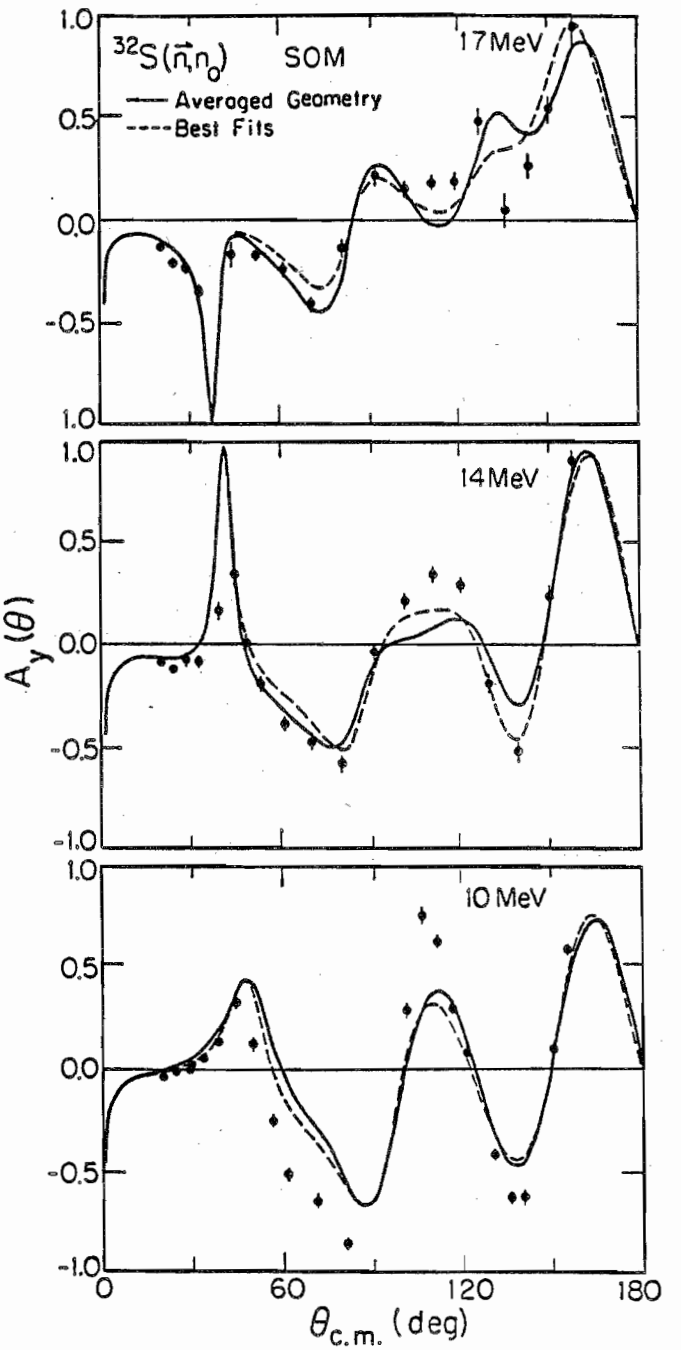

Figure 8.4. SOM calculations compared to $A_y(\theta)$ data for $^{32}S+\vec{n}$. The solid curves represent the fits with constant geometry, and the dashed curves are the "best" fits. All curves include the calculated contribution (with $A_y^{CN} \equiv 0$) for CN elastic scattering.

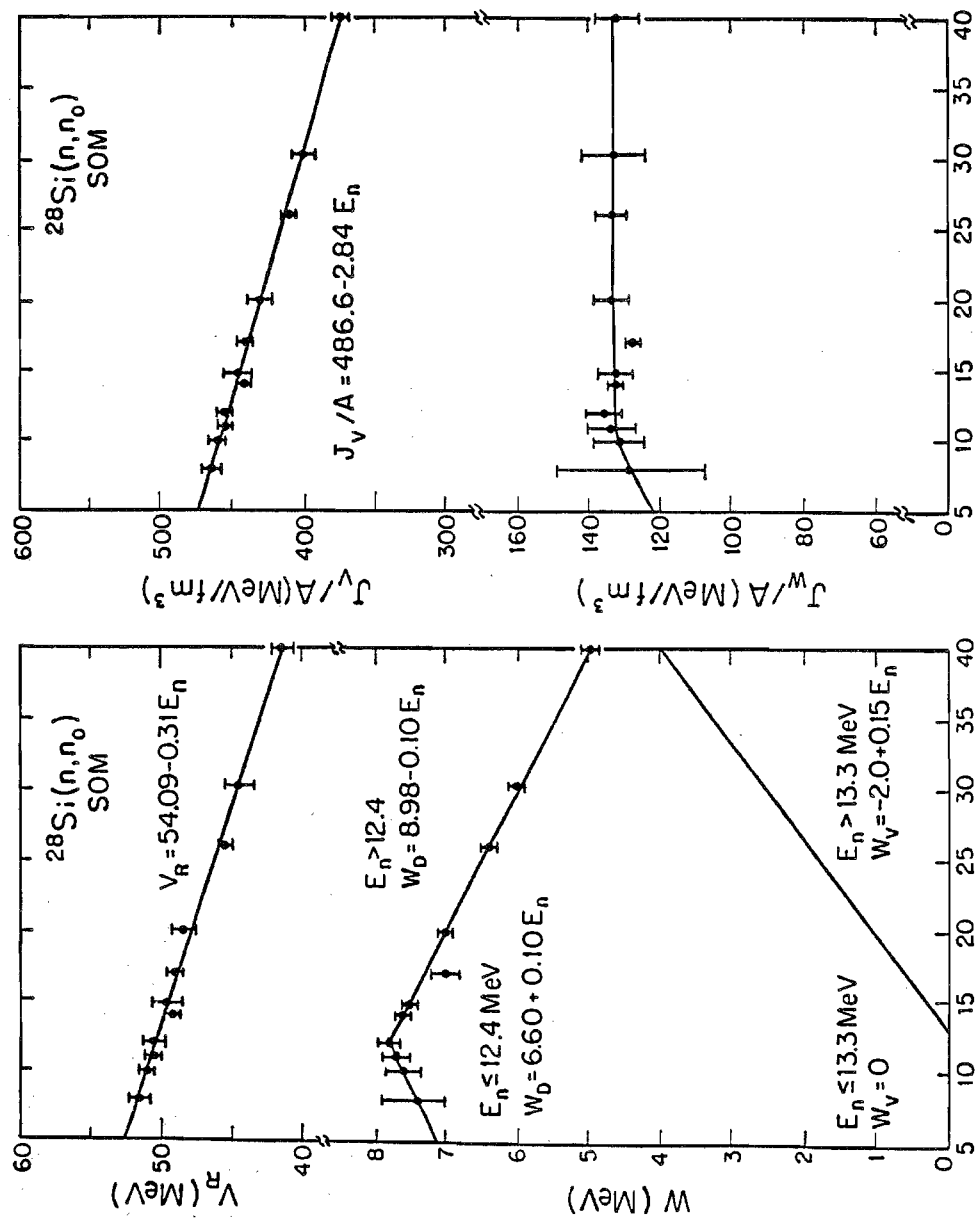

Figure 8.5. Plots of the potential strengths and the corresponding volume integrals per nucleon resulting from the present SOM analysis of ^{28}Si+n. The lines through the points represent least-square fits.

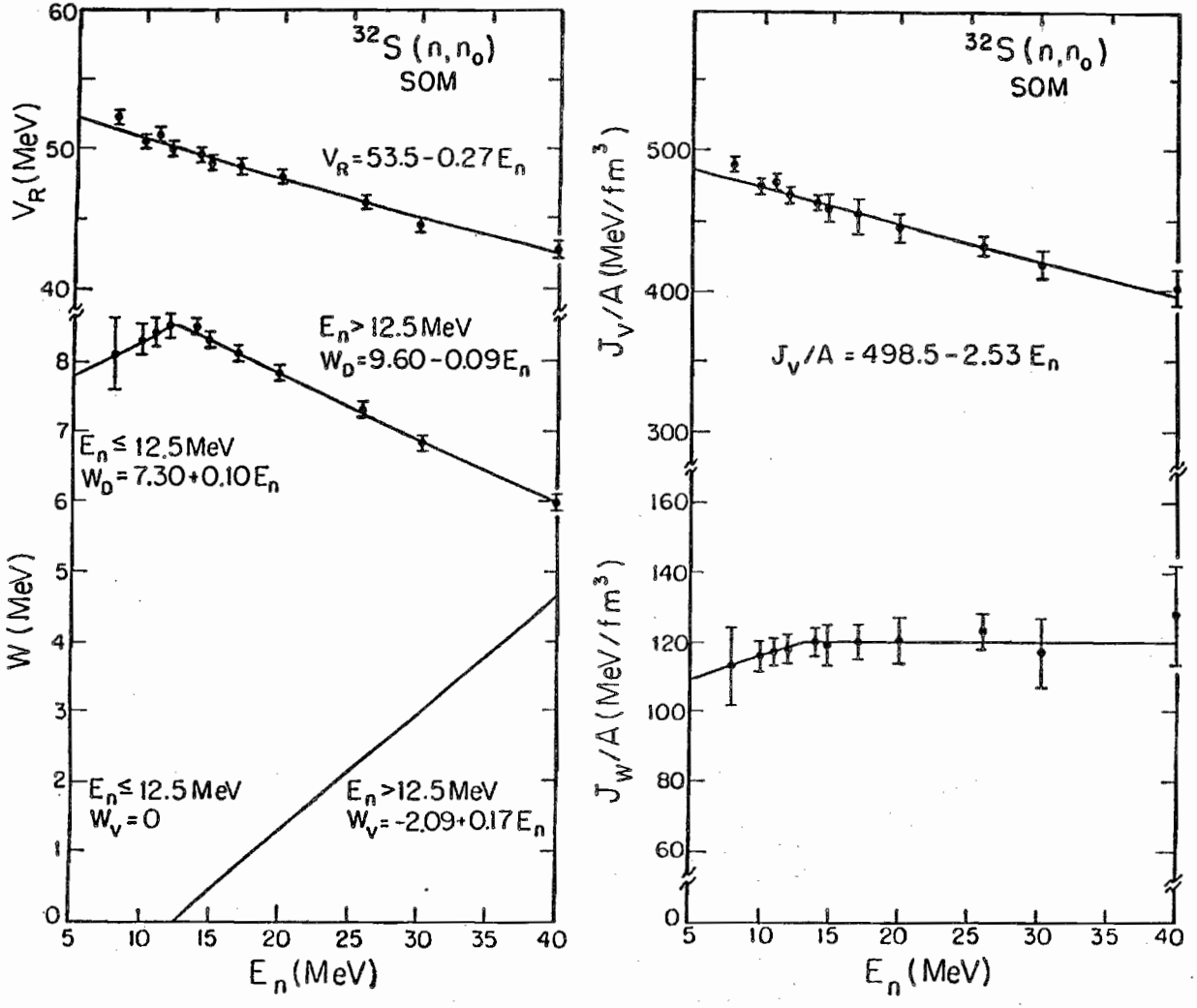

Figure 8.6. Plots of the potential strengths and the corresponding volume integrals per nucleon resulting from the present SOM analysis of ^{32}S+n. The lines through the points represent least-square fits.

solid curves in figures 8.1 through 8.4. The agreement between the $\sigma(\theta)$ data and the calculations, especially above 12 MeV, is almost as exceptional as the best-fit calculations. Although systematic discrepancies are obvious, the calculations for $A_y(\theta)$ reproduce the general shape of the $A_y(\theta)$ data. Keep in mind that CN contributions have been added to the calculations for both $\sigma(\theta)$ and $A_y(\theta)$ at energies below 14 MeV. The potential strengths and the corresponding volume integrals per nucleon are plotted in figures 8.5 and 8.6. The error bars assigned to the potential strengths and to the corresponding volume integrals represent estimates of the uncertainties in determining the value of the strength parameters.

In the last step of the analysis, a simple linear energy dependence was assumed for the well depths. The strengths of the real wells resulting from the searches at energies above 10 MeV were fit with a least-square fitting routine in which all points were given equal weighting. The lines shown in figures 8.5 and 8.6 are the resulting fits to the points. The lines through the volume integrals per nucleon for the real wells were determined in the same fashion. The potential strengths of the surface part of the imaginary wells were divided into two energy regions and fit with the same least-square fitting routine. The resultant energy dependencies of the potential well strengths were:

for silicon

$$V_R = 54.09 - 0.31\ E_n$$

$$W_D = 6.60 + 0.10\ E_n \qquad \text{for } E_n \leq 12.4 \text{ MeV}$$

$$= 8.98 - 0.10\ E_n \qquad \text{for } E_n > 12.4 \text{ MeV}$$

$$W_v = 0.00 \qquad \text{for } E_n \leq 13.3 \text{ MeV}$$
$$= -2.00 + 0.15\, E_n \qquad \text{for } E_n > 13.3 \text{ MeV}$$

and for sulfur

$$V_R = 53.50 - 0.27\, E_n$$

$$W_D = 7.30 + 0.10\, E_n \qquad \text{for } E_n \leq 12.5 \text{ MeV}$$
$$= 9.60 - 0.09\, E_n \qquad \text{for } E_n > 12.5 \text{ MeV}$$

$$W_v = 0.00 \qquad \text{for } E_n \leq 12.5 \text{ MeV}$$
$$= -2.09 + 0.17\, E_n \qquad \text{for } E_n > 12.5 \text{ MeV}$$

For the sake of clarity, calculations using these linear energy dependencies are not shown in figures 8.1 to 8.4. In fact, the calculations look very similar to those for the solid curves.

The determination of the energy dependencies can be made less dependent on the specific choice of geometrical parameters by comparing volume integrals per nucleon instead of potential well strengths. The volume integrals per nucleon, which also are often used to compare models, can be calculated using the following relationships (Rapaport 1979):

for the real well

$$J_v/A = \tfrac{4}{3}\pi r_R^3 V_R \left[1 + \left(\frac{\pi a_R}{r_R A^{1/3}}\right)^2\right]$$

and for the imaginary well

$$J_w/A = \tfrac{4}{3}\pi r_I^3 W_v \left[1 + \left(\frac{\pi a_I}{r_I A^{1/3}}\right)^2\right] + \frac{16\pi r_I^2}{A^{1/3}}\, a_I W_D \left[1 + \tfrac{1}{3}\left(\frac{\pi a_I}{r_I A^{1/3}}\right)^2\right].$$

The benefits of comparing volume integrals instead of well strengths will become more apparent in chapter 9 in the discussion concerning the determination of the Coulomb correction term to the optical potential.

The volume integrals per nucleon for the real wells can be represented by the lines

$$J_v/A = 486.6 - 2.84\ E_n \qquad \text{for silicon}$$

and

$$J_v/A = 498.5 - 2.53\ E_n \qquad \text{for sulfur.}$$

The volume integrals per nucleon for the imaginary wells cannot be as simply represented by a straight line (see figures 8.5 and 8.6). However, for both nuclei, the value of J_w/A increased linearly until about 12.4 MeV and then remained essentially constant over the remainder of the energy range.

8.4 Conclusions

In conclusion, the SOM is capable of describing the differential cross sections very well and the analyzing powers reasonably well for elastically scattered neutrons from silicon and sulfur at incident energies between 8 and 40 MeV. The geometrical parameters were held constant over the entire energy range and the potential strengths had simple linear energy dependences. The model successfully described the neutron total cross section for silicon between 8 and 50 MeV, but had some difficulty reproducing the total cross section for sulfur as shown in fig.

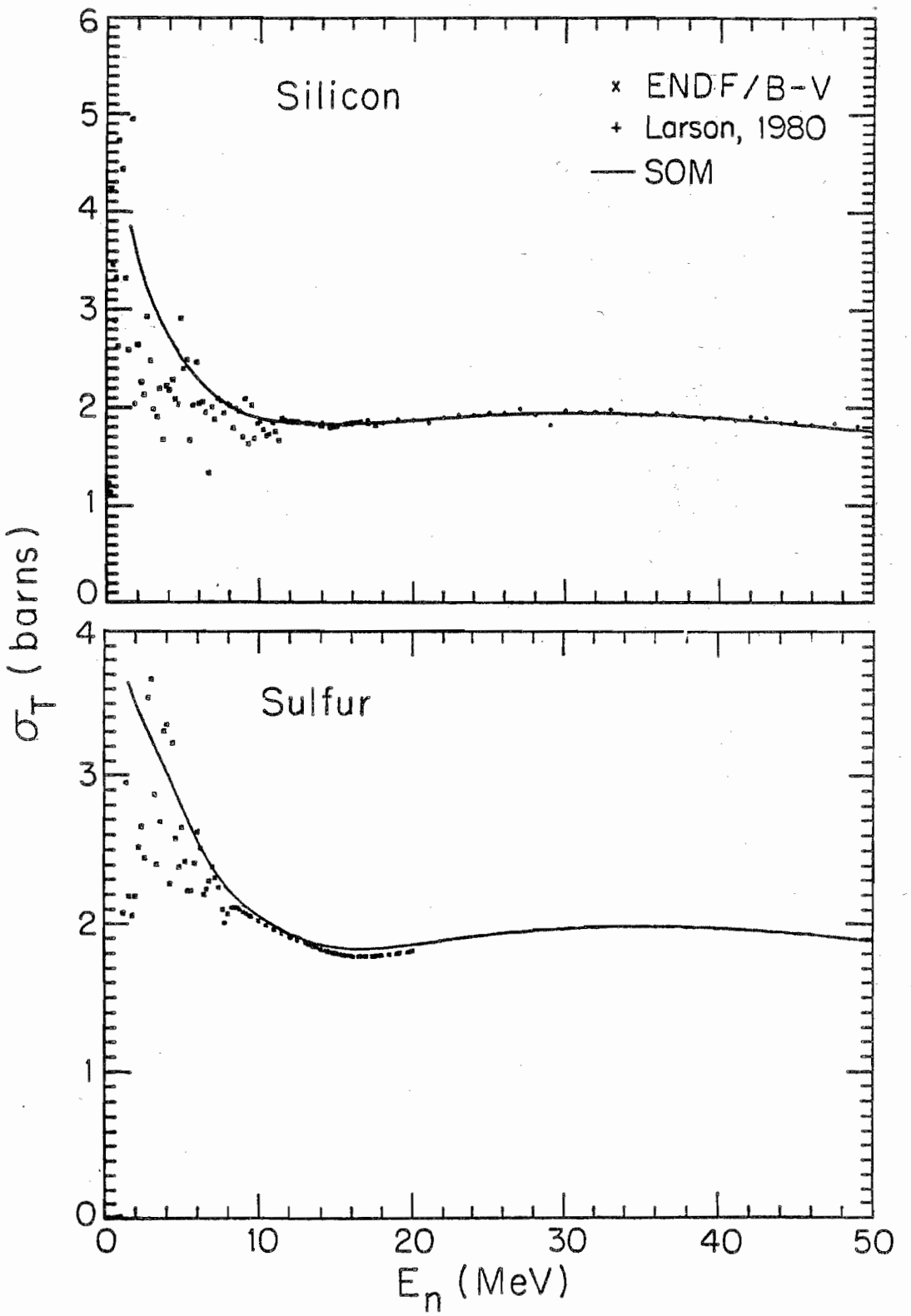

Figure 8.7. Plots of the neutron total cross section for silicon and sulfur. The curves through the data are the predictions of the present SOM analysis.

8.7. The inability to describe the neutron total cross section for sulfur with a SOM has been previously attributed to the combined effects of nuclear deformation and the formation of single particle states (Glasgow 1970).

Because of the good agreement between the SOM calculations and the experimentally observed data, it was concluded that the available data were consistent with each other and also consistent with the trends of the OM. Plots of the experimentally observed integrated elastic cross sections are shown in fig. 8.8. The curves through the data are SOM predictions using the set-B geometrical parameters and the linear energy dependencies for the potential strengths that were determined in the present analysis. The integrated cross section at 14.8 MeV (BLC 1982) was approximately 10% lower than the SOM calculations, while the TUNL data at 17 MeV was about 10% higher than the calculations. Also, comparison of the calculated angular distributions (shown in figures 8.1 and 8.2 as the solid curves) to the experimentally observed data suggest a 15% difference between calculation and experiment at 14.8 MeV and a 10% difference at 17 MeV. The calculations at these two energies fit the forward angle data reasonably well, but the mid to back angle calculations miss the data. Since the forward angle data contributes over 85% of the integrated cross section, the plots shown in fig. 8.8 are mainly measures of the model's ability to describe the forward angle data. Therefore, normalization errors in differential cross section data for neutron scattering will be evident in the forward angular region, while failures in the nuclear model to explain the data will probably result in shape differences between the calculations and data at mid to back angles. Presumably, such shape

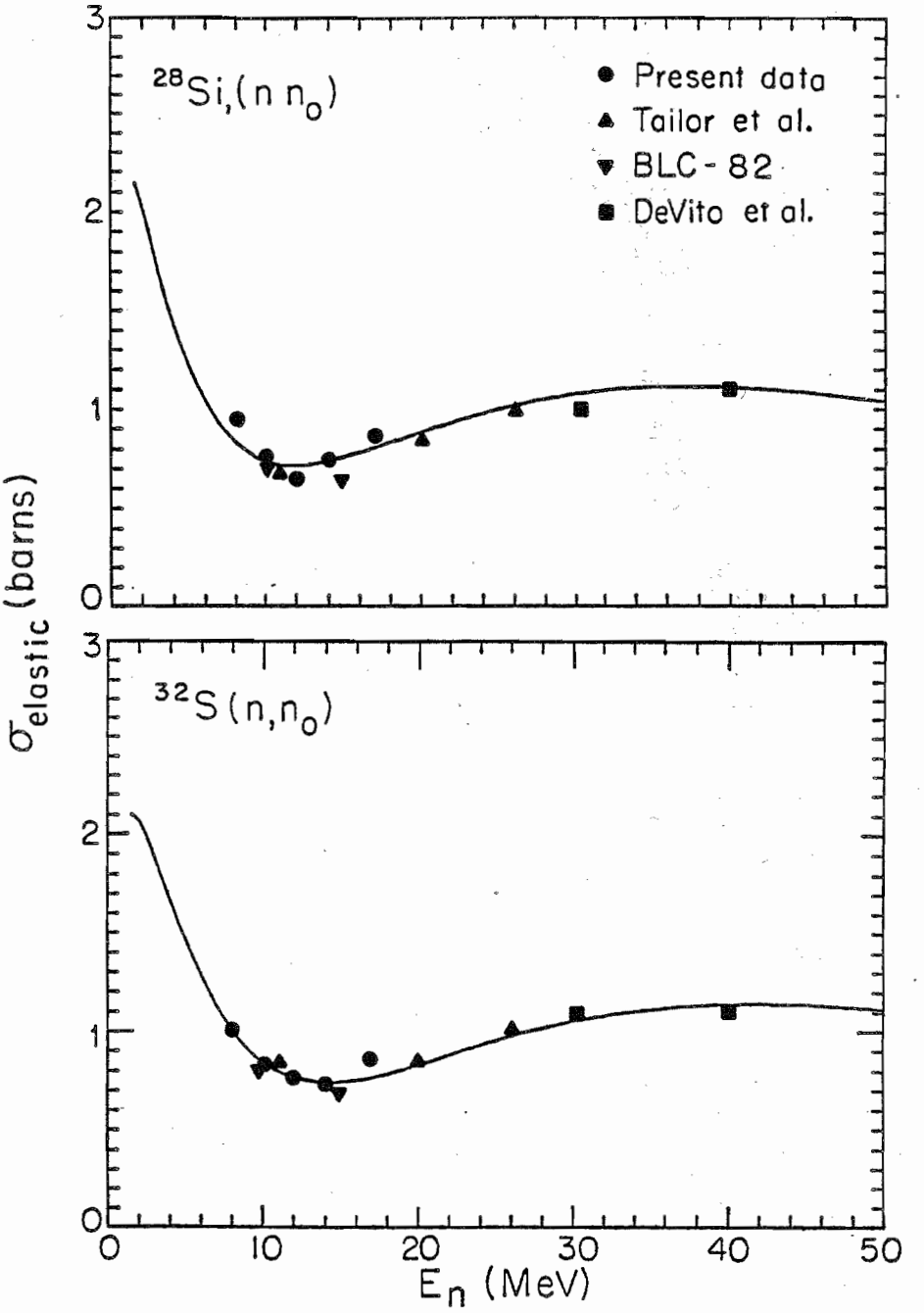

Figure 8.8. Plots of the integrated elastic cross sections for neutron scattering from ^{28}Si and ^{32}S. The data points were computed using Legendre polynomial fits to the angular distributions. The curves through the data were computed using the smooth energy dependencies determined in the present SOM analysis.

differences as exemplified at 14.8 and 17 MeV are primarily due to the effects of collective motion of the nucleus and can be corrected by explicitly coupling to excited states in the target nucleus (see chapter 9).

The broad energy range spanned by the present data and the high quality of the data has permitted a substantial reduction of the ambiguities in the optical-model parameters for neutron scattering from ^{28}Si and ^{32}S. These highly defined parameters were used to gain information about the differences between the proton-nucleus and neutron-nucleus optical-model potentials for ^{28}Si and ^{32}S. The results of the present analyses were compared to the findings of Fabrici et al. (Fabrici 1980) and De Swiniarski et al. (De Swiniarski 1976a) for their SOM analyses of ^{28}Si+p and ^{32}S+p, respectively. To reduce ambiguities even further, the comparisons were made between volume integrals per nucleon instead of the normal OM parameters (see section 8.3). For both nuclei, the volume integrals of the real well for the present neutron analyses were equivalent to those resulting from the corresponding proton analyses. On the other hand, the volume integrals of the absorptive well for the present analyses were consistently larger than those of (Fabrici 1980) or (De Swiniarski 1976a). The above findings suggested that the neutron data can be described with the OM parameters of the proton analyses, provided the absorption is increased for neutrons. The full implications of these observations concerning the Coulomb corrections to the optical-model potential will be discussed in chapter 9.

One of the most recent products of the neutron-scattering studies conducted at TUNL has been the global SOM developed by Guss (Guss 1982a).

This model reliably predicts $A_y(\theta)$, $\sigma(\theta)$, and $\sigma_t(E)$ for neutron scattering from nuclei in the mass region between A = 12 and A = 238 at incident energies from 4 to 26 MeV. Therefore, it is useful to see how the present parameters and data fit in the global picture that has been painted by Guss, since these nuclei are at the lower limit of the mass range of Guss's model. For both ^{28}Si and ^{32}S, most of the geometrical parameters of the central well agreed with Guss's global parameter set within 2%; the only noticeable discrepancy was between the diffuseness parameters a_I of the absorptive wells. Even with the discrepancy between the a_I parameters, the present parameters are amazingly similar to those reported by Guss (i.e., r_R = 1.169 fm, a_R = 0.689 fm, r_I = 1.250 fm, and a_I = 0.616 fm). Therefore, we have concluded that the present data can be incorporated in Guss's global analysis with only a small change in a_I. The parameterization of the spin-orbit potential will be considered next.

The present $A_y(\theta)$ data are the first complete data sets for neutron scattering from ^{28}Si and ^{32}S and as such provided the first solid opportunity to parameterize the spin-orbit potentials for neutron scattering from these nuclei. The most outstanding feature of the searches upon the parameters of spin-orbit potential was that the data for both nuclei preferred $r_{so} < 1.0$ fm and $a_{so} < 0.50$ fm at all energies. However, reasonably good fits were obtained to the data by setting r_{so} and a_{so} to the more conventional values of r_{so} = 1.01 fm and a_{so} = 0.50 fm and searching upon V_{so}. Our final parameters were very similar to the values for protons (Becchetti 1969), although the diffuseness parameter a_{so} was significantly smaller than the value for protons, a_{so} = 0.75 fm. As in the case for the central well, our parameters for the spin-orbit potential

were in excellent agreement with Guss's global parameter set (V_{so} ~ 6.0 MeV, r_R = 1.047 fm, and a_{so} = 0.50 fm) (Guss 1982a). This latter finding provides additional incentive for incorporating these data in Guss's global SOM.

CHAPTER 9

COUPLED-CHANNELS ANALYSES

9.1 Introduction

In this chapter coupled-channels (CC) calculations which were used to deduce properties of the phenomenological nucleon-nucleus optical model potential (OMP) will be described. First, the collective model of the nucleus will be reviewed. Second, phenomenological CC analyses of neutron scattering from silicon and sulfur for incident energies from 8 to 40 MeV will be presented. Various calculations will be performed to determine the sensitivity of the data to the sign of the deformation parameters and to the magnitude of the spin-orbit deformation parameter. Third, the analysis of neutron-scattering data will be compared to the corresponding analysis of proton-scattering data to deduce information about the Coulomb correction terms to the real and imaginary parts of the OMP. And finally, the effects of single particle states on the neutron total cross section of sulfur will be deduced by comparing the calculated cross sections to the experimentally observed values.

9.2 Review of the Collective Model of the Nucleus

Presently, there is no single nuclear model that successfully explains and describes all nuclear structure and properties. Therefore, we must rely on many models to explain various characteristics and properties of nuclei. The underlying similarity between all nuclear models is that they must be in agreement with the fundamental properties of internucleonic forces, i.e., the nuclear force is strong, short ranged, saturable, tensor, and essentially a two-body interaction. The applications of the existing models can be more or less divided into two categories: those that are designed to explain nuclear structure (e.g., energy levels, spins, parities, and electric and magnetic moments of states) and those constructed to describe nuclear reactions (e.g., scattering cross sections, stripping reactions, and resonance capture). The combination of the statistical, shell, and collective models provide a reasonably good description of most nuclear phenomena.

Our primary goal in this chapter is to describe elastic and inelastic neutron scattering from silicon and sulfur while being cognizant of nuclear structure. Thus, we use the statistical and collective models in conjunction with the optical model to simultaneously explain both nuclear reactions and nuclear structure. The statistical model has been described in chapter 7 and therefore will receive no further discussion here.

Prior to the work of Cohen and Rubin (Cohen 1958), calculations of inelastic scattering used shell-model wave functions and effective nucleon-nucleon interactions to evaluate the transition matrix elements. These calculations consistently resulted in predictions of inelastic cross

sections that were substantially smaller than the experimentally observed values (Hodgson 1971). The discrepancy between the inelastic scattering cross sections observed by Cohen and Rubin and various shell-model calculations suggested that the observed inelastic scattering was primarily due to the excitation of collective states in the target nucleus; the unexpectedly large inelastic scattering cross sections were thought to be caused by the cooperative effects of the nucleons in the target nucleus.

This collective motion of the nucleons results in nuclear shapes that deviate from sphericity. The magnitude of the inelastic scattering cross sections are indicative of the size of the nuclear deformation. Nuclei with both filled neutron and filled proton shells seem to be mostly spherical, while partially filled shells tend to add non-spherical components to the nuclear shape. Nuclei having N or Z close to the "magic numbers" usually exhibit small deformations. In this case, an incident particle excites the nucleus into some mode of collective motion about a spherical equilibrium. This type of nuclear deformation is known as dynamic deformation and the nucleus is said to undergo shape oscillations. Therefore, for small deformations the nucleus is usually modeled as a vibrator. On the other hand, nuclei with N or Z far from the magic numbers tend to be very deformed and therefore are treated as having permanent or static deformations. In this case the nucleus is usually modeled as a rotating ellipsoid with deformation parameter β. The deformation parameter can be either positive or negative, depending on the shape of the nucleus. For $\beta < 0$ the nucleus is oblate (pancake-like) and for $\beta > 0$ it is prolate (cigar-shaped).

The shape of the nuclear surface can be specified in terms of the radius R. If the nucleus is spherical, but is susceptible to vibrations about that spherical shape, then R can be expressed in terms of the equilibrium radius R_0 and the space-fixed angular coordinates θ and φ,

$$R(\theta,\varphi) = R_0\left[1 + \sum_{\lambda\mu} \alpha_{\lambda\mu} Y_{\lambda\mu}(\theta,\varphi)\right] . \qquad (9.1)$$

If the nucleus is permanently deformed and axially symmetric, then R can be written as a function of the body-fixed angular coordinate θ',

$$R(\theta') = R_0\left[1 + \sum_{\lambda} \beta_\lambda Y_{\lambda 0}(\theta')\right] . \qquad (9.2)$$

It was concluded in chapter 8 that the data for the elastically scattered neutrons from silicon and sulfur could be successfully described using a phenomenological spherical-optical-model potential (SOMP) as the interaction potential between the incident neutron and the target nucleus. This OMP is extended below to explain the observables for inelastic scattering to the first few excited states of these nuclei. These states are believed to be collective in nature because of their large inelastic scattering cross sections and their large electromagnetic transition rates. The collective model of the nucleus attributed the excitation of these low-lying states to vibrations about a mean spherical shape or to rotations of a statically deformed nucleus about a space-fixed axis.

The above modes of collective motion have been parameterized in equations (9.1) and (9.2). The OMP is assumed to depend on the distance

from the nuclear surface (r−R). A Taylor expansion of the optical-model potential U(r−R) for a vibrational nucleus gives

$$U(r-R) = U(r-R_0) - \left[\sum_{\lambda\mu} \alpha_{\lambda\mu} Y_{\lambda\mu}(\theta,\phi) \right] R_0 \frac{dU}{dr}$$

$$+ \frac{1}{2}\left[\sum_{\lambda\mu} \alpha_{\lambda\mu} Y_{\lambda\mu}(\theta,\phi) \right]^2 R_0^2 \frac{d^2U}{dr^2} + \cdots \qquad (9.3)$$

and for a rotational nucleus

$$U(r-R) = U(r-R_0) - \left[\sum_{\lambda} \beta_\lambda Y_{\lambda 0}(\theta') \right] R_0 \frac{dU}{dr}$$

$$+ \frac{1}{2}\left[\sum_{\lambda} \beta_\lambda Y_{\lambda 0}(\theta') \right]^2 R_0^2 \frac{d^2U}{dr^2} + \cdots \qquad (9.4)$$

The first term in both expressions for U(r−R) is the spherical optical model potential (SOMP), which is used to describe elastic scattering. The other terms are identified with inelastic interactions and with second order corrections to the elastic scattering potential.

It can be shown that the radial wave functions in the elastic and inelastic channels are given by the coupled equations

$$\left[\frac{d^2}{dr^2} - \frac{L(L+1)}{r^2} + k_\alpha^2 - W_{\alpha\alpha}(r) \right] u_\alpha(r) = \sum_{\alpha' \neq \alpha} W_{\alpha\alpha'}(r) u_{\alpha'}(r)$$

where

$$W_{\alpha\alpha'}(r) = \frac{2m}{\hbar^2} \sum_{LM} \int Y^*_{L'M'}(\theta,\phi) V_{\alpha\alpha'}(r)\, Y_{LM}(\theta,\phi)\, d\Omega$$

and

$$V_{\alpha\alpha'}(r) = \int \chi^{*}_{\alpha}(\xi) V(r,\xi)\ \chi_{\alpha'}(\xi) d\xi \ .$$

The nuclear states are defined as

$$H(\xi)\chi_{\alpha}(\xi) = \varepsilon_{\alpha}\chi(\xi) \ .$$

The unprimed and primed subscripts denote the initial and final states of the nucleus. The function $H(\xi)$ is the nuclear Hamiltonian, the ξ represents all the nuclear coordinates and the ε_{α} are the energy eigenvalues. The nuclear Hamiltonian describes the internal motion of the target nucleus, i.e., vibrational or rotational. In this coupled-channels (CC) approach the interaction potential $V(r,\xi)$ is assumed to be the optical-model potential $U(r-R)$.

The solution to the above set of coupled differential equations are used to compute the elastic and inelastic scattering matrix elements, from which cross section and polarization observables are calculated. The coupled-channels code ECIS79 by Raynal (Raynal 1979) was used in the present analysis to solve the system of coupled equations. This code uses an iterative method to solve the equations. A serious condition for this approach is that the computer time needed to solve the set of equations is proportional to the cube of the number of states coupled in the calculation (Tamura 1965). This is,

$$\text{CPU TIME} \propto (\text{number of states coupled})^{3} \ .$$

In cases where the coupling between the elastic and inelastic channels is weak ($\beta < 0.1$), the scattering matrix elements can be

calculated using the distorted-wave Born approximation (DWBA). This approximation, which can be evaluated more rapidly than the CC case, is not valid for silicon and sulfur because of their large deformations ($\beta > 0.25$). For more complete discussions on DWBA and CC calculations see (Tamura 1965, Marmier 1971, Hodgson 1971, and Perey 1974).

9.3 Coupled-Channels Analysis of ^{28}Si + n

9.3.1 Description of the Data with Coupled-Channels Calculations

As described below, angular distributions of cross sections and analyzing powers for elastically and inelastically scattered neutrons from ^{28}Si over the energy range from 8 to 40 MeV have been successfully described with CC calculations. Inelastic scattering cross sections for the lowest 2^+ and 4^+ states were also obtained from the references listed in chapter 8. The analyzing power data measured at TUNL, using the techniques described in chapter 2, were emphasized over the only other available data in this energy range, that of Böttcher et al. (Böttcher 1983) (see chapter 6). The lowest 2^+ and 4^+ excited states in ^{28}Si were modeled as collective states in the K = 0 rotational band. The expansion of the OMP in eqn. (9.4) was used as the interaction potential in these calculations. For the entire energy range of the analysis, the geometrical and deformation parameters were fixed. As mentioned earlier, the code ECIS79 by Raynal was used to perform the analysis. The code has the capability of searching both on OM parameters and on deformation parameters.

As stated above, it was assumed that the first 0^+, 2^+, and 4^+ states

formed the lower levels of the $K^{\pi} = 0^{+}$ rotational band in ^{28}Si. The above assumption is well justified by both experiment and theory. Measurements of the electromagnetic transition probability $B(E_2)$ for the $0^{+} \rightarrow 2^{+}$ transition suggest that ^{28}Si has a large ground state deformation. Within the scheme of the collective model, this implies that excitation of the 2^{+} state sets the permanently deformed nucleus into rotation about some space-fixed axis. In addition, the energy spacings between the ground state and first two excited states as shown in fig. 9.1 are strongly indicative of a rotational spectrum. Furthermore, the rotational character of the low-lying states has been well established by previous studies (Mermaz 1969, Aleonard 1970, De Swiniarski 1973, and De Swiniarski 1976a). Therefore, all calculations were performed using a symmetric rotational model with coupling to the 2^{+} and 4^{+} states.

The average geometrical OM parameters from the SOM analysis were used as starting parameters. The initial CN calculations were performed using the SOM parameters from chapter 8. Both geometrical parameters and potential strengths were searched upon to produce a minimum χ^2 fit for elastic and inelastic data. Because the differential cross sections $\sigma(\theta)$ for elastic scattering to back angles were found to be very sensitive to the spin-orbit (SO) interaction, it was important to reduce the ambiguities in the SO potential at the onset of the analysis. Changes in the SO potential parameters at a later point in the analysis could have required substantial adjustments of the central well paramters to compensate for the effects of changing the SO interaction. In order to determine the parameterization of the SO potential early in the analysis, the energies where both $\sigma(\theta)$ and analyzing power $A_y(\theta)$ data were available

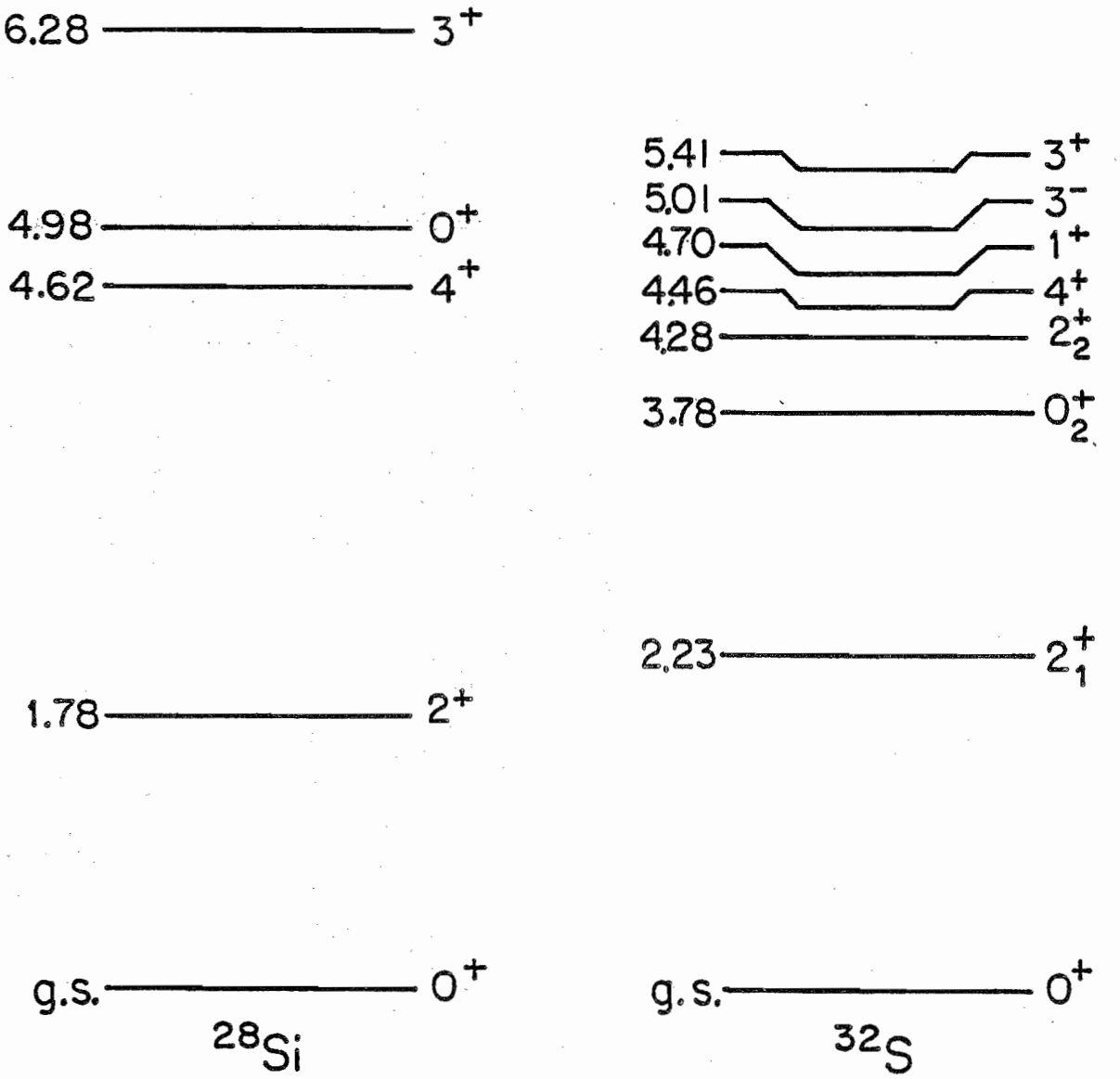

Figure 9.1. Energy-level scheme for ^{28}Si and ^{32}S

(i.e., 10, 14, and 17 MeV) were analyzed first.

Best fits were obtained at each energy where both $\sigma(\theta)$ and $A_y(\theta)$ data were available was obtained. These fits were obtained in an iterative fashion, and the same constraints applied to the OM parameters in the SOM analyses were employed here (see section 8.2). First, the fits to the $\sigma(\theta)$ data for elastic scattering were used to determine the geometrical parameters of the central well. Second, the SO parameters were searched upon to optimize the fits to the elastic $A_y(\theta)$ data; these data preferred $r_{so} < 1.0$ and $a_{so} < 0.5$ fm. The need for the unconventionally small geometrical parameters of the SO potential for ^{28}Si have also been cited by De Swiniarski *et al.* (De Swiniarski 1973 and De Swiniarski 1976a) and by Böttcher *et al.* (Böttcher 1983). However, to be consistent with the constraints that $r_{so} \geq 1.0$ and $a_{so} \geq 0.5$ fm, the values of these parameters were fixed to $r_{so} = 1.01$ fm and $a_{so} = 0.5$ fm. Third, the quadrupole deformation parameter β_2 was adjusted for optimum fits to the 2^+ $\sigma(\theta)$ data, while the hexadecapole deformation parameter was fixed to the value $\beta_4 = +0.20$ as reported by Haouat *et al.* (Haouat 1982). During this stage of the analysis, the ratio of the SO deformation length ($\delta_{so} = \beta_{so}R_{so}$) to the deformation length of the central well ($\delta_c = \beta_c R$) was adjusted to optimize the fits to the 2^+ $A_y(\theta)$ data. In the final step, the potential strengths and geometrical parameters of the central well and the deformation parameter β_2 were fine tuned to simultaneously optimize the fits to the elastic and inelastic $\sigma(\theta)$ and $A_y(\theta)$ data. After best fits were obtained at each of the three energies, the SO potential parameters were averaged and used to obtain best fits to the $\sigma(\theta)$ data at the remaining energies.

As in the case of the best fits, the final OM parameters for the CC calculations were obtained in an iterative fashion. First, an energy-averaged value for each geometrical parameter was computed using the results of the best fits at energies above 10 MeV. The mean quadrupole deformation parameter over the energy range from 10 to 40 MeV was found to be $\beta_2 = -0.36$ with $\delta_{so} = 1.2\delta_c$. Second, fixing the geometrical parameters and the deformation parameters to their energy-averaged values and confining the value of the volume absorption strength to the line $W_v = 0$ for $E_n < 13.33$ MeV and $W_v = -2.0 + 0.15\ E_n$ for $E_n \geq 13.33$ MeV, the potential strengths V_R and W_D were searched upon to optimize the fits at each energy. At this point the CN calculations were updated to reflect the influences of coupling. The new estimate of the CN contributions were added to the CC calculations of $\sigma(\theta)$ and $A_y(\theta)$ for elastic scattering and inelastic scattering to the 2^+ state at energies below 14 MeV. Also, it was necessary to adjust the 4^+ calculations for CN contributions at energies up to 17 MeV (see discussion section 7.7). And finally, with the new CN calculations, the potential strengths V_R and W_D were searched upon at each energy below 20 MeV to obtain the final OM parameters.

The results of these searches are summarized in set-A of table 9-1 and are represented by the solid curves in figures 9.2 and 9.3. The resultant potential strengths are plotted in fig. 9.4. The lines through the data represent least square fits with equal weight given to all the points. The error bars assigned to the points reflect the normal ambiguities in the strengths of the real and imaginary potentials; the quality of the fits achieved with values of V_R and W_D varied within the range of the error bars are essentially equivalent. The final energy

TABLE 9-1

OPTICAL-MODEL PARAMETERS USED IN COUPLED-CHANNELS CALCULATIONS FOR ^{28}Si+n

	E_n (MeV)	V_R (MeV)	W_D (MeV)	J_V/A (MeV·fm^3)	J_W/A (MeV·fm^3)	χ^2/N_σ 0+	χ^2/N_σ 2+	χ^2/N_σ 4+	χ^2/N_A 0+	χ^2/N_A 2+	Model
Set-A	8.0	51.7 ± 0.7	2.5 ± 0.4	463 ± 6	43 ± 7	22.0	4.1				Sym. Rot. (0^+, 2^+, 4^+);
	10.0	51.8 ± 0.5	5.5 ± 0.3	463 ± 5	93 ± 5	15.0	6.2	4.1	36.1	6.9	$\beta_2 = -0.36$, $\beta_4 = +0.20$;
	11.0	50.9 ± 0.5	6.0 ± 0.3	455 ± 5	100 ± 5	12.1	2.9				$\delta_{so} = 1.2\delta_c$ ($\beta_{so} = 1.4\beta_c$)
	12.0	51.0 ± 0.7	5.5 ± 0.2	457 ± 6	92 ± 3	13.9	11.5				
	14.0	49.2 ± 0.5	5.6 ± 0.1	440 ± 5	96 ± 2	6.1	23.0		10.1	7.5	$r_R = 1.170$ fm $a_R = 0.654$ fm
	14.8	49.2 ± 1.0	5.5 ± 0.2	440 ± 9	95 ± 4	2.1	3.0	3.4			$r_I = 1.278$ fm $a_I = 0.580$ fm
	17.0	48.5 ± 0.5	5.4 ± 0.1	434 ± 5	98 ± 2	58.1	25.8		5.0	1.5	$r_{so} = 1.010$ fm $a_{so} = 0.500$ fm
	20.0	49.3 ± 0.9	5.3 ± 0.2	441 ± 8	101 ± 4	2.6	1.8				$V_{so} = 6.0$ MeV
	26.0	45.8 ± 0.4	6.1 ± 0.2	410 ± 4	124 ± 4	1.9	1.6				
	30.3	46.1 ± 1.0	5.8 ± 0.4	412 ± 9	125 ± 9	7.8					
	40.0	42.2 ± 0.7	4.2 ± 0.2	378 ± 8	113 ± 5	4.1					

TABLE 9-1 Continued

	E_n (MeV)	V_R (MeV)	W_D (MeV)	J_v/A (MeV·fm^3)	J_w/A (MeV·fm^3)	χ^2/N_σ 0+	χ^2/N_σ 2+	χ^2/N_σ 4+	χ^2/N_A 0+	χ^2/N_A 2+	Model
Set-B	8.0	51.6 ± 0.9	2.5 ± 0.4	439 ± 8	47 ± 8	20.5	1.4				Sym. Rot. (0^+, 2^+, 4^+);
	10.0	52.3 ± 0.6	5.1 ± 0.3	450 ± 5	95 ± 6	16.5	4.1	4.4	36.1	6.9	$\beta_2 = -0.39$, $\beta_4 = +0.16$;
	11.0	52.1 ± 0.6	5.6 ± 0.6	447 ± 5	105 ± 11	14.5	1.1				$\beta_{so} = 1.5\beta_c$ ($\delta_{so} = 1.3\delta_c$)
	12.0	51.5 ± 0.8	5.3 ± 0.2	442 ± 7	99 ± 4	18.1	8.1				
	14.0	50.1 ± 0.5	5.3 ± 0.2	431 ± 4	103 ± 4	9.4	21.0		18.6	4.8	$r_R = 1.148$ fm $a_R = 0.663$ fm
	14.8	50.0 ± 0.7	5.2 ± 0.2	430 ± 6	102 ± 4	5.2	1.8	7.0			$r_I = 1.330$ fm $a_I = 0.600$ fm
	17.0	47.7 ± 0.7	4.6 ± 0.1	410 ± 6	95 ± 2	41.7	33.1		13.1	1.6	$r_{so} = 1.020$ fm $a_{so} = 0.680$ fm
	20.0	49.7 ± 1.0	5.0 ± 0.2	427 ± 9	108 ± 4	3.6	1.3				$V_{so} = 6.3$ MeV
	26.0	45.8 ± 0.5	5.4 ± 0.1	394 ± 4	127 ± 2	2.7	1.5				
	30.3	46.3 ± 1.2	4.6 ± 0.3	398 ± 10	121 ± 8	7.7					
	40.0	42.1 ± 0.7	2.9 ± 0.2	362 ± 6	108 ± 8	3.8					

Set-A

$W_v = 0.0$ MeV for $E_n \leq 13.33$ MeV

$= (0.15E_n - 2.0$ MeV) for $E_n > 13.33$ MeV

Set-B

$W_v = 0.0$ MeV for $E_n \leq 12.5$ MeV

$= (0.16E_n - 2.0$ MeV) for $E_n > 12.5$ MeV

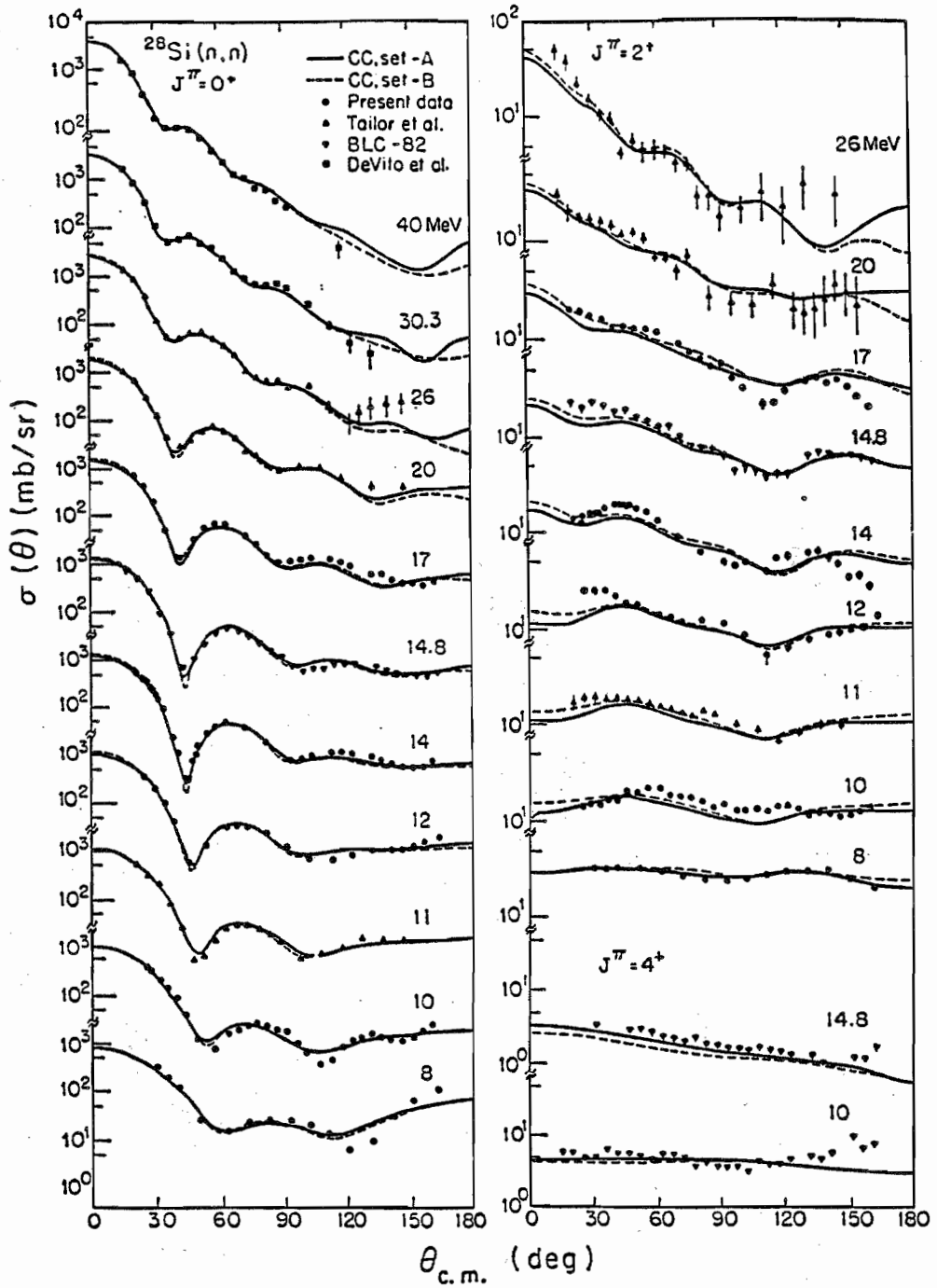

Figure 9.2. The $\sigma(\theta)$ for elastic and inelastic scattering of neutrons from ^{28}Si. The curves through the data are the results of CC calculations which model ^{28}Si as a rotational nucleus with coupling between the first three states of the $K^\pi = 0^+$ rotational band (0^+, 2^+, 4^+). The OM parameters are listed in table 9-1.

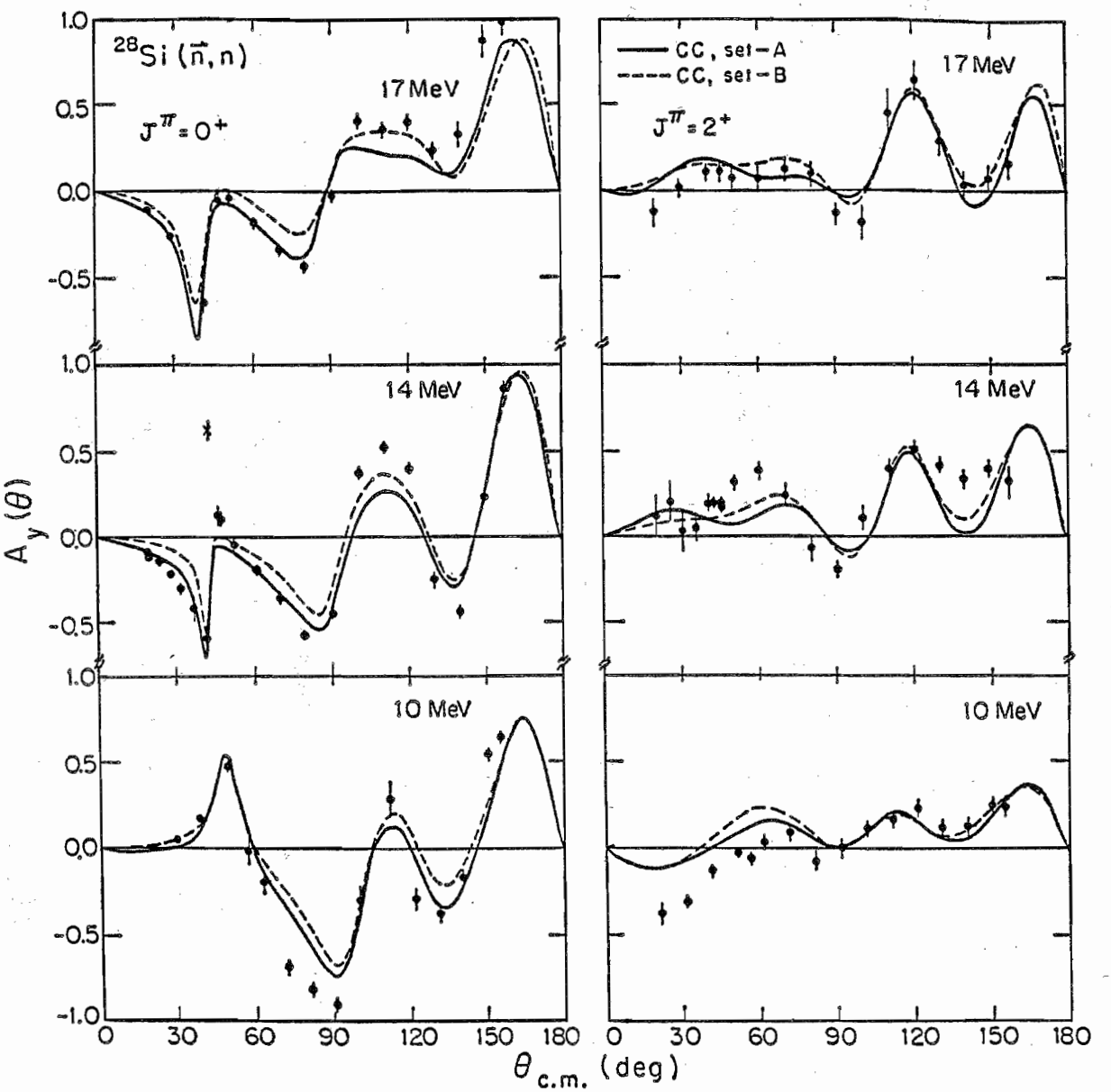

Figure 9.3. The $A_y(\theta)$ for elastic and inelastic scattering of polarized neutrons from ^{28}Si. The curves through the data are the results of CC calculations which model ^{28}Si as a rotational nucleus with coupling between the first three states of the $K^{\pi} = 0^+$ rotational band (0^+, 2^+, 4^+). The OM parameters are listed in table 9-1.

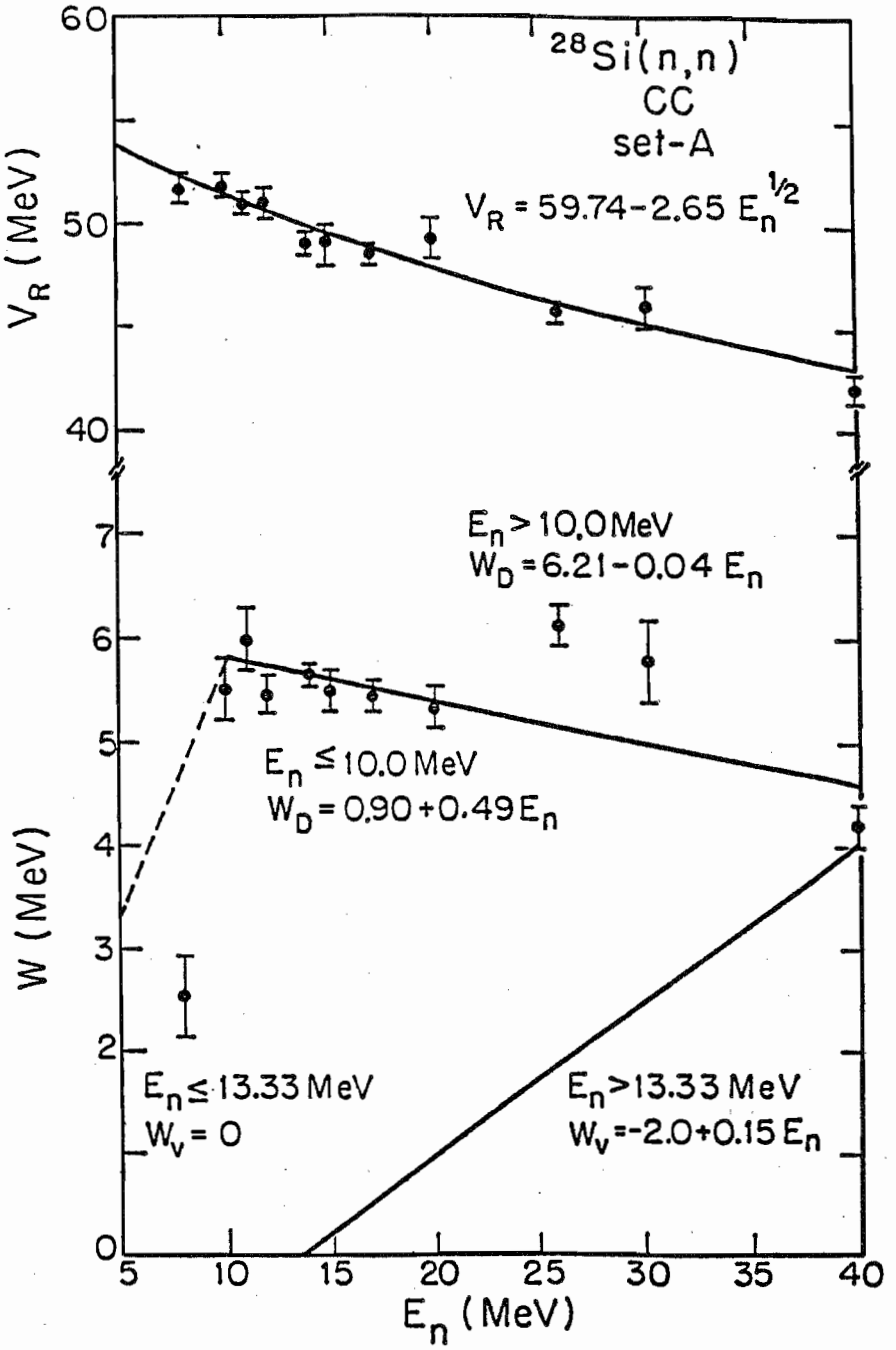

Figure 9.4. Potential strengths of the real and imaginary wells versus incident neutron energy. The points are the result of searches on V_R and W_D at each energy. The resulting parameters are listed as set-A in table 9-1. The curves through the potential strengths represent least-square fits. The dashed line is an extrapolation of W_D based on fitting the average neutron total cross section at low energies.

dependences, which are shown by the curves, are

$$V_R = 59.74 - 2.65\ E_n^{1/2}$$

$$W_D = 0.90 + 0.49\ E_n \quad \text{for } E_n \leq 10.0 \text{ MeV}$$
$$= 6.21 - 0.04\ E_n \quad \text{for } E_n > 10.0 \text{ MeV}$$

$$W_v = 0.00 \quad \text{for } E_n < 13.33 \text{ MeV}$$
$$= -2.00 + 0.15\ E_n \quad \text{for } E_n \geq 13.33 \text{ MeV} .$$

The calculations also accurately reproduce the experimentally observed neutron total cross sections from 8 to 40 MeV. The square-root energy dependence of V_R is necessary to describe the average neutron total cross section at energies below 3.0 MeV with constant geometrical parameters. The quality of agreement between experiment and theory is displayed in fig. 9.5. The solid curve is predicted using the parameters in set-A of table 9-1. Tables 9-2 and 9-3 provide a comparison of various OM analyses of neutron and proton scattering from ^{28}Si. Comparison of the average parameters for proton and neutron scattering reveal only slight differences in the two analyses. The diffuseness parameters a_R, a_I, and a_{so} and the radius parameter r_I are slightly smaller for neutron scattering (even with the constraint that $a_{so} \geq 0.5$ fm). However, it will be shown below that these small differences are important and lead to substantial disagreement between the calculated and experimental neutron total cross sections.

The sensitivity of σ_t to W_D at low energies ($E_n \leq 3.0$ MeV) was sufficient to determine upper and lower limits to the values of W_D, and

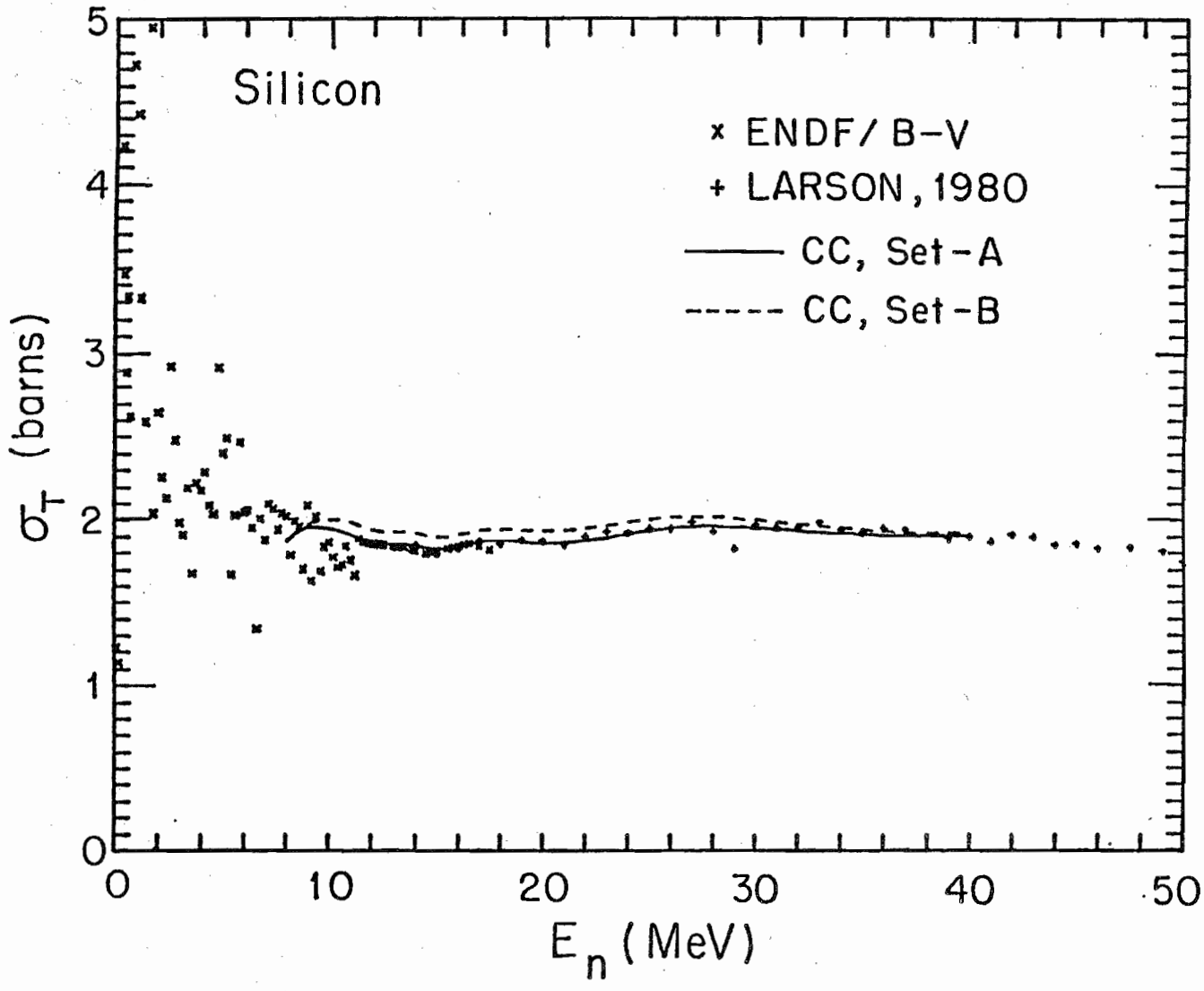

Figure 9.5. A plot of neutron total cross section for silicon. The curves are predictions of CC calculations. The solid curve represents the prediction using parameter set-A of table 9-1, and the dashed curve is the prediction using parameter set-B.

TABLE 9-2

SUMMARY OF GEOMETRICAL PARAMETERS FROM OPTICAL-MODEL ANALYSES OF ^{28}Si+n AND ^{28}Si+p

Reference	E (MeV)	No. of Dist.'s $\sigma(\theta)$	No. of Dist.'s $A_y(\theta)$	Model[c]	r_R (fm)	a_R (fm)	r_I (fm)	a_I (fm)	V_{so} (MeV)	r_{so} (fm)	a_{so} (fm)	β_2	β_4	δ_{so}/δ_c
Neutrons														
Present	8 - 40	22	6	CC	1.17	0.654	1.278	0.580	6.0	1.01	0.500	-0.36	+0.20	1.2
Present	8 - 40	11	3	SOM	1.16	0.689	1.310	0.574	6.6	1.01	0.500			
DeVito 1983	14 - 40	5		SOM	1.17	0.673	1.330	0.575	6.0	1.07	0.78			
Böttcher 1983	14	2	2	CC	1.198	0.623	1.295	0.590	5.83	1.06	0.49	-0.39		1.33
Haouat 1982	10 - 15	6		CC	1.15	0.61	1.15	0.58	6.0	1.15	0.58	-0.42	+0.20	
Tailor 1982	11 - 26	6		CC	1.148	0.663	1.330	0.60	6.3	1.02	0.68	-0.39	+0.16	1.33
Kliczewski 1978	14	2		CC	1.27	0.68	1.23	0.45	9.42	1.27	0.68	+0.39		
Obst 1972	10	2		CC	1.15	0.78	1.25	0.47	4.9	1.15	0.78	-0.48		
Martin 1968	6	2		CC	1.139	0.660	1.257	0.48	7.5	1.25	0.65	+0.40		
Mean	6 - 40	58	11		1.167	0.662	1.280	0.571	6.13[a]	1.02[a]	0.498[a]	-0.38[b]	+0.194[b]	1.23[a,b]
Variance					0.022	0.031	0.047	0.003	0.31	0.02	0.004	0.03	0.015	0.06

TABLE 9-2 Continued

Reference	E (MeV)	No. of Dist.'s $\sigma(\theta)$	No. of Dist.'s $A_y(\theta)$	Model[c]	r_R (fm)	a_R (fm)	r_I (fm)	a_I (fm)	V_{so} (MeV)	r_{so} (fm)	a_{so} (fm)	β_2	β_4	δ_{so}/δ_c
Protons[d]														
Hosono 1982	65	2	2	DWBA	1.205	0.733	1.315	0.397	5.28	1.061	0.623			
Sakaguchi 1982	65	1	1	SOM	1.176	0.7248	1.241	0.5656	5.970	1.007	0.6181			
Fabrici 1980	14 - 40	25	3	SOM	1.148	0.663	1.33	0.60	6.3	1.02	0.68			
De Leo 1979	14 - 40	58	4	CC	1.17	0.673	1.33	0.60	5.4	1.17	0.673	-0.363	+0.15	1.0
Toba 1978	52	3		DWBA	1.18	0.7	1.182	0.692	5.4	1.18	0.7	+0.42		
De Swiniarski 1976a	30.3	3	3	CC	1.11	0.68	1.34	0.54	6.43	0.86	0.55	-0.40	+0.10	1.16
De Swiniarski 1973	25.3	3	3	CC	1.15	0.65	1.33	0.67	6.55	0.92	0.52	-0.40	+0.15	1.20
Mean	14 - 65	95	16		1.162	0.673	1.324	0.595	6.00[a]	1.01[a]	0.613[a]	-0.369[b]	+0.146[b]	1.11[a,b]
Variance					0.018	0.016	0.027	0.047	0.53	0.12	0.066	0.014	0.014	0.03

$$\text{Mean } (x) = \frac{\sum N_i X_i}{\sum N_i}$$

N_i = Number of distributions included in the i^{th} analysis.

a) This average includes only analyses that incorporated $A_y(\theta)$ data.

b) This average includes only CC analyses.

c) All CC analyses were performed with a symmetric rotational model.

d) r_c = 1.25 fm for all proton calculations.

TABLE 9-3

SUMMARY OF POTENTIAL STRENGTHS FROM OPTICAL-MODEL ANALYSES OF ^{28}Si+n AND ^{28}Si+p

Reference	E (MeV)	No. of Dist.'s $\sigma(\theta)$	No. of Dist.'s $A_y(\theta)$	Model[c)]	V_0 (MeV)	W_{D0} (MeV)	W'_{D0} (MeV)	W_{V0} (MeV)	E_1 (MeV)	E_2 (MeV)	a	b	b'	c
Neutrons														
Present	8 - 40	22	6	CC	53.82		6.21	-2.0		13.33	0.283		0.04	0.15
Present	8 - 40	11	3	SOM	54.09	6.60	8.98	-2.0	12.4	13.3	0.31	0.10	0.10	0.15
DeVito	14 - 40	5		SOM	53.53		9.57	-1.36		5.3	0.334		0.21	0.26
Böttcher 1983	14	2	2	CC	48.47	6.38								
Haouat 1982	10 - 15	6		CC	55.00		4.90				0.30	0.12		
Tailor 1982	11 - 26	6		CC	53.08	4.72		-2.0		12.5	0.28	0.01		0.16
Kliczewski 1978	14	2		CC	42.82	9.62								
Obst 1972	10	2		CC	52.00	7.50								
Martin 1968	6	2		CC	45.34	9.20								

TABLE 9-3 Continued

Reference	E (MeV)	No. of Dist.'s $\sigma(\theta)$	No. of Dist.'s $A_y(\theta)$	Model[c]	V_0 (MeV)	W_{D0} (MeV)	W'_{D0} (MeV)	W_{V0} (MeV)	E_1 (MeV)	E_2 (MeV)	a	b	b'	c
Protons														
Hosono 1982	65	2	2	DWBA	31.06	2.83		10.93[a]						
Sakaguchi 1982	65	1	1	SOM	33.912	5.348		9.917[b]						
Fabrici 1980	14 - 40	25	3	SOM	56.0		6.6	-2.0		12.5	0.30		0.10	0.16
De Leo 1979	14 - 40	58	4	CC	54.9	6.3	11.8	-8.0	22.0	25.0	0.32	0.0	0.25	0.32
Toba 1978	52	3		DWBA	36.46	1.394		7.043						
De Swiniarski 1976a	30.3	3	3	CC	50.72	6.10								
De Swiniarski 1973	25.3	3	3	CC	48.20	5.14								

a) $r_{wv} = 0.872$ fm, $a_{wv} = 0.778$ fm

b) $r_{wv} = 0.8388$ fm, $a_{wv} = 0.3660$ fm

c) All CC analyses were performed with a symmetric rotational model.

$V_R = V_0 - aE$

$W_D = W_{DO} + bE$ for $E \leq E_1$; $= W'_{DO} - b'E$ for $E > E_1$

$W_V = 0$ for $E \leq E_2$; $= W_{VO} + cE$ for $E > E_2$

thereby permitted a description of W_D to be deduced at low energies as illustrated by the dashed line in fig. 9.4. At low energies, where S-wave scattering dominates, σ_t mostly depends upon the radius parameter r_R and the potential parameter V_R. According to Marmier and Sheldon (Marmier 1969), the total cross section for S-wave scattering at low energies, kR << 1, can be written as

$$\sigma_t = 4\pi a^2 + \lambda^2 \frac{\Gamma_n}{2D} .$$

In the above formula, the a is the scattering length, the λ is the wave length of the incident neutron, the Γ_n is the partial width of the neutron channel, and the D is the average level spacing. The first term in the expression for σ_t represents the cross section for shape elastic scattering σ_{el}^{shape}, and the second term is the absorptive cross section σ_{abs}. Although the scattering length is predominantly determined by the OM parameters r_R and V_R, it is also dependent upon the other parameters. For instance, at E_n = 1.0 MeV, increasing W_D from 1.0 MeV to 4.6 MeV increased σ_{abs} from 752 mb to 1637 mb and decreased σ_{el}^{shape} from 3018 mb to 2079 mb, thus keeping σ_t essentially constant. On the other hand, reducing r_R and r_I by 20% lowered σ_{el}^{shape} by about 40% and did not change σ_{abs}, thereby resulting in a 25% reduction in σ_t. Similarly, a 20% increase in V_R produced a 30% decrease in σ_t.

9.3.2 Sensitivities to the Sign of the Deformation Parameters

A recent study by Thompson and Eck (Thompson 1977) strongly suggested negative quadrupole and positive hexadecapole potential deformation parameters ($\beta_2 < 0$ and $\beta_4 > 0$) for the K = 0 rotational band in ^{28}Si. Thompson and Eck extracted the values of β_2 and β_4 from existing analyses of scattering observed with a wide variety of probes. Their evaluation included the analyses of data for elastic and inelastic scattering to the 2^+ and 4^+ states of ^{28}Si with n, p, d, ^{3}He, ^{4}He, and ^{12}C. The description of these data in the various analyses consistently preferred $\beta_2 < 0$ and $\beta_4 > 0$. A more recent analysis by Böttcher *et al.* (Böttcher 1983) showed that the predictions for $A_y(\theta)$ at back angles for neutron scattering to the 2^+ state in ^{28}Si were very sensitive to the sign of β_2. In their analysis the negative value of β_2 was also preferred. Furthermore, the evaluation by Thompson and Eck and the analysis by Böttcher *et al.* were in good agreement with the Hartree-Fock calculations of Lee and Cusson (Lee 1972).

Because the above reports showed that scattering observables are sensitive to the sign of the potential deformation parameters, various calculations were performed to test the sensitivity of the present data and calculations to the signs of β_2 and β_4. These calculations were made at 14 and 17 MeV because both $\sigma(\theta)$ and $A_y(\theta)$ data were available at these energies and the CN contributions were negligible for elastic scattering and inelastic scattering to the first 2^+ state. However, it was necessary to add the CN contributions to the calculations of the 4^+ observables. The results of these tests are shown in figures 9.6 and 9.7. The

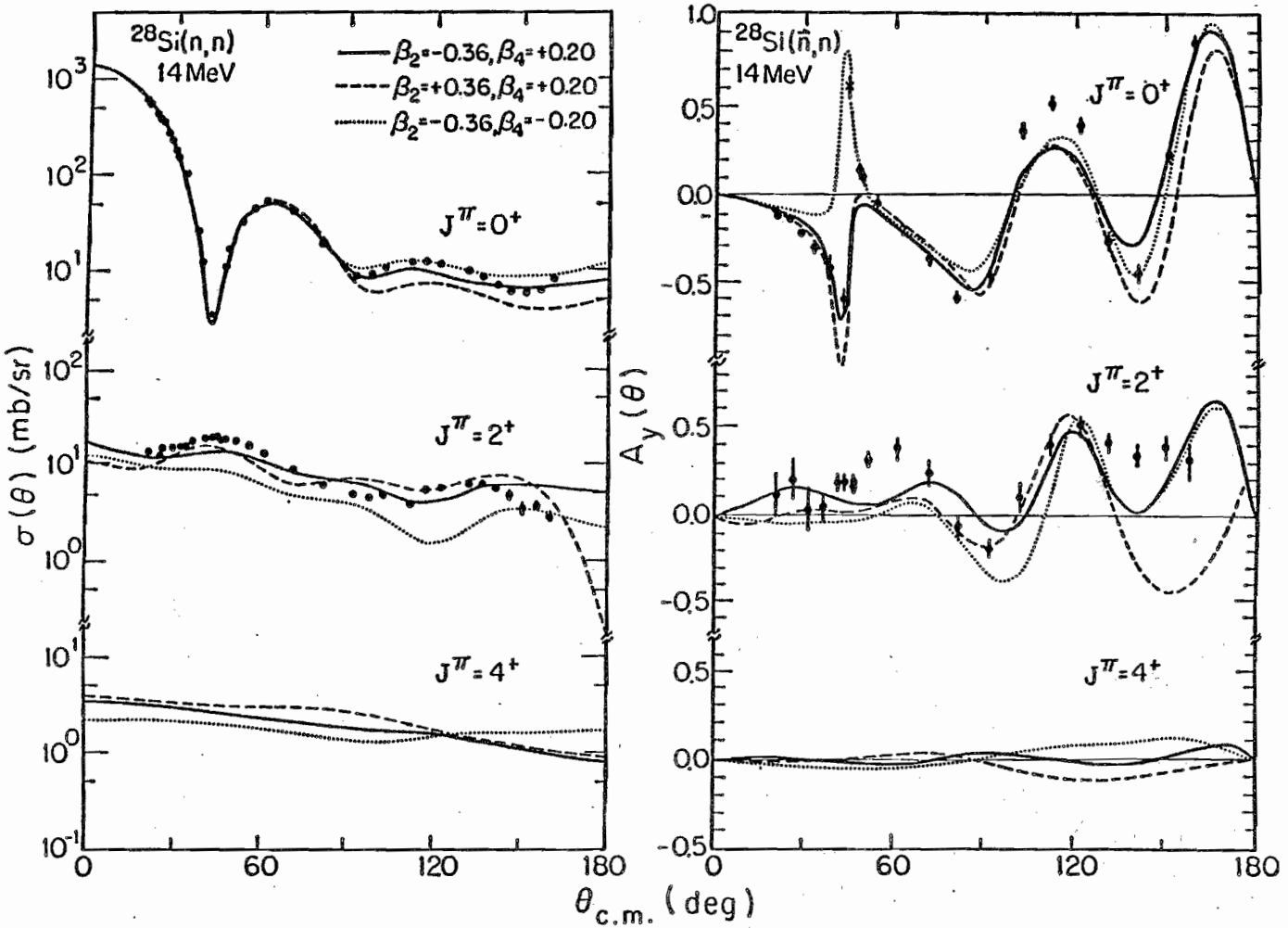

Figure 9.6. CC calculations of ^{28}Si+n at 14 MeV which illustrate the sensitivity of the data and calculations to the signs of the β_2 and β_4. In all cases, $\delta_{so} = 1.2\delta_c$, $W_v = 0$, and V_R and W_D were searched upon to optimize the fits. The geometrical OM parameters were taken from set-A of table 9-1.

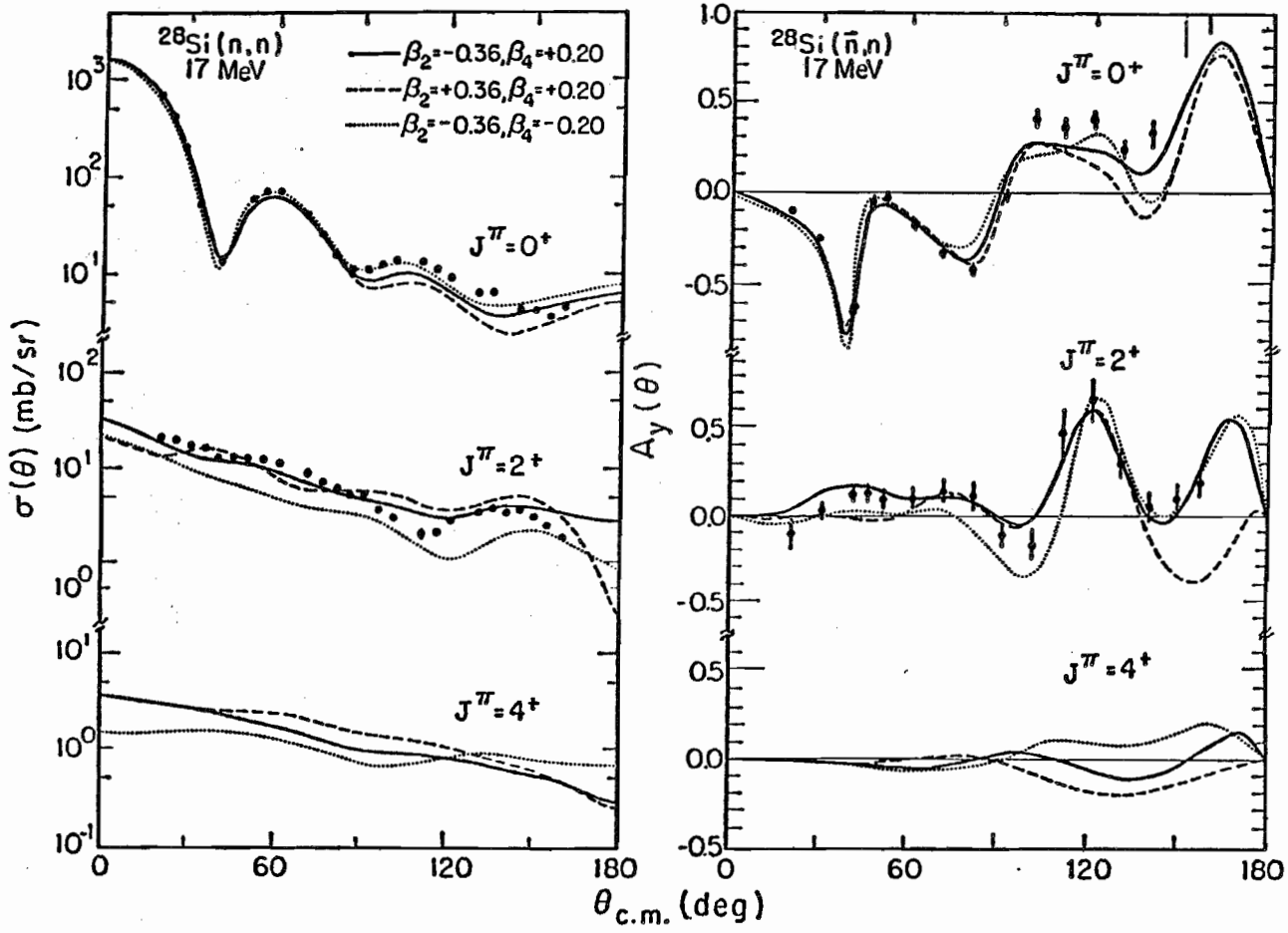

Figure 9.7. CC calculations of ^{28}Si+n at 17 MeV to illustrate the sensitivity of the data and calculations to the signs of the β_2 and β_4. In all cases, $\delta_{so} = 1.2\delta_c$, $W_v = 0$, and V_R and W_D were searched upon to optimize the fits. The geometrical OM parameters are listed in table 9-1.

geometrical parameters are listed in set-A of table 9-1. The spin-orbit deformation length δ_{so} was fixed to $\delta_{so} = 1.2\delta_c$. In each case W_v was set to zero, and V_R and W_D were searched on to optimize the fits.

The fits to the $\sigma(\theta)$ and $A_y(\theta)$ data at 14 and 17 MeV preferred an oblate shaped potential ($\beta_2 < 0$) with $\beta_4 > 0$. The description of the elastic scattering $\sigma(\theta)$ at back angles was very sensitive to the sign of β_2; slightly better fits were obtained with $\beta_2 < 0$, than with $\beta_2 > 0$. The quality of the fits to the $\sigma(\theta)$ data for inelastic scattering to the 2^+ state were about the same for both signs of β_2. The calculated $\sigma(\theta)$ for inelastic scattering to the 2^+ state was substantially lower than the data when $\beta_4 < 0$. Perhaps this discrepancy between calculation and data could have been corrected by adjusting the geometrical parameters of the imaginary potential. The calculations of $\sigma(\theta)$ for scattering to the 4^+ state showed little sensitivity to the signs of β_2 or β_4.

The $A_y(\theta)$ data of the elastically scattered neutrons showed only little sensitivity to the sign of β_2. However, at 14 MeV, the calculated $A_y(\theta)$ for elastic scattering around $\theta_{c.m.} = 40^\circ$ was extremely sensitive to the sign of β_4. Similarly, Böttcher *et al.* (Böttcher 1983) cited a sensitivity around $\theta_{c.m.} = 40^\circ$ to the values of the SO potential parameters, especially to a_{so}. In the present analysis, we also found that the $A_y(\theta)$ in this narrow angular region was very sensitive to the parameterization of the central well. We concluded that the high sensitivity of the $A_y(\theta)$ around $\theta_{c.m.} = 40^\circ$ to the OM parameters was probably due to the combination of partial waves necessary to produce the deep minimum in the elastic differential cross section around $\theta_{c.m.} = 40^\circ$, and therefore, the description of the $A_y(\theta)$ in this narrow angular region

did not provide a valid test for determining either the sign of β_4 or the magnitude of a_{so}.

The $A_y(\theta)$ at back angles for inelastic scattering to the 2^+ state were very sensitive to the sign of β_2. These data showed little sensitivity to the sign of β_4. One pronounced observation was that the data and calculations for back angle scattering showed a significantly higher sensitivity to the shape of the nuclear potential than did the forward angle scattering. Intuitively, on would expect that observables that are sensitive to the shape of the nuclear potential to be most sensitive at back angles. This is because back angle scattering is mainly due to projectiles with low incident angular momenta (small ℓ-values), meaning that these projectiles come closer to the nucleus than those that scatter to forward angles (large ℓ-values), and therefore they are influenced more by the shape of the nuclear surface.

The results of the above tests were in good agreement with the accepted signs of β_2 and β_4 (Lee 1972 and Thompson 1977); our calculations of both $\sigma(\theta)$ and $A_y(\theta)$ data preferred $\beta_2 < 0$ and $\beta_4 > 0$, thus adding more evidence of the oblate shape of ^{28}Si. We found that the most sensitive observable to the sign of β_2 was the $A_y(\theta)$ data for inelastic scattering to the 2^+ state and that the $A_y(\theta)$ for inelastic scattering to the 4^+ state was the most sensitive observable to the sign of β_4. The availability of more $A_y(\theta)$ data for inelastic nucleon scattering to the 4^+ state, in particular neutron scattering for which no data exist at present, will provide additional information for reducing the ambiguities in the sign of β_4. The calculations showed sizable sensitivities to the sign of β_4 at energies above 15 MeV, i.e., energies at which the CN

contributions are small (see fig. 7.5).

9.3.3 Deformation of the Spin-orbit Potential Deduced from $^{28}Si + n$

Prior to the works of Guss et al. (Guss 1982b), Floyd et al. (Floyd 1983), and Böttcher et al. (Böttcher 1983) all of the information about the deformation of the SO part of the neutron-nucleus optical-model potential had been deduced from the analysis of proton inelastic scattering data. Guss et al. analyzed $A_y(\theta)$ data for neutron inelastic scattering from medium weight nuclei at 10 MeV with CC calculations. From these analyses they deduced that the ratio of the deformation lengths of the spin-orbit potential (SOP) to that of the central potential was about unity, that is, $\delta_{so}/\delta_c = \beta_{so}r_{so}/\beta_c r_c \sim 1$. For comparison to proton scattering, they analyzed the corresponding $(\vec{p},p')$ data with an optical potential that employed geometrical parameters which were derived in their analysis of the $(\vec{n},n')$ data. They found that the ratio δ_{so}/δ_c was about unity for both proton and neutron inelastic scattering, and that the deformation of the SOP was remarkably independent of the isospin of the incident nucleon. This marked the first useful comparison between the SO deformation parameter derived from $(\vec{p},p')$ data and that deduced from $(\vec{n},n')$ data. On the other hand, Floyd et al. (Floyd 1983) and Guss et al. (Guss 1982b) had to enhance the deformation of the SOP by a factor of two ($\delta_{so} = 2\delta_c$) in order to describe their $A_y(\theta)$ data for neutron inelastic scattering from ^{54}Fe at 10 MeV. These results were consistent with the corresponding $^{54}Fe(\vec{p},p')$ analysis by Guss et al. (Guss 1982b) and therefore provided support for the above findings of Guss et al. (i.e., the deformation of the SOP is essentially independent of the isospin of

the incident nucleon). Böttcher et al. were able to describe their $A_y(\theta)$ data for neutron inelastic scattering from ^{28}Si at 14 MeV with $\beta_{so} = 1.5\beta_c$ (i.e., $\delta_{so} = 1.33\delta_c$). Similarly, De Swiniarski et al. (De Swiniarski 1973 and De Swiniarski 1976a) described their $A_y(\theta)$ data for $^{28}Si(\vec{p},p')$ at 25.3 and 24.5 MeV equally well with $\beta_{so} = 1.5\beta_c$ or with $\delta_{so} = 1.18\delta_c$. Comparison of the above results for $^{28}Si(\vec{n},n')$ with the results of the $^{28}Si(\vec{p},p')$ analyses provided additional evidence that the deformation of the SOP shows only a small dependence on the isospin of the incident nucleon.

The high quality of the present $A_y(\theta)$ data and the success in describing these data with a symmetric rotational model encouraged us to attempt to accurately determine the deformation of the SO part of the optical potential for $^{28}Si + \vec{n}$. For this series of calculations, the parameters in set-A of table 9-1 were used. However, the $A_y(\theta)$ data at 10 MeV was excluded because the earlier model calculations failed to reproduce the large negative values of the inelastic $A_y(\theta)$ data at forward angles. The analyzing powers at 14 and 17 MeV were computed for the three cases of $\delta_{so} = 0$, $\delta_{so} = \delta_c$, and $\delta_{so} = 2\delta_c$. For each calculation, W_v was set to zero, and V_R and W_D were searched upon for optimum fits to both $\sigma(\theta)$ and $A_y(\theta)$. The results of these calculations are shown in fig. 9.8. The fits to the $\sigma(\theta)$ data are effected only slightly by changes in δ_{so} and are not shown here. The best fits were obtained with $\delta_{so} = (1.2 \pm 0.2)\delta_c$ or with $\beta_{so} = (1.4 \pm 0.2)\beta_c$. These values of δ_{so}/δ_c are in the same range as those obtained in the previous findings for all the other nuclei investigated (Guss 1982b) except for the unusual case of ^{54}Fe (Guss 1982b and Floyd 1983). In addition, these results supported the findings of

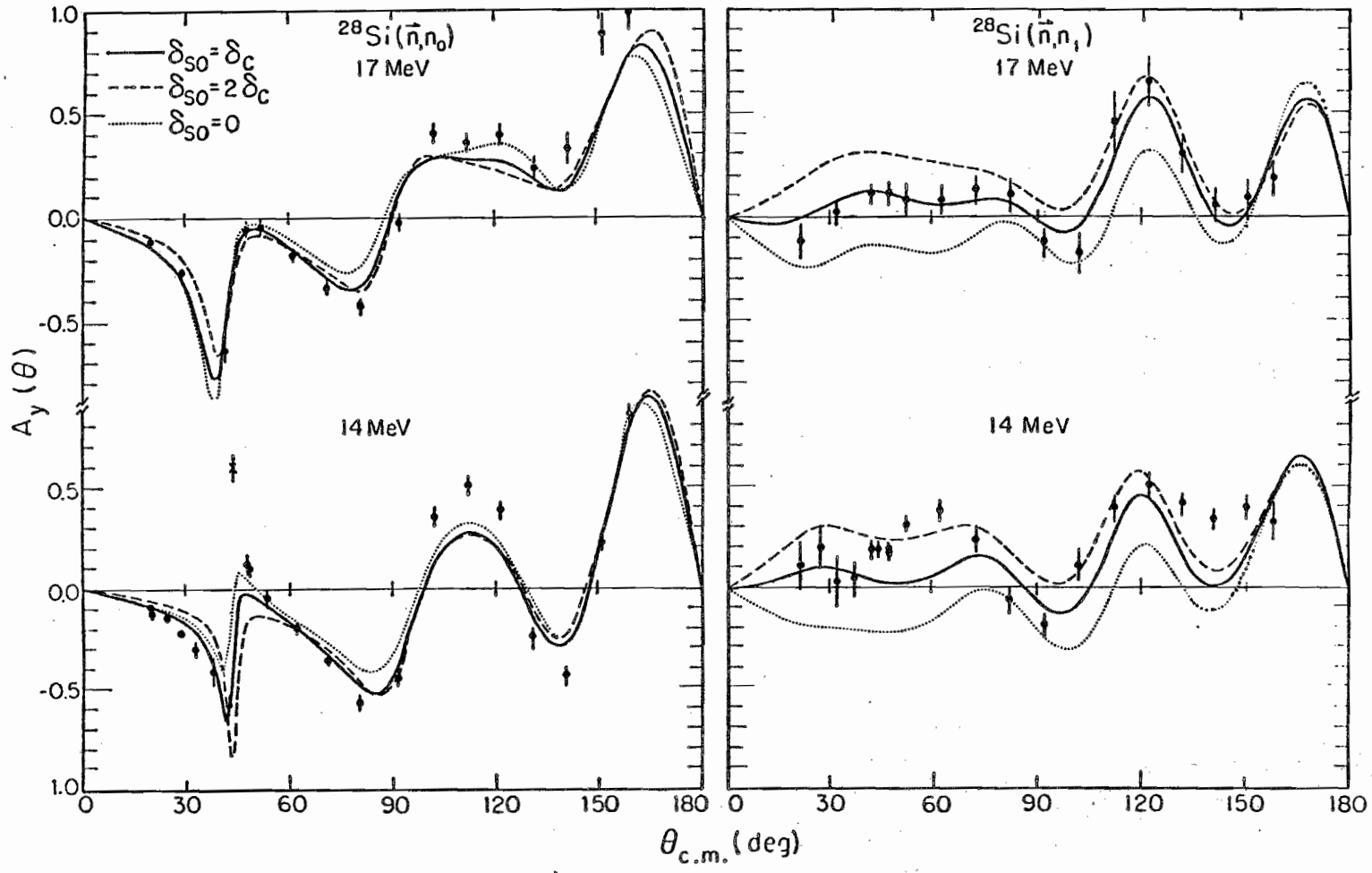

Figure 9.8. CC calculations of $^{28}Si+\vec{n}$ at 14 and 17 MeV to deduce information about the deformation parameter of the spin-orbit potential. The geometrical parameters of set-A in table 9-1 were used in these calculations. The value of the deformation parameters of the central well were fixed to $\beta_2 = -0.36$ and $\beta_4 = +0.20$.

Guss et al. that the deformation of the SOP for $(\vec{n},n')$ is very similar to that derived from the corresponding $(\vec{p},p')$ analysis.

9.3.4 Coulomb Correction to OMP for ^{28}Si

The phenomenological local OMP may be expressed as a sum of the terms

$$-U(r,E) = U_N(r,E) - V_c(r) - U_{so}(r) \quad . \qquad (9.5)$$

The notation is chosen to be consistent with the expressions cited by Rapaport et al. (Rapaport 1979). In the above expression, $V_c(r)$ is the Coulomb potential due to a uniformly charged sphere and $U_{so}(r)$ is the SO potential described in chapter 8. We shall concentrate our attention on the nuclear part $U_N(r,E)$, which as mentioned in chapter 8 is a complex potential $U_N(r,E) = V_N(r,E) + iW_N(r,E)$. According to the Lane model (Lane 1962), U_N can be separated into isoscalar and isovector parts

$$U_N(r,E) = U_0(r,E) \pm \varepsilon U_1(r,E) + \Delta U_c(r,E) \quad .$$

The nuclear asymmetry parameter is represented by $\varepsilon = (N-Z)/A$ with the + sign for incident protons and the - sign for incident neutrons. The Coulomb-correction term $\Delta U_c(r,E)$ has typically been parameterized only as a real term, $\Delta V_c f(r) = 0.4zZ/A^{1/3} f(r)$ (Perey 1963a). For nuclei with T = 0, that is, when N=Z, the nuclear potential depends only on the isoscalar component and therefore can be written as

$$U_N(r,E) = U_0(r,E) + \Delta U_c(r,E) \quad .$$

Thus, information for T=0 nuclei is particularly useful to study the ΔU_c term, since it does not get confused with the U_1 term, which is still not well parameterized either.

The $\Delta U_c(r,E)$ term is a consequence of the momentum dependence of the OMP. The strength of the nuclear potential is determined by the momentum of the incident nucleon inside the nucleus (Lane 1957 and Bohr 1969). The nuclear potential becomes increasely absorptive as the momentum of the incident nucleon is decreased. This momentum dependence can be expressed as an energy dependence as implied by eqn. (9.5). Because the momentum of the proton is reduced by the Coulomb repulsion of the target nucleus, a proton incident on a nucleus will experience a more absorptive potential than a neutron of equal energy.

9.3.4.1 Coulomb Correction to the Real Component of the OMP

For T = 0 nuclei, the real part of the OMP may be written as

$$V_N(r,E) = V_0(r,E) + \Delta V_c(r,E) \ .$$

If we assume the same radial dependence for $V_0(r,E)$ and $\Delta V_c(r,E)$, which is normally the Woods-Saxon type (Perey 1963a), then we need to consider only the relative strengths given by

$$V_N(E) = V_0(E) + \Delta V_c(E) \ .$$

Furthermore, assuming a linear energy dependence for $V_0(E)$ will permit $\Delta V_c(E)$ to be energy independent (Satchler 1969). Thus, the strengths of the nuclear potential for proton and neutron scattering can be expressed

simply as

$$V_p(E) = V_{00} - \alpha E + \Delta V_c \qquad (9.6)$$

and

$$V_n(E) = V_{00} - \alpha E \ . \qquad (9.7)$$

It is clear from the above equations that information about the Coulomb-correction term ΔV_c can be deduced by comparing the results of OM analyses of proton and neutron scattering from the same T = 0 nucleus. The Coulomb correction for the real part of the OMP has been deduced for several T = 0 nuclei by Rapaport _et al_. (Rapaport 1983). As cited by Rapaport _et al_. (Rapaport 1979), the determination of ΔV_c can be made less dependent on the choice of geometrical parameters provided the volume integrals per nucleon are compared instead of potential strengths. In terms of volume integrals per nucleon, the expressions corresponding to equations (9.6) and (9.7) become

$$(J_v/A)_p = (J_{v_0}/A) - \alpha' E + (\Delta J_v/A)_c \qquad (9.8)$$

and

$$(J_v/A)_n = (J_{v_0}/A) - \alpha' E \ . \qquad (9.9)$$

To extract the value of $(\Delta J_v/A)_c$, we re-analyzed the ^{28}Si + n data with a symmetric rotational model using the OM parameters that had been deduced from the analysis of ^{28}Si + p data over a similar energy range.

We used the geometrical parameters reported by Fabrici et al. (Fabrici 1980) and the deformation parameters of De Leo et al. (De Leo 1979). The fits to the ^{28}Si+n data were optimized by searching upon V_R and W_D. The resulting fits are shown as dashed curves in figures 9.2, 9.3 and 9.5, and the parameters are listed in table 9-1 as set-B. Although the angular distributions were well described by this model, the predicted total neutron cross section σ_t was consistently about 5% higher than the experimentally observed values. Because the parameters in set-A accurately reproduced the total cross section, the discrepancy in σ_t when calculated with the parameters of set-B was believed to be due to the radius parameters of the real and imaginary wells. The corresponding CC analysis of the proton data of De Leo et al. (De Leo 1979) was performed by Tailor (Tailor 1982). He used the same geometrical and deformation parameters as described above and searched upon V_R and W_D to obtain best fits at each energy. His results are listed as set-A in table 5-4 of (Tailor 1982). The volume integrals per nucleon resulting from Tailor's analysis are plotted as open circles in fig. 9.9.

The volume integrals per nucleon J_v/A derived from the (n,n) and the (p,p) analyses were separately fitted with equal-weight least-square routines. The slopes of the resultant lines were identical, having m = -2.77 MeV$\cdot$fm^3/MeV. Thus, the parameter α' in equations (9.8) and (9.9) was taken as $\alpha' = 2.77$ MeV$\cdot$fm^3/MeV. The Coulomb-correction term was obtained by taking the difference of the following energy-averaged relations:

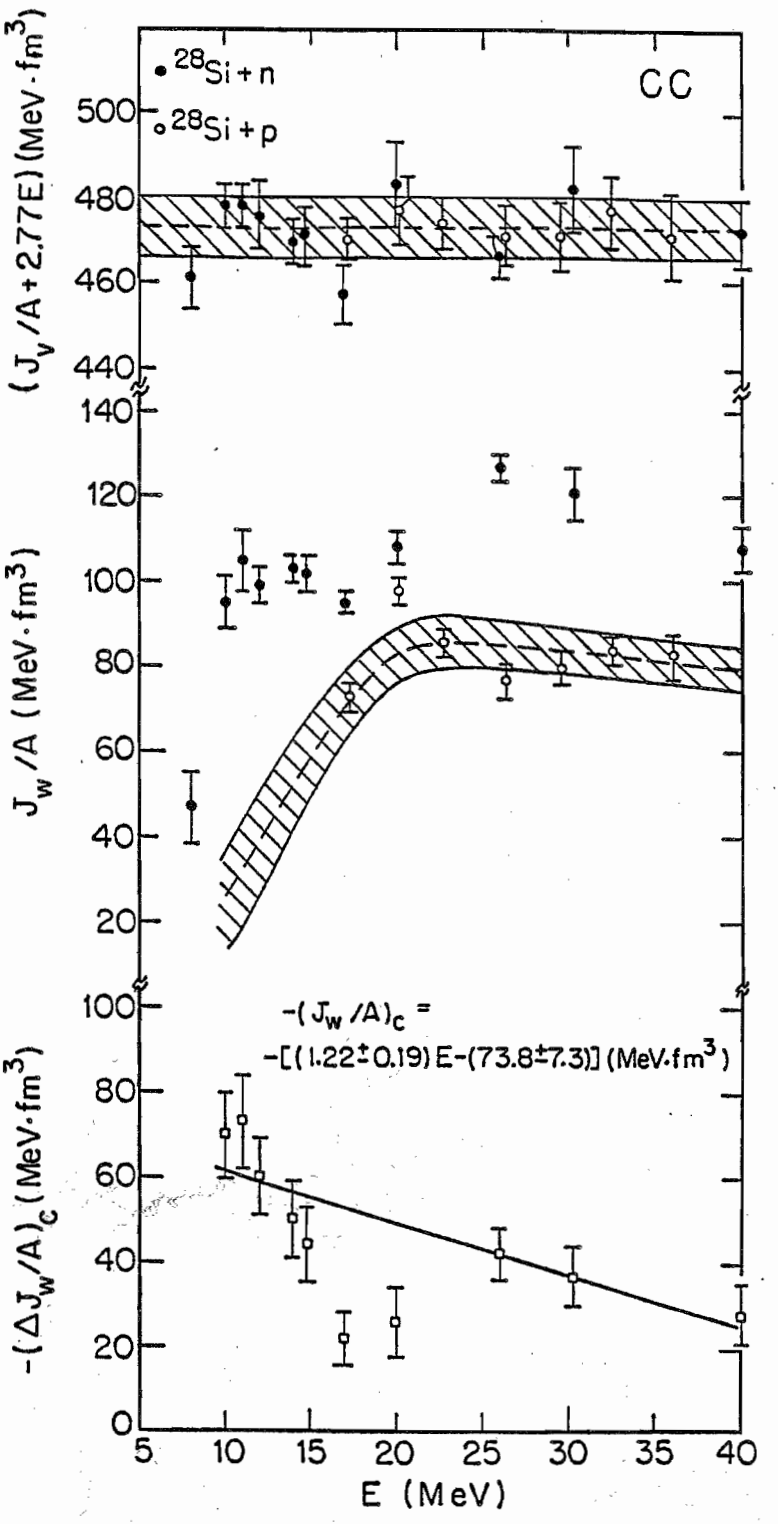

Figure 9.9. Volume integrals per nucleon versus incident projectile energy. Comparison of ^{28}Si(n,n) and ^{28}Si(p,p) CC analyses to deduce the Coulomb corrections to the real and imaginary parts for the OMP.

$$(J_{v_0}/A) + (\Delta J_v/A)_c = [(J_v/A)_p + 2.77\ E]$$

$$(J_{v_0}/A) = [(J_v/A)_n + 2.77\ E]\ .$$

The values of $[(J_v/A)_p + 2.77\ E]$ and $[(J_v/A)_n + 2.77\ E]$ for proton and neutron scattering data were plotted as a function of projectile energy E as shown in fig. 9.9. The mean value of $[(J_v/A)_p + 2.77\ E]$ was (469 ± 12) MeV fm^3 and that of $[(J_v/A)_n + 2.77\ E]$ was (473 ± 8) Mev fm^3. The mean value deduced from the neutron data is represented by the dashed line in fig. 9.9. The shaded region represents the standard deviation in this mean value, which is about 1.7%. The numerical closeness of the mean values and the size of the uncertainties precluded a meaningful extraction of the Coulomb correction $(\Delta J_v/A)_c$.

Because natural samples were used in the ^{28}Si + n and ^{28}Si + p experiments, it was thought that the T = 1 and T = 2 impurities in the data due to the presence of ^{29}Si and ^{30}Si in the samples distorted the results. The relative abundances of the isotopes in natural silicon are listed in table 2-1. Calculations showed that the presence of the T = 1 and T = 2 components of isospin effected the determination of the strength of the real potentials by less than 0.5%.

The amount and quality of the available (n,n) and (p,p) data permitted the relatively accurate determination of the mean values of the volume integrals per nucleon for neutrons and protons. The uncertainty in the mean value for neutrons was 30% lower than the uncertainties deduced by Tailor (Tailor 1982) and Rapaport (Rapaport 1982). However, like Tailor and Rapaport, the uncertainties in the mean values of the volume integrals for neutrons and protons were still too large to permit the

extraction of a meaningful value for $(\Delta J_v/A)_c$. Because the OM has many free parameters and several inherent ambiguities, many of the uncertainties in the mean values of the volume integrals per nucleon were due to the inability of OM analyses to accurately define the OM parameters. Therefore, we conclude that the limiting factor in deducing the Coulomb correction to the real part of the OMP for ^{28}Si can be attributed to the inherent ambiguities in the OM and that the inclusion of more accurate nucleon scattering data probably will only slightly reduce the uncertainties in the mean values of the volume integrals per nucleon.

9.3.4.2 Coulomb Correction to the Absorptive Component of the OMP

Unlike the real term, the imaginary part of the OMP usually consists of two parts, the volume and the surface absorptive potentials. These two parts follow different energy dependences and have different radial dependences, usually Woods-Saxon and its derivative. Therefore, it is convenient to determine the energy dependences of the imaginary wells in terms of volume integrals. These quantities can be computed using the expressions given in chapter 8. The volume integrals per nucleon of the Coulomb correction to the absorptive potential $(\Delta J_w/A)_c$ can be deduced by comparing the volume integrals per nucleon obtained from proton scattering $(J_w/A)_p$ to those obtained from neutron scattering $(J_w/A)_n$,

$$(J_w/A)_p = J_{w_0}(E)/A + (\Delta J_w/A)_c$$

and

$$(J_w/A)_n = J_{w_0}(E)/A \ .$$

Thus, $(\Delta J_w/A)_c$ may be written as

$$-(\Delta J_w/A)_c = (J_w/A)_n - (J_w/A)_p \ .$$

The volume integrals for the proton data were taken from set-A of (Tailor 1982) and the neutron values were obtained from set-B in table 9-1 of the present analysis. The volume integrals per nucleon were plotted against projectile energy as shown in fig. 9.9. The solid circles represent the neutron values and the proton values are represented by the open circles. The curve through the proton points is a guide to show the trend of the data. Because Tailor did not include proton data in his analysis below 17 MeV, the curve is not well defined at the lower energies. The shaded region around the curve was chosen to reflect the uncertainties in the proton values; the width of the shaded region was progressively increased with decreasing energies below 17 MeV because there were no available proton points to define the curve at these lower energies. The volume integrals per nucleon for the negative of the Coulomb correction $-(J_w/A)_c$ were computed for $E \geq 10$ MeV at energies where neutron data were available. The values of $(J_w/A)_p$ were taken from the curve and the height of the shaded region represented the uncertainties in these proton values. The values of $-(J_w/A)_c$ were plotted as open squares. The errors on these points were computed as the sum of squares of the uncertainties in the neutron points and the proton curve. The line through the values of $-(J_w/A)_c$ represents a least-square fit in which all values received equal weighting. The points at 17 and 20 MeV were excluded from this fit because of normalization uncertainities in the neutron data (see chapter 8 for details). The Coulomb correction to the

absorptive potential was found to be

$$(J_w/A)_c = -\left[(74 \pm 7) - (1.22 \pm 0.19)E\right] \text{ MeV}\cdot\text{fm}^3 ,$$

which intersects the energy axis at about 61 MeV. This is in agreement with the value reported by DeVito *et al.* (Devito 1983) for ^{28}Si:

$$(J_w/A)_c = -\left[(51 \pm 8) - (0.66 \pm 0.17)E\right] \text{ MeV}\cdot\text{fm}^3 ,$$

which is zero at about 77 MeV.

9.4 Coupled-Channels Analysis of ^{32}S + n

9.4.1 Description of the Data with Coupled-Channels Calculations

As described below, angular distributions of cross sections and analyzing powers for elastically and inelastically scattered neutrons from ^{32}S over the energy range from 8 to 40 MeV have been successfully described with CC calculations. In this analysis the low-lying states in ^{32}S were modeled as the lower levels of a vibrational band. All elastic scattering cross sections used in this analysis were obtained from the references listed in chapter 8. The inelastic scattering cross sections for the first 2^+ state at 8, 10, 12, 14, and 17 MeV were measured at TUNL as described in chapter 2. Differential cross sections for neutron inelastic scattering to the 2_1^+, 2_2^+, and 4^+ states at 10 and 14.8 MeV were obtained from (BLC-82). In addition, differential cross sections for inelastic scattering to the 2_1^+ state at 20 MeV and for inelastic

scattering to the 2_1^+, 2_2^+, and 3^- states at 26 MeV were obtained from (Tailor 1982). All analyzing power data were measured at TUNL using the techniques described in chapter 2. These data were the first $A_y(\theta)$ data to be reported for neutron scattering from ^{32}S at energies above 8 MeV, and as such, this analysis marked the first determination of the parameters for the SO part of the OMP for neutron scattering from ^{32}S. Furthermore, the high quality of these $A_y(\theta)$ data permitted an accurate determination of the parameters of the spin-orbit potential. As in the earlier case of ^{28}Si, the code ECIS79 by Raynal was used to perform the CC calculations.

Previous analyses of nucleon scattering from ^{32}S with phenomenological collective models of the nucleus have concluded that elastic scattering and inelastic scattering to the first excited state can be described equally well with either a rotational or vibrational model (Obst 1973, De Swiniarski 1976a, Yamanouti 1977, Haouat 1982, and Tailor 1982). On the other hand, the large intrinsic quadrupole moment of ^{32}S (Stelson 1965, Häusser 1971, Lee 1972, and De Swiniarski 1976b) suggests that the nucleus is permanently deformed and therefore should be modeled as a rigid rotor as explained in section 9.2. However, the energy level spacings and the conclusions derived from analyses of lifetime measurements (Garvey 1969, Ollerhead 1970, Garvey 1971, and Coetzee 1972) and measurements of electromagnetic transition probabilities $B(E\lambda)$ (Garvey 1971, Häusser 1971, Ingebretsen 1971, and Coetzee 1972) are strongly indicative of the vibrational character of the collective states in ^{32}S. That is, simultaneous descriptions of the energy spectrum and $B(E\lambda)$ values have required the collective excitations of ^{32}S to be modeled as

vibrational states with quadrupole and octupole modes of vibration. However, there is much evidence that the low-lying states in ^{32}S can not be modeled as simple vibrational states. Explanations of the non-zero $B(E_2)$ value for the $2_2^+ \rightarrow 0_1^+$ transition has required the mixing of the one-phonon 2_1^+ vibrational state and the two-phonon 2_2^+ state (Häusser 1971, Garvey 1971, Ingebretsen 1971, Coetzee 1972, and Olin 1974). In addition, as seen in the energy diagram of ^{32}S in fig. 9.1, the splitting of the quadrupole triplet (0_2^+, 2_2^+, 4^+) indicated that the separation of the states deviated from the simple harmonic vibrational model and probably could be described better with an anharmonic model (Häusser 1971 and Olin 1974).

The findings of Lombard and Raynal (Lombard 1973), who analyzed differential cross sections and analyzing powers for elastic and inelastic scattering of 24.5 MeV protons from ^{32}S, were in good agreement with the results of the above electromagnetic studies. They compared the data to CC calculations that were performed with four different models; a symmetric rotor, an asymmetric rotor, a simple harmonic vibrator, and an anharmonic vibrator. Appreciably better fits were obtained using the anharmonic vibrational model with an admixture of one-phonon and two-phonon states. They described the wavefunctions for the 2_1^+, 2_2^+, and 4^+ states as a mixture of one-phonon and two-phonon states using the method introduced by Tamura (Tamura 1966). According to Tamura, a state of spin I can be represented as

$$|I\rangle = \cos(\phi)|\text{one phonon}\rangle + \sin(\phi)|\text{two phonon}\rangle .$$

Lombard and Raynal coupled the 0^+, 2_1^+, 2_2^+, and 4^+ states and determined the one-phonon component of each state. The resulting phonon-admixing angles and deformation parameters are listed below:

Level	β	ϕ
2_1^+	0.30	-28°
2_2^+	0.30	62°
4^+	0.23	-25°

Turning now to neutron scattering from ^{32}S, in a recent analysis using the coupled-channels method, Tailor (Tailor 1982) described differential cross sections for scattering to the 2_1^+, 2_2^+, and 3^- states. Because the simple harmonic vibrational model underestimated the cross section of the 2_2^+ state by a factor of 10, Tailor adapted the approach that Lombard and Raynal (Lombard 1973) used for protons. Starting with their parameters, Tailor searched on V_R, W_D, β_2, β_3, and the phonon-admixing angles. Since he did not have neutron cross section data for the 4^+ state, the values of β_4 and the phonon-admixing angle for the 4^+ state were fixed to the values reported by Lombard and Raynal. The results of his analysis are listed below:

Level	β	ϕ
2_1^+	0.35	-34°
2_2^+	0.35	56°
4^+	0.23	-25°
3^-	0.32	

Because the vibrational character of the excited states in ^{32}S has been well established by the above studies, the present analysis concentrated on the vibrational model. Differential cross sections $\sigma(\theta)$ and analyzing powers $A_y(\theta)$ for elastically and inelastically scattered neutrons from ^{32}S over the energy range from 8 to 40 MeV were successfully described with a vibrational model in which one-phonon and two-phonon wavefunctions were mixed. As in the ^{28}Si + n analysis, these calculations were performed with the CC code ECIS79 by Raynal. The 0^+, 2_1^+, 2_2^+, 4^+, and 3^- states were coupled with the the 2_1^+ and 2_2^+ states being described as admixtures of one-phonon and two-phonon states. Unlike the analyses of Lombard and Raynal (Lombard 1973) and Tailor (Tailor 1982), the 4^+ state was modeled as a pure two-phonon state in order to be consistent with the reported γ-ray branching ratios (Endt 1978).

The SOM parameters listed as set-B in table 8-2 were used as the starting parameters. All OM parameters, with the exception of W_v, were included in the search. The values for W_v were taken from the results of SOM analysis. For expedience, the geometrical parameters and the parameters of the spin-orbit potential were determined in preliminary CC calculations in which coupling to only three states (i.e., the 0^+, 2_1^+, and 2_2^+) was included.

The magnitudes of the quadrupole deformation parameter β_2 and the phonon-admixing angle ϕ_2 were adjusted to simultaneously describe the $\sigma(\theta)$ and $A_y(\theta)$ of the 2_1^+ state and the $\sigma(\theta)$ of the 2_2^+ state. The inelastic data were very sensitive to the symmetry of the wavefunctions for the 2_1^+ and 2_2^+ states. The inelastic $A_y(\theta)$ at back angles were especially sensitive to the symmetry of the wavefunctions. Significantly better fits

were obtained to all data with a symmetric 2_1^+ state (i.e., $\sin(\varphi_1) > 0$) and an anti-symmetric 2_2^+ state (i.e., $\sin(\varphi_2) < 0$). The resulting parameters were $\beta_2 = +0.31$ and $\varphi_2 = -56^\circ$. Because the wavefunctions for the 2_1^+ and 2_2^+ states must be orthogonal, the phonon-admixing angle φ_1 was computed as $\varphi_1 = \varphi_2 + 90^\circ = 34^\circ$. The octupole deformation parameter β_3 was determined by fitting the $\sigma(\theta)$ of the 3^- state at 10 and 26 MeV.

After all geometrical parameters, spin-orbit potential parameters, and phonon-admixing angles had been determined, V_R and W_D were searched upon to optimize the fits at each energy. The resulting potential strengths are listed as set-A in table 9-4, and are plotted in fig. 9.10. The solid curves are least-square fits to the points. The dashed curve is an extrapolation based on a study of the neutron total cross section σ_t at energies below 3.0 MeV. A square-root energy dependence on V_R was necessary to describe the average σ_t at low energies (i.e., $E_n \leq$ 3.0 MeV). The resulting potential strengths were described as

$$V_R = 56.91 - 2.06\ E_n^{1/2}$$

$$W_D = 1.71 + 0.35\ E_n \quad \text{for } E_n \leq 11.0 \text{ MeV}$$
$$= 5.98 - 0.04\ E_n \quad \text{for } E_n > 11.0 \text{ MeV}$$

$$W_v = 0.00 \quad \text{for } E_n \leq 12.50 \text{ MeV}$$
$$= -2.09 + 0.17\ E_n \quad \text{for } E_n > 12.50 \text{ MeV}\ .$$

The fits to the $\sigma(\theta)$ and $A_y(\theta)$ data are represented by the solid curves in figures 9.11 through 9.13. Compound nucleus (CN) contributions were added to the CC calculations for the ground state and 2_1^+ $\sigma(\theta)$ and

TABLE 9-4

OPTICAL-MODEL PARAMETERS USED IN COUPLED-CHANNELS CALCULATIONS FOR $^{32}S+n$

	E_n (MeV)	V_R (MeV)	W_D (MeV)	J_V/A (MeV·fm^3)	J_W/A (MeV·fm^3)	χ^2/N_σ 0+	χ^2/N_σ 2+	χ^2/N_A 0+	χ^2/N_A 2+	Model
Set-A	8.0	52.1 ± 0.5	3.9 ± 0.4	476 ± 5	59 ± 6	31.8	6.2			H. Vib. (0^+, 2_1^+, 2_2^+, 4^+, 3^-);
	10.0	50.2 ± 0.3	5.3 ± 0.2	459 ± 5	82 ± 3	12.3	7.5	31.1	7.4	$\beta_2 = +0.31$, $\beta_3 = +0.33$;
	11.0	50.5 ± 0.5	5.6 ± 0.2	461 ± 5	85 ± 3	9.4				$\beta_{so} = \beta_c$
	12.0	49.5 ± 0.4	5.5 ± 0.2	452 ± 5	85 ± 3	5.7	7.5			$\phi_1 = 34^\circ$, $\phi_2 = -56^\circ$
	14.0	49.2 ± 0.4	5.5 ± 0.2	450 ± 5	87 ± 3	10.7	37.7	7.6	2.6	
	14.8	48.2 ± 0.9	6.4 ± 0.3	441 ± 9	102 ± 5	6.3	10.9			$r_R = 1.18$ fm $a_R = 0.683$ fm
	17.0	46.8 ± 1.0	5.3 ± 0.2	428 ± 9	88 ± 3	30.5	23.3	6.5	1.4	$r_I = 1.21$ fm $a_I = 0.612$ fm
	20.0	47.1 ± 1.0	5.4 ± 0.3	431 ± 9	95 ± 5	2.8	2.0			$r_{so} = 1.04$ fm $a_{so} = 0.542$ fm
	26.0	46.0 ± 0.5	5.0 ± 0.2	420 ± 4	98 ± 4	6.2	3.3			$V_{so} = 5.30$ MeV
	30.3	45.4 ± 1.1	4.7 ± 0.4	415 ± 10	101 ± 9	23.0				
	40.0	44.7 ± 1.3	4.6 ± 0.5	408 ± 12	114 ± 13	10.1				

TABLE 9-4 Continued

	E_n (MeV)	V_R (MeV)	W_D (MeV)	J_v/A (MeV·fm^3)	J_w/A (MeV·fm^3)	χ^2/N_σ 0+	χ^2/N_σ 2+	χ^2/N_A 0+	χ^2/N_A 2+	Model
Set-B	8.0	54.3 ± 0.8	5.2 ± 0.5	481 ± 7	84 ± 8	47.4	8.2			Sym. Rot. (0^+, 2_1^+);
	10.0	52.9 ± 0.4	6.2 ± 0.2	468 ± 4	101 ± 3	8.3	4.2	24.8	14.6	β_2 = +0.283;
	11.0	52.1 ± 0.5	6.8 ± 0.2	461 ± 4	111 ± 3	7.5				$\delta_{so} = \delta_c$
	12.0	52.1 ± 0.4	6.4 ± 0.2	461 ± 4	105 ± 3	6.7	7.7			
	14.0	51.2 ± 0.5	6.6 ± 0.1	453 ± 4	107 ± 2	8.6	35.1	11.1	5.7	r_R = 1.158 fm a_R = 0.703 fm
	14.8	51.2 ± 1.0	7.4 ± 0.3	453 ± 9	121 ± 5	3.6	11.9			r_I = 1.215 fm a_I = 0.640 fm
	17.0	48.0 ± 0.7	6.5 ± 0.2	425 ± 6	105 ± 3	18.0	17.5	7.7	1.7	r_{so} = 1.029 fm a_{so} = 0.661 fm
	20.0	49.4 ± 0.7	7.2 ± 0.2	437 ± 6	117 ± 3	1.2	1.5			V_{so} = 6.08 MeV
	26.0	47.5 ± 0.5	5.6 ± 0.2	420 ± 4	115 ± 4	3.4	4.2			
	30.3	45.6 ± 1.1	4.7 ± 0.3	404 ± 10	116 ± 7	18.4				
	40.0	43.3 ± 1.3	2.7 ± 0.4	383 ± 12	121 ± 18	6.1				

Set-A

W_v = 0.0 MeV for $E_n \leq$ 12.5 MeV

= (0.17E_n - 2.09 MeV) for $E_n >$ 12.5 MeV

Set-B

W_v = 0.0 MeV for $E_n \leq$ 19.9 MeV

= (0.4E_n - 7.96 MeV) for $E_n >$ 19.9 MeV

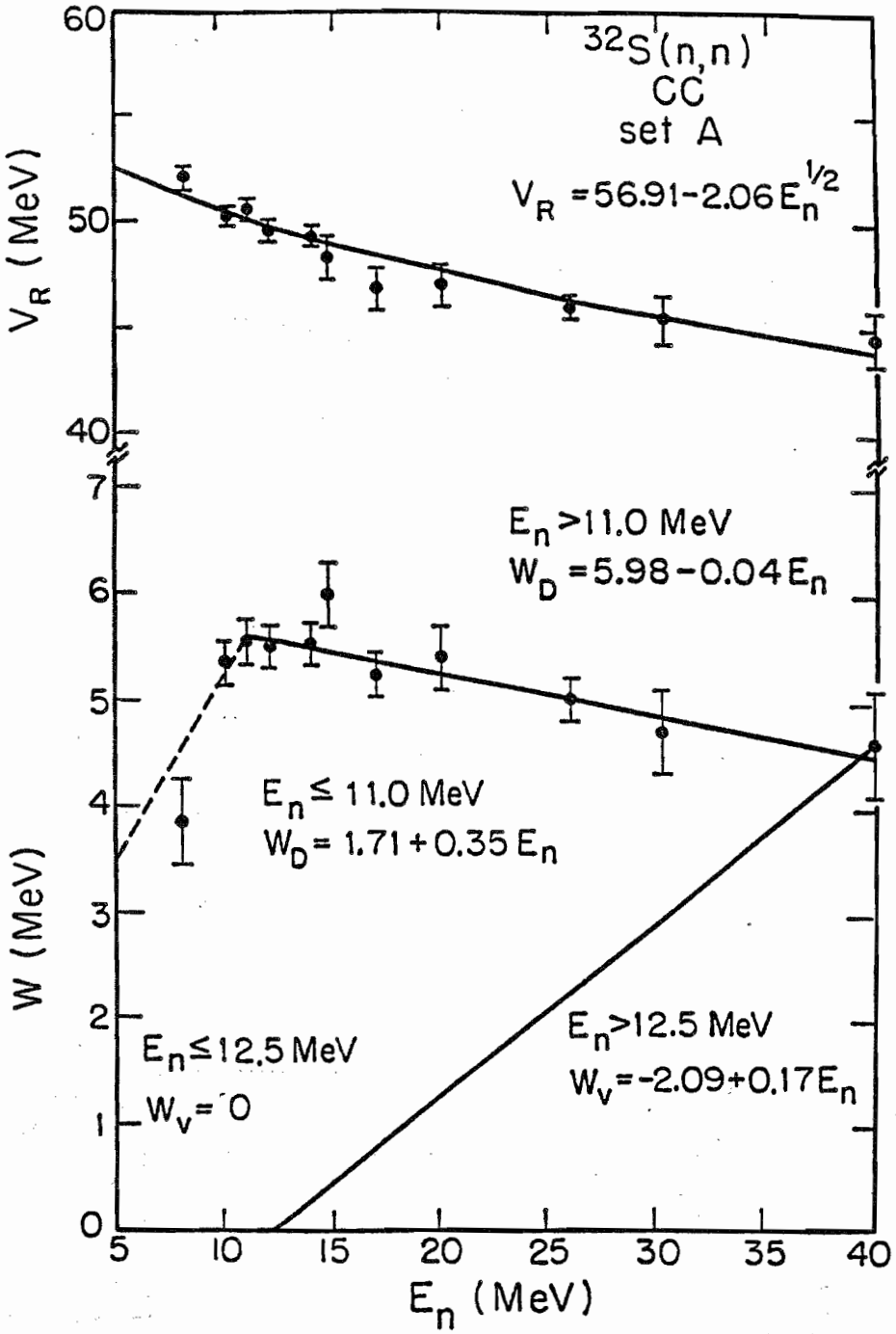

Figure 9.10. Potential strengths of the real and imaginary wells versus incident neutron energy for $^{32}S+n$. The points are the result of searches on V_R and W_D at each energy. The resulting parameters are listed as set-A in table 9-4. The curves through the potential strengths represent least-square fits. The dashed line is an extrapolation of W_D based on fitting the average neutron total cross section at low energies.

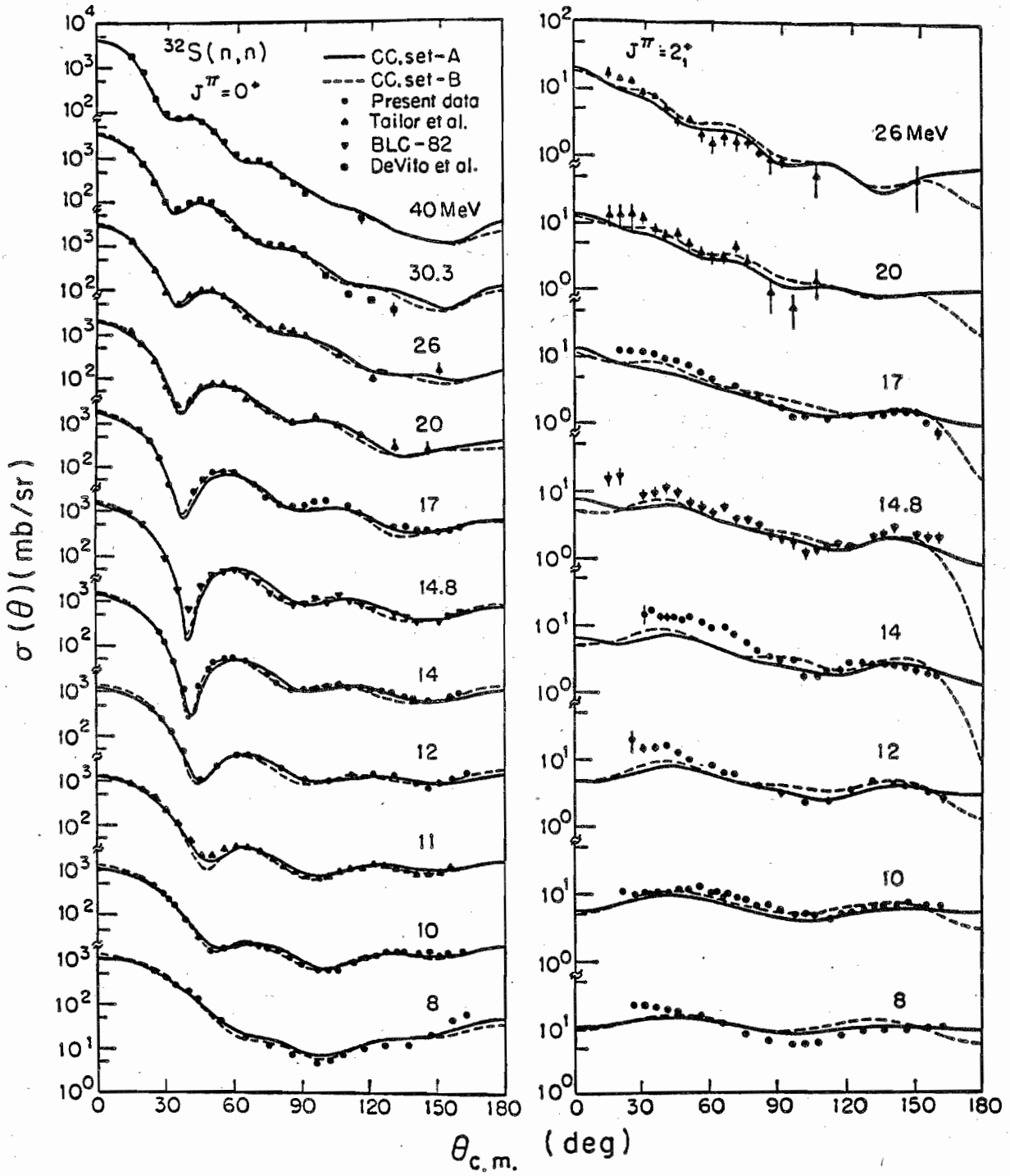

Figure 9.11. The $\sigma(\theta)$ for elastic and inelastic scattering of neutrons from ^{32}S. The solid curves through the data are the results of CC calculations which model ^{32}S as a vibrator with admixing of one-phonon and two-phonon states. The dashed curves result from an axially symmetric rotational model. All OM parameters are listed in table 9-4.

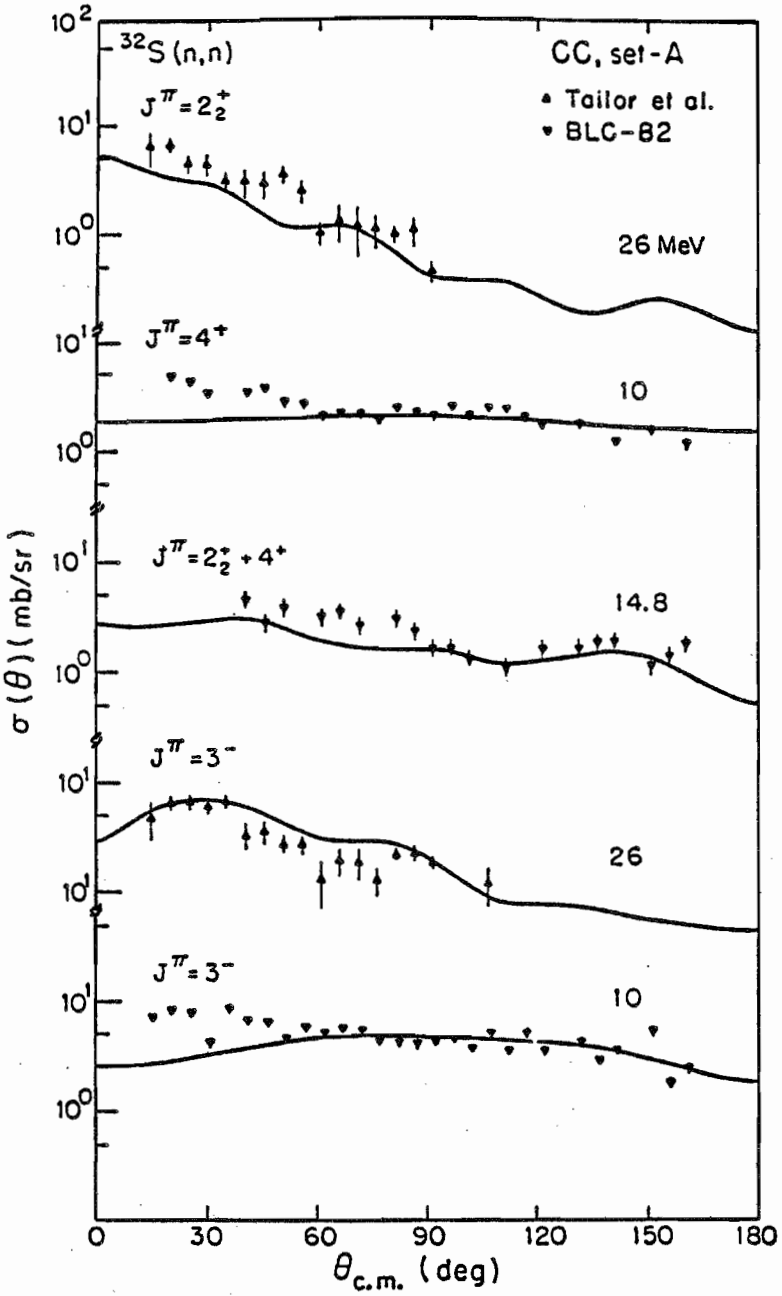

Figure 9.12. The $\sigma(\theta)$ for inelastic scattering to the 2_2^+, 4^+, and 3^- states in ^{32}S. The curves through the data are the results of CC calculations which model ^{32}S as a vibrator with admixing of one-phonon and two-phonon states. These curves were generated using the parameters in set-A of table 9-4.

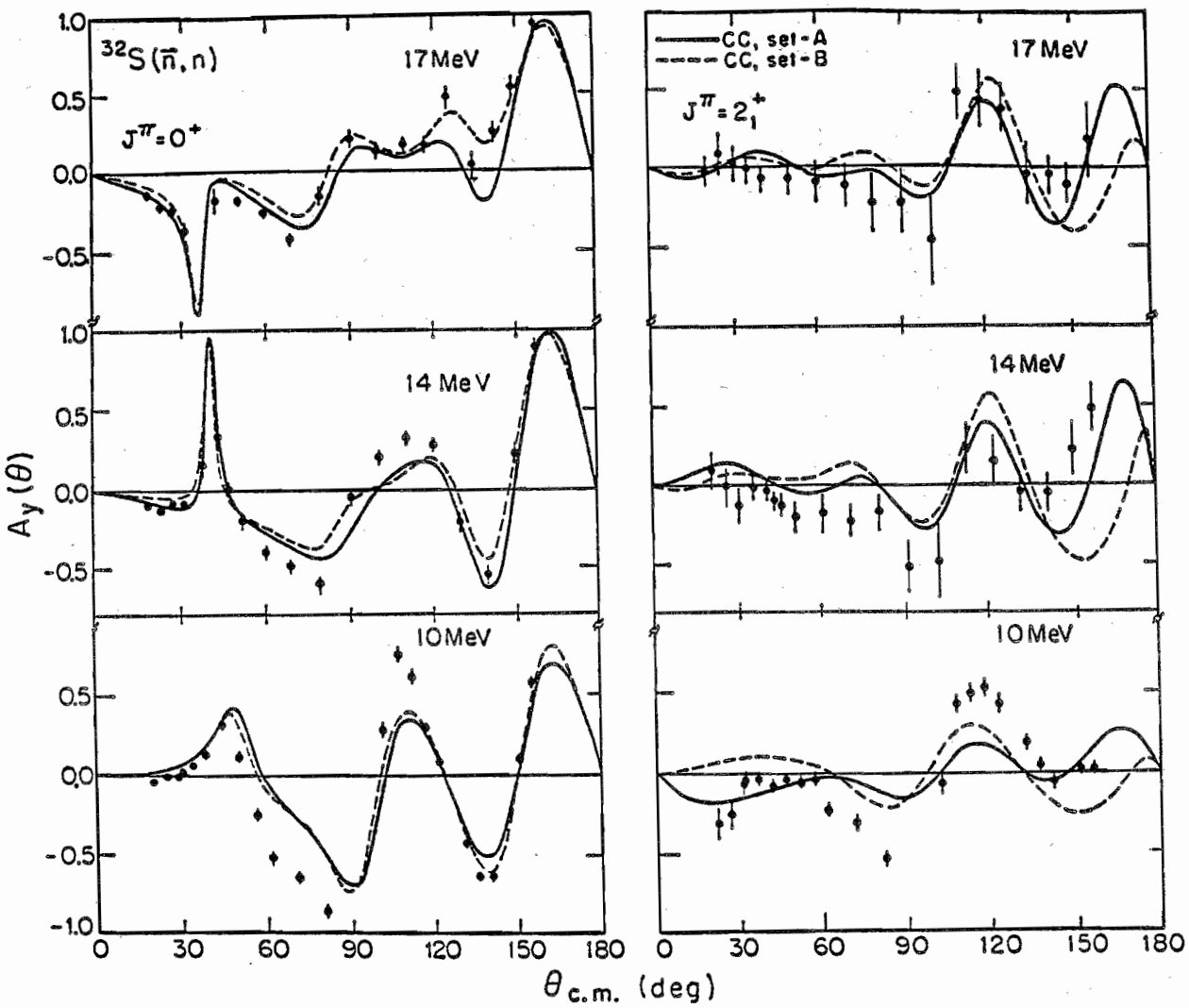

Figure 9.13. The $A_y(\theta)$ for elastic and inelastic scattering of neutrons from ^{32}S. The solid curves through the data are the results of CC calculations which model ^{32}S as a vibrator with admixing of one-phonon and two-phonon states. The dashed curves result from an axially symmetric rotational model. All OM parameters are listed in table 9-4.

$A_y(\theta)$ at energies below 14 MeV. The CC calculations for the higher excited states were corrected for CN effects at energies up to 17 MeV. The good agreement, shown in figures 9.11 through 9.13, between the data and calculations provided additional evidence that the higher collective excitations in ^{32}S can be described as being part of a vibrational band.

The vibrational model accurately reproduced the neutron total cross section σ_t at energies below 14 MeV but deviated from the experimental values at higher energies, as illustrated in fig. 9.14 by the solid curve. Because the model successfully described the angular distributions and was consistent with electromagnetic studies, the discrepancy between the calculated and the experimentally observed σ_t provided a measure of the relative effects of collective nuclear motion to the influences of the formation of particle-hole states (Block 1963, Lane 1964, and Glasgow 1970).

9.4.2 Coulomb Correction to OMP for ^{32}S

The same method as applied to deduce an approximate Coulomb correction to the OMP for nucleon scattering from ^{28}Si was applied to the case of ^{32}S. In order to compare to the ^{32}S+p results of Tailor et al. (Tailor 1982), the neutron scattering data for ^{32}S were analyzed with a symmetric rotational model with coupling between the 0^+ ground state and the 2^+ first excited state. The OM parameters and quadrupole deformation parameter β_2 were set equal to the values used by Tailor, and the potential strengths V_R and W_D were searched upon to optimize the fits at each energy. The resulting parameters are listed in set-B of table 9-4, and the corresponding fits are represented by the dashed curves in figures

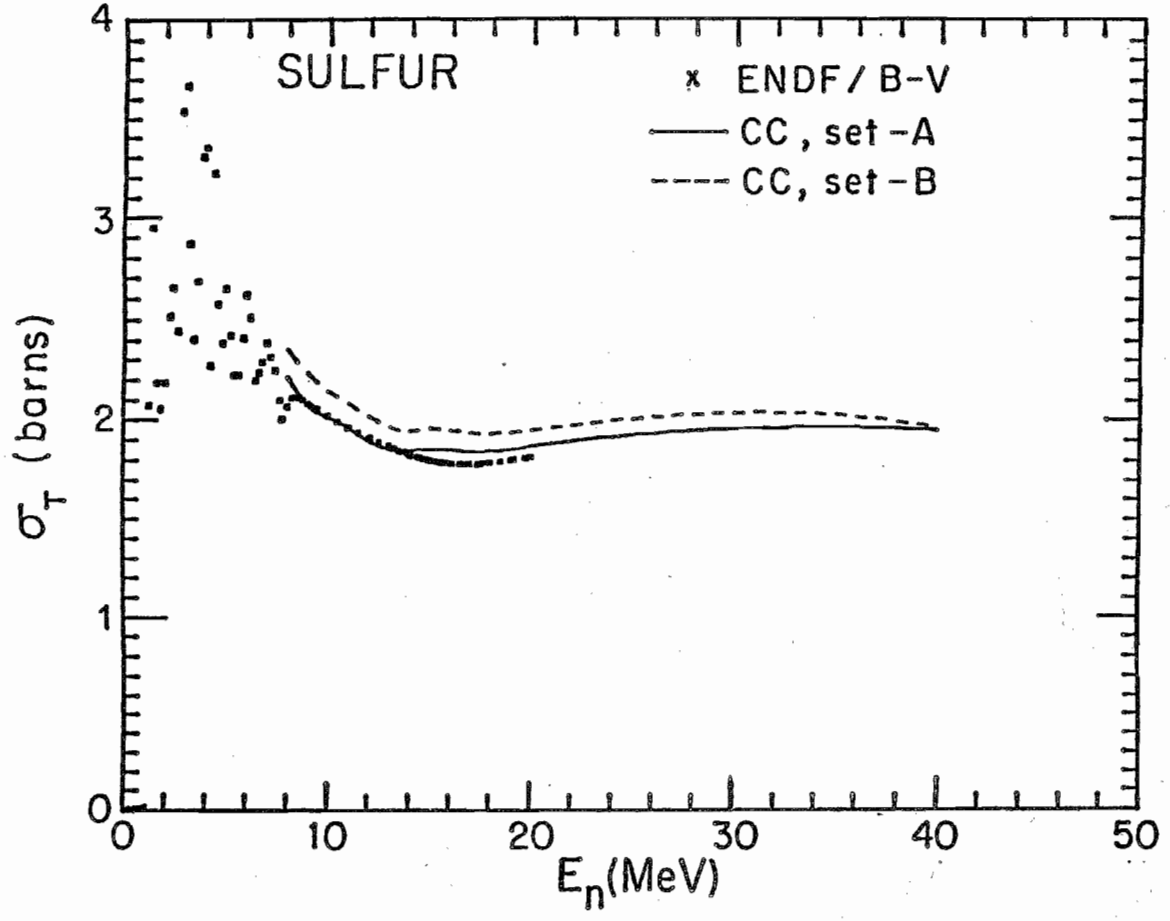

Figure 9.14. A plot of neutron total cross section for sulfur. The curves are predictions of CC calculations. The solid curve represents the prediction of a vibrational model which includes the mixing of one-phonon and two-phonon states. The dashed curve is the prediction based on an axially symmetric model. All OM parameters are listed in table 9-4.

9.11 to 9.13. Comparison of the solid curves to the dashed curves shows that the quality of the fits to the 0^+ and 2_1^+ data obtained with the rotational model was equivalent to those achieved with the more complete vibrational model (discussed in section 9.4.1). Because we were able to accurately describe the data for elastic scattering and inelastic scattering to the 2_1^+ state with the rotational model, we concluded that a valid estimate of the Coulomb correction to the OMP could be deduced by comparing ^{32}S+n to ^{32}S+p within the framework of the rotational model.

Although the quality of the fits to the 0^+ and 2_1^+ data was essentially the same for the vibrational and rotational models, there were some subtle differences in the fits obtained with the two models. For instance, the inelastic analyzing powers at back angles were described slightly better with the vibrational model. At all energies the rotational model could not reproduce the shape of the inelastic $A_y(\theta)$ data at angles beyond $130^\circ_{c.m.}$. In additon, the rotational model consistently overestimated the neutron total cross section σ_t at all energies, as shown in fig. 9.14 by the dashed curve. This discrepancy between the calculations and the experimental σ_t was probably due to the over simplification of the problem by modeling ^{32}S as an axially symmetric rotor with coupling only between the 0^+ and 2_1^+ states. It has been suggested by Bar-Touv and Goswami (Bar-Touv 1969) that within the rotational model there is an inverted coexistence of a deformed 0_1^+ ground state with a spherical 0_2^+ excited state in ^{32}S; according to Bar-Touv and Goswami, the deformed ground state is the head of a rotational band 0^+, 2_2^+, 4^+, ...

9.4.2.1 Coulomb Correction to the Real Component of the OMP

Using the same method outlined in section 9.3.4.1, the resulting volume integrals per nucleon J_v/A obtained in the present neutron analysis and in Tailor's analysis of protons (Tailor 1982) are expressed in an energy independent form: $[(J_v/A) + 2.85\ E]$ $(Mev \cdot fm^3)$. The values of $[(J_v/A) + 2.85\ E]$ $(Mev \cdot fm^3)$ for protons and neutrons are plotted in fig. 9.15 as open and solid circles, respectively. The mean value of the above quantity for neutrons is 493 ± 7 $MeV \cdot fm^3$, and for protons it is 489 ± 17 $MeV \cdot fm^3$. The mean value for neutrons is represented by the dashed line in fig. 9.15. The shaded region represents the standard deviation in this mean value, which is about 1.4%. As in the case of ^{28}Si, the difference between the mean values of the volume integrals per nucleon for neutron scattering and for proton scattering is smaller than our assigned uncertainty in the difference. Therefore, we are unable to determine the size of the Coulomb correction to the OMP for ^{32}S, but we conclude that $(\Delta J_v/A)_c$ is probably less than 24 $MeV \cdot fm^3$. The weakness in our method for extracting the Coulomb-correction term seems to be associated in part with the intrinsic ambiguities in the optical model.

9.4.2.2 Coulomb Correction to the Absorptive Component of the OMP

Figure 9.15 also shows a plot of the volume integrals per nucleon of the absorptive well J_w/A versus energy for neutrons (solid circles) and protons (open circles). The dashed curve through the proton points is a guide to show the trend of the data. Because Tailor did not include proton data in his analysis below 17 MeV, the curve is not well defined at

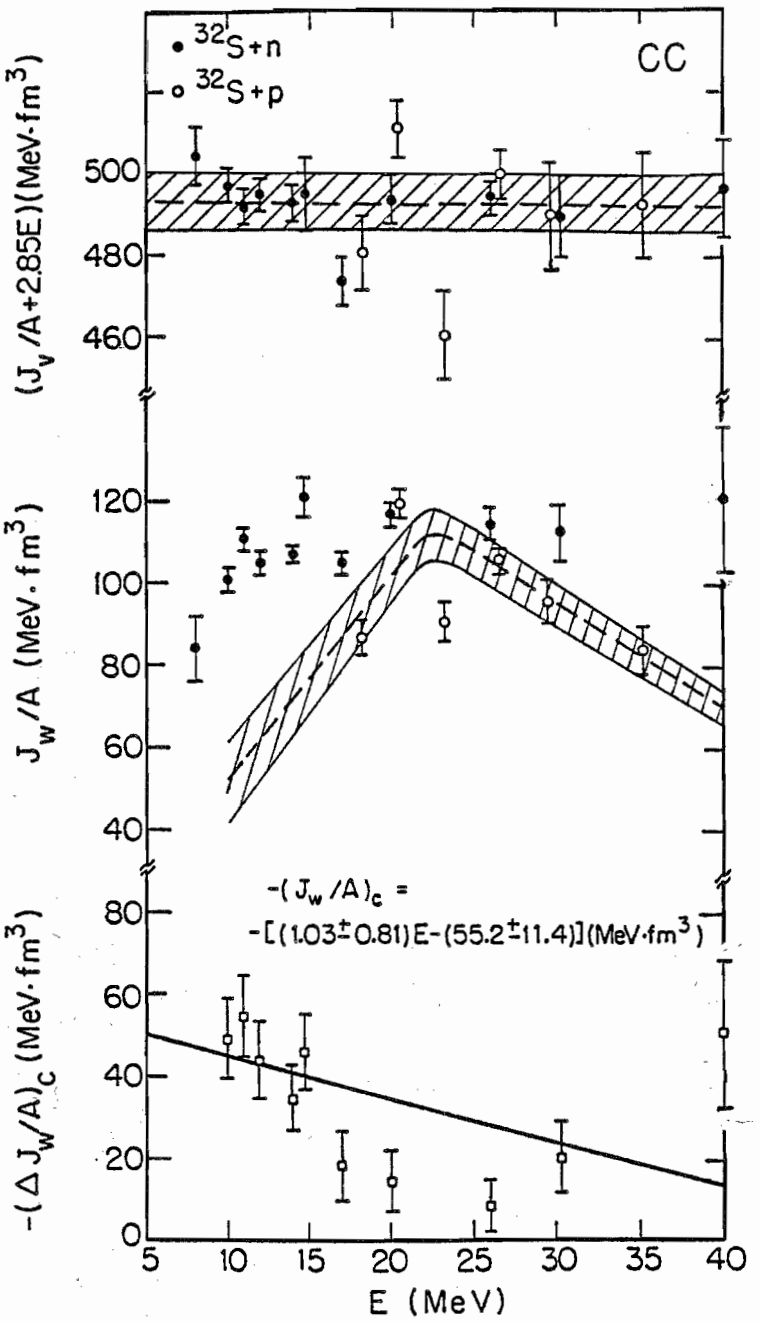

Figure 9.15. Volume integrals per nucleon versus incident projectile energy. Comparison of ^{32}S(n,n) and ^{32}S(p,p) CC analyses to deduce the Coulomb corrections to the real and imaginary parts for the OMP.

the lower energies. The shaded region around the curve was chosen to reflect the uncertainties in the proton values; the width of the shaded region was progressively increased with decreasing energies below 17 MeV because there were no available proton points to define the curve at these lower energies. The volume integral per nucleon for the Coulomb correction to the absorptive part of the OMP $(\Delta J_w/A)_c$ was computed as the negative of the difference between the neutron data point and the corresponding value on the dashed curve. These values for $-(\Delta J_w/A)_c$ are plotted as open squares in fig. 9.15. For simplicity, the energy dependence of the Coulomb-correction term was assumed to be linear; the values of $-(\Delta J_w/A)_c$ were fit with a least-square routine in which all points were given equal weight in the fit. (Note that the value at 40 MeV was included in the fit.) The resulting line is shown in fig. 9.15. The volume integral per nucleon for the Coulomb correction was parameterized as

$$(J_w/A)_c = -\left[(55.2 \pm 11.4) - (1.22 \pm 0.81)E\right] \text{ MeV} \cdot \text{fm}^3,$$

which intersects the energy axis around 54 MeV. This parameterization is in good agreement with our result for ^{28}Si. It is also consistent with the results obtained by Rapaport (Rapaport 1982) for ^{40}Ca and DeVito et al. (DeVito 1983) for ^{28}Si.

CHAPTER 10

SUMMARY AND CONCLUSIONS

The purpose of this study was to investigate the collective features of the low-lying states in ^{28}Si and ^{32}S. Elastic and inelastic differential cross sections $\sigma(\theta)$ for neutron scattering from ^{28}Si and ^{32}S were measured at incident neutron energies of 8, 10, 12, 14, and 17 MeV with the neutron facilities at TUNL. In addition, the analyzing powers $A_y(\theta)$ were measured for the scattering of polarized neutrons from ^{28}Si and ^{32}S at 10, 14, and 17 MeV. These measurements were conducted using pulsed polarized deuterons, the $^{2}H(\vec{d},\vec{n}_0)^{3}He$ source reaction, and the neutron time-of-flight system at TUNL. The present $\sigma(\theta)$ data was found to be consistent with the existing data. However, there was a serious discrepancy between the present $A_y(\theta)$ data for ^{28}Si at 14 MeV and the values reported by the Erlangen group (Böttcher 1983). The Erlangen group reported a large positive $A_y(\theta)$, about 0.60 ± 0.05, near the minimum of $\sigma(\theta)$, around 40° c.m. Our data did not show this large positive spike.

Because the calculated $A_y(\theta)$ in this narrow angular region was very sensitive to the optical model (OM) parameters, especially to a_{so}, it was necessary to resolve the discrepancy between the two data sets before performing OM calculations. Therefore, a careful measurement of $A_y(\theta)$ near the minimum of $\sigma(\theta)$ was performed. Because precise values of the location and magnitude of the minimum of $\sigma(\theta)$ were necessary to properly correct the $A_y(\theta)$ data near the minimum of $\sigma(\theta)$ for multiple-scattering and finite-geometry effects, the magnitude and location of the minimum in

$\sigma(\theta)$ were determined to an accuracy of $\pm 7\%$ and $\pm 0.5^{o}$, respectively. In addition to finding an explanation for the discrepant Erlangen data, the measurements of $\sigma(\theta)$ and $A_y(\theta)$ near the minimum of $\sigma(\theta)$ also provided data to be used for testing our computer methods of correcting the observed data for finite geometry effects.

At incident energies below 14 MeV, the contributions that were due to the formation of a compound nucleus (CN) were added to the OM calculations for comparison to the measured data. These CN cross sections were computed using the computer code HAUSSER*5 by Mann (Mann 1979), which applied the Hausser-Feshbach statistical model of nuclear reactions. The n, p, d, and α particle exit channels were included in the computations. The calculations were able to reproduce previously reported neutron total cross sections and the (n,p) and (n,α) reaction cross sections for ^{28}Si and ^{32}S.

In order to study the systematic behavior of neutron scattering from ^{28}Si and ^{32}S, data from several references for incident neutron energies ranging from 8 to 40 MeV were collected. The data from the various references were consistent with each other to within the 5% normalization uncertainty that was assigned to most of the data sets. The angular distributions for elastic scattering were successfully described with a spherical optical model (SOM). The neutron total cross section σ_t for ^{28}Si was accurately reproduced by the SOM. However, the σ_t for ^{32}S was consistently overestimated by the calculations. This discrepancy between the calculations and the experimentally observed σ_t was believed to be due to the combination of the effects of collective nuclear motion and the formation of particle-hole states.

The present CC analysis successfully described the available $\sigma(\theta)$ and $A_y(\theta)$ data for elastic and inelastic neutron scattering from ^{28}Si and ^{32}S. A square-root energy dependence on V_R was necessary to properly describe σ_t at low bombarding energies. The nucleus ^{28}Si was modeled as a symmetric rotor with coupling to the 2^+ and 4^+ states, which were modeled as excitations of a $K^\pi = 0^+$ rotational band. The quadrupole and hexadecapole deformation parameters deduced from this analysis were $\beta_2 = -0.36$ and $\beta_4 = +0.20$ with $\delta_{so} = 1.2\delta_c$. These findings were consistent with those of previous analyses of $^{28}Si+n$ and $^{28}Si+p$ data.

For ^{32}S it was found in the present analysis that elastic scattering and inelastic scattering to the first excited state could be described equally well with a rotational or vibrational model. However, in order to describe the higher collective excitations in ^{32}S, it was necessary to use a vibrational model which permitted the mixing of one-phonon and two-phonon states. In this model the 0^+, 2_1^+, 2_2^+, 4^+, and 3^- states were coupled. The strength of the coupling constants β_2 and β_3 were adjusted to describe the corresponding inelastic data and were found to be $\beta_2 = 0.31$ and $\beta_3 = 0.33$ with $\beta_{so} = \beta_c$. The resulting phonon-admixing angle of $\phi = 34^o$ was in good agreement with the findings of electromagnetic studies (Garvey 1971, Ingebretsen 1971, Olin 1974, and Coetzee 1972). Although the sign was opposite, its magnitude was consistent with those deduced from previous analyses of nucleon-scattering data (Lombard 1973 and Tailor 1982). In addition, these calculations successfully reproduced σ_t below 14 MeV, but overestimated it at higher energies. The differences between the calculations and the data at energies above 14 MeV were believed to represent a measure of the influences due to the formation of particle-

hole states.

Due to the intrinsic ambiguities in the OM, the magnitudes of the Coulomb-correction terms to the the real part of the optical-model potentials for the T=0 nuclei of ^{28}Si and ^{32}S were found to be smaller than their uncertainties. Unlike the case of ^{40}Ca, the size of the Coulomb corrections to the potentials of the optical models for ^{28}Si and ^{32}S were small. For both nuclei, we concluded that the Coulomb-correction was less than 2% of the strength of the real potential. In addition, we were able to deduce estimates of the Coulomb corrections to the absorptive potentials of the optical models. These corrections were noticeably larger than those for the real potential.

APPENDIX I

TABULATION OF THE CROSS SECTION DATA

In this appendix, the data are presented with Legendre polynomial fits. The following form was used to fit the cross section data:

$$\sigma(\theta,E) = \sum_{\ell} a_{\ell}(E)\, P^{0}_{\ell}(\cos(\theta)) \ .$$

The parameters of the fits are listed below:

ORDER = number of terms in fit minus one

COEF = $a_{\ell}(E)$

UNCOEF = $\Delta a_{\ell}(E)$

RATIO = $a_{\ell}(E)/a_{1}(E)$

UNRATIO = $\Delta a_{\ell}(E)/a_{1}(E)$

ANGLE = θ(center-of-mass)

CAL. SIGMA = Legendre polynomial fit

EXP. SIGMA = measured $\sigma(\theta,E)$

DEVIATION = (EXP SIGMA) - (CAL SIGMA)

UNCEXPSIG = $\Delta\sigma(\theta,E)$ - does not include normalization uncertainty.

The calculated Wick's limit is based on the available measured total cross section and is assigned a $\pm$20% uncertainty for the fitting procedure.

TARGET ATOMIC MASS		28.0855 amu
EXCITATION ENERGY		0.000 MeV
INCIDENT NEUTRON ENERGY		7.958 MeV
ANGLE-INDEPENDENT ERROR		5.00 %
TOTAL CROSS SECTION		1.895 barn
CALCULATED WICK'S LIMIT	843.05 +/-	84.30 mb/sr
ZERO DEGREE CROSS SECTION	950.90 +/-	47.55 mb/sr
INTEGRATED CROSS SECTION	0.949 +/-	0.049 barn
CHI SQUARE PER DEGREE FREEDOM		0.44

ORDER	COEF	UNCOEF	RATIO	UNRATIO
0	75.54079	0.81561	1.00000	0.00000
1	118.94947	2.27759	1.57464	0.01534
2	212.81386	3.22829	2.81720	0.01464
3	159.07613	3.70012	2.10583	0.02958
4	202.70273	3.30856	2.68335	0.01915
5	97.53662	2.99062	1.29118	0.02898
6	61.98787	1.87228	0.82059	0.01867
7	22.29176	1.47498	0.29510	0.01790

ANGLE	EXP. SIGMA	CAL. SIGMA	DEVIATION	UNCEXPSIG	PCHSQ
29.51	329.93	326.33	3.61	11.75	0.094
34.79	206.26	204.90	1.36	7.28	0.035
39.59	122.10	121.48	0.62	4.17	0.022
50.40	26.31	26.51	-0.20	1.06	0.036
62.65	15.69	15.67	0.02	0.73	0.001
72.58	24.53	24.21	0.32	0.81	0.155
82.28	26.29	26.95	-0.66	0.86	0.583
92.17	25.64	25.18	0.46	0.85	0.291
101.47	21.33	21.27	0.06	0.69	0.007
110.47	14.32	14.56	-0.24	0.58	0.176
120.30	6.67	6.59	0.08	0.34	0.055
132.07	9.88	10.02	-0.14	0.69	0.044
141.78	33.34	33.57	-0.23	1.61	0.021
150.96	71.88	70.59	1.29	2.48	0.269
162.43	118.86	119.66	-0.80	3.30	0.058

TARGET ATOMIC MASS	28.0855	amu
EXCITATION ENERGY	-1.780	MeV
INCIDENT NEUTRON ENERGY	7.958	MeV
ANGLE-INDEPENDENT ERROR	5.00	%
INTEGRATED CROSS SECTION	0.346 +/- 0.017	barn
CHI SQUARE PER DEGREE FREEDOM	0.73	

ORDER	COEF	UNCOEF	RATIO	UNRATIO
0	27.55183	0.16842	1.00000	0.00000
1	2.02790	0.35740	0.07360	0.01275
2	1.00409	0.51693	0.03644	0.01870
3	1.79098	0.65680	0.06500	0.02378
4	-9.52078	0.61552	-0.34556	0.02266

ANGLE	EXP. SIGMA	CAL. SIGMA	DEVIATION	UNCEXPSIG	PCHSQ
31.02	32.20	30.59	1.60	1.76	0.830
36.57	31.76	31.94	-0.18	0.94	0.037
41.61	32.31	32.64	-0.33	0.92	0.129
52.22	32.01	32.20	-0.19	0.99	0.039
62.29	29.95	29.72	0.23	1.10	0.043
72.36	26.17	26.47	-0.30	0.73	0.163
82.50	24.25	24.03	0.23	0.62	0.135
92.64	24.23	23.59	0.64	0.54	1.418
102.17	24.65	25.15	-0.50	0.42	1.391
111.56	27.78	27.76	0.02	0.57	0.001
121.34	30.19	30.21	-0.02	0.58	0.001
131.00	30.95	30.95	0.00	0.56	0.000
140.56	30.38	29.30	1.08	0.74	2.102
150.05	24.90	25.60	-0.70	0.70	0.998
161.85	19.92	19.90	0.02	0.48	0.002

TARGET ATOMIC MASS	28.0855 amu
EXCITATION ENERGY	0.000 MeV
INCIDENT NEUTRON ENERGY	9.948 MeV
ANGLE-INDEPENDENT ERROR	5.00 %
TOTAL CROSS SECTION	1.864 barn
CALCULATED WICK'S LIMIT	1019.66 +/- 101.97 mb/sr
ZERO DEGREE CROSS SECTION	967.58 +/- 48.39 mb/sr
INTEGRATED CROSS SECTION	0.746 +/- 0.039 barn
CHI SQUARE PER DEGREE FREEDOM	0.95

ORDER	COEF	UNCOEF	RATIO	UNRATIO
0	59.33421	0.82451	1.00000	0.00000
1	121.52202	2.27096	2.04809	0.01152
2	176.80402	3.41369	2.97980	0.01890
3	176.09489	3.82768	2.96785	0.02691
4	180.18568	3.86877	3.03679	0.02836
5	133.39175	3.27164	2.24814	0.02966
6	82.46719	2.76798	1.38988	0.03248
7	20.74759	1.74011	0.34967	0.02607
8	17.03145	1.20048	0.28704	0.01832

ANGLE	EXP. SIGMA	CAL. SIGMA	DEVIATION	UNCEXPSIG	PCHSQ
25.01	396.34	400.57	-4.23	12.33	0.118
27.86	326.93	318.23	8.70	11.45	0.577
31.63	217.37	222.07	-4.70	7.68	0.373
35.37	148.79	144.76	4.03	6.10	0.436
38.84	89.46	90.11	-0.65	3.92	0.027
43.76	38.26	39.01	-0.75	1.83	0.169
49.23	12.31	12.19	0.13	0.70	0.032
57.06	7.59	7.66	-0.07	0.46	0.021
63.29	16.00	15.37	0.63	0.70	0.794
67.40	19.73	20.67	-0.94	0.83	1.262
71.96	24.59	24.71	-0.13	0.89	0.020
76.63	27.25	26.15	1.11	0.92	1.433
81.31	23.92	24.88	-0.97	1.00	0.938
86.01	20.36	21.43	-1.07	0.82	1.729
90.69	18.09	16.64	1.46	0.71	4.178
95.88	10.64	10.99	-0.35	0.51	0.466
100.36	7.07	6.92	0.15	0.34	0.191
106.77	4.03	4.05	-0.02	0.21	0.012
112.80	4.98	5.26	-0.28	0.30	0.859
117.91	9.04	8.59	0.45	0.45	0.988
122.54	12.46	12.17	0.29	0.52	0.313
127.08	14.80	14.95	-0.14	0.63	0.052
131.61	16.85	16.13	0.71	0.77	0.864
136.23	15.12	15.53	-0.41	0.60	0.477
141.07	13.31	13.76	-0.46	0.54	0.736
146.18	12.52	12.49	0.03	0.52	0.004
151.48	14.68	14.23	0.45	0.66	0.451
156.07	20.39	19.59	0.79	0.81	0.954
160.83	27.95	28.94	-0.99	0.93	1.124

TARGET ATOMIC MASS	28.0855 amu
EXCITATION ENERGY	-1.780 MeV
INCIDENT NEUTRON ENERGY	9.948 MeV
ANGLE-INDEPENDENT ERROR	5.00 %
INTEGRATED CROSS SECTION	0.191 +/- 0.010 barn
CHI SQUARE PER DEGREE FREEDOM	1.81

ORDER	COEF	UNCOEF	RATIO	UNRATIO
0	15.22688	0.17753	1.00000	0.00000
1	3.13903	0.31347	0.20615	0.01997
2	-1.29453	0.44079	-0.08502	0.02926
3	-4.58866	0.58577	-0.30135	0.03965
4	-2.42533	0.71196	-0.15928	0.04719
5	-0.64504	0.71221	-0.04236	0.04696
6	2.98850	0.80911	0.19626	0.05213

ANGLE	EXP. SIGMA	CAL. SIGMA	DEVIATION	UNCEXPSIG	PCHSQ
26.46	14.24	13.87	0.37	0.70	0.272
29.55	15.00	14.51	0.49	0.67	0.544
33.65	14.76	15.53	-0.77	0.65	1.390
37.73	16.40	16.68	-0.28	0.64	0.192
41.54	16.61	17.77	-1.16	0.71	2.648
46.83	20.33	19.17	1.16	0.69	2.791
51.60	19.90	20.11	-0.20	0.73	0.079
56.59	22.34	20.59	1.75	0.71	6.020
62.04	21.82	20.43	1.38	1.12	1.537
66.52	18.60	19.79	-1.19	0.63	3.584
71.52	17.72	18.65	-0.93	0.62	2.244
76.55	17.29	17.26	0.04	0.51	0.006
81.58	15.93	15.85	0.08	0.66	0.015
86.64	13.86	14.64	-0.78	0.54	2.045
91.71	14.88	13.79	1.08	0.36	8.980
97.28	12.94	13.34	-0.40	0.67	0.360
101.77	12.91	13.28	-0.37	0.33	1.223
107.24	13.36	13.43	-0.07	0.60	0.014
112.19	12.83	13.59	-0.76	0.60	1.609
117.06	14.13	13.62	0.52	0.72	0.520
121.90	14.40	13.44	0.96	0.71	1.860
126.74	13.34	13.06	0.28	0.79	0.128
131.57	11.74	12.54	-0.81	0.79	1.054
136.43	12.18	12.03	0.15	0.73	0.043
141.34	12.03	11.68	0.35	0.71	0.251
146.24	11.29	11.64	-0.35	0.69	0.261
151.13	11.68	11.99	-0.31	0.76	0.160
155.48	12.69	12.61	0.08	0.46	0.031
160.23	13.58	13.55	0.03	0.47	0.004

TARGET ATOMIC MASS	28.0855 amu
EXCITATION ENERGY	0.000 MeV
INCIDENT NEUTRON ENERGY	11.936 MeV
ANGLE-INDEPENDENT ERROR	5.00 %
TOTAL CROSS SECTION	1.840 barn
CALCULATED WICK'S LIMIT	1192.13 +/- 119.21 mb/sr
ZERO DEGREE CROSS SECTION	922.18 +/- 46.12 mb/sr
INTEGRATED CROSS SECTION	0.625 +/- 0.034 barn
CHI SQUARE PER DEGREE FREEDOM	1.75

ORDER	COEF	UNCOEF	RATIO	UNRATIO
0	49.77438	1.07758	1.00000	0.00000
1	101.84811	2.97132	2.04620	0.01886
2	140.30188	4.44085	2.81876	0.03485
3	148.51329	4.98677	2.98373	0.04251
4	162.90747	4.91177	3.27292	0.03498
5	145.98112	4.28229	2.93286	0.03037
6	105.74267	3.66205	2.12444	0.03883
7	49.19291	2.61370	0.98832	0.03927
8	17.91751	1.82375	0.35997	0.03291

ANGLE	EXP. SIGMA	CAL. SIGMA	DEVIATION	UNCEXPSIG	PCHSQ
24.69	332.86	323.04	9.81	12.05	0.664
29.26	199.87	196.88	2.99	8.10	0.136
33.71	101.79	104.07	-2.28	4.85	0.222
38.16	41.98	43.56	-1.59	2.26	0.491
44.81	5.82	5.85	-0.02	0.40	0.004
53.35	13.47	12.67	0.80	0.89	0.817
62.11	32.21	31.56	0.65	1.07	0.370
67.13	33.26	35.38	-2.12	1.21	3.065
71.48	32.39	33.87	-1.47	1.30	1.276
80.96	23.48	22.46	1.02	0.96	1.116
90.83	12.45	11.94	0.52	0.57	0.832
101.38	7.15	7.40	-0.25	0.30	0.683
112.29	6.89	6.75	0.14	0.40	0.124
122.12	8.68	8.48	0.20	0.46	0.185
131.62	10.77	10.70	0.07	1.04	0.005
141.07	11.30	11.37	-0.07	0.41	0.031
145.83	10.76	11.46	-0.70	0.51	1.865
151.28	12.82	12.32	0.50	0.51	0.958
157.10	15.83	15.01	0.82	0.63	1.667
163.61	19.43	20.29	-0.86	0.75	1.315

TARGET ATOMIC MASS	28.0855 amu
EXCITATION ENERGY	-1.780 MeV
INCIDENT NEUTRON ENERGY	11.936 MeV
ANGLE-INDEPENDENT ERROR	5.00 %
INTEGRATED CROSS SECTION	0.152 +/- 0.008 barn
CHI SQUARE PER DEGREE FREEDOM	1.06

ORDER	COEF	UNCOEF	RATIO	UNRATIO
0	12.07634	0.19836	1.00000	0.00000
1	7.36173	0.50640	0.60960	0.03538
2	5.15402	0.72182	0.42679	0.05539
3	-1.85873	0.94040	-0.15391	0.07947
4	0.70302	0.92125	0.05821	0.07565
5	-2.47150	0.95739	-0.20466	0.08131
6	-4.17969	0.87439	-0.34611	0.07589
7	-2.78757	0.79525	-0.23083	0.06709

ANGLE	EXP. SIGMA	CAL. SIGMA	DEVIATION	UNCEXPSIG	PCHSQ
26.32	24.33	23.90	0.43	1.47	0.084
31.32	24.10	24.33	-0.24	1.27	0.034
36.33	24.15	23.48	0.67	1.32	0.257
41.31	21.32	21.60	-0.28	0.66	0.179
46.08	18.02	19.26	-1.24	1.16	1.136
51.14	17.14	16.73	0.40	0.72	0.314
61.36	13.72	13.23	0.49	0.51	0.923
67.12	12.57	12.52	0.05	0.67	0.006
71.91	11.41	12.40	-0.99	0.67	2.179
81.79	11.77	12.20	-0.43	0.65	0.448
91.54	11.19	10.74	0.44	0.42	1.114
101.55	8.26	8.25	0.00	0.27	0.000
111.99	5.19	6.42	-1.23	0.95	1.687
122.15	6.24	6.33	-0.10	0.37	0.070
131.87	7.53	7.24	0.29	0.46	0.397
141.21	8.37	8.30	0.07	0.27	0.064
145.87	8.98	8.86	0.12	0.83	0.022
151.23	9.46	9.59	-0.13	0.36	0.128
157.05	9.88	10.53	-0.64	0.56	1.290
163.60	13.15	11.70	1.44	0.93	2.411

TARGET ATOMIC MASS	28.0855 amu
EXCITATION ENERGY	0.000 MeV
INCIDENT NEUTRON ENERGY	13.965 MeV
ANGLE-INDEPENDENT ERROR	5.00 %
TOTAL CROSS SECTION	1.773 barn
CALCULATED WICK'S LIMIT	1295.05 +/- 129.51 mb/sr
ZERO DEGREE CROSS SECTION	1256.97 +/- 62.85 mb/sr
INTEGRATED CROSS SECTION	0.740 +/- 0.038 barn
CHI SQUARE PER DEGREE FREEDOM	0.73

ORDER	COEF	UNCOEF	RATIO	UNRATIO
0	58.92640	0.50241	1.00000	0.00000
1	127.27483	1.42530	2.15989	0.00804
2	166.02173	2.13623	2.81744	0.01708
3	187.63242	2.61620	3.18418	0.02336
4	199.79074	2.56192	3.39051	0.01965
5	197.85895	2.48964	3.35773	0.01912
6	168.56731	2.09100	2.86064	0.01710
7	100.44868	1.89478	1.70465	0.02324
8	41.89859	1.44073	0.71103	0.02125
9	8.55090	1.01582	0.14511	0.01673

ANGLE	EXP. SIGMA	CAL. SIGMA	DEVIATION	UNCEXPSIG	PCHSQ
19.89	590.82	582.07	8.75	20.14	0.189
20.36	564.52	558.96	5.56	18.65	0.089
23.53	412.17	412.44	-0.27	15.48	0.000
24.45	376.56	372.97	3.59	15.16	0.056
25.28	361.69	338.60	23.09	15.21	2.307
27.12	265.66	268.20	-2.55	10.96	0.054
28.19	233.47	230.67	2.80	9.64	0.084
29.71	185.32	182.68	2.64	12.42	0.045
30.56	150.93	158.54	-7.61	6.85	1.233
33.07	102.20	98.07	4.13	5.35	0.595
37.91	25.67	26.61	-0.93	1.49	0.393
39.66	12.07	13.55	-1.48	0.83	3.157
42.99	3.61	3.43	0.18	0.24	0.592
46.53	8.26	7.75	0.51	0.77	0.441
48.17	11.46	12.94	-1.48	0.99	2.253
48.84	16.32	15.38	0.94	1.15	0.672
53.42	31.66	33.69	-2.03	1.59	1.623
57.39	44.25	46.43	-2.18	1.58	1.899
61.69	52.92	52.70	0.23	1.65	0.019
61.82	54.07	52.75	1.32	1.54	0.732
70.81	41.59	41.62	-0.03	1.46	0.001
80.48	19.84	19.39	0.45	0.82	0.297
91.95	9.09	9.21	-0.12	0.43	0.073
97.36	9.47	9.62	-0.15	0.44	0.112
102.39	10.97	10.81	0.16	0.48	0.107
111.61	12.59	12.38	0.21	0.54	0.146
116.43	12.60	12.55	0.05	0.54	0.010

121.71	12.02	12.21	-0.19	0.51	0.135
131.24	10.11	10.20	-0.10	0.43	0.049
136.02	8.70	8.71	-0.01	0.38	0.001
140.90	7.28	7.23	0.05	0.37	0.017
145.93	6.35	6.20	0.15	0.36	0.188
151.08	6.04	6.02	0.03	0.36	0.005
156.13	6.50	6.83	-0.33	0.35	0.890
160.49	8.44	8.16	0.28	0.42	0.441

TARGET ATOMIC MASS	28.0855	amu
EXCITATION ENERGY	-1.780	MeV
INCIDENT NEUTRON ENERGY	13.965	MeV
ANGLE-INDEPENDENT ERROR	5.00	%
INTEGRATED CROSS SECTION	0.104 +/- 0.005	barn
CHI SQUARE PER DEGREE FREEDOM	2.48	

ORDER	COEF	UNCOEF	RATIO	UNRATIO
0	8.28754	0.13794	1.00000	0.00000
1	6.97361	0.20987	0.84146	0.02570
2	2.75847	0.29193	0.33285	0.03694
3	-2.32890	0.36826	-0.28101	0.04445
4	-6.61226	0.42961	-0.79786	0.05503
5	-2.23578	0.45392	-0.26978	0.05613

ANGLE	EXP. SIGMA	CAL. SIGMA	DEVIATION	UNCEXPSIG	PCHSQ
21.37	13.49	12.37	1.12	0.56	4.002
25.50	12.39	14.02	-1.63	0.69	5.511
26.36	14.48	14.35	0.13	0.58	0.046
29.45	15.16	15.46	-0.29	0.58	0.257
32.69	15.36	16.45	-1.09	1.01	1.158
33.70	15.35	16.71	-1.36	0.58	5.422
36.70	17.28	17.35	-0.07	0.76	0.010
41.44	18.48	17.88	0.60	0.46	1.749
43.52	18.48	17.90	0.58	0.55	1.090
45.53	18.44	17.81	0.63	0.55	1.276
46.34	17.99	17.74	0.25	0.69	0.125
47.57	18.28	17.60	0.68	0.59	1.320
51.27	17.15	16.93	0.22	0.67	0.108
56.15	15.73	15.55	0.18	0.59	0.090
61.08	12.90	13.73	-0.84	0.48	2.995
71.14	8.68	9.57	-0.88	0.39	5.097
81.49	6.15	6.02	0.13	0.33	0.153
92.17	4.94	4.23	0.71	0.40	3.148
97.16	4.49	4.06	0.43	0.38	1.266
102.16	4.86	4.21	0.65	0.38	2.922
111.78	3.92	4.96	-1.03	0.29	12.533
116.82	5.30	5.36	-0.06	0.28	0.039
122.23	5.55	5.65	-0.10	0.43	0.056
131.75	6.03	5.64	0.39	0.43	0.803
136.43	6.17	5.39	0.78	0.42	3.499
141.09	5.45	5.01	0.44	0.42	1.091
145.77	4.70	4.54	0.16	0.45	0.131
150.52	3.41	4.02	-0.61	0.42	2.089
155.41	3.58	3.48	0.09	0.36	0.070
159.88	2.76	3.03	-0.27	0.23	1.363

TARGET ATOMIC MASS	28.0855 amu
EXCITATION ENERGY	0.000 MeV
INCIDENT NEUTRON ENERGY	16.917 MeV
ANGLE-INDEPENDENT ERROR	5.00 %
TOTAL CROSS SECTION	1.849 barn
CALCULATED WICK'S LIMIT	1678.65 +/- 167.87 mb/sr
ZERO DEGREE CROSS SECTION	1694.65 +/- 84.76 mb/sr
INTEGRATED CROSS SECTION	0.861 +/- 0.047 barn
CHI SQUARE PER DEGREE FREEDOM	3.05

ORDER	COEF	UNCOEF	RATIO	UNRATIO
0	68.48921	1.55830	1.00000	0.00000
1	155.23274	4.49655	2.26653	0.01494
2	197.09073	6.92888	2.87769	0.03751
3	223.86493	8.62342	3.26862	0.05421
4	241.14050	9.33879	3.52085	0.05966
5	248.64474	9.28285	3.63042	0.05850
6	232.08475	8.62107	3.38863	0.05758
7	172.47475	7.72458	2.51828	0.06542
8	96.32115	6.34747	1.40637	0.06757
9	40.71939	4.71852	0.59454	0.05879
10	14.53527	2.87642	0.21223	0.03867
11	4.05324	1.26300	0.05918	0.01769

ANGLE	EXP. SIGMA	CAL. SIGMA	DEVIATION	UNCEXPSIG	PCHSQ
19.86	676.35	669.27	7.08	15.97	0.196
24.51	405.45	384.45	21.00	12.48	2.832
29.05	190.13	183.03	7.10	7.24	0.960
34.14	50.95	55.93	-4.98	1.72	8.354
41.03	13.82	13.35	0.48	0.38	1.580
47.57	33.39	38.31	-4.92	1.55	10.052
52.26	57.83	59.38	-1.55	1.09	2.040
57.03	69.83	69.60	0.24	0.53	0.198
61.70	68.23	66.92	1.31	1.11	1.389
71.28	39.94	39.79	0.15	0.88	0.028
76.19	25.62	25.70	-0.08	0.71	0.014
81.32	15.44	15.73	-0.29	0.36	0.622
86.77	11.08	11.09	0.00	0.22	0.000
92.21	11.26	10.91	0.35	0.26	1.810
97.32	12.24	12.46	-0.22	0.30	0.528
102.18	13.46	13.67	-0.21	0.28	0.567
111.26	12.86	12.72	0.14	0.28	0.256
116.10	11.03	10.96	0.07	0.28	0.063
120.99	9.14	9.14	0.00	0.24	0.000
130.80	6.40	6.61	-0.21	0.19	1.243
135.68	6.34	5.73	0.60	0.25	5.956
140.55	4.72	4.93	-0.21	0.18	1.414
145.47	4.24	4.28	-0.04	0.14	0.071
150.44	4.18	3.96	0.21	0.13	2.468
155.38	3.72	4.05	-0.33	0.15	4.488
160.67	4.59	4.39	0.19	0.17	1.200

TARGET ATOMIC MASS	28.0855 amu
EXCITATION ENERGY	-1.780 MeV
INCIDENT NEUTRON ENERGY	16.917 MeV
ANGLE-INDEPENDENT ERROR	5.00 %
INTEGRATED CROSS SECTION	0.094 +/- 0.005 barn
CHI SQUARE PER DEGREE FREEDOM	2.48

ORDER	COEF	UNCOEF	RATIO	UNRATIO
0	7.48856	0.13637	1.00000	0.00000
1	8.75840	0.33452	1.16957	0.02976
2	4.82920	0.45523	0.64488	0.05366
3	0.66978	0.51302	0.08944	0.06763
4	-0.36826	0.48543	-0.04918	0.06518
5	2.19185	0.35526	0.29269	0.04611

ANGLE	EXP. SIGMA	CAL. SIGMA	DEVIATION	UNCEXPSIG	PCHSQ
20.98	20.52	20.31	0.21	1.94	0.012
26.04	19.50	18.92	0.58	1.54	0.142
31.10	17.45	17.51	-0.06	0.94	0.003
36.46	16.35	16.08	0.26	0.55	0.231
41.04	12.85	14.97	-2.12	0.96	4.858
46.11	13.00	13.86	-0.87	0.69	1.602
51.46	12.48	12.82	-0.34	0.65	0.278
56.78	12.31	11.85	0.46	0.26	3.204
61.84	11.51	10.94	0.57	0.47	1.468
71.92	8.80	8.96	-0.16	0.38	0.177
76.93	7.21	7.86	-0.66	0.37	3.146
81.91	6.24	6.73	-0.48	0.21	5.330
86.87	5.26	5.61	-0.35	0.23	2.417
91.84	5.43	4.56	0.87	0.21	17.492
96.83	3.84	3.68	0.16	0.21	0.587
101.86	3.11	3.00	0.10	0.14	0.521
111.52	2.13	2.46	-0.34	0.23	2.120
116.60	2.18	2.55	-0.37	0.18	4.242
121.60	2.92	2.80	0.12	0.27	0.190
131.33	3.60	3.43	0.17	0.29	0.361
136.14	3.93	3.63	0.30	0.27	1.249
140.89	3.49	3.66	-0.17	0.20	0.743
145.60	3.82	3.50	0.32	0.18	3.168
150.29	3.16	3.16	0.00	0.18	0.000
154.93	2.58	2.67	-0.08	0.13	0.383
159.97	1.96	2.03	-0.07	0.14	0.278

TARGET ATOMIC MASS	32.0640	amu
EXCITATION ENERGY	0.000	MeV
INCIDENT NEUTRON ENERGY	7.956	MeV
ANGLE-INDEPENDENT ERROR	5.00	%
TOTAL CROSS SECTION	2.069	barn
CALCULATED WICK'S LIMIT	1009.06 +/- 100.91	mb/sr
ZERO DEGREE CROSS SECTION	970.74 +/- 48.54	mb/sr
INTEGRATED CROSS SECTION	1.003 +/- 0.051	barn
CHI SQUARE PER DEGREE FREEDOM	1.43	

ORDER	COEF	UNCOEF	RATIO	UNRATIO
0	79.79276	0.76807	1.00000	0.00000
1	164.55418	2.11502	2.06227	0.00824
2	239.88229	3.05642	3.00632	0.01304
3	191.18474	3.53301	2.39602	0.02567
4	163.56949	3.45117	2.04993	0.02928
5	79.23334	3.06612	0.99299	0.03226
6	49.08359	1.99941	0.61514	0.02185
7	3.43635	1.31321	0.04307	0.01627

ANGLE	EXP. SIGMA	CAL. SIGMA	DEVIATION	UNCEXPSIG	PCHSQ
25.21	537.89	524.03	13.86	8.22	2.844
30.06	401.58	399.16	2.41	7.24	0.111
34.93	279.51	286.84	-7.33	5.54	1.749
39.82	186.40	193.64	-7.23	3.95	3.347
44.24	129.48	128.55	0.93	2.80	0.110
54.39	43.94	43.61	0.33	1.09	0.094
65.14	17.77	17.45	0.32	0.49	0.444
75.48	11.92	12.22	-0.29	0.37	0.648
85.35	7.68	7.74	-0.06	0.32	0.038
96.01	4.96	4.77	0.19	0.24	0.657
102.04	5.62	5.64	-0.02	0.19	0.010
107.66	7.73	7.76	-0.03	0.27	0.013
117.22	10.98	11.33	-0.35	0.30	1.337
126.72	12.52	12.18	0.33	0.31	1.128
136.80	13.56	13.42	0.14	0.41	0.117
147.03	22.65	23.97	-1.32	0.80	2.730
156.60	46.45	46.17	0.28	1.13	0.059
162.57	63.61	63.38	0.23	0.71	0.105

TARGET ATOMIC MASS		32.0640 amu
EXCITATION ENERGY		-2.230 MeV
INCIDENT NEUTRON ENERGY		7.956 MeV
ANGLE-INDEPENDENT ERROR		5.00 %
INTEGRATED CROSS SECTION	0.139 +/-	0.007 barn
CHI SQUARE PER DEGREE FREEDOM		1.43

ORDER	COEF	UNCOEF	RATIO	UNRATIO
0	11.08293	0.12984	1.00000	0.00000
1	6.16642	0.28990	0.55639	0.02253
2	7.81426	0.40719	0.70507	0.03286
3	0.09456	0.50820	0.00853	0.04581
4	-3.08059	0.52165	-0.27796	0.04831
5	-0.71465	0.47593	-0.06448	0.04327

ANGLE	EXP. SIGMA	CAL. SIGMA	DEVIATION	UNCEXPSIG	PCHSQ
26.11	21.67	21.64	0.03	1.13	0.001
31.14	22.50	21.33	1.17	0.86	1.853
36.19	20.90	20.73	0.17	0.72	0.059
41.24	18.92	19.80	-0.88	0.84	1.112
45.79	17.81	18.69	-0.88	0.49	3.188
55.85	15.98	15.48	0.49	0.47	1.086
65.83	12.14	11.84	0.29	0.38	0.600
75.86	8.57	8.60	-0.02	0.31	0.004
86.05	6.45	6.46	0.00	0.31	0.000
96.38	5.75	5.78	-0.03	0.24	0.017
102.00	5.95	5.97	-0.02	0.16	0.012
107.53	6.21	6.45	-0.24	0.23	1.092
117.37	8.00	7.67	0.33	0.27	1.464
127.03	9.20	8.90	0.31	0.27	1.346
136.67	9.66	9.80	-0.14	0.32	0.195
146.32	9.48	10.28	-0.80	0.38	4.388
155.98	10.50	10.41	0.09	0.53	0.030
162.15	10.66	10.39	0.28	0.33	0.687

TARGET ATOMIC MASS	32.0640 amu
EXCITATION ENERGY	0.000 MeV
INCIDENT NEUTRON ENERGY	9.947 MeV
ANGLE-INDEPENDENT ERROR	5.00 %
TOTAL CROSS SECTION	2.020 barn
CALCULATED WICK'S LIMIT	1202.53 +/- 120.25 mb/sr
ZERO DEGREE CROSS SECTION	1247.54 +/- 62.39 mb/sr
INTEGRATED CROSS SECTION	0.824 +/- 0.043 barn
CHI SQUARE PER DEGREE FREEDOM	1.05

ORDER	COEF	UNCOEF	RATIO	UNRATIO
0	65.56115	0.91409	1.00000	0.00000
1	143.76459	2.61181	2.19283	0.01056
2	207.80458	3.85258	3.16963	0.01677
3	220.04196	4.64428	3.35629	0.02806
4	208.75957	4.69498	3.18420	0.03251
5	179.50957	4.44353	2.73805	0.03713
6	124.02827	3.68884	1.89180	0.03676
7	63.29818	2.98473	0.96548	0.03679
8	27.87555	1.85266	0.42518	0.02484
9	6.89589	1.17939	0.10518	0.01735

ANGLE	EXP. SIGMA	CAL. SIGMA	DEVIATION	UNCEXPSIG	PCHSQ
19.95	660.76	660.85	-0.09	20.19	0.000
24.63	464.65	463.37	1.28	15.23	0.007
29.32	304.65	294.24	10.41	12.86	0.655
31.19	233.73	238.03	-4.30	8.96	0.231
34.01	167.57	166.74	0.83	6.61	0.016
38.78	81.08	81.69	-0.60	3.48	0.030
44.19	32.06	32.00	0.06	1.30	0.002
49.43	16.00	16.34	-0.34	0.76	0.207
55.78	18.43	17.57	0.85	0.64	1.789
60.87	20.81	21.94	-1.13	0.86	1.744
62.76	21.87	23.05	-1.18	0.97	1.477
65.55	24.35	23.82	0.54	0.98	0.298
67.41	24.35	23.74	0.60	0.77	0.616
71.17	21.99	22.35	-0.36	0.81	0.195
74.98	19.51	19.76	-0.25	0.93	0.072
79.82	16.64	15.80	0.84	0.77	1.199
84.75	11.92	11.99	-0.07	0.45	0.025
89.82	8.77	8.90	-0.13	0.42	0.100
97.25	6.18	6.31	-0.13	0.23	0.309
101.65	6.32	6.01	0.31	0.24	1.779
105.99	6.43	6.65	-0.22	0.26	0.706
113.15	9.46	9.53	-0.07	0.42	0.024
117.98	12.28	12.16	0.11	0.43	0.072
122.71	14.43	14.61	-0.18	0.63	0.079
127.41	16.81	16.38	0.43	0.58	0.554
132.14	16.85	17.21	-0.36	0.70	0.263
134.99	17.19	17.27	-0.08	0.57	0.021

141.73	15.89	16.61	-0.73	0.64	1.304
146.61	17.55	16.05	1.50	0.60	6.278
151.51	14.62	15.90	-1.28	0.65	3.845
154.44	16.23	16.11	0.13	0.55	0.054
161.17	17.38	17.30	0.09	0.56	0.024

TARGET ATOMIC MASS	32.0640 amu
EXCITATION ENERGY	-2.230 MeV
INCIDENT NEUTRON ENERGY	9.947 MeV
ANGLE-INDEPENDENT ERROR	5.00 %
INTEGRATED CROSS SECTION	0.097 +/- 0.005 barn
CHI SQUARE PER DEGREE FREEDOM	2.78

ORDER	COEF	UNCOEF	RATIO	UNRATIO
0	7.72587	0.08978	1.00000	0.00000
1	3.46178	0.15973	0.44808	0.01945
2	1.76177	0.20452	0.22803	0.02645
3	-2.56146	0.27334	-0.33154	0.03508
4	-2.20707	0.30796	-0.28567	0.03995
5	0.81992	0.34557	0.10613	0.04446

ANGLE	EXP. SIGMA	CAL. SIGMA	DEVIATION	UNCEXPSIG	PCHSQ
21.26	10.87	10.01	0.86	0.33	6.994
26.28	9.73	10.44	-0.71	0.48	2.237
31.35	10.48	10.87	-0.39	0.41	0.889
33.37	10.05	11.03	-0.98	0.44	4.936
36.39	10.69	11.26	-0.57	0.38	2.278
41.43	10.66	11.54	-0.88	0.47	3.511
46.46	12.15	11.68	0.48	0.27	3.070
50.47	11.72	11.66	0.06	0.60	0.009
55.50	12.96	11.44	1.51	0.38	16.277
60.49	10.69	11.02	-0.32	0.53	0.370
62.50	10.96	10.79	0.17	0.57	0.087
65.49	9.03	10.39	-1.36	0.58	5.498
67.49	10.36	10.09	0.27	0.27	0.988
71.48	8.91	9.41	-0.50	0.37	1.857
75.46	8.41	8.68	-0.26	0.57	0.214
80.45	6.78	7.72	-0.94	0.38	6.047
85.44	6.96	6.78	0.18	0.23	0.599
90.47	5.79	5.95	-0.16	0.28	0.314
97.54	4.92	5.07	-0.16	0.14	1.223
101.61	5.05	4.77	0.27	0.14	3.906
105.69	4.76	4.63	0.12	0.14	0.775
112.77	4.26	4.75	-0.48	0.22	4.648
117.76	5.07	5.04	0.03	0.17	0.027
122.68	5.31	5.45	-0.13	0.32	0.173
127.56	5.86	5.88	-0.03	0.24	0.012
132.39	6.37	6.29	0.08	0.36	0.054
135.28	6.50	6.49	0.01	0.23	0.004
141.99	6.51	6.79	-0.28	0.35	0.643
146.76	7.24	6.84	0.40	0.27	2.178
151.52	6.16	6.75	-0.59	0.39	2.248
154.36	6.75	6.65	0.10	0.26	0.154
160.97	6.28	6.30	-0.03	0.25	0.012

TARGET ATOMIC MASS	32.0640 amu
EXCITATION ENERGY	0.000 MeV
INCIDENT NEUTRON ENERGY	11.933 MeV
ANGLE-INDEPENDENT ERROR	5.00 %
TOTAL CROSS SECTION	1.914 barn
CALCULATED WICK'S LIMIT	1295.20 +/- 129.52 mb/sr
ZERO DEGREE CROSS SECTION	1221.64 +/- 61.09 mb/sr
INTEGRATED CROSS SECTION	0.758 +/- 0.039 barn
CHI SQUARE PER DEGREE FREEDOM	0.63

ORDER	COEF	UNCOEF	RATIO	UNRATIO
0	60.32108	0.88310	1.00000	0.00000
1	128.64995	2.50177	2.13275	0.01171
2	175.87689	3.73415	2.91568	0.02205
3	197.48946	4.48355	3.27397	0.02994
4	201.52129	4.54217	3.34081	0.03017
5	184.14217	4.32968	3.05270	0.03221
6	148.36688	3.68102	2.45962	0.03123
7	80.70902	3.01952	1.33799	0.03521
8	34.88828	2.06883	0.57838	0.02848
9	9.67292	1.19559	0.16036	0.01854

ANGLE	EXP. SIGMA	CAL. SIGMA	DEVIATION	UNCEXPSIG	PCHSQ
24.44	403.40	400.97	2.43	14.62	0.028
28.99	235.97	237.33	-1.36	9.22	0.022
33.46	121.78	121.31	0.46	5.70	0.007
38.31	45.12	45.96	-0.84	2.06	0.168
45.56	10.43	10.27	0.16	0.59	0.070
52.79	20.61	20.83	-0.22	0.98	0.050
61.84	36.43	37.10	-0.67	1.16	0.333
66.42	38.53	37.32	1.21	1.61	0.565
70.98	33.08	32.96	0.12	1.16	0.011
80.68	19.19	19.11	0.07	0.82	0.008
91.19	10.51	10.67	-0.16	0.51	0.097
101.85	10.78	10.68	0.10	0.43	0.058
111.78	14.14	13.97	0.17	0.58	0.082
121.27	14.83	15.57	-0.74	0.64	1.349
130.64	13.54	13.00	0.54	0.56	0.925
140.42	8.74	8.62	0.12	0.34	0.120
145.65	7.17	7.67	-0.50	0.41	1.519
150.90	8.51	8.40	0.11	0.40	0.074
156.86	11.54	11.00	0.54	0.59	0.838
163.38	14.44	14.80	-0.36	0.69	0.274

TARGET ATOMIC MASS	32.0640 amu
EXCITATION ENERGY	-2.230 MeV
INCIDENT NEUTRON ENERGY	11.933 MeV
ANGLE-INDEPENDENT ERROR	5.00 %
INTEGRATED CROSS SECTION	0.086 +/- 0.005 barn
CHI SQUARE PER DEGREE FREEDOM	0.96

ORDER	COEF	UNCOEF	RATIO	UNRATIO
0	6.82145	0.19225	1.00000	0.00000
1	6.99236	0.50938	1.02506	0.05030
2	6.53037	0.66715	0.95733	0.07639
3	2.52339	0.72823	0.36992	0.09878
4	-0.78305	0.67454	-0.11479	0.10106
5	1.43943	0.50636	0.21101	0.07135

ANGLE	EXP. SIGMA	CAL. SIGMA	DEVIATION	UNCEXPSIG	PCHSQ
25.91	19.56	18.73	0.83	6.61	0.016
30.94	14.97	17.14	-2.17	1.92	1.274
35.95	15.34	15.52	-0.19	1.39	0.018
41.03	16.88	13.92	2.96	1.52	3.803
46.08	12.59	12.41	0.18	0.83	0.045
51.15	10.49	10.99	-0.51	0.74	0.462
61.24	8.71	8.46	0.25	0.43	0.325
66.25	6.79	7.32	-0.54	0.50	1.143
71.25	6.31	6.27	0.04	0.35	0.015
81.25	4.36	4.43	-0.07	0.33	0.049
91.38	3.40	3.13	0.27	0.32	0.716
101.71	2.63	2.63	-0.01	0.20	0.001
111.95	2.71	3.01	-0.30	0.31	0.944
121.81	3.87	3.88	-0.01	0.37	0.002
131.42	5.33	4.66	0.67	0.37	3.382
140.91	4.65	4.85	-0.20	0.25	0.658
145.62	4.48	4.66	-0.19	0.35	0.283
150.31	4.44	4.30	0.14	0.29	0.231
155.91	3.65	3.70	-0.04	0.36	0.015
162.41	2.95	2.90	0.05	0.39	0.017

TARGET ATOMIC MASS	32.0640 amu
EXCITATION ENERGY	0.000 MeV
INCIDENT NEUTRON ENERGY	13.922 MeV
ANGLE-INDEPENDENT ERROR	5.00 %
TOTAL CROSS SECTION	1.830 barn
CALCULATED WICK'S LIMIT	1381.36 +/- 138.14 mb/sr
ZERO DEGREE CROSS SECTION	1288.11 +/- 64.43 mb/sr
INTEGRATED CROSS SECTION	0.721 +/- 0.040 barn
CHI SQUARE PER DEGREE FREEDOM	0.91

ORDER	COEF	UNCOEF	RATIO	UNRATIO
0	57.34176	1.39119	1.00000	0.00000
1	123.82652	3.93235	2.15945	0.01699
2	161.97987	6.04020	2.82482	0.03841
3	183.33521	7.19466	3.19724	0.05037
4	196.38727	7.65703	3.42486	0.05309
5	194.97052	7.09388	3.40015	0.04371
6	176.48611	6.33354	3.07779	0.03961
7	119.49134	4.91966	2.08385	0.03940
8	57.71551	3.72814	1.00652	0.04399
9	15.43037	2.22631	0.26909	0.03364
10	1.14915	1.27089	0.02004	0.02185

ANGLE	EXP. SIGMA	CAL. SIGMA	DEVIATION	UNCEXPSIG	PCHSQ
28.42	204.11	195.89	8.22	10.06	0.668
31.03	122.86	122.22	0.64	6.41	0.010
34.75	45.54	50.83	-5.29	2.48	4.570
39.36	10.92	10.54	0.38	0.49	0.597
45.56	12.04	12.46	-0.42	0.67	0.395
50.49	30.75	32.26	-1.51	1.74	0.759
52.54	41.16	40.32	0.84	1.79	0.220
57.46	54.30	52.94	1.36	1.82	0.559
60.94	54.98	54.48	0.50	1.70	0.087
66.34	47.92	46.55	1.37	1.68	0.665
70.03	35.33	37.12	-1.79	1.30	1.901
75.78	22.85	22.56	0.29	0.94	0.095
79.99	15.03	15.08	-0.05	0.59	0.008
86.28	10.36	10.39	-0.02	0.33	0.005
91.30	10.93	10.60	0.33	0.43	0.584
97.40	11.95	12.34	-0.38	0.44	0.749
101.24	12.89	13.13	-0.24	0.51	0.216
106.99	14.09	13.30	0.79	0.52	2.264
110.85	12.61	12.86	-0.25	0.47	0.292
116.67	11.99	11.82	0.17	0.45	0.144
120.57	10.64	11.04	-0.40	0.42	0.918
126.38	9.92	9.78	0.14	0.41	0.112
130.24	9.13	8.87	0.26	0.38	0.463
136.07	7.26	7.46	-0.21	0.31	0.438
140.05	6.70	6.65	0.04	0.30	0.020

146.16	6.10	6.08	0.03	0.27	0.009
150.78	6.43	6.41	0.02	0.25	0.004
156.29	7.62	7.68	-0.06	0.33	0.034
160.12	9.00	8.97	0.04	0.38	0.009

TARGET ATOMIC MASS	32.0640 amu
EXCITATION ENERGY	-2.230 MeV
INCIDENT NEUTRON ENERGY	13.922 MeV
ANGLE-INDEPENDENT ERROR	5.00 %
INTEGRATED CROSS SECTION	0.074 +/- 0.005 barn
CHI SQUARE PER DEGREE FREEDOM	1.93

ORDER	COEF	UNCOEF	RATIO	UNRATIO
0	5.92311	0.21585	1.00000	0.00000
1	6.70717	0.59981	1.13237	0.06306
2	3.24893	0.82791	0.54852	0.12166
3	-1.38607	0.89250	-0.23401	0.15815
4	-3.43674	0.70062	-0.58022	0.13590
5	-0.75086	0.45039	-0.12677	0.07907

ANGLE	EXP. SIGMA	CAL. SIGMA	DEVIATION	UNCEXPSIG	PCHSQ
31.25	14.98	13.51	1.48	4.39	0.113
34.31	16.99	13.70	3.29	1.80	3.345
38.28	13.46	13.78	-0.32	1.71	0.034
41.28	13.40	13.69	-0.29	1.23	0.056
44.29	13.17	13.47	-0.30	0.50	0.354
48.28	12.40	12.98	-0.57	0.54	1.138
50.78	13.23	12.56	0.67	0.60	1.273
56.76	11.25	11.25	0.00	0.52	0.000
60.74	9.76	10.20	-0.44	0.39	1.329
66.70	9.31	8.47	0.84	0.37	5.202
70.67	7.34	7.31	0.03	0.35	0.006
76.59	5.75	5.67	0.08	0.36	0.047
80.58	4.40	4.69	-0.30	0.25	1.432
86.12	3.54	3.59	-0.05	0.11	0.178
90.71	3.12	2.92	0.20	0.23	0.735
96.95	3.15	2.37	0.78	0.28	7.750
101.11	1.81	2.21	-0.40	0.22	3.394
107.28	1.93	2.20	-0.27	0.36	0.538
111.32	2.28	2.30	-0.02	0.20	0.007
117.24	2.28	2.51	-0.23	0.22	1.176
121.14	2.89	2.66	0.23	0.17	1.712
126.93	3.00	2.82	0.18	0.20	0.811
130.77	2.81	2.87	-0.06	0.17	0.116
136.51	2.81	2.84	-0.03	0.16	0.036
140.32	2.73	2.76	-0.03	0.16	0.032
146.00	2.51	2.54	-0.03	0.15	0.048
150.26	2.29	2.33	-0.05	0.27	0.030
155.52	2.02	2.04	-0.02	0.15	0.014
159.31	1.90	1.83	0.08	0.18	0.174

TARGET ATOMIC MASS	32.0640 amu
EXCITATION ENERGY	0.000 MeV
INCIDENT NEUTRON ENERGY	16.917 MeV
ANGLE-INDEPENDENT ERROR	5.00 %
TOTAL CROSS SECTION	1.782 barn
CALCULATED WICK'S LIMIT	1591.62 +/- 159.16 mb/sr
ZERO DEGREE CROSS SECTION	1830.29 +/- 91.53 mb/sr
INTEGRATED CROSS SECTION	0.855 +/- 0.045 barn
CHI SQUARE PER DEGREE FREEDOM	1.08

ORDER	COEF	UNCOEF	RATIO	UNRATIO
0	68.06806	1.22005	1.00000	0.00000
1	154.05461	3.52341	2.26324	0.01231
2	193.53592	5.48434	2.84327	0.03246
3	222.44019	6.93397	3.26791	0.04785
4	246.72090	7.55893	3.62462	0.05135
5	259.58862	7.52457	3.81366	0.04758
6	256.29599	6.99335	3.76529	0.04111
7	210.89336	6.21828	3.09827	0.04289
8	129.99559	5.10210	1.90979	0.04710
9	59.29136	3.92577	0.87106	0.04617
10	22.69131	2.49934	0.33336	0.03288
11	6.71337	1.10903	0.09863	0.01541

ANGLE	EXP. SIGMA	CAL. SIGMA	DEVIATION	UNCEXPSIG	PCHSQ
19.55	686.91	672.13	14.78	25.19	0.344
24.00	377.51	369.36	8.16	16.15	0.255
28.16	168.83	167.68	1.15	8.28	0.019
32.79	41.31	42.07	-0.76	1.74	0.192
43.83	27.65	26.54	1.11	2.09	0.282
48.03	52.33	55.16	-2.83	2.47	1.312
52.02	75.02	74.57	0.45	2.11	0.045
56.43	79.92	81.28	-1.36	2.17	0.391
61.03	75.64	73.41	2.23	2.33	0.914
70.56	39.90	37.74	2.16	1.47	2.155
75.61	21.45	22.62	-1.17	0.76	2.402
81.11	14.07	14.06	0.02	0.45	0.001
86.76	12.91	12.56	0.35	0.42	0.703
91.98	14.53	14.66	-0.13	0.48	0.077
96.84	16.85	16.84	0.01	0.55	0.000
101.56	16.84	17.42	-0.58	0.56	1.062
110.96	13.40	12.91	0.48	0.50	0.946
115.77	9.50	9.41	0.09	0.35	0.060
120.76	6.49	6.57	-0.08	0.26	0.093
131.02	4.44	4.57	-0.12	0.19	0.453
135.93	4.73	4.42	0.31	0.23	1.882
140.75	4.03	4.16	-0.13	0.20	0.445
145.65	3.92	3.83	0.10	0.17	0.311

150.65	3.63	3.73	-0.09	0.17	0.309
155.63	3.97	4.02	-0.05	0.20	0.060
160.45	4.61	4.47	0.14	0.23	0.377

TARGET ATOMIC MASS	32.0640 amu
EXCITATION ENERGY	-2.230 MeV
INCIDENT NEUTRON ENERGY	16.917 MeV
ANGLE-INDEPENDENT ERROR	5.00 %
INTEGRATED CROSS SECTION	0.052 +/- 0.003 barn
CHI SQUARE PER DEGREE FREEDOM	1.21

ORDER	COEF	UNCOEF	RATIO	UNRATIO
0	4.11342	0.05926	1.00000	0.00000
1	5.68088	0.14502	1.38106	0.02321
2	4.45317	0.19776	1.08260	0.04047
3	1.84816	0.23809	0.44930	0.05528
4	0.02562	0.22186	0.00623	0.05391
5	0.52892	0.18983	0.12858	0.04586

ANGLE	EXP. SIGMA	CAL. SIGMA	DEVIATION	UNCEXPSIG	PCHSQ
20.88	12.31	14.33	-2.03	1.20	2.874
25.90	12.34	13.25	-0.91	0.91	1.007
30.94	12.21	12.07	0.14	0.45	0.096
35.98	11.22	10.85	0.36	0.47	0.604
41.03	9.69	9.63	0.05	0.54	0.009
46.08	8.85	8.46	0.39	0.40	0.951
51.13	7.61	7.36	0.25	0.28	0.800
56.18	6.19	6.34	-0.15	0.28	0.287
61.22	4.90	5.41	-0.51	0.32	2.596
71.30	3.90	3.84	0.06	0.22	0.075
76.33	3.03	3.19	-0.16	0.17	0.828
81.37	2.62	2.63	-0.01	0.15	0.004
86.42	2.21	2.17	0.05	0.12	0.137
91.47	1.91	1.80	0.11	0.12	0.904
96.54	1.43	1.54	-0.10	0.12	0.724
101.61	1.46	1.38	0.08	0.13	0.335
111.66	1.33	1.33	0.00	0.13	0.000
121.58	1.53	1.50	0.03	0.12	0.054
131.34	1.56	1.69	-0.13	0.11	1.372
136.20	1.54	1.73	-0.19	0.14	1.911
141.04	1.76	1.70	0.06	0.14	0.157
145.89	1.72	1.62	0.10	0.12	0.765
150.70	1.80	1.47	0.33	0.12	6.978
155.49	1.24	1.28	-0.04	0.12	0.110
160.26	0.86	1.08	-0.22	0.13	2.894

APPENDIX II

TABULATION OF THE ANALYZING POWER DATA

In this appendix, the data are presented with fits that were derived from associated Legendre polynomial fits to the product of the analyzing powers and cross sections. The following form was used to fit the product of the analyzing power data and the cross section data:

$$\sigma(\theta,E)\cdot A_y(\theta,E) = \sum_{\ell} b_{\ell}(E)\, P_{\ell}^{1}(\cos(\theta)) \ .$$

Also given are the F tests of the multiple-correlation coefficient (a multiple-correlation coefficient of $R \simeq 1$ indicates a good fit and the inclusion of additional terms is not necessary).

$$F_R = \frac{R^2(N-n-1)}{(1-R^2)n}$$

$$F_{\chi} = \frac{\chi^2_{n-1}-\chi^2_n}{\chi^2_n}(N-n-1) \ .$$

Here N is the number of data points, n is the number of terms in the fit, and R is the multiple-correlation coefficient. Below is the key:

L = number of terms in fit

B(L) = $b_{\ell}(E)$

DB(L) = $\Delta b_{\ell}(E)$

REDB(L) = $b_{\ell}(E)/b_1(E)$

REDDB(L) = $\Delta b_{\ell}(E)/b_1(E)$

REGCC = F_R

FVAL = F_χ

ANGLE = θ(center-of-mass)

CALPOL = associated Legendre polynomial fit

EXPOL = $A_y(\theta)$

ERROR = $\Delta A_y(\theta)$ - does not include 3% normalization uncertainty

CHISQR = $(\text{POL-EXPOL})^2/\text{ERROR}^2$.

NEUTRON VECTOR ANALYZING POWER

TARGET ATOMIC MASS	28.09 amu
INCIDENT ENERGY	10.00 MeV
EXCITATION ENERGY	0.00 MeV
J^{π}	0+

LMAX = 10

L	B(L)	DB(L)	REDB(L)	REDDB(L)	REGCC	FVAL
1	-4.97031	0.31461	1.00000	-0.06330	0.00000	15.00000
2	0.44610	0.29566	-0.08975	-0.05949	6.48678	0.04634
3	5.27209	0.32506	-1.06072	-0.06540	4.01401	10.55608
4	1.94469	0.34800	-0.39126	-0.07002	9.76568	2.55280
5	0.22740	0.31836	-0.04575	-0.06405	9.21002	3.63872
6	-3.08927	0.30965	0.62154	-0.06230	28.73739	39.63512
7	0.73336	0.24244	-0.14755	-0.04878	38.96944	9.35111
8	-0.19155	0.23906	0.03854	-0.04810	44.72617	5.63631
9	-0.64839	0.18177	0.13045	-0.03657	36.00953	0.40747
10	-0.69789	0.14946	0.14041	-0.03007	92.34877	13.88512

ANGLE	EXPOL	ERROR	CALPOL	CHISQR
20.7169	0.0091	0.0120	0.0073	0.0232
29.8466	0.0500	0.0117	0.0571	0.3641
38.8494	0.1732	0.0181	0.1595	0.5701
49.3487	0.4683	0.0336	0.4750	0.0393
57.4142	-0.0186	0.0800	0.0142	0.1678
63.2579	-0.1916	0.0604	-0.2959	2.9812
72.2459	-0.6749	0.0462	-0.5829	3.9666
81.4564	-0.8062	0.0426	-0.8465	0.8967
90.8052	-0.8972	0.0545	-0.8909	0.0132
100.3842	-0.2956	0.0832	-0.2941	0.0003
112.3386	0.2877	0.1011	0.3011	0.0176
122.2359	-0.2871	0.0699	-0.3168	0.1811
131.3011	-0.3712	0.0489	-0.3585	0.0679
140.7111	-0.1608	0.0450	-0.1579	0.0040
151.1493	0.5482	0.0442	0.5361	0.0755
155.9600	0.6482	0.0394	0.6573	0.0537

CHISQR/DEG OF FREEDOM = 1.570 CHISQR/PT = 0.589

NEUTRON VECTOR ANALYZING POWER

TARGET ATOMIC MASS	28.09 amu
INCIDENT ENERGY	10.00 MeV
EXCITATION ENERGY	-1.78 MeV
J^{π}	2+

LMAX = 8

L	B(L)	DB(L)	REDB(L)	REDDB(L)	REGCC	FVAL
1	0.71162	0.25566	1.00000	0.35927	0.00000	15.00000
2	-1.48474	0.15376	-2.08641	0.21607	14.43353	22.57200
3	-0.28677	0.13316	-0.40298	0.18712	9.47454	1.40632
4	-0.58911	0.12657	-0.82784	0.17786	16.21605	11.25930
5	-0.35441	0.10349	-0.49804	0.14543	17.17886	5.29044
6	-0.34053	0.10415	-0.47853	0.14635	32.12630	9.11216
7	0.24531	0.10471	0.34472	0.14714	32.86052	6.81768
8	-0.08083	0.10151	-0.11359	0.14265	26.95535	0.81239

ANGLE	EXPOL	ERROR	CALPOL	CHISQR
21.8629	-0.3769	0.0633	-0.3827	0.0084
31.9234	-0.3071	0.0403	-0.2948	0.0928
41.9536	-0.1257	0.0348	-0.1435	0.2623
52.0006	-0.0254	0.0226	-0.0268	0.0039
56.9258	-0.0541	0.0475	0.0084	1.7309
61.8678	0.0399	0.0475	0.0288	0.0544
71.7691	0.0932	0.0504	0.0284	1.6530
81.7564	-0.0679	0.0587	-0.0039	1.1886
91.9286	0.0093	0.0521	0.0046	0.0082
102.0163	0.1189	0.0486	0.1007	0.1405
111.9069	0.1712	0.0476	0.1936	0.2212
121.5541	0.2344	0.0580	0.2006	0.3390
131.2121	0.1261	0.0497	0.1452	0.1480
140.8242	0.1331	0.0533	0.1308	0.0019
150.5105	0.2499	0.0597	0.2212	0.2307
155.2970	0.2447	0.0591	0.2686	0.1629

CHISQR/DEG OF FREEDOM = 0.781 CHISQR/PT = 0.390

NEUTRON VECTOR ANALYZING POWER

TARGET ATOMIC MASS	28.09 amu
INCIDENT ENERGY	14.00 MeV
EXCITATION ENERGY	0.00 MeV
J^{π}	0+

LMAX = 13

L	B(L)	DB(L)	REDB(L)	REDDB(L)	REGCC	FVAL
1	-5.93803	0.28728	1.00000	-0.04838	0.00000	20.00000
2	-6.98230	0.27307	1.17586	-0.04599	1.57393	2.57095
3	-3.59616	0.29227	0.60562	-0.04922	1.15806	0.10623
4	-2.46849	0.33549	0.41571	-0.05650	2.05689	0.72776
5	-4.01084	0.36383	0.67545	-0.06127	2.41643	0.47087
6	-5.05254	0.36293	0.85088	-0.06112	21.16241	103.85175
7	-1.48230	0.36715	0.24963	-0.06183	21.82384	2.42372
8	-1.01112	0.31075	0.17028	-0.05233	124.76094	47.69398
9	0.09901	0.27997	-0.01667	-0.04715	160.67427	17.01630
10	0.42927	0.22861	-0.07229	-0.03850	168.31802	0.55365
11	0.35001	0.20076	-0.05894	-0.03381	143.46954	1.12895
12	0.17230	0.14363	-0.02902	-0.02419	153.40257	0.06194
13	0.14135	0.09908	-0.02380	-0.01669	280.68073	1.50706

ANGLE	EXPOL	ERROR	CALPOL	CHISQR
20.0612	-0.0932	0.0170	-0.1070	0.6568
20.4465	-0.1271	0.0169	-0.1106	0.9566
24.6409	-0.1447	0.0202	-0.1559	0.3068
28.7119	-0.2203	0.0139	-0.2142	0.1922
32.8115	-0.3011	0.0354	-0.2979	0.0084
38.0298	-0.4149	0.0700	-0.4987	1.4342
42.6220	-0.5854	0.0577	-0.5733	0.0441
47.8792	0.1201	0.0512	0.1230	0.0033
48.7335	0.0981	0.0360	0.0889	0.0660
53.7281	-0.0498	0.0373	-0.0578	0.0466
61.9598	-0.1937	0.0268	-0.1895	0.0243
71.2667	-0.3589	0.0318	-0.3423	0.2726
80.4619	-0.5702	0.0357	-0.5933	0.4172
91.5490	-0.4468	0.0382	-0.4267	0.2768
102.0020	0.3588	0.0413	0.3177	0.9910
111.7188	0.5101	0.0412	0.5693	2.0640
121.3099	0.3868	0.0370	0.3393	1.6478
130.8452	-0.2442	0.0444	-0.1971	1.1252
140.4536	-0.4327	0.0426	-0.4527	0.2200
150.5091	0.2253	0.0429	0.2338	0.0394
158.4620	0.8550	0.0497	0.8502	0.0093

CHISQR/DEG OF FREEDOM = 1.350 CHISQR/PT = 0.514

NEUTRON VECTOR ANALYZING POWER

TARGET ATOMIC MASS	28.09 amu
INCIDENT ENERGY	14.00 MeV
EXCITATION ENERGY	-1.78 MeV
J^{π}	2+

LMAX = 8

L	B(L)	DB(L)	REDB(L)	REDDB(L)	REGCC	FVAL
1	2.12383	0.15737	1.00000	0.07410	0.00000	19.00000
2	0.46308	0.12313	0.21804	0.05798	1.63123	0.13800
3	0.85826	0.09895	0.40411	0.04659	13.39860	28.85213
4	-0.12417	0.11008	-0.05846	0.05183	10.26159	6.13837
5	-0.58835	0.09201	-0.27702	0.04332	27.76798	18.09286
6	-0.03984	0.07911	-0.01876	0.03725	26.51842	6.57661
7	0.30746	0.07120	0.14477	0.03353	39.34269	14.23234
8	0.14396	0.06363	0.06779	0.02996	47.22296	8.48224

ANGLE	EXPOL	ERROR	CALPOL	CHISQR
21.0920	0.1130	0.1156	0.1447	0.0753
26.8469	0.1987	0.1137	0.1034	0.7032
31.9168	0.0340	0.1288	0.0915	0.1993
36.7547	0.0483	0.0808	0.1070	0.5285
41.7160	0.1902	0.0465	0.1477	0.8354
43.6335	0.1913	0.0355	0.1686	0.4084
46.5702	0.1689	0.0327	0.2043	1.1714
46.6487	0.1878	0.0284	0.2053	0.3791
51.5315	0.3130	0.0457	0.2679	0.9759
61.2771	0.3797	0.0545	0.3521	0.2567
71.6074	0.2401	0.0759	0.2683	0.1378
81.6114	-0.0571	0.0667	-0.0304	0.1606
91.8128	-0.1823	0.0508	-0.2028	0.1621
101.6883	0.1101	0.0788	0.1229	0.0264
111.8907	0.3980	0.0650	0.4323	0.2785
121.8590	0.5060	0.0588	0.4699	0.3759
131.3615	0.4149	0.0503	0.4126	0.0021
140.6743	0.3416	0.0581	0.3746	0.3216
150.0066	0.3948	0.0608	0.3665	0.2166
157.8410	0.3244	0.0961	0.3457	0.0491

CHISQR/DEG OF FREEDOM = 0.605 CHISQR/PT = 0.363

NEUTRON VECTOR ANALYZING POWER

TARGET ATOMIC MASS	28.09 amu
INCIDENT ENERGY	17.00 MeV
EXCITATION ENERGY	0.00 MeV
J^{π}	0+

LMAX = 11

L	B(L)	DB(L)	REDB(L)	REDDB(L)	REGCC	FVAL
1	-5.52184	0.32584	1.00000	-0.05901	0.00000	16.00000
2	-8.51391	0.32436	1.54186	-0.05874	11.24411	21.91477
3	-4.80060	0.33181	0.86938	-0.06009	9.79730	3.12560
4	-3.50659	0.35976	0.63504	-0.06515	7.20001	0.06130
5	-4.11733	0.34909	0.74564	-0.06322	5.28398	0.98691
6	-4.78226	0.29844	0.86606	-0.05405	16.33341	13.10609
7	-2.71619	0.26736	0.49190	-0.04842	26.39807	18.19496
8	-1.29323	0.22970	0.23420	-0.04160	105.01113	18.89871
9	-0.38845	0.21121	0.07035	-0.03825	111.55335	10.59086
10	0.02354	0.16556	-0.00426	-0.02998	86.45337	0.01025
11	0.03607	0.11238	-0.00653	-0.02035	73.09876	0.05633

ANGLE	EXPOL	ERROR	CALPOL	CHISQR
20.2347	-0.1134	0.0123	-0.1124	0.0064
29.2059	-0.2624	0.0155	-0.2594	0.0384
38.9985	-0.9000	0.0500	-0.9507	1.0263
41.7685	-0.6383	0.0502	-0.5692	1.8924
47.9038	-0.0573	0.0339	-0.0768	0.3315
52.2710	-0.0449	0.0324	-0.0754	0.8858
61.4996	-0.1814	0.0249	-0.1703	0.1998
71.0213	-0.3393	0.0274	-0.3235	0.3319
81.1012	-0.4291	0.0393	-0.4629	0.7406
91.9572	-0.0240	0.0335	0.0024	0.6210
101.9400	0.4025	0.0495	0.3173	2.9647
111.4453	0.3507	0.0496	0.4133	1.5926
121.2293	0.3911	0.0499	0.3730	0.1312
130.9736	0.2303	0.0582	0.2232	0.0147
140.6986	0.3242	0.0738	0.3465	0.0914
150.5690	0.8785	0.1008	0.8479	0.0921
158.3520	0.9827	0.0824	0.9919	0.0125

CHISQR/DEG OF FREEDOM = 1.829 CHISQR/PT = 0.645

NEUTRON VECTOR ANALYZING POWER

TARGET ATOMIC MASS	28.09 amu
INCIDENT ENERGY	17.00 MeV
EXCITATION ENERGY	-1.78 MeV
J^{π}	2+

LMAX = 10

L	B(L)	DB(L)	REDB(L)	REDDB(L)	REGCC	FVAL
1	0.68566	0.17278	1.00000	0.25199	0.00000	15.00000
2	-0.01197	0.14260	-0.01746	0.20797	0.02856	0.47730
3	0.15423	0.11973	0.22493	0.17461	1.98446	2.88689
4	-0.13956	0.12321	-0.20355	0.17970	1.45028	2.23564
5	-0.39244	0.10970	-0.57235	0.16000	5.70512	6.38796
6	-0.08520	0.10411	-0.12425	0.15184	4.30542	2.05238
7	-0.03691	0.10085	-0.05383	0.14708	3.71757	5.18406
8	-0.28131	0.10243	-0.41027	0.14939	101.37949	17.59047
9	-0.09120	0.08543	-0.13301	0.12459	113.55030	40.72798
10	0.04911	0.06659	0.07162	0.09711	800.70422	50.55001

ANGLE	EXPOL	ERROR	CALPOL	CHISQR
21.2053	-0.1192	0.0854	-0.1149	0.0025
31.2402	0.0208	0.0546	0.0175	0.0036
41.4151	0.1101	0.0473	0.1122	0.0019
46.5042	0.1114	0.0522	0.1091	0.0019
51.5592	0.0778	0.0779	0.0855	0.0097
61.6607	0.0757	0.0738	0.0679	0.0111
71.6878	0.1265	0.0665	0.1294	0.0019
81.6979	0.0993	0.0757	0.1019	0.0012
91.5056	-0.1245	0.0633	-0.1275	0.0022
101.6637	-0.1813	0.1039	-0.1769	0.0018
111.7759	0.4470	0.1486	0.4431	0.0007
121.8329	0.6440	0.1173	0.6478	0.0010
131.5109	0.2891	0.0814	0.2838	0.0043
141.0131	0.0411	0.0850	0.0504	0.0120
150.4294	0.0816	0.0877	0.0736	0.0083
157.8460	0.1720	0.0821	0.1743	0.0008

CHISQR/DEG OF FREEDOM = 0.011 CHISQR/PT = 0.004

NEUTRON VECTOR ANALYZING POWER

TARGET ATOMIC MASS	32.06 amu
INCIDENT ENERGY	10.00 MeV
EXCITATION ENERGY	0.00 MeV
J^{π}	0+

LMAX = 9

L	B(L)	DB(L)	REDB(L)	REDDB(L)	REGCC	FVAL
1	-4.56490	0.17852	1.00000	-0.03911	0.00000	21.00000
2	-1.43735	0.15085	0.31487	-0.03304	0.49629	1.01102
3	1.31424	0.16233	-0.28790	-0.03556	0.80862	0.12602
4	1.73320	0.15566	-0.37968	-0.03410	9.48227	7.11780
5	-0.10730	0.16617	0.02350	-0.03640	10.59090	6.86840
6	-3.98296	0.13602	0.87252	-0.02980	40.97848	58.07498
7	-0.09752	0.14052	0.02136	-0.03078	32.80710	9.48253
8	-1.44263	0.09954	0.31603	-0.02181	259.80508	119.87715
9	-0.17224	0.10644	0.03773	-0.02332	218.93550	1.32560

ANGLE	EXPOL	ERROR	CALPOL	CHISQR
20.4836	-0.0389	0.0098	-0.0238	2.3792
24.9918	-0.0128	0.0102	-0.0175	0.2138
29.5851	-0.0034	0.0054	0.0011	0.6889
30.0475	0.0155	0.0132	0.0040	0.7630
34.0703	0.0509	0.0097	0.0408	1.0810
38.9292	0.1274	0.0186	0.1277	0.0002
44.9109	0.3200	0.0284	0.3009	0.4500
50.6500	0.1159	0.0308	0.1547	1.5880
56.7366	-0.2564	0.0319	-0.3012	1.9738
61.7849	-0.5216	0.0316	-0.4872	1.1845
71.1456	-0.6481	0.0268	-0.6775	1.2012
80.8623	-0.8617	0.0290	-0.8423	0.4452
101.5916	0.2789	0.0437	0.2938	0.1160
106.9595	0.7498	0.0426	0.6832	2.4451
111.9787	0.6129	0.0405	0.6288	0.1536
116.8639	0.2902	0.0315	0.3627	5.2919
121.7628	0.0763	0.0293	0.0428	1.3104
131.1462	-0.4247	0.0320	-0.4825	3.2662
135.9063	-0.6360	0.0277	-0.6224	0.2411
140.6063	-0.6323	0.0318	-0.6029	0.8520
150.5796	0.0939	0.0278	0.0913	0.0089
155.4110	0.5745	0.0279	0.5701	0.0249

CHISQR/DEG OF FREEDOM = 1.975 CHISQR/PT = 1.167

NEUTRON VECTOR ANALYZING POWER

TARGET ATOMIC MASS	32.06 amu
INCIDENT ENERGY	10.00 MeV
EXCITATION ENERGY	-2.23 MeV
J^{π}	2+

LMAX = 8

L	B(L)	DB(L)	REDB(L)	REDDB(L)	REGCC	FVAL
1	-0.94157	0.11150	1.00000	-0.11842	0.00000	21.00000
2	-1.09539	0.06995	1.16336	-0.07429	5.33924	10.63820
3	0.46555	0.06579	-0.49444	-0.06987	4.44420	0.00288
4	0.54690	0.05317	-0.58084	-0.05647	9.82007	17.20442
5	-0.48534	0.05270	0.51546	-0.05597	14.18060	5.66828
6	-0.40340	0.05404	0.42844	-0.05739	37.50183	38.47168
7	0.17672	0.05650	-0.18768	-0.06001	53.18785	8.09941
8	-0.06522	0.04877	0.06927	-0.05179	48.30170	1.01002

ANGLE	EXPOL	ERROR	CALPOL	CHISQR
21.8261	-0.3160	0.0991	-0.1668	2.2664
26.7170	-0.2620	0.0752	-0.1295	3.1047
31.4410	-0.0661	0.0671	-0.0857	0.0853
31.7199	-0.0450	0.0250	-0.0831	2.3276
36.6106	-0.0370	0.0391	-0.0432	0.0255
41.6293	-0.0818	0.0457	-0.0186	1.9140
46.5639	-0.0394	0.0403	-0.0169	0.3108
51.6174	-0.0567	0.0361	-0.0415	0.1771
56.6129	-0.0384	0.0358	-0.0919	2.2368
61.5552	-0.2306	0.0440	-0.1650	2.2201
71.4574	-0.3083	0.0435	-0.3573	1.2711
81.5007	-0.5406	0.0408	-0.5242	0.1609
101.5212	-0.0633	0.0573	0.0200	2.1159
106.7755	0.4368	0.0548	0.3194	4.5875
111.7915	0.4988	0.0614	0.5104	0.0359
116.7430	0.5384	0.0566	0.5568	0.1055
121.6641	0.4381	0.0567	0.4786	0.5095
131.3934	0.1914	0.0548	0.1718	0.1285
136.1819	0.0470	0.0406	0.0423	0.0132
140.8590	-0.0519	0.0465	-0.0341	0.1468
150.5833	0.0222	0.0418	-0.0157	0.8203
155.2780	0.0243	0.0437	0.0555	0.5096

CHISQR/DEG OF FREEDOM = 1.791 CHISQR/PT = 1.140

NEUTRON VECTOR ANALYZING POWER

TARGET ATOMIC MASS	32.06 amu
INCIDENT ENERGY	14.00 MeV
EXCITATION ENERGY	0.00 MeV
J^{π}	0+

LMAX = 9

L	B(L)	DB(L)	REDB(L)	REDDB(L)	REGCC	FVAL
1	-5.40879	0.29780	1.00000	-0.05506	0.00000	18.00000
2	-5.65646	0.26653	1.04579	-0.04928	1.01677	0.79858
3	-1.78310	0.22593	0.32967	-0.04177	1.10514	0.34035
4	-0.16095	0.21793	0.02976	-0.04029	4.83367	1.18814
5	-1.42043	0.20533	0.26261	-0.03796	3.62339	7.19953
6	-4.14569	0.18464	0.76647	-0.03414	7.42808	22.07050
7	-2.28145	0.17924	0.42180	-0.03314	7.73667	0.37181
8	-2.01002	0.14547	0.37162	-0.02689	107.97610	124.48928
9	-0.30680	0.10182	0.05672	-0.01882	101.68768	7.25824

ANGLE	EXPOL	ERROR	CALPOL	CHISQR
20.0740	-0.0886	0.0110	-0.0823	0.3274
24.3440	-0.1187	0.0212	-0.0993	0.8366
28.5440	-0.0756	0.0204	-0.1122	3.2270
32.5820	-0.0848	0.0219	-0.1097	1.2879
39.3220	0.1611	0.0490	0.2243	1.6633
44.6740	0.3347	0.0584	0.2875	0.6524
48.5390	0.0050	0.0477	-0.0407	0.9192
53.3120	-0.1914	0.0394	-0.1846	0.0301
61.4710	-0.3835	0.0335	-0.3263	2.9194
70.3270	-0.4733	0.0363	-0.4853	0.1101
80.3340	-0.5796	0.0396	-0.5890	0.0569
91.7260	-0.0345	0.0426	-0.0287	0.0186
101.6670	0.2133	0.0395	0.2150	0.0018
111.2790	0.3383	0.0398	0.3389	0.0002
120.9320	0.2870	0.0457	0.2711	0.1210
130.6010	-0.1874	0.0516	-0.1617	0.2485
140.3180	-0.5244	0.0535	-0.5395	0.0792
150.6000	0.2386	0.0562	0.2441	0.0096
158.3360	0.9067	0.0510	0.9062	0.0001

CHISQR/DEG OF FREEDOM = 1.251 CHISQR/PT = 0.658

NEUTRON VECTOR ANALYZING POWER

TARGET ATOMIC MASS	32.06 amu
INCIDENT ENERGY	14.00 MeV
EXCITATION ENERGY	-2.23 MeV
J^{π}	2+

LMAX = 7

L	B(L)	DB(L)	REDB(L)	REDDB(L)	REGCC	FVAL
1	-0.74915	0.19554	1.00000	-0.26102	0.00000	18.00000
2	-0.44658	0.14119	0.59612	-0.18847	12.54352	17.45871
3	0.21331	0.10766	-0.28473	-0.14371	9.02209	0.94260
4	0.16196	0.11337	-0.21620	-0.15134	10.61994	0.61879
5	0.10904	0.10583	-0.14555	-0.14127	10.08541	2.96200
6	0.03773	0.08852	-0.05036	-0.11816	7.75940	1.09721
7	0.20975	0.07605	-0.27999	-0.10151	8.88497	12.64088

ANGLE	EXPOL	ERROR	CALPOL	CHISQR
21.7580	0.0910	0.1102	0.0952	0.0014
26.6360	-0.0018	0.1204	0.0453	0.1532
31.5980	-0.1238	0.1079	-0.0094	1.1249
36.4580	-0.0159	0.0639	-0.0565	0.4045
41.4460	-0.0349	0.0627	-0.0921	0.8310
43.9400	-0.0982	0.0639	-0.1041	0.0086
46.3980	-0.1255	0.0715	-0.1125	0.0333
51.3360	-0.1927	0.0920	-0.1200	0.6238
61.3130	-0.1697	0.1219	-0.1208	0.1611
71.0370	-0.2265	0.1037	-0.1606	0.4040
80.9500	-0.1696	0.1070	-0.2991	1.4649
91.0370	-0.5176	0.1640	-0.4450	0.1957
101.5900	-0.4771	0.2308	-0.2342	1.1079
111.7970	0.2280	0.1532	0.1124	0.5695
121.5890	0.1408	0.1562	0.1323	0.0029
131.1630	-0.0476	0.1245	-0.0082	0.0999
140.6090	-0.0560	0.1162	-0.0484	0.0043
150.0750	0.2160	0.1654	0.1675	0.0858
157.3920	0.4729	0.1619	0.4902	0.0114

CHISQR/DEG OF FREEDOM = 0.607 CHISQR/PT = 0.384

NEUTRON VECTOR ANALYZING POWER

TARGET ATOMIC MASS	32.06 amu
INCIDENT ENERGY	17.00 MeV
EXCITATION ENERGY	0.00 MeV
J^{π}	0+

LMAX = 12

L	B(L)	DB(L)	REDB(L)	REDDB(L)	REGCC	FVAL
1	-6.11272	0.37621	1.00000	-0.06155	0.00000	17.00000
2	-8.60560	0.34110	1.40782	-0.05580	3.28304	6.21782
3	-5.43746	0.31531	0.88953	-0.05158	5.87406	4.94059
4	-3.49102	0.34787	0.57111	-0.05691	4.30892	2.74240
5	-3.34693	0.34034	0.54753	-0.05568	3.18507	0.80080
6	-5.10690	0.32891	0.83545	-0.05381	2.99288	1.75780
7	-4.78487	0.30719	0.78277	-0.05025	3.33847	1.40504
8	-3.62455	0.28494	0.59295	-0.04661	17.30488	28.56354
9	-1.67784	0.24381	0.27448	-0.03989	20.44178	9.85155
10	-0.91163	0.22468	0.14914	-0.03676	27.29028	3.56040
11	-0.47813	0.18293	0.07822	-0.02993	27.07525	2.73006
12	-0.15749	0.12094	0.02576	-0.01979	21.65114	0.64912

ANGLE	EXPOL	ERROR	CALPOL	CHISQR
19.9850	-0.1352	0.0103	-0.1406	0.2710
24.3040	-0.2112	0.0202	-0.1812	2.2040
28.4730	-0.2375	0.0278	-0.2392	0.0037
32.9680	-0.3595	0.0484	-0.3858	0.2943
43.8600	-0.1701	0.0664	-0.1238	0.4857
52.1110	-0.1711	0.0245	-0.1811	0.1678
61.0870	-0.2431	0.0318	-0.2643	0.4424
70.6010	-0.4099	0.0352	-0.3738	1.0530
81.0050	-0.1375	0.0479	-0.1704	0.4707
91.9660	0.2192	0.0525	0.2556	0.4796
101.4910	0.1512	0.0433	0.1495	0.0016
110.9500	0.1824	0.0428	0.1337	1.2959
118.7650	0.1862	0.0545	0.2819	3.0838
126.9020	0.4796	0.0648	0.3832	2.2110
135.9200	0.0506	0.0867	0.1896	2.5718
143.5760	0.2673	0.0606	0.2235	0.5218
150.4260	0.5464	0.0714	0.5696	0.1057
158.3440	0.9554	0.1094	0.9448	0.0094

CHISQR/DEG OF FREEDOM = 2.612 CHISQR/PT = 0.871

NEUTRON VECTOR ANALYZING POWER

TARGET ATOMIC MASS	32.06 amu
INCIDENT ENERGY	17.00 MeV
EXCITATION ENERGY	-2.23 MeV
J^{π}	2+

LMAX = 7

L	B(L)	DB(L)	REDB(L)	REDDB(L)	REGCC	FVAL
1	-0.17331	0.15887	1.00000	-0.91668	0.00000	17.00000
2	-0.24615	0.12196	1.42029	-0.70370	3.38639	3.21206
3	0.09792	0.10047	-0.56500	-0.57971	2.12625	2.02495
4	0.13220	0.09344	-0.76282	-0.53918	5.01904	10.85415
5	-0.03894	0.09246	0.22467	-0.53350	10.56932	0.67504
6	0.05619	0.08346	-0.32420	-0.48159	8.19488	1.33017
7	0.13678	0.06022	-0.78920	-0.34746	7.85200	13.44001

ANGLE	EXPOL	ERROR	CALPOL	CHISQR
21.1640	-0.0229	0.0930	0.0501	0.6154
26.1370	0.0832	0.1299	0.0286	0.1767
31.1580	0.0234	0.1140	-0.0023	0.0510
36.1120	-0.0131	0.0818	-0.0353	0.0734
41.1550	-0.0682	0.0823	-0.0632	0.0037
51.2470	-0.0732	0.1034	-0.0796	0.0039
61.2670	-0.0881	0.1278	-0.0573	0.0581
71.3510	-0.1127	0.1398	-0.0878	0.0317
81.3040	-0.2189	0.1863	-0.2401	0.0129
91.4090	-0.2142	0.2087	-0.3668	0.5347
101.5320	-0.4517	0.2760	-0.0951	1.6698
111.6310	0.4860	0.1701	0.4004	0.2530
119.5830	0.4378	0.1890	0.4924	0.0833
127.4080	0.3824	0.1504	0.3209	0.1672
136.1650	-0.0290	0.1957	0.0659	0.2354
143.8470	-0.0326	0.1151	-0.0590	0.0527
150.5100	-0.0922	0.1250	-0.0450	0.1423
158.1580	0.1922	0.2298	0.1050	0.1441

CHISQR/DEG OF FREEDOM = 0.392 CHISQR/PT = 0.239

LIST OF REFERENCES

Aleonard 1970 — M. M. Aleonard, D. Castera, P. Hubert, F. Leccia, P. Mennrath, Nucl. Phys. A146(1970)90.

Bar-Touv 1969 — J. Bar-Touv and A. Goswami, Phys. Lett. 28B(1969)391.

Becchetti 1969 — F. D. Becchetti, Jr., and G. W. Greenlees, Phys. Rev. 182(1969)1190.

Bevington 1969 — P. Bevington, Data Reduction and Error Analysis for the Physical Sciences, (New York: McGraw-Hill, 1969).

Beyerle 1981 — A. Beyerle, Ph.D. Dissertation, North Carolina State University (1981).

Block 1963 — B. Block and H. Feshback, Ann. Phys. 23(1963)47.

BLC-81 — Bruyeres-le-Châtel annual report, Report CEA-R-5144 (1981)70.

BLC-82 — Private communications with members of the group at Bruyeres-le-Châtel (1982).

Bohr 1969 — A. Bohr and B. R. Mottelson, Nuclear Structure, Vol. I, (New York: W. A. Benjamin, Inc. 1969).

Böttcher 1983 — J. Böttcher, H. Blank, E. Finckh, C. Forstner, W. Jaumann, G. Schall, H. Scheuring, U. Schneidereit, K. Stauber, A. Weipert, W. Tornow, and E. Woye, J.

Phys. G: Nucl. Phys. 9(1983)L65.

Browne 1978 — E. Browne, J. M. Dairiki, R. E, Doebler, A. A. Shihab-Eldin, L. J. Jardine, J. K. Tuli, and A. B. Buyrn, Table of Isotopes, 7 th ed., eds. C. M. Lederer and V. S. Shirley (New York: John Wiley and Sons, Inc. 1978).

Bulski 1982 — G. Bulski, W. Grum, J. W. Hammer, H. Postner, G. Schleussner, and E. Speller, Proceedings of the International Conference on Nuclear Data for Science and Technology, (Boston: D. Reidel Publishing Company, 1982)783.

Byrd 1978 — R. C. Byrd, Ph.D. Dissertation, Duke University (1978).

Byrd 1983 — R. C. Byrd, P. W. Lisowski, W. Tornow, and R. L. Walter, Nucl. Phys. A404(1983)29.

Coetzee 1972 — W. F. Coetzee, M. A. Meyer, and D. Reitmann, Nucl. Phys. A185(1972)644.

Cohen 1958 — B. L. Cohen and A. G. Rubin, Phys. Rev. 111(1958)1568.

De Leo 1979 — R. De Leo, G. D'Erasmo, A. Pantaleo, G. Pasquariello, G. Viesti, M. Pignanelli, and H. V. Geramb, Phys. Rev. C19(1979)646.

De Leo 1980 — R. De Leo, G. D'Erasmo, E. M. Fiore, G. Guarino, A. Pantaleo, and S. Micheletti, Il Nuovo Cimento 59A

(1980)101.

De Swiniarski 1973 R. de Swiniarski, H. E. Conzett, C. R. Lamontagne, B. Frois, and R. J. Slobodrian, Can. J. of Phys. 51 (1973)1293.

De Swiniarski 1976a R. de Swiniarski, F. G. Resmini, D. L. Hendrie, and A. D. Bacher, Nucl. Phys. A261(1976)111.

De Swiniarski 1976b R. de Swiniarski and D. L. Pham, Lett Al Nuovo Cimento 16(1976)391.

DeVito 1983 R. P. DeVito, Sam M. Austin, U. E. P. Berg, R. De Leo, and W. A. Sterrenburg, Phys. Rev. C28(1983)2530; and private communications.

Duhm 1968 H. H. Duhm, Nucl. Phys. A118(1968)563.

El-Kadi 1981 El-Kadi, Ph.D. Dissertation, Duke University (1981).

El-Kadi 1983 S. M. El-Kadi, C. E. Nelson, F. O. Purser, R. L. Walter, A. Beyerle, C. R. Gould, and L. W. Seagondollar, Nucl. Phys. A390(1982)509.

ENDF/B-V Evaluations of silicon and sulfur, (available from NNDC, Brookhaven National Laboratory).

Endt 1978 P. M. Endt and C. van der Leun, Nucl. Phys. A310(1978)340.

Fabrici 1980 E. Fabrici, S. Micheletti, M. Pignanelli, F. G. Resmini, R. De Leo, G. D'Erasmo, A. Pantaleo, J. L. Escudié,

and A. Tarrats, Phys. Rev. C21(1980)830.

Floyd 1982 C. E. Floyd, R. L. Walter, and R. G. Seyler, Bull. Amer. Phys. Soc. 27(1982)722.

Floyd 1983 C. E. Floyd, P. P. Guss, R. C. Byrd, K. Murphy, R. L. Walter, and J. P. Delaroche, Phys. Rev. C28 (1983)1498.

Garvey 1969 G. T. Garvey, K. W. Jones, L. E. Carlson, A. G. Robertson, and D. F. H. Start, Phys. Lett. 29B (1969)108.

Garvey 1971 G. T. Garvey, K. W. Jones, L. E. Carlson, D. A. Hutcheon, A. G. Robertson, and D. F. H. Start, Nucl. Phys. A160(1971)25.

GI69 S. M. Grimes, Nucl. Phys. A124(1969)369.

Gilbert 1965 A. Gilbert and A. G. W. Cameron, Canadian J. of Phys., 43(1965)1446.

Glasgow 1970 D. W. Glasgow and D. G. Foster, Jr., Phys. Rev. C3 (1970)604.

Glendinning 1980 S. G. Glendinning, Ph.D. Dissertation, Duke University (1980).

Gould 1981 C. R. Gould, L. G. Holzsweig, S. E. King, Y. C. Lau, R. V. Poore, N. R. Roberson, and S. A. Wender, IEEE Trans. Nucl. Sci., NS-28 No. 5, (1981)3708.

Gruppelaar 1977 — H. Gruppelaar and G. Reffo, Nucl. Science and Engineering 62(1977)62.

Guss 1982a — P. P. Guss, Ph.D. Dissertation, Duke University (1982).

Guss 1982b — P. P. Guss, C. E. Floyd, K. Murphy, C. R. Howell, R. S. Pedroni, G. M. Honoré, H. G. Pfutzner, G. Tungate, R. C. Byrd, R. L. Walter, J. P. Delaroche, Phys. Rev. C25(1982)2854.

Haouat 1982 — G. Haouat, Ch. Lagrange, Y. Patin, R. de Swiniarski, F. Dietrich, and A. Virdis, Proceedings of the International Conference on Nuclear Data for Science and Technology, (Boston: D. Reidel Publishing Company, 1982)796; and private communications.

Häusser 1971 — O. Häusser, T. K. Alexander, A. B. McDonald, and W. T. Diamond, Nucl. Phys. A175(1971)593.

Hodgson 1971 — P. E. Hodgson, Nuclear Reactions and Nuclear Structure, (London: Oxford Univ. Press, 1971).

Hogue 1977 — H. H. Hogue, Ph.D. Dissertation, Duke University (1977).

Holzsweig 1981 — L. G. Holzsweig and R. V. Poore, IEEE Trans. Nucl. Sci., NS-28 No. 5, (1981)3815.

Hopkins 1971 — J. C. Hopkins and G. Breit, Nucl. Data Tables A9 (1971)137.

Hosono 1982 — K. Hosono, N. Matsuoka, K. Hatanaka, T. Saito, T. Noro,

M. Kondo, S. Kato, K. Okada, K. Ogino, and Y. Kadota, Phys. Rev. C26(1982)1440.

Howell 1982a — C. R. Howell, R. S. Pedroni, G. M. Honoré, K Murphy, R. C. Byrd, G. Tungate, and R. L. Walter, Bull. Am. Phys. Soc. 27(1982)543.

Howell 1982b — C. R. Howell and S. A. Wender, Nucl. Instr. and Meth. 195(1982)443.

Howell 1982c — C. R. Howell et al., TUNL annual report, TUNL XXI (Aug. 1982)133.

Howell 1983a — C. R. Howell and R. L. Walter, IEEE Trans. Nucl. Sci., NS-30 No. 2 (1983)1132.

Howell 1983b — C. R. Howell et al., TUNL annual report, TUNL XXII (Aug. 1983)113.

Ingebretsen 1971 — F. Ingebretsen, B. W. Sargent, A. J. Ferguson, J. R. Leslie, A. Henrikson, and J. H. Montague, Nucl. Phys. A161(1971)433.

King 1981 — S. E. King, Y. C. Lau, and C. R. Gould, IEEE Trans. Nucl. Sci., NS-28 No. 5, (1981)3822.

Klein 1982 — H. Klein, H. J. Brede, and B. R. L. Siebert, Nucl. Instr. and Meth. 193(1982)635.

Kliczewski 1978 — S. Kliczewski and Z. Lewandowski, Nucl. Phys. A304 (1978)269.

Lane 1957 — A. M. Lane, Rev. Mod. Phys. 29(1957)191.

Lane 1962 — A. M. Lane, Phys. Rev. Lett. 8(1962)171; Nucl. Phys. 35(1962)676.

Lane 1964 — A. Lane and B. Block, Phys. Rev. Lett. 12(1964)334.

Larson 1980 — D. C. Larson, D. M. Hetrick, and J. A. Harvey, Bull. Amer. Phys. Soc. 25(1980)543; and private communication.

Lee 1972 — H. C. Lee and R. Y. Cusson, Annals of Phys. 72(1972)353.

Lejeune 1974 — C. Lejeune Nucl. Instr. and Meth. 116(1974)417.

Lisowski 1975 — P. W. Lisowski, R. L. Walter, C. E. Busch, and T. B. Clegg, Nucl. Phys. A242(1975)298.

Lombard 1973 — R. M. Lombard and J. Raynal, Phys. Rev. Lett. 31 (1973)1015.

MA63 — B. Mainsbridge, T. W. Bonner, and T. A. Rabson, Nucl. Phys. 48(1963)83.

Mann 1979 — F. M. Mann, HEDL-TME 78-83 UC-79d, Hanford Engineering Development Laboratory, Richland, WA (1979).

Marmier 1969 — P. Marmier and E. Sheldon, Physics of Nuclei and Particles Vol. I, (New York: Academic Press Inc., 1969).

Marmier 1971 — P. Marmier and E. Sheldon, Physics of Nuclei and

Particles Vol. II, (New York: Academic Press Inc., 1971).

Martin 1968 — J. Martin, D. T. Stewart, and W. M. Currie, Nucl. Phys. A113(1968)564.

McFadden 1966 — L. M. McFadden and G. R. Satchler, Nucl. Phys. 84 (1966)177.

Mermaz 1969 — M. C. Mermaz, C. A. Whitten, Jr., and D. A. Bromley, Phys. Rev. 187(1969)1466.

MI71 — D. W. Mingay, J. P. J. Sellschop, and P. M. Johnson, Nucl. Instr. and Meth. 94(1971)497.

Milner 1979 — W. T. Milner, IEEE Trans. Nucl. Sci., NS-26 No. 1, (1979)1445.

Obst 1972 — A. W. Obst and J. L. Weil, Phys. Rev. C7(1972)1076.

Ohlsen 1973 — G. G. Ohlsen and P. W. Keaton, Jr., Nucl. Instr. and Meth. 109(1973)41.

Olin 1974 — A. Olin, O. Häusser, T. K. Alexander, A. J. Ferguson, and W. Witthuhn, Nucl. Phys. A221(1974)555.

Ollerhead 1970 — R. W. Ollerhead, T. K. Alexander, and O. Häusser, Can. J. Phys. 48(1970)47.

Perey 1963a — F. G. Perey, Phys. Rev. 131(1963)745.

Perey 1963b — C. M. Perey and F. G. Perey, Phys. Rev. 132(1963)755.

Perey 1974 — F. G. Perey, Nuclear Spectroscopy and Reactions, Part B, ed. Joseph Cerny (New York: Academic Press 1974).

Rapaport 1977 — J. Rapaport, J. D. Carlson, D. Bainum, T. S. Cheema, and R. W. Finlay, Nucl. Phys. A286(1977)232.

Rapaport 1979 — J. Rapaport, V. Kulkarni, and R. W. Finlay, Nucl. Phys. A330(1979)15.

Rapaport 1982 — J. Rapaport, Phys. Report 87(1982)25.

Raynal 1979 — J. Raynal, code ECIS79 (unpublished).

Roberson 1981 — N. R. Roberson and S. E. Edwards, IEEE Trans. Nucl. Sci., NS-28 No. 5, (1981)3834.

Sakaguchi 1982 — H. Sakaguchi, M. Nakamura, K. Hatanaka, A. Goto, T. Noro, F. Ohtani, H. Sakamoto, H. Ogawa, and S. Kobayashi, Phys. Rev. C26(1982)944.

Satchler 1969 — G. R. Satchler, Isospin in Nuclear Physic, ed. D. H. Wilkinson (Amsterdam: North-Holand 1969).

Stelson 1965 — P. H. Stelson and L. Grodzins, Nucl. Data Sheets 1 (1965)21.

Tailor 1982 — R. C. Tailor, Ph.D. Dissertation, Ohio University (1982).

Tamura 1965 — Taro Tamura, Rev. of Mod. Phys. 37(1965)679.

Tamura 1966 — Taro Tamura, Supp. of the Prog. of Ther. Phys. 37 and 38 (1966)383.

Thompson 1977 W. J. Thompson and J. S. Eck, Phys. Lett. 67B(1977)151.

Toba 1978 Yoshiyuki Toba, Harutaka Sakaguchi, Akira Goto, Fumihiko Ohtani, Noriyoshi Nakanishi, Norio Kishida, Masaharu Yasue, and Takeo Hasegawa, J. of Phys. Soc. of Japan 45(1978)367.

Trainor 1973 T. Trainor, Ph.D. Dissertation, University of North Carolina at Chapel Hill (1973).

Van Oers 1977 W. T. H. Van Oers, Huang Haw, N. E. Davison, A. Ingemarsson, B. Fagerstrom, and G. Tibell, Phys. Rev. C10(1974)307.

Wender 1980 S. A. Wender, C. E. Floyd, T. B. Clegg, and W. R. Wylie, Nucl. Instr. and Meth. 174(1980)341.

Wender 1981 S. A. Wender, IEEE Trans. Nucl. Sci., NS-28 No. 2, (1981)1465.

Woye 1980 E. Woye and W. Tornow, private communications (1980).

Yamanouti 1977 Y. Yamanouti, Nucl. Phys. A283(1977)23.

BIOGRAPHY

Calvin Rudolph Howell

PERSONAL: Born in Warrenton, N.C., December 7, 1955

EDUCATION: B.S. Davidson College, 1978

M.A. Duke University, 1980

POSITIONS: Research Assistant, Duke University, 1980-1984

Physics Instructor, University of North Carolina, at Chapel Hill, summers 1982-1983

SAAP; a special program for minority students

Teaching Assistant, Duke University, 1979-1980

Lab Assistant, Naval Research Laboratory, Washington, D.C., summers 1975-1979

MEMBERSHIPS: Omicron Delta Kappa (national honorary service organization)

Sigma Pi Sigma

American Physical Society

Sigma Xi

PUBLICATIONS:

1. "Measurements of Analyzing Power for $^{2}H(\vec{n},n)^{2}H$ Scattering at 14.1 MeV and Comparisons to $^{2}H(\vec{p},p)^{2}H$", W. Tornow, R.C. Byrd, C.R. Howell, R.S. Pedroni, and R.L. Walter, Physical Review C27(1983)2439.

2. "Spin-Orbit Deformations Deduced from Analyzing Powers for Inelastic Neutron Scattering from ^{54}Fe", P.P. Guss, C.E. Floyd, K. Murphy, C.R. Howell, R.S. Pedroni, G.M. Honore', H.G. Pfutzner, G. Tungate, R.C. Byrd, R.L. Walter, and J.P. Delaroche, Physical Review C25(1982)2854.

3. "Analyzing Powers for Neutron Elastic Scattering at Forward Angles", C.E. Floyd, P.P. Guss, K. Murphy, C.R. Howell, R.C. Byrd, G. Tungate, S.A. Wender, R.L. Walter and T.B. Clegg, Physical Review C25 (1982)1682.

4. "Neutron Elastic and Inelastic Scattering Cross Sections for Carbon-13 between 10 and 18 MeV", J.H. Dave', C.R. Gould, L.W. Seagondollar, C.R. Howell, R.S. Pedroni, F.O. Purser, and R.L. Walter, Nuclear Science and Engineering 80(1982)388-392.

5. "Simultaneous Measurements of Analyzing Powers and Differential Cross Sections for n + ^{28}Si", C.R. Howell and R.L. Walter, IEEE Transactions on Nuclear Science, NS-30(1983)1132.

6. "Analyzing Power Measurements for $^{2}H(\vec{n},n)^{2}H$ Scattering at 10 MeV Compared to Few-Nucleon Calculations and Data for $^{2}H(\vec{p},p)^{2}H$ Scattering", W. Tornow, C.R. Howell, R.C. Byrd, R.S. Pedroni, and R.L. Walter, Physical Review Letters 49(1982)312.

7. "A Linear Voltage Ramp Generator for a Three Stage Bunching System", C.R. Howell and S.A. Wender, Nucl. Instr. and Meth. 195(1982)443-446.

8. Semi-Automatic Network Analyzer, C. Howell, R. Gurney, and A. Elia, NRL Memorandum Report 4100, March 6, 1981.

ABSTRACTS:

1. "Differential Cross Section and Analyzing Power for the Scattering of 17 MeV Neutrons from ^{54}Fe and ^{58}Ni", R.S. Pedroni, C.R. Howell, G.M. Honoré, H.G. Pfützner, M.L. Roberts, R.C. Byrd, and R.L. Walter, at Fall meeting of the division of nuclear physics, Notre Dame, Indiana (1983), Bulletin of the American Physical Society (Bull. Am. Phys. Soc.) 28(1983)998.

2. "Scattering of 17-MeV Polarized Neutrons", C.R. Howell, R.S. Pedroni, G.M. Honoré, H.G. Pfutzner, R.C. Byrd, and R.L. Walter, at annual Spring meeting of the American Physical Society, Baltimore, Md. (1983), Bull. Am. Phys. Soc. 28(1983)736.

3. "Differential Cross Sections and Analyzing Powers for the Elastic Scattering of Neutrons from ^{89}Y", G.M. Honoré, R.S. Pedroni, C.R. Howell, H.G. Pfutzner, P.P. Guss, K. Murphy, R.C. Byrd, G. Tungate, and R.L. Walter, Bull. Am. Phys. Soc. 28(1983)736.

4. "A Linear Voltage Ramp for a Cyclotron Injector Source", C.R. Howell, at the NTA region II student symposium on The Futures in Science and Technology, Fort Meade, Md. (April 1983), co-sponsored by The National Security Agency (NSA), and The National Technical Association (NTA).

5. "The Scattering of Neutrons from Deuterons at 14 MeV", W. Tornow, R.C. Byrd, C.R. Howell, G.M. Honoré, R.S. Pedroni, and R.L. Walter, Bull. Am. Phys. Soc. 27(1982)700.

6. "Analyzing Power and Differential Cross Section Measurements for Neutron Elastic and Inelastic Scattering from Silicon", C.R. Howell, R.S. Pedroni, G.M. Honoré, K. Murphy, R.C. Byrd, G. Tungate, and R.L. Walter, Bull. Am. Phys. Soc. 27(1982)722.

7. "Differential Cross Sections and Analyzing Powers for the Elastic Scattering of Neutrons from ^{93}Nb", R.S. Pedroni, G.M. Honoré, C.R. Howell, P.P. Guss, K. Murphy, R.C. Byrd, G. Tungate, and R.L. Walter, Bull. Am. Phys. Soc.
27(1982)722.

8. "Spin-Orbit Deformations Deduced from Analyzing Powers for Inelastic Neutron Scattering from ^{54}Fe", P.P. Guss, C.E. Floyd, K. Murphy, C.R. Howell, R.S. Pedroni, G.M. Honoré, H.G. Pfutzner, G. Tungate, R.C. Byrd, R.L. Walter, and J.P. Delaroche, Bull. Am. Phys. Soc. 27 (1982)542.

9. "Scattering of 10-MeV Polarized Neutrons from Deuterons", W. Tornow, C.R. Howell, R.S. Pedroni, G.M. Honore', R.C. Byrd, and R.L. Walter, Bull. Am. Phys. Soc. 27(1982)543.

10. "Neutron Elastic Scattering from 1P-Shell Nuclei between 10-15 MeV", J.H. Dave', C.R. Gould, L.W. Seagondollar, S.G. Glendenning, C.R. Howell, R.S. Pedroni, F.O. Purser, and R.L. Walter, Bull. Am. Phys. Soc. 26(1981)551.

11. "A Linear Voltage Ramp Generator for the TUNL Three Stage Bunching System", C. Howell, S.A. Wender, and T.B. Clegg, Bull. Am. Phys. Soc. 26(1981)593.

12. "Accurate Forward Angle Measurements with Polarized Neutrons", C.E. Floyd, P.P. Guss, G. Tungate, R.C. Byrd, K. Murphy, C.R. Howell, S.A. Wender, and R.L. Walter, Bull. Am. Phys. Soc. 26(1981)623.

13. "Neutron Scattering from ^{208}Pb between 8 and 26 MeV", R.L. Walter, C.E. Floyd, P.P. Guss, K. Murphy, C. Howell, R.C. Byrd, G. Tungate, S.A. Wender, and T.B. Clegg, Bull. Am. Phys. Soc. 26(1981)1139.